INSTITUTE OF GEOSCIENCES

Source studies of small earthquakes in the AlpArray: CMT inversion, seismo-tectonic analysis and methodological developments

Gesa M. Petersen

Cumulative dissertation

to obtain the academic degree "doctor rerum naturalium" (Dr. rer. nat.)
in the scientific discipline Geophysics.

Submitted to the
Faculty of Mathematics and Natural Sciences
at the University of Potsdam, Germany.

Prepared at Section 2.1 - Physics of Earthquakes and Volcanoes,
Department of Geophysics, Helmholtz Centre Potsdam -
GFZ German Research Centre for Geosciences.
&
Institute of Geosciences, University of Potsdam, Germany.

Date and place of the disputation: Potsdam, October 01, 2021

Principal supervisor: Prof. Dr. Torsten Dahm, University of Potsdam
& GFZ Potsdam, Germany.
Second supervisor: Dr. Simone Cesca, GFZ Potsdam, Germany.

Reviewers: Prof. Dr. Torsten Dahm, University of Potsdam & GFZ Potsdam, Germany.
Prof. Dr. Jirí Zahradník, Charles University, Prague, Czech Republic.
Prof. Dr. Daniel Stich, Universidad De Granada, Spain.

Examining committee: apl. Prof. Dr. Frank Krüger, University of Potsdam, Germany.
Prof. Dr. Eva Eibl, University of Potsdam, Germany.
Prof. Dr. Oliver Korup, University of Potsdam, Germany.

https://doi.org/10.25932/publishup-52563
https://nbn-resolving.org/urn:nbn:de:kobv:517-opus4-525635

Statement of Originality

I hereby declare that this thesis is the product of my own work. All the assistance received in preparing this thesis and the sources used have been acknowledged. The work contained in this thesis has not been previously submitted for a PhD degree at any other higher education institution.

Potsdam, ______________

____

Gesa M. Petersen

Table of Contents

Abstract

Centroid moment tensor inversion can provide insight into ongoing tectonic processes and active faults. In the Alpine mountains (central Europe), challenges result from low signal-to-noise ratios of earthquakes with small to moderate magnitudes and complex wave propagation effects through the heterogeneous crustal structure of the mountain belt. In this thesis, I make use of the temporary installation of the dense AlpArray seismic network (AASN) to establish a work flow to study seismic source processes and enhance the knowledge of the Alpine seismicity. The cumulative thesis comprises four publications on the topics of large seismic networks, seismic source processes in the Alps, their link to tectonics and stress field, and the inclusion of small magnitude earthquakes into studies of active faults.

Dealing with hundreds of stations of the dense AASN requires the automated assessment of data and metadata quality. I developed the open source toolbox *AutoStatsQ* to perform an automated data quality control. Its first application to the AlpArray seismic network has revealed significant errors of amplitude gains and sensor orientations. A second application of the orientation test to the Turkish KOERI network, based on Rayleigh wave polarization, further illustrated the potential in comparison to a P wave polarization method.

Taking advantage of the gain and orientation results of the AASN, I tested different inversion settings and input data types to approach the specific challenges of centroid moment tensor (CMT) inversions in the Alps. A comparative study was carried out to define the best fitting procedures. The application to 4 years of seismicity in the Alps (2016-2019) substantially enhanced the amount of moment tensor solutions in the region. We provide a list of moment tensors solutions down to magnitude Mw 3.1. Spatial patterns of typical focal mechanisms were analyzed in the seismotectonic context, by comparing them to long-term seismicity, historical earthquakes and observations of strain rates. Additionally, we use our MT solutions to investigate stress regimes and orientations along the Alpine chain.

Finally, I addressed the challenge of including smaller magnitude events into the study of active faults and source processes. The open-source toolbox *Clusty* was developed for the clustering of earthquakes based on waveforms recorded across a network of seismic stations. The similarity of waveforms reflects both, the location and the similarity of source mechanisms. Therefore the clustering bears the opportunity to identify earthquakes of similar faulting styles, even when centroid moment tensor inversion is not possible due to low signal-to-noise ratios of surface waves or oversimplified velocity models. The toolbox is described through an application to the Zakynthos 2018 aftershock sequence and I subsequently discuss its potential application to weak earthquakes (Mw<3.1) in the Alps.

Zusammenfassung

Die Erforschung der Bruchmechanismen von Erdbeben in den Alpen bietet Einblicke in aktuelle tektonische Prozesse. Typischerweise niedrige bis mittlere Erdbebenmagnituden und die heterogene Krustenstruktur des alpinischen Gebirges erschweren die zu dieser Erforschung durchgeführten Momententensorinversionen. In dieser Dissertation stelle ich einen Arbeitsablauf vor, mit dem ich die Bruchprozesse von Erdbeben zwischen 2016 und 2019 studiert habe. Datengrundlage bildet dabei das temporäre AlpArray Netzwerk (AASN - AlpArray seismic network). Die kumulative Dissertation besteht aus vier Publikationen, die sich einerseits mit den Möglichkeiten und Herausforderungen von großen seismischen Netzwerken und andererseits mit der Erforschung der Bruchprozesse beschäftigen. Dabei wird sowohl auf die Verbindung von den Herdmechanismen und anderen Informationen wie Seismizität, Tektonik und Spannungsfeld eingegangen, als auch untersucht, wie kleinere Erdbeben unser Wissen erweitern können.

Die Nutzung der großen Anzahl von Sensoren des AASN erfordert eine sorgfältige Kontrolle von Wellenformdaten und Stations-Metadaten. Um diese aufwändige Aufgabe weitmöglichst zu automatisieren, habe ich die open source toolbox *AutoStatsQ* entwickelt. Die Verwendung von *AutoStatsQ* zur Überprüfung des AASN zeigte mehrere signifikante Fehler in den Wellenform-Amplituden und in den Orientierungen der Horizontalkomponenten der Sensoren. Bei einer zweiten Anwendung des Orientierungstests von *AutoStatsQ* auf das türkische KOERI Netzwerk zeigten sich ebenfalls zahlreiche fehlerhaft orientierte Sensoren. Ein Vergleich mit einer zweiten Methode, basierend auf P-Wellen anstatt von Rayleigh-Wellen, zeigt weitestgehend übereinstimmende Ergebnisse.

Basierend auf der Datenqualitätsstudie des AASN werden in der dritten Publikation systematisch verschiedene Einstellungen (z.B. Frequenzbänder, Datentypen, Azimuthale Abdeckung) für Momententensorinversionen getestet und vergleichen. Anschließend wurden Bruchprozesse von Erdbeben zwischen 2016 und 2019 mit Magnituden ab Mw 3.1 analysiert. Zur Interpretation der Ergebnisse im seismotektonischen Zusammenhang werden zusätzlich ältere Momententensorlösungen, Seismizitätskataloge ab 1970, historische Erdbeben und Deformation basierend auf Satellitendaten betrachtet.

Aufgrund des Signal-Rausch-Verhältnisses von Oberflächenwellen müssten im Falle von Erdbeben mit kleineren Magnituden ($Mw<3.1$) höherfrequentere Raumwellen genutzt werden. Je höher der Frequenzbereich, desto größer sind die Einflüsse von Heterogenitäten entlang der Laufwege, sodass einfache 1-D Geschwindigkeitsmodelle nicht ausreichen. Um trotzdem kleinere Erdbeben in die Studien von aktiven Störungen einzubeziehen, haben wir die open-source toolbox *Clusty* entwickelt. Diese nutzt die Ähnlichkeit von Wellenformen in einem seismischen Netzwerk, um Erdbeben zu gruppieren. Die Ähnlichkeit von Wellenformen zweier Erdbeben über ein Netzwerk resultiert dabei sowohl aus der Ähnlichkeit der Herdmechanismen als auch aus der Lokation der Beben. Der Ketten-ähnliche clustering Ansatz ermöglicht es dabei, graduelle Wellenform-Unterschiede aufgrund von Lokationsänderungen entlang einer Störungszone zu berücksichtigen. Das clustering bietet folglich die Möglichkeit, Beben mit ähnlichen Herdmechanismen zu identifizieren und somit Störungszonen nachzuzeichnen. Die toolbox wird in der vierten Publikation anhand einer Anwendung auf die Nachbebensequenz des Zakynthos Bebens von 2018 beschrieben. Anschließend daran diskutiere ich, wie eine Anwendung auf die Alpen unsere Studien der Bruchprozesse und aktiven Störungen erweitern kann.

CHAPTER 1

Introduction

This thesis comprises four publications covering multiple aspects of the study of seismic sources and faults in the AlpArray project. The temporal deployment of the dense AlpArray seismic network, the low to moderate seismicity and the challenges arising from a heterogeneous crust and topography form the exceptional conditions of this work. After a brief introduction into the study area, the AlpArray project and MT inversion of small earthquakes, I will provide a detailed overview of the structure of this thesis.

1.1 The Alps: Tectonic and seismological overview

The Alpine orogenic belt in central Europe is characterized by a highly heterogeneous lithospheric structure [e.g. TRANSALP Working Group et al., 2002; Handy et al., 2010, 2015; Schmid et al., 2004; Hetényi et al., 2018]. Different tectonic units are located in close proximity to forearc and backarc sedimentary foreland basins. The Alpine mountains were tectonically shaped by the interaction of oceanic and continental lithospheric micro-plates in multiple stages of convergence between Africa and Europe, dominantly in Cretaceous and Triassic times. Geological studies indicate that the convergence of Europe and Africa caused a rotation of the detached Adriatic microplate, which is the upper plate in the subduction of European Tethys across the Alps [e.g. Le Breton et al., 2017; Schmid et al., 2008; Handy et al., 2015, and references therein]. The subduction involved the accretion of continental units and sediments of the European plate onto the upper Adriatic plate [e.g. Schmid et al., 2008; Handy et al., 2015]. The terranes of the Mesozoic Tethys ocean were compressed, rotated, faulted and stacked [e.g. Handy et al., 2010]. Subduction directions are reversed in the Apennines and the Dinarides, where the Adriatic plate was the lower plate during Neogene roll-back subduction and Cretaceous to Cenozoic orogenic evolution, respectively [e.g. Schmid et al., 2004; Handy et al., 2010]. Velocity profiles obtained from tomographic and seismic studies confirm a complex lithospheric structure across the Alps [e.g. Diehl et al., 2009; Fry et al., 2010; Molinari et al., 2015; Kästle et al., 2018].

The Northern Alps and the Southern Alps are separated by the Periadriatic line, a right-lateral strike-slip fault system [e.g. Handy et al., 2005] running from NW Italy to Slovenia (Fig. 1.1). With a length of about 700 km, it is one of the main faults of the Alps. Following geological conventions, the Alps north of the Periadriatic line are usually divided into the Western Alps, the Central Alps and the Eastern Alps [e.g. Le Breton et al., 2017; Handy et al., 2015]. South of the Periadriatic line, the Giudicarie-Lessini fault system forms the boundary between the central Southern Alps and the eastern Southern Alps [Viganò et al., 2008]. E-W oriented thrust faults are dominant in the SE Alps [Pondrelli et al., 2006; Cheloni et al., 2014], while NW-SE oriented right-lateral strike-slip faults are dominant along the Northern Dinarides [Pondrelli et al., 2006; Moulin et al., 2016].

Lombardi et al. [2008] obtain depths of the European Moho from receiver functions for the Central and Western Alps, ranging from less than 30 km beneath the Northern Alpine Foreland to a maximum depth of 55 km below the Europe-Africa suture zone in the Central Alps. The Moho of the Adriatic crust, south of the suture, is found at 35 to 45 km depth [Lombardi et al., 2008]. The TRANSALP seismic profile in the Eastern Alps similarly found a European Moho deepening from North to South from 35 km to 60 km at the suture zone and a Adriatic Moho at relatively stable depth of about 40 km [Kummerow et al., 2004]. Isolines follow roughly the bending of the Alpine arc [Lombardi et al., 2008], as also described by Spada et al. [2013].

Today the Alps and neighboring regions are characterized by varying tectonic movement in close proximity, which can be observed by surface displacements as well as by seismic activity. Surface displacement observations suggest a principal division of the eastern Southern Alps, which show significantly larger horizontal movement, from the Central to Western Alps [e.g. Cheloni et al., 2014; Serpelloni et al., 2016]. The collision of the Adriatic micro-plate and the Eurasian plate is mainly accommodated in the eastern Southern Alps [Cheloni et al., 2014]. Vertical surface displacements from GNSS data show a general correlation between uplift and topographic features across the Alps [Sternai et al., 2019]. Uplift rates of 2-2.5 mm/a are observed in the NW and Central Alps, while uplift rates are lower in the E to SW Alps (about 1 mm/a) [Sternai et al., 2019]. Horizontal velocities point at the shortening and crustal thickening in the eastern Southern and Eastern Alps and very little deformation in the Central and Western Alps, thus implying that the observed uplift patterns in the Central and Western Alps result from other mechanisms [Sternai et al., 2019]. These possible mechanisms comprise isostatic adjustment to deglaciation and erosion, as well as mantle-related processes such as slab detachment or asthenospheric upwelling [Sternai et al., 2019]. Furthermore, Anderlini et al. [2020] propose that the inter seismic accumulation of elastic strain at thrust faults significantly contributes to the uplift in the SE Alps.

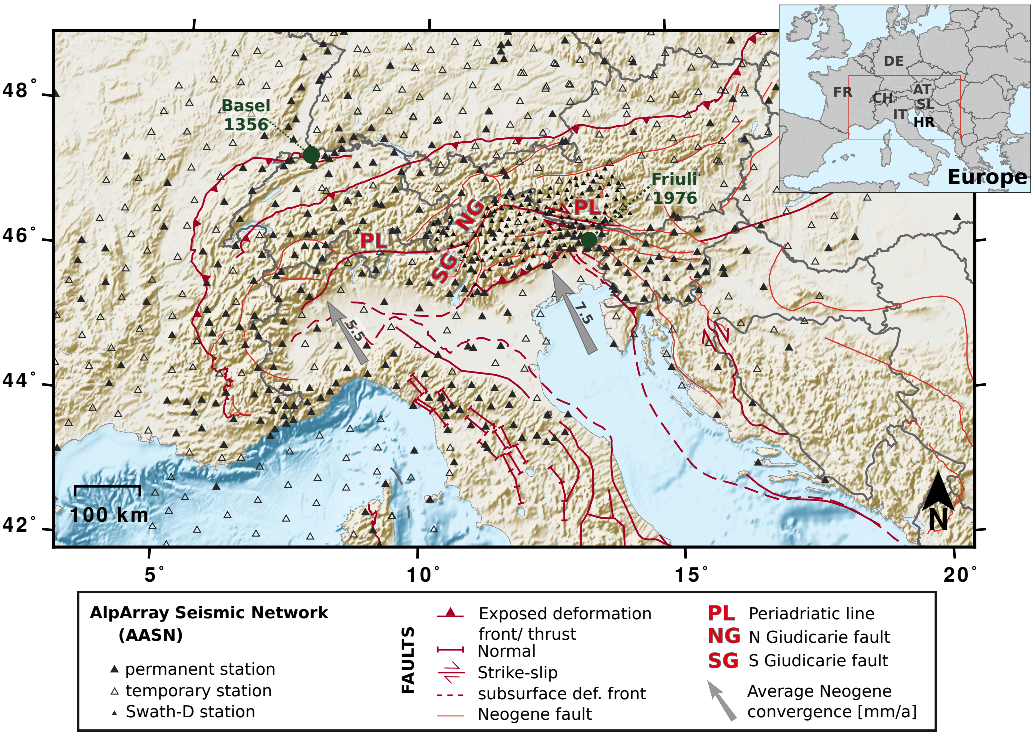

Figure 1.1: The AlpArray and Swath-D seismic networks. Arrows indicate average Neogene (20-0 Ma) Adria-Europe convergence rates from Le Breton et al. [2017]. Exposed and subsurface faults simplified from Schmid et al. [2004, 2008]; Handy et al. [2010, 2015]; Patacca et al. [2008]. Topographic data from SRTM-3 [Farr et al., 2007] and ETOPO1 [Amante and Eakins, 2009]. Figure modified from Petersen et al. [2021a].

Local patterns of seismic activity across the Alps have been described in many studies (for an overview see also Introduction in Petersen et al. [2019], chapter 6). All types of faulting mechanisms, namely thrust faulting, normal faulting and strike-slip faulting, can be observed across the mountain belt and imply changes of the dominant stress regimes from N-S compression in the SE Alps [e.g. Cheloni et al., 2014] to extensional regimes in the W Alps [e.g. Delacou et al., 2004; Sue et al., 2007; Mathey et al., 2020]. Seismic activity in the Alps is generally of small to moderate magnitudes. Only few events with magnitudes Mw>4.0 occur per year. Largest earthquakes and increased seismicity rates are observed in the SE Alps, at the location of the Mw 6.5 Friuli earthquake in 1976 [Poli and

Zanferrari, 2018], and at the transition between the SE Alps and the northern Dinarides. Seismicity in the SE Alps occurs mainly on E-W to NE-SW oriented thrust faults, which separate the Venetian-Friulian plain from the Eastern Alps [e.g. Pondrelli et al., 2006; Cheloni et al., 2014]. According to Cheloni et al. [2014] the thrust front absorbs about 70 % of the convergence between the Adria and the Eurasia plate. Seismicity in the Northern Dinarides occurs dominantly on the NW-SE oriented strike-slip faults. Moderately increased rates of seismic activity are further observed in the region around Lake Garda [Viganò et al., 2008] and in parts of the Western Alps [Delacou et al., 2004], while seismicity is particularly low in the Eastern Alps north of the Periadriatic line.

The complex seismic and tectonic activity across the mountain range is not simply dominated by the main active deformation fronts at the southern and northern margin of the Alps, but also occurs on smaller fault systems across the entire region. This thesis aimes for a broad perspective of seismic activity at minor and major fault systems, and a regional description of dominant faulting types and related deformation regimes across the entire mountain range.

1.2 The AlpArray initiative

Despite many geological and geophysical studies on local crustal structures, the knowledge and understanding of mountain building processes of the entire Alpine orogen are still limited. The AlpArray initiative aims at providing insights into the complex mountain building processes from initial to final phases, including interactions of small plates and micro-ocean subduction (Hetényi et al. [2018]; http://www.alparray.ethz.ch/en/research/overview/, last access Feb. 2021).

The AlpArray project is a European initiative to study the orogenesis of the Alps and related geodynamic and geophysical processes like seismic activity, mantle dynamics, plate motion and surface processes following multi-disciplinary approaches [Hetényi et al., 2018]. More than 35 European institutes joined resources to operate the AlpArray Seismic Network (AASN), which consists of more than 600 stations. Permanent regional networks were densified by more than 200 temporary installations [AlpArray Seismic Network, 2015] to obtain an average spacing of <60 km across the entire study area (Fig. 1.1). These temporary stations were installed between summer 2015 and 2017 and were operated for several months (OBS stations) up to several years. Minimum operation times until end of 2018 were planned to assure two years of simultaneous operation [Hetényi et al., 2018], while some temporary stations were operated until end of 2019 or even longer. Installation periods varied due to heterogeneous funding schemes [Hetényi et al., 2018]. The permanent stations of the AlpArray are part of existing European regional networks (RD, GU , CZ, ST, G, CH, OE, MN, HU, GE, RF, FR, IV, BW, SX, NI, TH, OX). The AASN is complemented by the denser Swath-D network in the eastern Alps [Heit et al., 2021], which was operated between summer 2017 and 2019 and covered the region with 163 stations with spacing of approximately 15 km.

Belonging to various instrument pools, the temporary stations of the AlpArray and the Swath-D comprise different sensor types and were set up in heterogeneous environments ranging from open-field to indoor installations in remote Alpine cabins as well as in basements or buildings in villages. Noise levels vary significantly. For the orientation of the sensors both hand held compasses and gyro compasses were used [Molinari et al., 2016; Fuchs et al., 2016; Vecsey et al., 2017; Heit et al., 2021]. Seismic studies rely on correct seismic data and station metadata. The assessment of these is an important task in the case of such a large seismic network. For this purpose, I developed the Automated Station Quality control toolbox *AutoStatsQ* [Petersen et al., 2019], which was published in 2019 and is presented as the first chapter of the main part of this thesis (chapter 4). The outstanding dense seismic network with a large number of seismic stations enables detailed seismic studies including high quality moment tensor inversions across the entire Alpine mountain belt and neighboring areas (see also chapter 6).

1.3 Moment tensor inversions of earthquakes from the Alpine region

Source processes of earthquakes are commonly approximated as seismic point sources, which can be represented by a second order tensor. This seismic moment tensor (MT) is a 3x3 matrix that describes the seismic point source based on generalized force couples [e.g. Dahm and Krüger, 2014]. The prevailing problem of seismic source studies such as moment tensor inversion is to isolate the information on the source process from path effects and instrument effects on the recorded waveforms [Jost and Herrmann, 1989]. The applied moment tensor inversion approach [Heimann et al., 2018] uses time domain displacement waveform data as well as extracted features (e.g. amplitude spectra and envelopes) as input to a non-linear inversion procedure. The path effect on the wave propagation between source and receiver, more precisely the impulse response of the Earth for a point source excitation, is described by Green's functions calculated for a representative velocity model. The Green's functions can be computed in advance to save time during the inversion [Heimann et al., 2019]. The observed seismograms, which are usually measured proportional to velocity, are integrated to displacement and deconvolved with the instrument response function. Correct instrument response functions are required for any moment tensor inversion.

Moment tensor inversions of moderate earthquakes in the Alps are routinely performed by several regional and global research institutes. GEOFON [Quinteros et al., 2021] regularly publishes MT solutions for the entire region for earthquakes with magnitudes above Mw 4.0, including a few smaller events. INGV provides MT solutions for earthquakes with ML≥3.5 occurring in Italy and in the neighboring countries [Scognamiglio et al., 2006, http://terremoti.ingv.it/en/help#TDMT, last access March 2021]. SED and ARSO publish a small number of MT solutions along with first motion mechanisms for Switzerland and Slovenia in yearly reports [e.g. Diehl et al., 2021; Ministrstvo za okolje in prostor Agencija RS za okolje, 2020]. SISMOAZUR provides MT solutions for earthquakes starting in 2019 [Delouis, 2014, http://sismoazur.oca.eu/focal_mechanism_emsc, last access March 2021]. The European-Mediterranean Regional Centroid-Moment Tensors catalog (EM-RCMT) lists MT solutions for earthquakes with M≥4.5, including additionally a few smaller events (M>4) [Pondrelli, 2002, http://rcmt2.bo.ingv.it/, last access March 2021]. Lastly, the Global Centroid-Moment-Tensor (GCMT) project provides global MT solutions for earthquakes with M>5.0 [Dziewonski et al., 1981; Ekström et al., 2012, https://www.globalcmt.org/, last access March 2021]. These various research institutes use different inversion set-ups and tools, mostly relying on surface waves records at local to regional seismic stations. Uncertainties, if provided at all, are difficult to compare among solutions reported by different institutes. Additionally, focal mechanisms for the Alps and neighboring areas have been reported in local studies of active tectonics, mostly relying on P and S polarities or amplitude ratios instead of full waveform MT inversions [e.g. Reiter et al., 2018; Viganò et al., 2008; Pondrelli et al., 2006]. To our knowledge, no recent study focused on moment tensor solutions across the entire Alpine chain.

Moment tensor inversions of large earthquakes (Mw>5) are a routine task in seismology that can be automatized to a large degree. This allows fast preliminary solutions, which are for example used for tsunami warnings or a rapid estimate of destructions [e.g. Kanamori and Rivera, 2008]. Moment tensor inversion of smaller earthquakes (Mw<4.0) remains challenging. Across large parts of the Central and Eastern Alps, earthquake magnitudes are rarely exceeding Mw 3.5. Therefore, few MT solutions are available. Smaller earthquakes usually excite waveforms at higher frequencies. While for magnitudes between Mw 3.5 to Mw 4.0, surface waves may still have a sufficient signal-to-noise ratio (SNR) at local to regional distances, for smaller events, often body waves are inverted instead. Stich et al. [2003] performed moment tensor inversions for small to moderate events and found that the waveforms of small events (m_b 3.5-3.9) were often too noisy for regional MT inversions. Similar, Bentz et al. [2018] observed that full waveform inversions were unable to reproduce the observed seismograms of earthquakes with magnitudes between Ml 2.2 and 3.8 sufficiently well and explained this by small-scale heterogeneities beneath the geothermal field. They obtained reliable moment tensor solutions by combining the full waveforms with P-wave first-motion amplitudes.

The stability of MT solutions strongly depends on the availability of representative subsurface velocity models, on the heterogeneities, which may introduce path effects, and on the availability of a sufficient number of close stations [e.g. Stich et al., 2003]. Errors in the velocity models may introduce phase errors [Dufumier and Cara, 1995] and oversimplified models may hinder modeling higher frequency contents of the seismogram. Kühn et al. [2020] and Dost et al. [2020] recently presented methodological tests and full waveform based MT solutions for small earthquakes (Mw$\geq$2.0) in the Groningen gas field, Netherlands. They relied on a close and dense network with about 15 stations within the first 10 km distance and used frequency bands between 1 Hz and 4 Hz to emphasize body waves.

In the study area, besides the low to moderate seismicity, further challenges for MT inversions result from the heterogeneous crustal structure and the high relief. Effects of a heterogeneous crust and the topography on wave propagation are difficult to model and often hinder forward modeling synthetic waveforms at frequencies >0.1 Hz. In this thesis, I investigate approaches to handle these challenges in order to include earthquakes with magnitudes between Mw 3.0 and Mw 4.0 as well as below Mw 3.0 into the study of seismic sources in the Alps. In areas with either low to moderate seismic activity or in the case of short deployment times, including small earthquakes may provide vital information to study active faults. For this purpose, I investigate different inversion set-ups including tests on input data types, frequency ranges and azimuthal station coverages. I rely on the results of the network quality control to avoid introducing errors resulting from erroneous seismometer orientations, errors in amplitude gains or transfer functions. I present MT solutions for 75 earthquakes with Mw$\geq$3.1, discuss them in the seismotectonic context of the Alps and finally develop an approach to include smaller magnitude earthquakes into the study of active faults.

1.4 Structure of the thesis

This thesis is a cumulative work. After an overview of the objectives (chapter 2) and the methodology (chapter 3), the main part comprises three peer-reviewed publications and one manuscript accepted for publication (chapter 4-7). The studies are discussed jointly in chapter 8 with respect to the research questions, which are formulated in chapter 2. Finally, an outlook to ongoing and future work is provided in chapter 9.

1.4.1 Overview of publications included as chapters of this thesis

My contributions as first author or co-author are provided in gray colored text below each reference.

- **Publication 1**: **Petersen, G.M.**, Cesca, S. and Kriegerowski, M., 2019. Automated Quality Control for Large Seismic Networks: Implementation and Application to the AlpArray Seismic Network. Seismological Research Letters, 90, 3, pp. 1177-1190.
  https://doi.org/10.1785/0220180342

  G.M. Petersen developed and implemented the open source toolbox *AutoStatsQ*, performed the quality analysis of the AlpArray seismic network and the Swath-D, interpreted the results and wrote the first draft of the manuscript.

  Publication 1 is included as chapter 4 in this thesis. In order to prepare the dataset that is used to study moment tensors in the subsequent chapter, I developed a toolbox for automated quality control of huge seismic networks.

- **Publication 2**: Büyükakpinar, P., Aktar, M., **Petersen, G.M.**, and Köseoğlu, A., 2021. Orientations of Broadband Stations of the KOERI Seismic Network (Turkey) from Two Independent Methods: P- and Rayleigh-Wave Polarization. Seismological Research Letters, 92, 3, pp. 1512-1521.
  https://doi.org/10.1785/0220200362.

G.M. Petersen applied the open source toolbox *AutoStatsQ* (Publication 1) to obtain orientations of seismic stations and helped comparing them to the P-Wave Polarization analysis. Furthermore she contributed to the analysis of the results and helped preparing the manuscript.

Publication 2 (chapter 5) is a study of sensor misorientations of the KOERI network, Turkey. Besides the application of the orientation test of *AutoStatsQ* [Petersen et al., 2019], a second approach is used and results are systematically compared, which allows an independent verification of our method.

- **Publication 3**: **Petersen, G.M.**, Cesca, S., Heimann, S., Niemz, P., Dahm, T., Kühn, D., Kummerow, J., Plenefisch, T. AlpArray Working Group (2021): Regional centroid MT inversion of small to moderate earthquakes in the Alps using the dense AlpArray seismic network: challenges and seismotectonic insights. Solid Earth, 12, pp. 1233–1257.
  https://doi.org/10.5194/se-12-1233-2021

  G.M. Petersen performed the moment tensor inversions, conceptualized and developed the methodological tests, analyzed and discussed the results in the seismo-tectonic context and wrote the original draft of the manuscript.

  The third publication is included as chapter 6. This publication presents a study on centroid moment tensor inversion in the course of the AlpArray project. It includes extensive methodological tests and perform CMT inversions for four years of seismic data from 2016 to 2019. The CMT solutions are subsequently analyzed in the seismotectonic context of historical and recent seismicity, GNSS strain observations and stress inversion.

- **Publication 4**: **Petersen, G.P.**, Niemz, P., Cesca, S., Mouslopoulou, V. and Bocchini, G.M. (2021): Clusty, the waveform-based network similarity clustering toolbox: concept and application to image complex faulting offshore Zakynthos (Greece). Geophys. J. Int., 224, 3, pp. 2044-2059.
  https://doi.org/10.1093/gji/ggaa568.

  G.M. Petersen and P. Niemz jointly conceptualized the study, implemented the toolbox, performed the analyses and wrote the first draft of the manuscript. More specifically, G. Petersen implemented the handling of the toolbox as a command line tool with a configuration file for the settings; the handling of input data, metadata and optional picks, the computation of arrival times, the thresholds for the selection of events and stations, parts of the methods to compute the network similarity from the cross-correlation values (e.g. the Mth root following Stuermer et al. [2011]) and the option to stack multiple components/ phases. Further, she implemented several analysis and result plots (e.g. map views, waveform plots, KNN, cumulative moment and Silhouette score plots). What is mentioned here as implementation, in most case also includes the study of the theory and ideas behind it. In addition, G.M. Petersen performed the CMT inversions for representative events of each cluster. Concerning the writing of the manuscript, she wrote the first drafts of the paragraphs that are related to the implementation, analysis and discussion of the aforementioned contributions to the code; as well as those paragraphs on the study of active faults in general and on the study area of Zakynthos.

  Publication 4 is included as chapter 7. It presents a toolbox for the clustering of earthquakes based on the similarity of waveforms recorded across a network of seismic stations. The clustering allows grouping events with a similar mechanism even in cases where MT inversion is at its limit.

1.4.2 Additional relevant work

In addition to the above publications, which are included as chapters in this thesis, I contributed to further studies during the PhD project.

- **Publication 5**: Cesca, S., Letort, J., Razafindrakoto, H.N.T., Heimann, S., Rivalta, E., Isken, M.P., Nikkhoo, M., Passarelli, L., **Petersen, G.M.**, Cotton, F., Dahm, T., 2020. Drainage of a deep magma reservoir near Mayotte inferred from seismicity and deformation. nature geoscience, 13, pp. 87-93. https://doi.org/10.1038/s41561-019-0505-5.

G.M. Petersen applied the open source toolbox *AutoStatsQ* [Petersen et al. 2019] to assess the seismic data quality.

In publication 5 the *AutoStatsQ* toolbox was applied to assess the data quality prior to the study of a deep magma reservoir near Mayotte. The seismic study in this multidisciplinary work comprised single station and multi station approaches for relocation, exact depth analysis and MT inversion. For all tasks correct sensor orientations and amplitude gains are of great importance.

- **Publication 6**: Kriegerowski, M., **Petersen, G.M.**, Vasyura-Bathke, H., Ohrnberger, M., 2019. A Deep Convolutional Neural Network for Localization of Clustered Earthquakes Based on Multistation Full Waveforms. Seismological Research Letters, 90, 2A, pp. 510-516. https://doi.org/10.1785/0220180320.

  M. Kriegerowski and G. Petersen developed the project idea and wrote the first draft of the manuscript; and G. Petersen contributed to the implementation and analysis of the results.

  Publication six expands the methods and tools that are applied in the other studies by a deep neural network for the rapid localization of swarm earthquakes. The network was developed and trained with an earthquake swarm dataset from West Bohemia to provide hundreds of earthquake locations in few seconds. The application to a large dataset of small earthquakes (Ml$\geq$-0.8) points to it's potential with respect to other study areas with clustered seismic activity, such as for example the eastern Southern Alps. The architecture and setup of the neural network was designed as a flexible toolbox.

- **Publication 7**: Mouslopoulou, V., Bocchini, G.M., Cesca, S., Saltogianni, V., Bedford, J., **Petersen, G.M.**, Gianniou, M., Oncken, O., 2020. Earthquake swarms, slow slip and fault interactions at the western-end of the Hellenic subduction system precede the Mw 6.9 Zakynthos earthquake, Greece. Geochemistry, Geophysics, Geosystems, 21, e2020GC009243. https://doi.org/10.1029/2020GC009243.

  G.M. Petersen contributed by performing moment tensor inversions for about 100 earthquakes with magnitudes between Mw 3.9 and Mw 6.9.

  Publication seven is a multidisciplinary study dealing with a slow-slip event prior to the Mw 6.9 Zakynthos Earthquake, Greece in 2018. Seismic activity and fault interactions in the five years before the large earthquake are studied as well as the aftershock sequence. The fourth publication [Petersen et al., 2021b] is based on the catalog and relocations of the 1-year-long seismic activity after the main shock provided by this work.

CHAPTER 2

Objectives and research questions

In this chapter, the research questions and objectives of my doctoral project are presented and linked to the corresponding parts of the cumulative thesis. The research questions cover mainly two topics: (1) The opportunities and challenges arising from large seismic networks with respect to studies of local seismicity, and (2), the inversion of seismic source processes for small to moderate earthquakes and their link to tectonic processes. The arising questions can mostly be transferred to other studies on local to regional source processes of small to moderate earthquakes and/or to other large seismic networks and thus contribute to ongoing methodological developments for handling large datasets and smaller magnitudes. The results of this thesis are discussed with respect to the research questions in chapter 8.

① **Which challenges and opportunities arise from working with large seismic networks in local to regional seismic source studies?**

- **Background**: With a total of more than 600 stations the AlpArray seismic network is the largest seismic network ever operated in Europe [Hetényi et al., 2018]. The uniform distribution of seismic stations across the Alps improves the detection abilities of small earthquakes and allows performing source studies in areas that were poorly covered before. However, the large number of seismic stations pose challenges for quality assessment, which is required prior to reliable seismic studies.
- **Related chapters**: The AutoStatsQ toolbox is presented and applied to the AASN in chapter 4. The publication in chapter 6 shows how the network coverage is exploited to test different moment tensor inversion work flows.

② **How can the magnitude threshold of centroid moment tensor inversion in the Alps be lowered?**

- **Background**: Focal mechanisms of moderate magnitude earthquakes (Mw ≥ 4.0 or Mw > 3.5) are routinely provided by several European institutes and data centers, often within national boundaries. In order to lower the magnitude threshold and to perform homogeneous MT inversions across the entire study area, numerous methodological tests are implemented guidelines developed. We finally provide moment tensor solutions for events with magnitudes down to Mw 3.1 for the installation time span of the AASN.
- **Related chapter**: The publication in chapter 6 presents extensive testings on CMT inversion set-ups to lower the magnitude threshold.

③ **Which types of seismic source processes are typically observed across the Alps?**

- **Background**: Many studies of focal mechanisms in the Alps focus on local tectonic features. I follow a different approach and look at the bigger picture across the entire mountain belt. I study groups of similar mechanisms based on the CMT inversion results for four years of seismic data (2016-2019) and published moment tensor solutions by other European institutes of the last decades.

- **Related chapter**: In the publication in chapter 6 we interpret groups of moment tensor inversion solutions.

④ How are the seismic source processes linked to the tectonic evolution and present stress field of the Alps?

- **Background**: Due to low seismicity across wide areas of the Alps the link between seismic activity and the recent tectonic evolution on regional scale is not easy to infer. We try to obtain new insights by supporting our own moment tensor solutions with existing recent and historical seismic catalogs and GNSS data.
- **Related chapter**: I discuss the link between seismicity, focal mechanisms, GNSS data, stress inversion results and the tectonic evolution in the publication in chapter 6.

⑤ Is it possible to establish an (semi-)automated work flow of CMT Inversion in the Alps? Which steps must be included?

- **Background**: As mentioned in research question 2, focal mechanisms of moderate magnitude earthquakes are provided by several European institutes and data centers. These studies follow multiple different approaches and work flows. I develop guidelines and best practices reaching from quality control to the evaluation of moment tensors solutions and study of active faults. I hereby try to understand which processes can be automated.
- **Related chapters**: In the publication in chapter 4 and 6 I present the methodology and results of quality control and moment tensor inversion studies in the Alps. In chapter 7 we extend the source studies by a waveform based clustering approach. In the discussion I link all approaches to discuss if and how (semi-)automated work flows can be established.

⑥ How can earthquakes, for which MT inversion is not feasible, be included into seismic source and fault studies?

- **Background**: In the case of earthquakes with magnitude below Mw 3.0 the SNR of surface waves is mostly not sufficient to perform moment tensor inversions. In order to include higher frequency body waves instead, more detailed velocity models are required to achieve a good fit between forward modeled synthetic waveforms and the observed data. In an area with a complex crustal structure this may only be possible when detailed (3D) velocity models exist. In an area with only few Mw>4 events like the Alps, small magnitude events need to be considered in the study of seismic source processes to obtain insights into the extent and orientation of active faults.
- **Related chapters**: In the publication in chapter 7 we present a waveform based network similarity clustering toolbox, which serves the purpose of mapping faults. I discuss how the developed toolbox can be applied in the Alps to enhance our knowledge of active faults in the discussion (chapter 8) and in the outlook (chapter 9).

CHAPTER 3

Overview of developed and applied methods

In order to answer the research questions that were presented in the previous section, various methods were developed and applied, which cover three research fields (Fig. 3.1): (1) Automated quality control of seismic networks, (2) Moment tensor inversion and (3) Waveform-based clustering. For the first and third research field, new methodology was developed and implemented in form of open-source toolboxes. These toolboxes are based on the seismological Python library *Pyrocko* [Heimann et al., 2017]. Examples of other studies, in which the toolboxes were applied, are provided and discussed in the chapter 8. In the second research field I applied and adapted the open source probabilistic inversion tool *Grond* [Heimann et al., 2018] to perform CMT inversions in the Alps. I performed extensive tests on different inversion set-ups, investigated the resolution of double-couple (DC) and non-DC components and implemented some small new features. The technical details of all methods can be found in the according publications and manuscripts of this cumulative thesis.

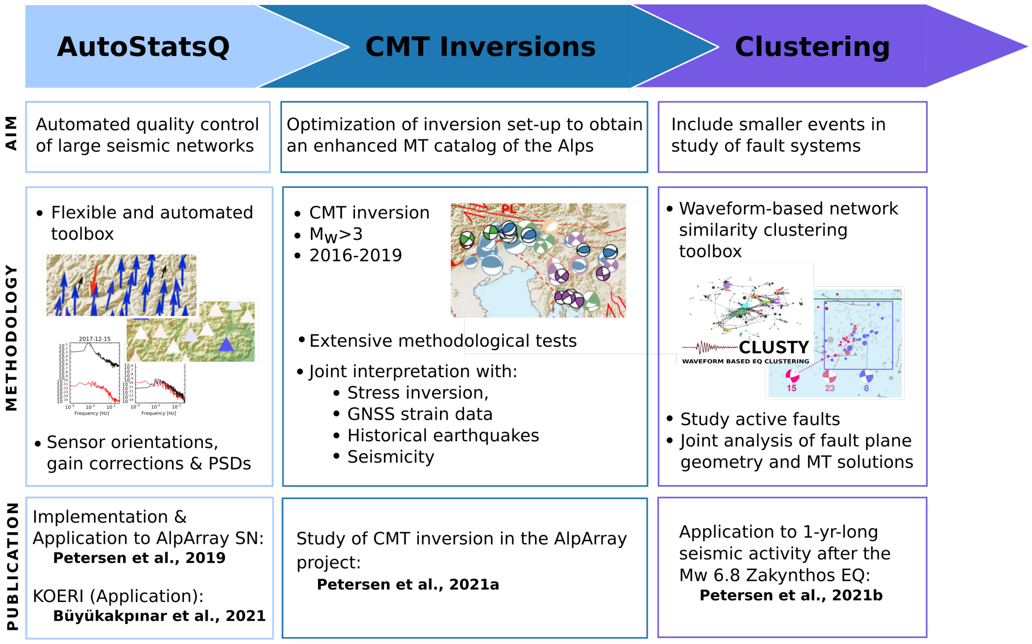

	AutoStatsQ	CMT Inversions	Clustering
AIM	Automated quality control of large seismic networks	Optimization of inversion set-up to obtain an enhanced MT catalog of the Alps	Include smaller events in study of fault systems
METHODOLOGY	• Flexible and automated toolbox • Sensor orientations, gain corrections & PSDs	• CMT inversion • $M_W>3$ • 2016-2019 • Extensive methodological tests • Joint interpretation with: • Stress inversion, • GNSS strain data • Historical earthquakes • Seismicity	• Waveform-based network similarity clustering toolbox • Study active faults • Joint analysis of fault plane geometry and MT solutions
PUBLICATION	Implementation & Application to AlpArray SN: **Petersen et al., 2019** KOERI (Application): **Büyükakpınar et al., 2021**	Study of CMT inversion in the AlpArray project: **Petersen et al., 2021a**	Application to 1-yr-long seismic activity after the Mw 6.8 Zakynthos EQ: **Petersen et al., 2021b**

Figure 3.1: Overview of the work flow of this thesis including applied methods and publications for the three research fields (1) Automated quality control of seismic networks, (2) Moment tensor inversions and (3) Waveform-based clustering.

① Toolbox *AutoStatsQ* - Automated quality control of large seismic networks

- Moment tensor inversions rely strongly on correct seismic data and metadata. Gain errors due to errors in the metadata, wrongly oriented seismometers, interchanged seismometer components or wrong transfer functions can significantly bias the results of seismic studies. However, manual checks of data and metadata quality are time consuming. Therefore, I developed the *AutoStatsQ* toolbox, which follows an automated work flow to check the quality of large seismic networks. This work flow ranges from an automated selection of teleseismic events, over data download from an FDSN server, to running tests on gain, sensor component orientations and power spectral densities (PSDs). Output for all tests is provided as figures and tables. The tool relies on teleseismic earthquakes to check amplitude gains, sensor orientations and event-PSDs.

- **Related chapters:** In chapter 6 I present the toolbox and its application to the AlpArray seismic network. In chapter 5 I applied the tool to check the orientations of the horizontal components of the stations of the KOERI network.

② **Centroid moment tensor inversion**

- I applied the open source inversion tool *Grond* [Heimann et al., 2018] to perform centroid moment tensor inversions in the AlpArray study area. I hereby systematically tested various input data types, frequency ranges, and the effect of varying azimuthal gaps. Furthermore, I studied the resolvability of non-DC components. I implemented some small features into the *Grond* code: The module *store_id_selector* for example allows an automated selection of Green's function databases in dependence of the earthquake location or using a predefined station-database mapping. To allow a further degree of automation, I extended the checks that are run prior to an inversion to check for a minimum number of available stations and to set a threshold of a maximum allowed azimuthal gap. Furthermore, I implemented smoothed envelopes for our applications. While the first modification was added to the main code of *Grond*, the other two were only applied in the AlpArray study, but are not yet available for other users.

- **Related chapters:** In chapter 6 I present extensive methodological testing of inversion setups for the Alps. Subsequently I present the obtained MT solutions and interpret them along with recent and historical seismicity, GNSS strain and stress inversion results.

③ ***Clusty* - Open source python toolbox for clustering of earthquakes based on waveform similarity across a seismic network**

- In the case of small magnitude events moment tensor inversions may be hindered due to high SNR only at high frequencies and due to insufficiently detailed subsurface velocity models. The similarity in mechanism (and location) between earthquakes is reflected by the similarity of recorded waveforms across a network of stations. In order to include earthquakes for which MT inversion is not feasible in the study of seismic fault, we developed a flexible and adaptable network similarity clustering toolbox. This tool can combine the cross-correlation values of event pairs at a network of stations following multiple implemented approaches to obtain a network similarity. The inverse of this network similarity is then used in a chain-like clustering approach. The clustering procedure is supported by automatically generated graphical outputs to facilitate a thorough tuning of all settings and parameters, and to assess the reliability of results. We designed the toolbox to provide a flexible choice of methods and settings, allowing for applications to a great variety of use cases.

- **Related chapters:** In chapter 6 we present the open source toolbox *Clusty* and its application to the 2018 Zakynthos aftershock sequence.

CHAPTER 4

Automated Quality Control for Large Seismic Networks: Implementation and Application to the AlpArray Seismic Network

Petersen, G.M., Cesca, S. and Kriegerowski, M. (2019)

Published in Seismological Research Letters, vol. 90 (3), pp.1177-1190.
https://doi.org/10.1785/0220180342

The following chapter contains the accepted manuscript (AM) of the above publication. Please refer to the citation to get access to the final, formatted publication. The supplementary material for this publication can be downloaded at https://doi.org/10.1785/0220180342.

Automated quality control for large seismic networks: Implementation and application to the AlpArray seismic network.

Gesa Maria Petersen (1)*, Simone Cesca (1), Marius Kriegerowski (2) and the AlpArray working group
* gesap@gfz-potsdam.de

Affiliations:
(1) Helmholtz Centre Potsdam German Research Centre for Geosciences - GFZ, Potsdam, Germany
(2) Institute of Earth and Environmental Sciences, University of Potsdam, Germany

Full address of first author:
Gesa Maria Petersen
Helmholtz Centre Potsdam German Research Centre for Geosciences - GFZ
Telegrafenberg
14473 Potsdam
Germany

Note: G. M. Petersen is also at Institute of Earth and Environmental Sciences, University of Potsdam, Germany.

Abstract

As a consequence of the rapid growing worldwide seismic data set, a huge variety of automatized data processing methods have been developed. To perform automatized, waveform based seismological studies aiming for magnitudes or source process inversion it is crucial to identify network stations with erroneous transfer functions, gain factors or component orientations. We developed a new tool dedicated to automated station quality control of dense seismic networks and arrays. The python based AutoStatsQ toolbox uses the `pyrocko` seismic data processing environment. The toolbox automatically downloads data and metadata for selected teleseismic events and performs different tests. As a result relative gain factors, sensor orientation corrections and reliable frequency bands are computed for all stations in a chosen time period. Relative gain factors are calculated for all stations and events in time domain based on maximum P-phase amplitudes. A Rayleigh wave polarization analysis is used to identify deviating sensor orientations. The power spectra of all stations in a given frequency range are compared to synthetic ones, accessing global CMT solutions. Frequency ranges of coinciding synthetic and recorded PSDs may serve as guidelines for choosing bandpass filters for moment tensor inversion and help to confirm the corner frequency of the instrument. The toolbox was applied to the permanent and temporary AlpArray networks as well as to the denser SWATH-D network, a total of above 750 stations. Stations with significantly deviating gain factors were identified as well as stations with inverse polarity and misorientations of the horizontal components. The tool can be used to quickly access network quality and to omit or correct stations before moment tensor inversion.

Introduction

In order to successfully apply waveform based methods aiming for magnitudes or moment tensor solutions, malfunctioning stations and errors in the metadata, such as wrong amplification factors, transfer functions or component orientations, need to be identified and corrected if possible. While the localization of events is not affected by incorrect gains, magnitude estimates are biased. Errors in transfer functions and gain factors as well as misoriented horizontal components can result in bad fits of synthetic and recorded waveforms as well as power spectra and hence lead to erroneous or unstable results of moment tensor (MT) inversion.

The data quality of seismic stations is routinely evaluated by network operators as well as before seismic studies based on background noise levels. Long-term noise levels are often compared to reference noise models (e.g. Peterson et al. [1993] and Berger et al. [2004]) or among the stations of a network. Bormann et al. [1997] analyzed the noise conditions for the German Regional Seismic Network (GRSN) by calculating displacement power spectra in 4 to 45 minutes long time windows for frequencies between 0.01 and 40 Hz. Time dependent changes in data quality and instrument response transfer functions can be monitored by comparing power levels over long time periods [Ringler et al., 2010]. McNamara and Boaz [2010] presented a seismic data quality control system based on probability density functions of power spectral densities (PSD) for operational and scientific applications like the characterization of noise levels of broadband stations, for detecting problems with the recording systems or sensors, and for evaluating the overall quality of data and metadata. Several publications deal with the identification and correction of timing errors, which are of high relevance for localizations but not so much for waveform-based methods (e.g. Gibbons [2006]). Therefore timing errors are not addressed here.

The data quality of the AlpArray Seismic Network, consisting of over 620 permanent and temporary stations (see Section *Application to the AlpArray* and Hetényi et al. [2018]), has mostly been checked with long-term PSDs by the individual responsible network operators (e.g. Fuchs et al. [2016], Molinari et al. [2016], Govoni et al. [2017], and Vecsey et al. [2017]). Additionally, Vecsey et al. [2017] presented an extensive data quality control for the Czech AlpArray and AlpArray EASI stations evaluating metadata and data with respect to noise levels, sensor orientations, timing problems and metadata errors.

This toolbox is designed to provide a simple and flexible environment to test the quality of waveform data. It provides correction factors for amplitude gains, corrections for misoriented horizontal components and recommendations for usable frequency ranges for moment tensor inversions and hence a check for indicated lower corner frequencies of the instruments. The tool follows different approaches: (1) Comparison of waveform characteristics among different stations to identify outliers, (2) analysis of horizontal and vertical components of single stations, and (3) comparison of observed and synthetic spectral features for single stations. Long-term PSDs, although very common for quality control, are not part of this toolbox for two reasons: Instead of assessing the background seismic noise, all implemented methods are based on comparing real and synthetic waveforms and power spectra of teleseismic events. Well-established tools for the computation of PSDs are already available (e.g. McNamara and Boaz [2010]). The AutoStatsQ toolbox offers a wide range of applications from small scale arrays to large, dense networks like the AlpArray with several hundreds of stations. The following paragraphs introduce current approaches and results of tests evaluating the amplitude gain, orientation and frequency ranges. The methods that are implemented in the AutoStatsQ toolbox are described in detail in the methodology section. The toolbox is freely available and can be downloaded at `https://github.com/gesape/AutoStatsQ`.

Amplitude gains

Gain amplification factors are provided as part of the station metadata. Occasionally, inaccurate metadata handling may result in erroneous amplification factors, exponentials or units.

Evaluating 15 years of teleseismic event data recorded at over 200 GSN (Global Seismographic Network) stations, Ekström et al. [2006] observed frequency-dependent modifications of the instrument responses of more than 15 stations. For long periods (about 250 s) the gains were significantly reduced. This change occurred gradually within several month to a few years. Davis et al. [2005] and [2007] used amplitudes of the radial mode ${}_0S_0$, which is expected to be globally uniform, as well as the Earth's tides to study the GSN network. Response variations over time were not observed. Ringler et al. [2010] monitored temporal amplitude changes using PSDs of continuous data in several frequency bands between 20 Hz to 0.001 Hz. Hutt and Ringler [2011] attributed temporal variations in the response of STS-1 sensors within the GSN to humidity. They observed lower sensitivities near the long period corner of 360 s. Colocating portable broadband seismometers in proximity to GSN sensors during field-maintenance visits was established to verify in-situ calibrations and orientations [Davis and Berger, 2012].

Ringler et al. [2015] compared daily microseism amplitude ratios between colocated broadband sensors of the IRIS/USGS seismic network and found that without errors in the metadata, the midband sensitivity has an error of less than ± 6 % (99 % confidence interval). Vecsey et al. [2017] found and corrected technical errors in one of the acquisition systems when checking the Czech stations of the AlpArray using ambient noise techniques. These errors biased waveform amplitudes.

Sensor orientation

Many seismological methods like shear-wave splitting measurements and moment tensor inversions depend on correctly oriented sensor components. When seismic stations are set up using a standard magnetic compass, deviations of $\pm 5^\circ$ are regularly observed [Vecsey et al., 2017]. Nearby magnetic intrusions, ore deposits or large magnetic constructions may lead to even larger errors. Therefore some large networks like GSN and ANSS (Advanced National Seismic System) stopped using magnetic methods [Ringler et al., 2013]. However, in many other contexts, handheld magnetic compasses are still in use.

Larson and Ekström [2002] developed a method for measuring azimuth arrival angles of surface waves recorded by the GSN using estimates of surface wave dispersion to isolate Love or Rayleigh waves. They found that large and invariant angle anomalies are consistent with horizontal misorientations of the seismometers. About 9 % of the examined seismometers had misorientations of more than ±10° (Table 4 in Larson and Ekström [2002]). Ekström and Busby [2008] compared surface wave waveforms on longitudinal and transverse components to synthetic waveforms for transportable and backbone stations of the USArray. They found that 4.4 % out of 473 stations had misorientations of above 10° and more than 24 % misorientations of at least 4°. Ringler et al. [2012] maximized the coherence of horizontal data with a reference station to evaluate the accuracy of different infield orientation methods.

Rayleigh wave polarization analyses are routinely used for determining the entirely unknown horizontal orientation of ocean bottom stations (OBS) [e.g. Stachnik et al. [2012] and Hannemann et al. [2017]]. The particle motion of Rayleigh waves is retrograde elliptical at the free surface and prograde elliptical at greater depth. Rayleigh waves are theoretically only observed on vertical and radial components, showing a 90° phase shift. By rotating the horizontal traces and searching for the maximum cross-correlation of the Hilbert-transformed radial component and the vertical component within a time window containing Rayleigh waves, the wave arrival azimuth and subsequently the sensor orientations can be determined (e.g. Stachnik et al. [2012]). Rueda and Mezcua [2015] used a similar method to calculate misorientations of the Spanish National Network, based on 1350 teleseismic events. They validated the results and hence the method by gyrocompass measurements.

Frequency range for MT inversion

Waveform analysis methods such as moment tensor inversions are frequency sensitive. Inverting for wide frequency bands can result in bad fits of synthetic and recorded waveforms and spectra and hence in erroneous or even rotated mechanisms [Barth et al., 2007]. Barth et al. [2007] introduced a frequency sensitive moment tensor inversion method using sliding frequency bands that are determined automatically depending on source-receiver locations and event magnitudes.

The misfit between synthetic and recorded waveforms depends on the velocity model that is used to compute synthetic waveforms, on correct instrument response functions and on noise levels. This part of the toolbox provides frequency ranges, at which the power spectral density (PSD) of synthetic and recorded data agree well or can be corrected by a simple, constant factor. Errors in the response function of the receiver instrument and problems in certain frequency bands due to high noise levels result in high misfits and can therefore be identified.

Methodology: The AutoStatsQ toolbox

The AutoStatsQ toolbox is written in `python` using the seismological data processing environment `pyrocko` (see Data and Resources). It comprises three independent tests and a data pre-processing section including the download of waveform data and metadata. Requiring a list of stations and a time frame, the toolbox performs as follows:

- Catalog search for teleseismic events and selection of subsets of events
- Data and metadata download for all stations and events
- Data restitution and rotation to ZRT
- Synthetic data computation
- Test 1: Relative gain factors
- Test 2: Orientation of horizontal components
- Test 3: Comparison of synthetic and observed PSDs, providing reliable frequency ranges

All steps can be executed individually. The toolbox can also process locally stored data and metadata. Results of the three tests are provided as both, easily interpretable figures and files.

Event selection and data preprocessing

The Global Centroid Moment Tensor (gCMT) catalog is queried by default for teleseismic events in a given period of time, satisfying magnitude and distance thresholds (see Data and Resources). For the gain test, which is based on a comparison of waveforms among all stations, the minimal station-event distance should be large compared to the spatial dimension of the array. For the other tools, which are not based on station-to-station comparisons, events of smaller distances can be included.

Two independent subsets of events with different depth ranges can be selected. The depth range should be chosen based on the tests that are about to be performed: For the surface wave polarization analyses shallow, events are preferred, while for the relative gain factor and PSD tests deeper events are favorable to evaluate body waves. Optionally, statistics of the catalogs can be saved as figures. The size of the downloaded catalog is reduced to select one or two subsets of events (Figure 1). A good azimuthal coverage is ensured by searching for events in defined backazimuth steps. The resulting event catalog contains information on origin times and locations as well as moment tensor solutions, seismic moments, and rupture durations, which are used for the computation of synthetic seismograms.

Data and metadata for the selected events are downloaded using the `pyrocko` fdsn client. For each station-event pair, data is requested from a list of data centers, such as GEOFON, ORFEUS and IRIS (see Data and Resources). The velocity waveform data is integrated, the instrument response is removed, the data is downsampled to the sampling rate of the chosen GF database (default 2s), rotated and bandpass-filtered (default 0.01 Hz - 0.2 Hz) to obtain displacement waveforms in Z,R,T coordinate system.

For all station-event pairs synthetic data can be rapidly calculated using the forward model and storage tool `fomosto` of `pyrocko` and a pre-calculated global GF database, based on the Preliminary reference Earth model (PREM) [Dziewonski and Anderson, 1981] (see Data and Resources). The Green's functions were computed using the `qssp` modeling code by Wang et al. [2017]. The database can be accessed online (see Data and Resources). The obtained synthetic Z, R and T traces are bandpass filtered in the same way as the recorded data.

Test 1: Gain correction factors

The preprocessed data of each station-event pair is used to compute gain factors for each station relative to one reference station in a narrow frequency band (default 0.01 to 0.2 Hz). The reference station can be defined either manually or automatically. The latter selects a station which recorded each event while having a medium amplitude for the first event evaluated. For each station i and event j, the ratio $A_{i,j}/A_{ref,j}$ of the maximum amplitude of the P-phase within time windows of 60 s around the first onset of station i and the reference station ref is calculated. P wave onset times are calculated using `cake`, a tool within the `pyrocko` environment that can solve classical seismic ray theory problems for a 1-D layered earth model.

Finally, the median of the amplitude ratios of all events is provided for each station as a relative gain correction factor (Figure 2). While the median ratio is independent of single outliers due to high noise peaks, the mean and standard deviation might be strongly distorted. Using the median might however be problematic if the gain changes over time. For a temporal overview it is possible to return results for the single events (cf. Figure S1, available in the electronic supplement to this article).

Test 2: Sensor orientation analysis

Within the AutoStatsQ toolbox, the sensor orientations are examined following the Rayleigh wave polarization method often used for OBS sensor orientations (e.g. Stachnik et al.

[2012] and Hannemann et al. [2017], see also Introduction). Waveforms of a set of shallow events are analyzed by rotating the radial traces in steps of 1°. For each step the cross-correlation coefficient of the Z component and the Hilbert-transformed, newly rotated R^* component is calculated. Cross-correlations are computed for time windows of a chosen length (default 8.5 min) starting 0.5 minutes before the theoretical Rayleigh wave arrival time computed using a wave propagation velocity of $v_R = 4km/s$. It is not necessary to exclude Love-waves from the selected time window, because their energy is supposed to vanish completely from the radial component if the components are correctly oriented [Hannemann et al., 2017]. As long as Love waves are present on the radial component, the cross-correlation with the vertical component is low.

Waveforms are bandpass-filtered between 100 and 20 s. A correct sensor orientation is indicated by a maximum of the cross-correlation coefficient at a correction angle of 0°, corresponding to no rotation correction. (Sensor orientations provided in the metadata are used to rotate to the original ZRT system.) This procedure is applied to all event-station pairs (e.g. Figure 3).

For each station the results of multiple events are combined computing the median, mean and standard deviation of the obtained correction angles. Only events having a maximum cross-correlation coefficient above a given threshold (default 0.8) are taken into account.

Using 10-20 teleseismic events that are not manually revised, the results are not as accurate as a gyrocompass and we do not recommend correcting any stations for deviations below 20°, but larger deviations and polarity errors can be identified. The obtained correction angles can be used to rotate waveform data or to identify stations that should be revisited. By using a larger manually revised set of events with high signal to noise ratios over a long time range the resolution of the method can be improved and temporal changes can be observed.

Test 3: Frequency ranges for MT inversion

The third part of the toolbox is designed to provide frequency ranges suitable for MT inversions. At the lower frequency end, the bandwidth is limited by the sensor's corner frequency. Therefore the obtained range can also be used to check the corner frequency provided in the metadata. At higher frequencies, synthetic seismograms lack information due to 1-D velocity models and low sampling rates. The maximum frequency is at most half of the sampling frequency of the Green's Function (GF) data base used for the computation of synthetic data.

The third test uses recorded and synthetic spectrograms instead of waveforms. PSDs of synthetic and observed waveforms are calculated for all station-component-event combinations in long time windows (default 30 minutes) (Figure 4a). The limits of the time windows are set relative to the theoretical arrival times of P wave and Rayleigh wave. For each pair of synthetic and observed PSDs, the ratio of both PSDs is calculated. Subsequently, the median power ratio over all events is computed for each frequency band of each station and component. Frequency ranges with a stable PSD ratio are determined by line fits to a given number of frequency ratio points (default 25). Successive lines having a slope below a given threshold (default 10) set up the recommended frequency ranges (Figure 4b). Higher thresholds and fitting more frequency ratio points can be used to search for large misfits due to erroneous amplitude gains or extremely noisy environments as well as to verify the instrument corner frequency. Finer, adjusted settings are needed to obtain frequency ranges suitable for moment tensor inversion.

Stations with significantly erroneous gains will be recognized as large shifts between observed and synthetic PSDs. In case of significant orientation errors, the comparison of observed and synthetic PSDs of the horizontal components may be biased. Therefore, it is recommended to run the orientation test beforehand.

Application to the AlpArray

The AlpArray initiative

The AlpArray initiative is an international program aiming for a better understanding of the geodynamic and geophysical processes associated with the orogenesis of the Alps and its relation to mantle dynamics, plate motion, surface processes and seismic hazard [Hetényi et al., 2018]. A Seismicity, seismotectonics and local earthquakes tomography working group was established to study the local seismicity.

Within the AlpArray subproject "From Top to Bottom – Seismicity, Motion Patterns & Stress Distribution in the Alpine Crust" we investigate the geodynamic processes controlling the multi-scale seismicity of the Alps, which is predominantly characterized by weak to moderate magnitudes. Relying on the outstanding network density and the adaption of modern inversion tools we aim to lower the magnitude threshold for automatized moment tensor inversions and provide new information on seismic source processes and stress distributions in the Alps.

The AlpArray Seismic Network (AASN) was deployed with contributions from 36 European institutes and consists of over 620 permanent and temporary stations distributed homogeneously over 11 countries [AlpArray Seismic Network, 2015]. The permanent stations of the AlpArray are part of existing European regional networks (Department of Earth and Environmental Sciences Geophysical Observatory University of Munchen [2001], SED at ETH Zurich [1983], Institute of Geophysics Academy of Sciences of the Czech Republic [1973], RESIF [1995], Institut de Physique du Globe de Paris & Ecole et Observatoire des Sciences de la Terre de Strasbourg [1982], GEOFON Data Centre [1993], University of Genova [1967], Kövesligethy Radó Seismological Observatory Geodetic and Geophysical Institute Research Centre for Astronomy and Earth Sciences [Hungarian Academy of Sciences], INGV Seismological Data Centre [1997], MedNet project partner institutions [1988], OGS and University of Trieste [2002], ZAMG - Central Institute for Meteorology and Geodynamics [1987], OGS [2016], Departement d'Analyse et Surveillance de l'Environnement du CEA [1962], University of Trieste [1993], Geological Survey-Provincia Autonoma di Trento [1981], Leipzig University [2001], Friedrich Schiller University Jena and Thuringian Institute of Environment and Geology [2009], see also Data and Resources). The temporary stations were installed between 2015 and 2017 and will run at least until July 2020. In regions which were not covered before the stations were set up with a spacing of 52 km [Hetényi et al., 2018]. The AASN is complemented by an OBS array and denser sub-networks like the SWATH-D seismic network [Heit et al., 2017] (Figure 5). The temporary SWATH-D network was deployed in summer and autumn of 2017 in Northern Italy and Austria and will run until end of summer 2019. It consists of 150 broadband stations with a spacing of 15 km [Heit et al. [2017], Heit et al. [2018]]. High-precision optical gyrocompasses as well as handheld compasses were used for the deployment of the temporary AlpArray and SWATH-D stations (Molinari et al. [2016], Fuchs et al. [2016], Vecsey et al. [2017], B. Heit, pers. communication, July 2018). For some stations that were set-up with a handheld compass, final orientations were or will be obtained using a gyrocompass (Molinari et al. [2016], Fuchs et al. [2016]).

While the large number of stations within the AlpArray enables detailed studies covering a broad region, quality control for this data set remains challenging. By applying our toolbox AutoStatsQ, we were able to routinely process hundreds of stations in the AlpArray in regard to station quality.

Quality assessment of the AASN and SWATH-D

For the evaluation of all permanent and temporary stations of the AASN and the SWATH-D network waveform data and station metadata of automatically selected events were downloaded.

For the AlpArray with a largest elongation of approximately 1200 km in East-West direction, we empirically chose a minimum event distance of 5000 km for the permanent and temporary AlpArray stations and 2900 km for the SWATH-D stations. Catalog information and the repositories queried for waveform data and metadata of each network are summarized in Table 1. For a list of used events see Table S1, available in the electronic supplement. For the amplitude gain and the frequency range tests, subsets of deeper events (25-700 km) were used in a minimum distance of 5000 km for the permanent and temporary AlpArray stations and 2900 km for the SWATH-D stations. For the frequency range test closer events could be used. However, since both methods use body waves, we used the same data set of deep (25-700 km) and distant events. For the orientation test, crustal events (0-60 km depth) in a minimum distance of 2000 km were used.

The results for all analyzed stations are available in the electronic supplement to this article (Tables S2-S7) and will be briefly described here. The number of events considered for each station orientation analysis is limited by a required minimum cross-correlation value of 0.8.

Relative gain factors

The maximum P-phase amplitudes of 393 permanent AlpArray stations, 218 temporary Z3 stations and 140 SWATH-D stations (ZS) were compared to reference stations

GE.MATE, Z3.A261A, ZS.D017, respectively (Table 2). Median amplitude ratios $A_{i,j}/A_{ref,j}$ below 0.1 or above 10 were found for 4.3% of the vertical components of the permanent stations and 1% of the Z3 stations. Noticeable are the results for the Slovakian stations SK.MODS and SK.ZST and the French station RD.MFF, indicating errors of several magnitudes. While large deviations are often explained by errors in the metadata, smaller deviations in the order of less than one magnitude are likely to result from site effects. Removing the largest outliers from the map in Figure 2 bears the opportunity to visualize the spatial distribution of smaller deviations that result from site effects (Figure 6).

In a first run of the toolbox on the SWATH-D (ZS) network, the median amplitude ratio indicated that the amplitudes of more than 20 SWATH-D stations were wrong by a factor 10. We informed the network operators, who detected and corrected an error in their metadata (S. Hemmleb & B. Heit, pers. communication, Oct. 2018). After correction, all of these stations appeared normal in the final run of the test. The maximum amplitudes of Station ZS.D046 recorded in Winter 2017/2018 indicated erroneous gain levels. The data acquisition system of this station was replaced in March 2018 [B. Heit, pers. communication] and has been working well ever since. All other relative gain factors of the SWATH-D stations are close to one and variations can be explained by subsurface differences (site-effects) and different noise-levels (Figure 7).

Sensor orientations

For about 95% of the permanent, the temporary (Z3) and the SWATH-D stations the Rayleigh wave polarization analysis confirmed the sensor orientation within 20° (Figure 8 and Table 3). Since we use only 5 to 27 events for this study, the standard deviations of mostly 7-10° do not allow to correct for smaller misorientations (see also Figure S2, available in the electronic supplement).

Most striking are correction angles around 180° obtained for four stations of the permanent network, two temporary Z3 stations and one ZS station: GU.RORO, IV.SARZ, IV.ZCCA, NI.VINO, Z3.A263A, Z3.A300A and ZS.D125 (see example in Figure 3b). Comparisons with neighboring stations indicate reverse polarities of the horizontal components of ZS.D125 (Figure S3, available in the electronic supplement to this article), IV.SARZ and IV.ZCCA and of the vertical component of GU.RORO (Figure 9). In case of NI.VINO, until mid of 2016 a minor misorientation of about 15° is observed while later occurring events indicate an inverse polarity (-165°) thereafter (Figure 10).

Suitable frequency ranges for MT inversion

For testing the Alp Array stations we computed PSDs for time windows of 600 s. Taking into account outliers at single frequencies, frequency ranges with increased power ratios spanning less than 0.02 Hz are ignored. Larger offsets between the synthetic and recorded PSDs were observed for those stations having significantly deviating relative amplitudes. Excluding or correcting stations with orientation or gain errors, the synthetic and recorded PSDs of the permanent and temporary AlpArray stations agree well in the frequency range between the lower corner frequency of the instrument (mostly 0.01 Hz) and the Nyquist frequency of 0.25 Hz. As expected the results for instruments with a corner period of 30 s indicate well agreeing PSDs for frequencies above 0.03 Hz (see for example Figure S4, available in the electronic supplement to this article). The fit of the PSDs is generally lower for horizontal components compared to vertical ones.

Similar to the waveform amplitude test, station ZS.D046 shows up with significant differences between the recorded and synthetic frequency spectra before the replacement of the acquisition system in March 2018 (Figure S5, available in the electronic supplement to this article). The results obtained for the remaining SWATH-D stations do not imply any limitations of the usable frequency ranges.

Discussion

The AutoStatsQ toolbox is designed to detect errors in data and metadata of seismic stations that will impede the successful usage for waveform analyses.

The reliability of each quality control test depends on the data availability. In case of short deployment times or data gaps the number of teleseismic events might not be sufficient to achieve stable results. A time period of at least one year combined with backazimuthal steps of 10° for the catalog preparation is recommended for a stable analysis. Longer time spans and smaller backazimuth steps will increase the number of events and the robustness of the results. While a few events can already hint at errors, we recommend a minimum number of 10 events to ensure stable results.

We have shown that the Rayleigh wave polarization method is very successful in detecting reverse polarities of components. In the case of the highest cross-correlation values for corrections of around 180° a manual comparison with neighboring stations helps to distinguish cases of wrong polarities of vertical or horizontal traces. Reverse polarities of the horizontal components may result from a wrong orientation during the installation of the sensor, from wrong cable connections or from sign errors in the digitization process. Absolute correction angles around 90° may indicate interchanged channels. For ten to twenty used events the standard deviation of the method is between

7 and 10°. We estimate that only corrections as large as 20° are reliable. Orientation errors can originate from the installation, but we also observed changes in orientation over time. One indoor sensor of the temporary network was rotated by staff of a cleaning service, while another outdoor sensor was moved by a rat living besides it (A. Schloemer (LMU) and Aladino Govoni (INGV), pers. communication, October 2018). A dependence of the obtained correction angles from the event backazimuth was not observed. However, the small number of events is not sufficient to exclude that large scale topography or geological features might bias the obtained correction angle. We assume that the method is robust when using the median angle of events having a good backazimuthal distribution.

The relative P-phase amplitude ratios provide information on metadata errors concerning amplification factors. In our experience large deviations from the reference station typically result from errors in the metadata. In some cases wrong exponentials of amplification factors were detected, while in other cases components of the instrument transfer function were completely missing. Smaller deviations that remain stable over time can result from site effects. Using the median amplitude ratio of all events is advantageous because the median is not affected by single outliers resulting from high noise peaks. However, temporal changes of relative gain factors were observed, which hint at malfunctioning sensors. Therefore the results for the single events are additionally provided.

Frequency spectra are routinely fitted in moment tensor inversion. Testing whether the frequency content of synthetic and recorded data is comparable is helpful to identify spectral anomalies, and to select optimal bandpass filters. Additionally, the lower corner frequency of the instrument can be compared to the lower end of the estimated frequency range to assure that the seismometer performs as expected. However, in order to automatically obtain frequency ranges of a stable ratio between the PSDs of synthetic and recorded data, a threshold indicating which slope of the line fit is regarded as stable must be defined. This threshold needs some tuning depending on the subsequent usage of the results. Using a 2 s GF database for teleseismic events limits the maximum frequency to below 0.25 Hz (Nyquist frequency). A GF database with a higher sampling may be used instead. However, this database is significantly larger ($>$ 500 Gigabytes for 1 s sampling rate) and therefore not routinely used.

All three tests can be performed independently and repeated after applying corrections. We recommend to correct for amplitude gains and sensor orientations before evaluating the frequency ranges.

The AutoStatsQ toolbox can be used for small to large arrays and networks consisting of hundreds of stations. The gain control based on station-to-station comparisons requires a dense spacing of the stations and a catalog of distant events. For the orientation analysis based on comparisons of R and Z components of single stations and for PSD control based on a comparison to synthetic data, a dense spacing and large distances are not required.

The orientation control implemented in the AutoStatsQ toolbox is based on the Rayleigh wave polarization method, which is routinely used for the orientation of horizontal OBS components. Consequentially, it can also be used to determine station orientations of OBSs. The gain and frequency range tests can be used for OBS quality control and to determine frequency ranges for waveform based methods like moment tensor inversion or magnitude estimates.

For the AlpArray project, more than 750 stations of three station subsets were checked: the permanent AlpArray stations belonging to various regional networks, the temporary Z3 stations and the SWATH-D ZS stations. Data from OBS-AlpArray stations in the Mediterranean was not yet available. Stations with significantly wrong sensor orientations and gain amplifications were identified and corrections provided. In summary, the orientation test shows deviations of at least 20° for 4.7 % of all analyzed stations. We provided correction angles for these misoriented stations. 2.5 % of all stations have median relative gain factors above 10 or below 0.1. The relative gain factors of 1 % of the stations differ by a factor of 100 or larger. The gain test of the SWATH-D stations led to the detection (and correction) of an amplification factor error in the metadata of more than 20 stations. Additionally, frequency ranges usable for moment tensor inversion were computed by a comparison of synthetic and recorded PSDs.

Besides quality control, especially the amplitude ratios provide insight to site-effects within the networks. Due to the low frequencies (< 0.25 Hz) the wavelengths are not sensitive to small scale changes but rather to larger geological features. There are large scale trends within the AlpArray area (Figure 6): In northern Italy, within the Po plain as well as in the surrounding northern Apennine Mountains and the southern Alps larger amplitudes are observed on the horizontal components. The flanks of the Rhône and Rhine river valleys show up with lower amplitudes on the horizontal components. The topographically flat regions in Hungary and western Slovakia are traced by tendentiously higher amplitudes on the horizontal components. Within the AlpArray temporary and permanent network the participating research institutes use various sensors with different bandwidths. Therefore it cannot be ruled out that parts of the observed regional pattern result from sensor characteristics. Within the SWATH-D network, the amplitudes are generally very similar and no clear geological or topographic trend is observed (Figure 7).

Conclusions

We presented a toolbox that is especially dedicated to dense networks with numerous stations requiring an automatized quality control work flow prior to waveform based analyses (e.g. magnitude determination and moment tensor inversion). Using a combination of observed and synthetic teleseismic event data, gain correction factors, orientation correction angles and frequency ranges, in which synthetic and recorded data agree well, are computed. Erroneous waveform amplitudes and misorientations of horizontal sensor components can be identified and corrected. The entire workflow is automatized requiring only a station file as input. Results are provided as graphical output and station reports. The code is freely available and can be downloaded at `https://github.com/gesape/AutoStatsQ`.

The toolbox was successfully applied to the permanent and temporary AlpArray network and to the smaller SWATH-D seismic array. Stations with erroneous amplitude gains and sensor orientations were identified and network operators were informed. The results for all stations are presented in the supplementary material and will be used for regional moment tensor inversion studies.

Data and Resources

The code for the AutoStatsQ toolbox is open to public and can be accessed at `https://github.com/gesape/AutoStatsQ` (last access January 2019).

Synthetic data was computed using a global pre-calculated Green's function database which can be downloaded from `http://kinherd.org:8080/gfws/static/stores/`, last access August 2018.

Some plots were made using the `Generic Mapping Tools` (version 5.2.1) (`http://www.soest.hawaii.edu/gmt/`, Wessel et al. [2013]). For topography SRTM-3 data (Farr et al. [2007]) was used.
Waveform data was obtained using the `pyrocko` fdsn client to access the databases of Bundesanstalt für Geologie und Rohstoffe (BGR; `http://eida.bgr.de`), Eidgenössische Technische Hochschule Zürich (ETHZ; `http://eida.ethz.ch`), GEOFOrschungsNetz (GEOFON; `https://geofon.gfz-potsdam.de/`), Instituto Nazionale di Geofisica e Vulcanologia (INGV; `http://webservices.ingv.it`), Institut de Physique du Globe de Paris (IPGP; `http://eida.ipgp.fr`), Incorporated Research Institutions for Seismology (IRIS; `https://www.iris.edu/hq/`)), Ludwig-Maximilians-Universität München (LMU; `http://erde.geophysik.uni-muenchen.de`), Observatories and Research Facilities for European Seismology (ORFEUS; `https://www.orfeus-eu.org/`), and Résau sismologique & géodésique français (RESIF; `http://ws.resif.fr`). All databases were last accessed in September 2018.
The permanent AlpArray stations belong to different European regional networks, those without a digital object identifier are listed below:
University of Zagreb (2001): Croatian Seismograph Network.
Seismologisches Zentralobservatorium GRF (1990): German Regional Seismic Network.
Polish Academy of Sciences (PAN) Polskiej Akademii Nauk (1990): Polish Seismological Network.

Acknowledgements

This work is part of the German DFG funded project 'From Top to Bottom - Seismicity, Motion Patterns & Stress Distribution in the Alpine Crust' (project number: 362440331), a sub-project of 'SPP 2017: Mountain Building Processes in 4D' (project number 313806092).

The authors thank the AlpArray Seismic Network Team for planning, building and maintaining the entire AlpArray seismic network. The members of the AlpArray Seismic Network Team are listed here:
`http://www.alparray.ethz.ch/en/seismic_network/backbone/data-policy-and-citation/`.

We thank the anonymous reviewers and the editors for their helpful comments and suggestions that improved the manuscript.

References

AlpArray Seismic Network (2015). AlpArray Seismic Network (AASN) temporary component. AlpArray Working Group. Other/Seismic Network. https://doi.org/10.12686/alparray/z3_2015.

Barth, A., Wenzel, F., and Giardini, D. (2007). Frequency sensitive moment tensor inversion for light to moderate magnitude earthquakes in eastern Africa. *Geophys Res Lett*, 34(15).

Berger, J., Davis, P., and Ekström, G. (2004). Ambient earth noise: a survey of the global seismographic network. *J Geophys Res: Solid Earth*, 109(B11).

Bormann, P., Wylegalla, K., and Klinge, K. (1997). Analysis of broadband seismic noise at the German Regional Seismic Network and search for improved alternative station sites. *Journal of Seismology*, 1(4):357–381.

Davis, P., Ishii, M., and Masters, G. (2005). An Assessment of the Accuracy of GSN Sensor Response Information. *Seismol Res Lett*, 76(6):678–683.

Davis, P., and Berger, J. (2007). Calibration of the Global Seismographic Network Using Tides. *Seismol Res Lett*, 78(4):454–459.

Davis, P., and Berger, J. (2012). Initial Impact of the Global Seismographic Network Quality Initiative on Metadata Accuracy. *Seismol Res Lett*, 83(4):697–703.

Departement d'Analyse et Surveillance de l'Environnement du CEA (1962). CEA/DASE Seismic Network. doi: 10.15778/RESIF.RD.

Department of Earth and Environmental Sciences, Geophysical Observatory, University of Munchen (2001). BayernNetz. International Federation of Digital Seismograph Networks. Other/Seismic Network. 10.7914/SN/BW.

Dziewonski, A., Chou, T.-A., and Woodhouse, J. (1981). Determination of earthquake source parameters from waveform data for studies of global and regional seismicity. *J Geophys Res: Solid Earth*, 86(B4):2825–2852.

Dziewonski, A. M. and Anderson, D. L. (1981). Preliminary reference Earth model. *Phys Earth Planet In*, 25(4):297–356.

Ekström, G. and Busby, R. W. (2008). Measurements of seismometer orientation at USArray transportable array and backbone stations. *Seismol Res Lett*, 79(4):554–561.

Ekström, G., Dalton, C. A., and Nettles, M. (2006). Observations of time-dependent errors in long-period instrument gain at global seismic stations. *Seismol Res Lett*, 77(1):12–22.

Ekström, G., Nettles, M., and Dziewoński, A. (2012). The global CMT project 2004–2010: Centroid-moment tensors for 13,017 earthquakes. *Phys Earth Planet In*, 200:1–9.

Farr, T. G., Rosen, P. A., Caro, E., Crippen, R., Duren, R., Hensley, S., Kobrick, M., Paller, M., Rodriguez, E., Roth, L., Seal, D., Shaffer, S., Shimada, J., Umland, J., Werner, M., Oskin, M., Burbank, D., and Alsdorf, D. (2007). The shuttle radar topography mission. *Rev. Geophys.*, 45(2005):1–33.

Friedrich Schiller University Jena and Thuringian Institute of Environment and Geology (2009). Thüringer Seismisches Netz (TSN). International Federation of Digital Seismograph Networks. Other/Seismic Networks. doi: 10.7914/SN/TH.

Fuchs, F., Kolínski, P., Bokelmann, G., and the AlpArray Working Group (2016). AlpArray in Austria and Slovakia: technical realization, site description and noise characterization. *Adv Geosci*, 43:1–13.

GEOFON Data Centre. (1993). GEOFON Seismic Network. Deutsches GeoForschungs-Zentrum GFZ. doi: 10.14470/TR560404.

Geological Survey-Provincia Autonoma di Trento (1981). Trentino Seismic Network. International Federation of Digital Seismograph Networks. Other/Seismic Network. doi:10.7914/SN/ST.

Gibbons, S. J. (2006). On the Identification and Documentation of Timing Errors: An Example at the KBS Station, Spitsbergen. *Seismol Res Lett*, 77(5):559.

Govoni, A., Bonatto, L., Capello, M., Cavaliere, A., Chiarabba, C., D'Alema, E., Danesi, S., Lovati, S., Margheriti, L., Massa, M., et al. (2017). AlpArray-Italy: Site description and noise characterization. *Adv Geosci*, 43:39.

Hannemann, K., Krüger, F., Dahm, T., and Lange, D. (2017). Structure of the oceanic lithosphere and upper mantle north of the Gloria Fault in the eastern mid-Atlantic by receiver function analysis. *J Geophys Res: Solid Earth*, 122(10):7927–7950.

Heimann, S., Kriegerowski, M., Isken, M., Cesca, S., Daout, S., Grigoli, F., Juretzek, C., Megies, T., Nooshiri, N., Steinberg, A., Sudhaus, H., Vasyura-Bathke, H., Willey, T., and Dahm, T. (2017). Pyrocko - an open-source seismology toolbox and library. v. 0.3. GFZ Data Services. http://doi.org/10.5880/GFZ.2.1.2017.001.

Heit, B., Weber, M., Haberland, C., Tilmann, F., Hemmleb, S., Schwarz, S., Handy, M., Jia, Y., and Pesaresi, D. (2018). The AlpArray SWATH-D experiment. *Geophysical Research Abstracts Vol. 20, EGU2018-11509, 2018 EGU General Assembly.*

Heit, B., Weber, M., Tilmann, F., Haberland, C., Jia, Y., and Pesaresi, D. (2017). The Swath-D seismic network in Italy and Austria. GFZ Data Services. Other/Seismic Network. https://doi.org/10.14470/mf7562601148.

Hetényi, G., Molinari, I., Clinton, J., Bokelmann, G., Bondár, I., Crawford, W. C., Dessa, J.-X., Doubre, C., Friedrich, W., Fuchs, F., Giardini, D., Gráczer, Z., Handy, M. R., Herak, M., Jia, Y., Kissling, E., Kopp, H., Korn, M., Magheriti, L., Meier, T., Mucciarelli, M., Paul, A., Pesaresi, D., Piromallo, C., Plenefisch, T., Plomerová, J., Ritter, J., Rümpker, G., Šipka, V., Spallarossa, D., Thomas, C., Tilmann, F., Wassermann, J., Weber, M., Wéber, Z., Wesztergom, V., Živčić, M., AlpArray Seismic Network Team, AlpArray OBS Cruise Crew, and AlpArray Working Group (2018). The AlpArray Seismic Network: A Large-Scale European Experiment to Image the Alpine Orogen. *Surv Geophys*, pages 1–25.

Hutt, C. R., and Ringler, A. T. (2011). Some Possible Causes of and Corrections for STS-1 Response Changes in the Global Seismographic Network. *Seismol Res Lett*, 82(4):560–570.

Institut de Physique du Globe de Paris, IPGP, & Ecole et Observatoire des Sciences de la Terre de Strasbourg, EOST (1982). GEOSCOPE, French Global Network of broad band seismic stations. Institut de Physique du Globe de Paris (IPGP). doi: 10.18715/geoscope.g

INGV Seismological Data Centre (1997). Rete Sismica Nazionale (RSN). Istituto Nazionale di Geofisica e Vulcanologia (INGV), Italy. doi: 10.13127/SD/X0FXnH7QfY.

Institute of Geophysics Academy of Sciences of the Czech Republic (1973). Czech Regional Seismic Network. International Federation of Digital Seismograph Networks. Other/Seismic Network. doi:10.7914/SN/CZ.

Kövesligethy Radó Seismological Observatory Geodetic and Geophysical Institute, Research Centre for Astronomy and Earth Sciences, Hungarian Academy of Sciences (MTA CSFK GGI KRSZO) (1992). Hungarian National Seismological Network. Deutsches GeoForschungsZentrum GFZ. doi: 10.14470/UH028726I

Larson, E. W. and Ekström, G. (2002). Determining surface wave arrival angle anomalies. *J Geophys Res: Solid Earth*, 107(B6):ESE–7.

Leipzig University (2001). SXNET Saxon Seismic Network. International Federation of Digital Seismograph Networks. Other/Seismic Network. doi:10.7914/SN/SX.

McNamara, D. and Boaz, R. (2010). PQLX: A seismic data quality control system description, aplications, and user manual. *U.S. Geological Survey Open-File Report*, 1292.

MedNet project partner institutions (1988). Mediterranean Very Broadband Seismographic Network (MedNet). Istituto Nazionale di Geofisica e Vulcanologia (INGV), Italy. doi: 10.13127/SD/fBBBtDtd6q.

Molinari, I., Clinton, J., Kissling, E., Hetényi, G., Giardini, D., Stipcevic, J., Dasovic, I., Herak, M., Sipka, V., Wéber, Z., et al. (2016). Swiss-AlpArray temporary broadband seismic stations deployment and noise characterization. *Adv Geosci*, 43:15.

ZAMG - Central Institute for Meteorology and Geodynamics (1987). Austrian Seismic Network. International Federation of Digital Seismograph Networks. Other/Seismic Network. doi: 10.7914/SN/OE

OGS (Istituto Nazionale di Oceanografia e di Geofisica Sperimentale) and University of Trieste (2002). North-East Italy Broadband Network. International Federation of Digital Seismograph Networks. Other/Seismic Network. doi:10.7914/SN/NI.

OGS (Istituto Nazionale di Oceanografia e di Geofisica Sperimentale) (2016). North-East Italy Seismic Network. International Federation of Digital Seismograph Networks. Other/Seismic Network. doi:10.7914/SN/OX.

Peterson, J. et al. (1993). Observations and modeling of seismic background noise. *U.S. Department of Interior Geological Survey Open-File Report 93-322*.

RESIF (1995). RESIF-RLBP French Broad-band network, RESIF-RAP strong motion network and other seismic stations in metropolitan France. RESIF - Réseau sismologique & géodésique français. doi: 10.15778/RESIF.FR.

Ringler, A., Edwards, J., Hutt, C., and Shelly, F. (2012). Relative azimuth inversion by way of damped maximum correlation estimates. *Computers & Geosciences*, 43:1–6.

Ringler, A., Gee, L., Hutt, C., and McNamara, D. (2010). Temporal variations in global seismic station ambient noise power levels. *Seismol Res Lett*, 81(4):605–613.

Ringler, A. T., Hutt, C. R., Persefield, K., and Gee, L. S. (2013). Seismic station installation orientation errors at ANSS and IRIS/USGS stations. *Seismol Res Lett*, 84(6):926–931.

Ringler, A. T., Storm, T., Gee, L. S., Hutt, C. R., and Wilson, D. (2015). Uncertainty estimates in broadband seismometer sensitivities using microseisms. *Journal of Seismology*, 19(2):317–327.

Rueda, J. and Mezcua, J. (2015). Orientation Analysis of the Spanish Broadband National Network Using Rayleigh-Wave Polarization. *Seismol Res Lett*, 86(3):929–940.

Stachnik, J. C., Sheehan, A. F., Zietlow, D. W., Yang, Z., Collins, J., and Ferris, A. (2012). Determination of New Zealand Ocean Bottom Seismometer Orientation via Rayleigh-Wave Polarization. *Seismol Res Lett*, 83(4):704–713.

Swiss Seismological Service (SED) at ETH Zurich (1983). National Seismic Networks of Switzerland; ETH Zürich. doi: 10.12686/sed/networks/ch.

University of Genova (1967): Regional Seismic Network of North Western Italy. International Federation of Digital Seismograph Networks. Other/Seismic Network. doi: 10.7914/SN/GU.

University of Trieste (1993). Friuli Venezia Giulia Accelerometric Network. International Federation of Digital Seismograph Networks. Other/Seismic Network. doi:10.7914/SN/RF.

Vecsey, L., Plomerová, J., Jedlicka, P., Munzarová, H., Babuska, V., and the AlpArray Working Group (2017). Data quality control and tools in passive seismic experiments exemplified on the Czech broadband seismic pool MOBNET in the AlpArray collaborative project. *Geosci Instrum Method Data Syst*, 6:505–521.

Wang, R., Heimann, S., Zhang, Y., Wang, H., and Dahm, T. (2017). Complete synthetic seismograms based on a spherical self-gravitating Earth model with an atmosphere-ocean-mantle-core structure. *Geophys J Int*, 210(3):1739–1764. doi: 10.1093/gji/ggx259.

Wessel, P., Smith, W. H. F., Scharroo, R., Luis, J. F., and Wobbe, F. (2013). Generic Mapping Tools: Improved version released. *EOS Trans. AGU*, 94:409–410.

List of mailing addresses of all authors

Gesa Maria Petersen
Helmholtz Centre Potsdam German Research Centre for Geosciences - GFZ
Telegrafenberg
14473 Potsdam, Germany
gesap@gfz-potsdam.de

Simone Cesca
Helmholtz Centre Potsdam German Research Centre for Geosciences - GFZ
Telegrafenberg
14473 Potsdam, Germany
simone.cesca@gfz-potsdam.de

Marius Kriegerowski
University of Potsdam
Institute for Geosciences
Karl-Liebknecht-Str. 24-25
14476 Potsdam, Germany
kriegero@uni-potsdam.de

Tables

Table 1: *Overview of the catalog and dataset used for testing the permanent AlpArray stations, the Z3 stations and the Swath-D seismic network. For each network, one subset with deeper events was used for the gain and frequency range test and a second subset of crustal events was used for the sensor orientation analysis. A complete list of events is provided in the electronic supplement (Table S1). For information on the repositories listed here see also Data and Resources.*

Net.	n_{stats}	Depth range	Time range	M_W range	Repositories	n_{events}
perm.	393	25-700 km	2015-2018	6.5-8.5	BGR, EIDA, ETHZ, GEOFON, INGV, IPCP, IRIS, LMU, ORFEUS, RESIF	23
perm.	393	0-60 km	2015-2018	6.5-8.5	BGR, EIDA, ETHZ, GEOFON, INGV, IPCP, IRIS, LMU, ORFEUS, RESIF	27
Z3	218	25-700 km	09/2017-07/2018	6.5-8.5	EIDA	15
Z3	218	0-60 km	09/2017-07/2018	6.5-8.5	EIDA	19
ZS	218	25-700 km	10/2017-10/2018	6.5-8.5	GEOFON	24
ZS	218	0-60 km	10/2017-10/2018	6.5-8.5	GEOFON	24

Table 2: *Permanent and temporary AlpArray stations i with P-phase amplitudes strongly deviating from reference stations GE.MATE, respectively Z3.A261A, on vertical channels. Median of* $A_{i,j}$ / $A_{ref,j}$ *amplitude ratios for all events j, if < 0.1 or > 10. The complete result tables are available in the electronic supplement to this article. Event catalogs: Permanent stations - 01/2015 - 03/2018; temporary stations: 09/2017 - 07/2018.* n_{ev} *is the number of events used to obtain the result.*

Station	Component	$A_{i,j}/A_{ref,j_{median}}$	$A_{i,j}/A_{ref,j_{mean}}$	$A_{i,j}/A_{ref,j_{stdev}}$	n_{ev}
BW.RNON	Z	152.5	400.7	530.4	22
CH.OTER1	Z	0.001	0.004	0.006	12
FR.RUSF	07,Z	110.3	135.5	121.5	23
GU.SARM	Z	22.4	44.7	71.4	9
NI.POLC	Z	0.01	0.01	0.06	13
RD.MFF	Z	$8.6e12$	$9.4e12$	$5.9e12$	22
RF.GEPF	Z	0.01	0.01	0.004	16
SK.MODS	Z	$2.8e11$	$2.6e11$	$1.4e11$	12
SK.ZST	Z	$4.9e08$	$6.3e08$	$5.e08$	21
CR.SMRN	Z	27.1	33.5	24.0	3
Z3.A112A	Z	0.02	0.02	0.01	10

Table 3: *Permanent and temporary AlpArray and SWATH-D stations with obtained correction angles* $|\alpha_c| \geq 20°$. n_{ev} *is the number of events used to obtain the result. Only results with cross-correlation values above 0.80 and* $n_{ev} \geq 5$ *are included.*
** Temporal change in orientation.*
*** Broken HHE channel in November and December 2017.*

Station	$median(\alpha_c)[°]$	$mean(\alpha_c)[°]$	$std(\alpha_c)[°]$	n_{ev}
CZ.OSTC	-23.5	-22.7	6.8	14
CZ.GOPC	144.0	149.9	13.5	12
FR.GRN	30.0	27.5	8.7	16
FR.LRVF	-59.0	-56.3	14.6	14
GU.MAIM	-22.0	-20.1	7.3	7
GU.PCP	-31.5	-31.3	4.8	10
GU.RORO	-168.0	-166.6	7.2	7
HU.EGYH	-20.0	-19.9	6.7	13
IV.CELB	23.0	19.6	7.6	9
IV.FIR	102.5	102.7	9.3	6
IV.MILN*	-34.0	-20.9	34.9	9
IV.MSSA	-23.0	-17.9	8.1	9
IV.SARZ	-163.5	-164.7	6.5	6
IV.ZCCA	164.0	161.8	9.9	11
NI.VINO*	-160.0	-92.3	95.8	12
TH.ZEU	-33.0	-35.6	7.9	15
Z3.A030A	-45.0	-43.3	10.0	6
Z3.A263A	169.5	165.3	13.9	6
Z3.A300A	163.0	172.4	11.5	7
Z3.A301A	-22.5	-23.7	12.3	8
ZS.D116	24.	21.	6.4	7
ZS.D141**	$-22.$	-13.0	30.7	6
ZS.D125	171.	171.4	4.2	5

List of figure captions

Figure 1: Example of a teleseismic event catalog downloaded from global CMT, 2015-2018, $6.5 < M_W < 8.5$, depth 1-60 km. The map is centered in the Alps. The blue stars show the locations of an automatically selected subset of azimuthally distributed events used for the orientation analysis of the permanent AlpArray stations. Other, not used events in red.

Figure 2: Automatically generated map showing the logarithm of the median amplitude ratios of all events j for each permanent station i of the AlpArray network, vertical component, relative to station GE.MATE (black rectangle).

Figure 3: Cross-correlation coefficient as a function of the correction angle for (a) station GR.BFO and (b) ZS.D125, and 4 example events each. The maximum cross-correlation of the Hilbert-transformed radial component and the vertical component of GR.BFO is obtained for a correction angle close to 0°. The horizontal components of ZS.D125 have inverse polarities, therefore the obtained correction angle is 180°.

Figure 4: PSD quality check result: Example station GE.MATE, 20 events, vertical component. (a) PSDs of synthetic (red) and observed (black) event data, vertical component. The sampling rate of synthetic and observed data is 2 s and the instrument's lower corner frequency is 0.01 Hz. For many events, the PSDs of the synthetic and the recorded data agrees well. (b) Median of the ratio of the synthetic and observed PSDs presented above at each frequency step. The dashed lines show the results of the line fits. The red line indicates the frequency range recommended to use for MT inversion.

Figure 5: Locations of the permanent (black) and temporary (red) broadband stations of the AlpArray seismic network and the SWATH-D stations (blue).

Figure 6: Maps showing the logarithm of the median amplitude ratios $A_{i,j}/A_{ref,j}$ of all events j for each permanent (a, c, e) and temporary (b, d, f) AlpArray station i. The reference stations GE.MATE, respectively Z3.A261A are marked by black rectangles. Outliers removed to emphasize potential site effects.

Figure 7: Maps showing the logarithm of the median amplitude ratios $A_{i,j}/A_{ref,j}$ of all events j for each station i of the SWATH-D network, relative to station ZS.D017 (black rectangle). (a) Z, (b) R and (c) T component. Minor amplitude variations are explained by site-effects and different noise levels.

Figure 8: Automatically generated maps showing the obtained sensor orientations ($o_N = 0° - \alpha_c$) of the (a) permanent, (b) temporary, and (c) SWATH-D AlpArray stations. The orientations of

the horizontal components of all stations are indicated by the vectors. The colors indicate the absolute misorientations. Tiny black arrows denote stations where less than five events could be used to obtain the results.

Figure 9: (a) M 7.9, 2018-01-23 09:32:03.970 Gulf of Alaska. P-phase onsets on vertical channels of GU network, bandpass filtered at 0.05-0.4 Hz. GU.RORO shows opposite polarity. (b) S-phase of the same event on horizontal and vertical channels of IV.SARZ and neighboring stations. The polarities of the HHN and HHE channels of IV.SARZ are reversed. The blue dotted line depicts the traces of IV.SARZ reoriented by the correction angle (Table 3).

Figure 10: Correction angle over time for NI.VINO showing a temporal change in summer 2016.

Figures

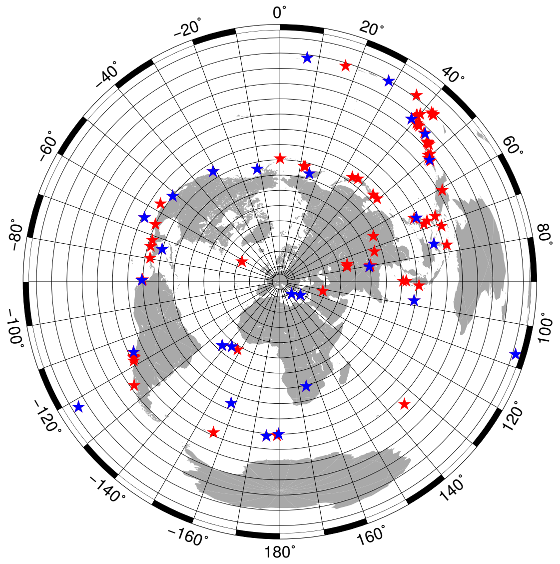

Figure 1: *Example of a teleseismic event catalog downloaded from global CMT, 2015-2018,* $6.5 < M_W < 8.5$*, depth 1-60 km. The map is centered in the Alps. The blue stars show the locations of an automatically selected subset of azimuthally distributed events used for the orientation analysis of the permanent AlpArray stations. Other, not used events in red.*

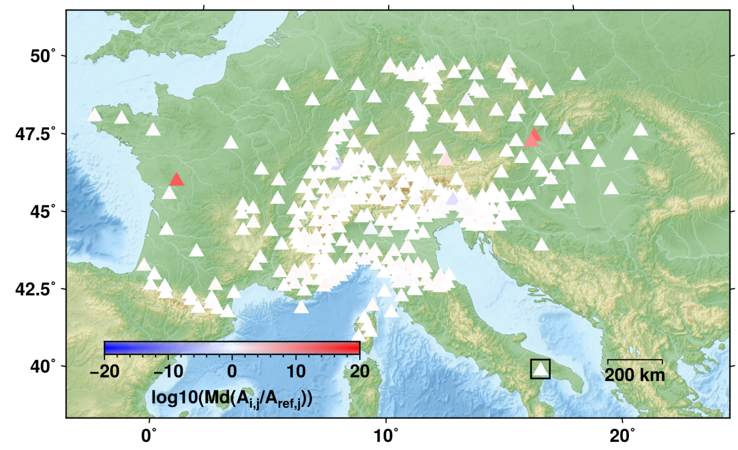

Figure 2: *Automatically generated map showing the logarithm of the median amplitude ratios of all events j for each permanent station i of the AlpArray network, vertical component, relative to station GE.MATE (black rectangle).*

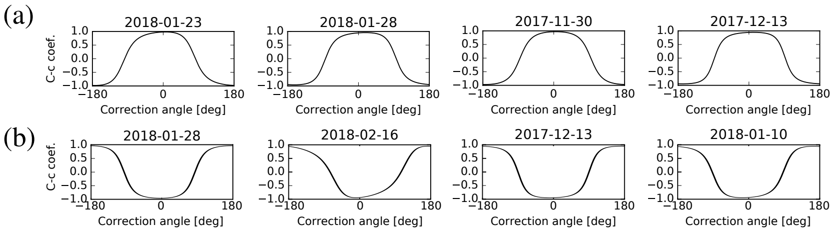

Figure 3: *Cross-correlation coefficient as a function of the correction angle for (a) station GR.BFO and (b) ZS.D125, and 4 example events each. The maximum cross-correlation of the Hilbert-transformed radial component and the vertical component of GR.BFO is obtained for a correction angle close to 0°. The horizontal components of ZS.D125 have inverse polarities, therefore the obtained correction angle is 180°.*

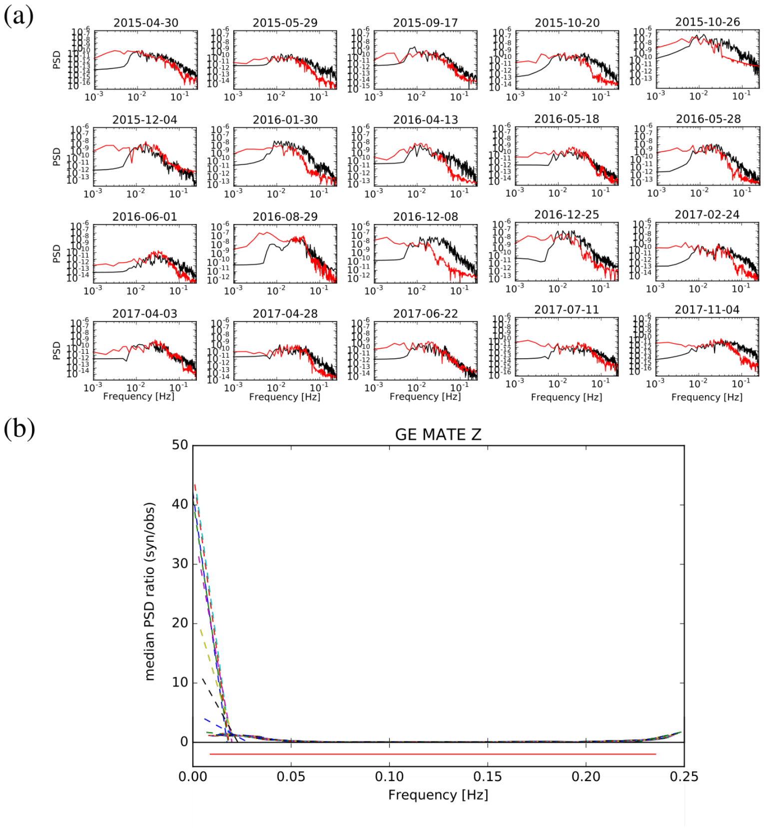

Figure 4: *PSD quality check result: Example station GE.MATE, 20 events, vertical component. (a) PSDs of synthetic (red) and observed (black) event data, vertical component. The sampling rate of synthetic and observed data is 2 s and the instrument's lower corner frequency is 0.01 Hz. For many events, the PSDs of the synthetic and the recorded data agrees well. (b) Median of the ratio of the synthetic and observed PSDs presented above at each frequency step. The dashed lines show the results of the line fits. The red line indicates the frequency range recommended to use for MT inversion.*

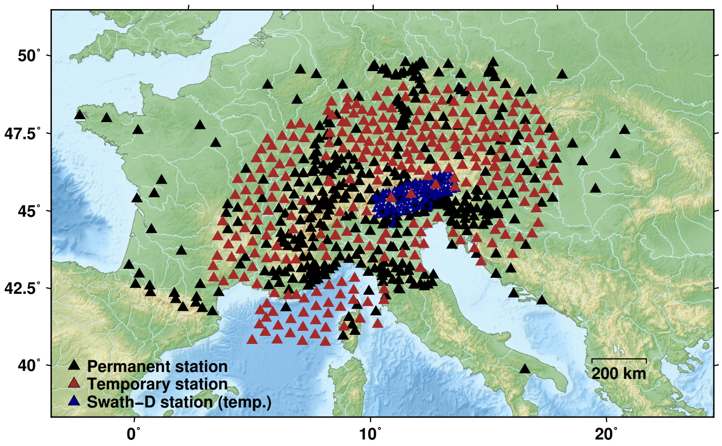

Figure 5: *Locations of the permanent (black) and temporary (red) broadband stations of the AlpArray seismic network and the SWATH-D stations (blue).*

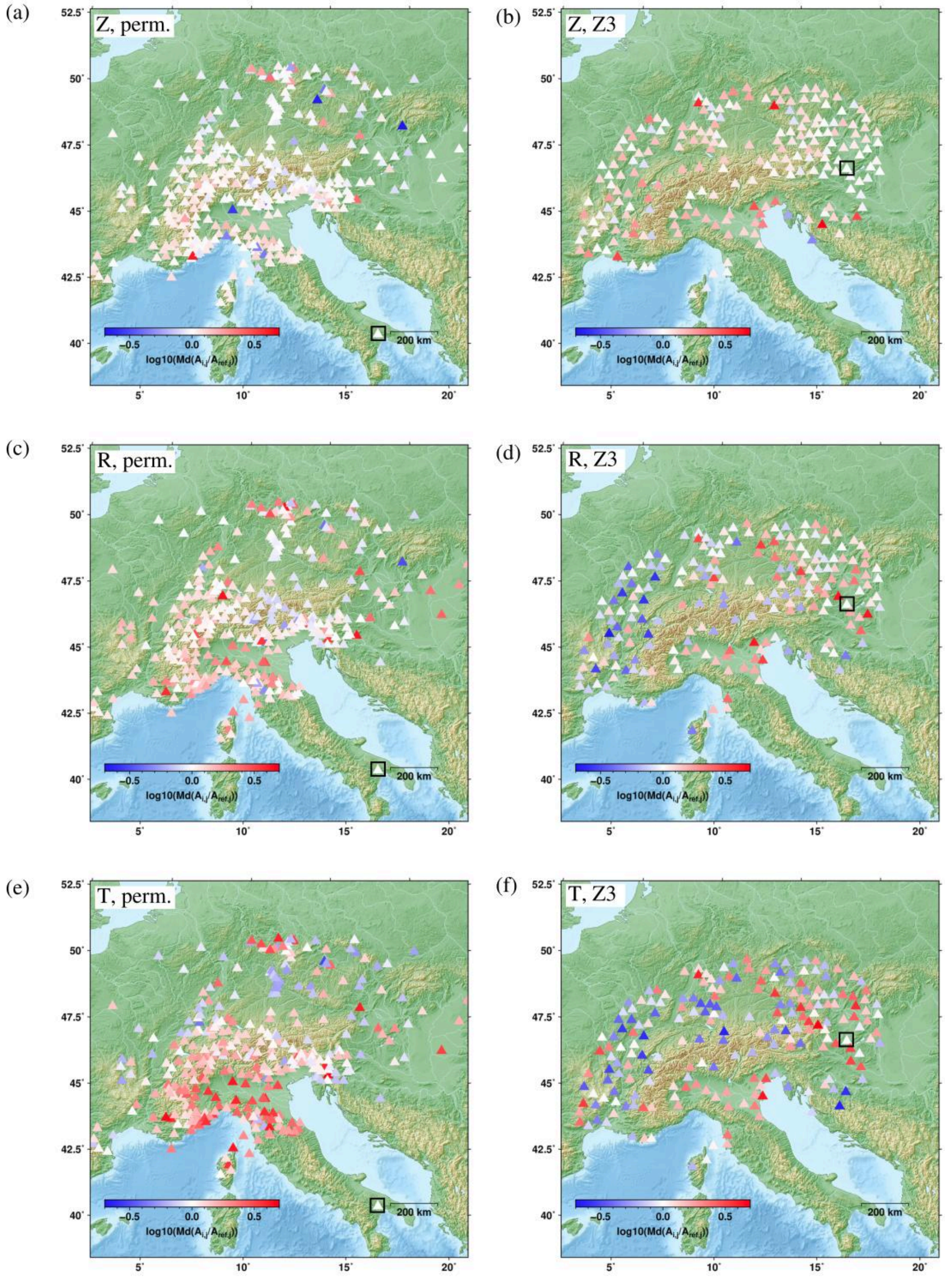

Figure 6: *Maps showing the logarithm of the median amplitude ratios $A_{i,j}/A_{ref,j}$ of all events j for each permanent (a, c, e) and temporary (b, d, f) AlpArray station i. The reference stations GE.MATE, respectively Z3.A261A are marked by black rectangles. Outliers removed to emphasize potential site effects.*

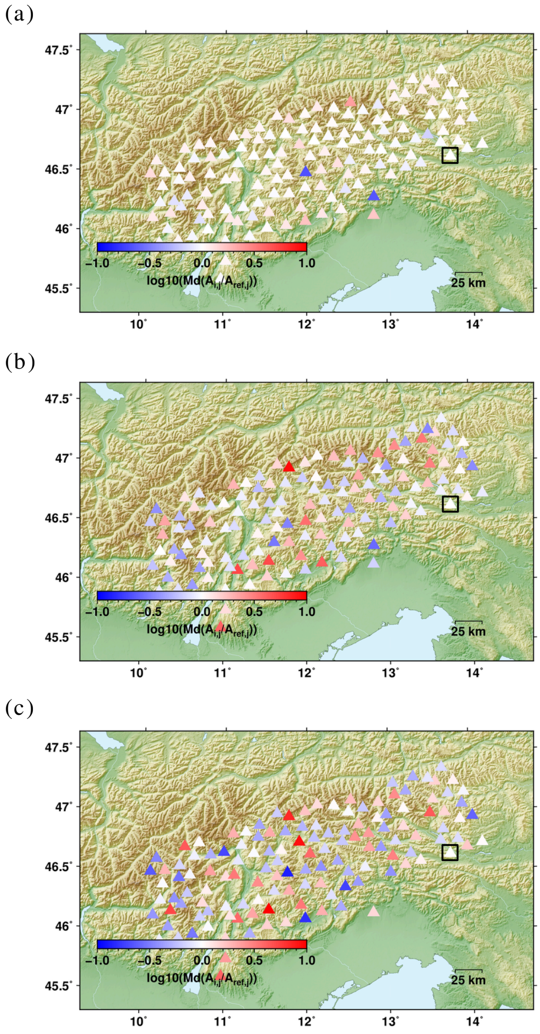

Figure 7: *Maps showing the logarithm of the median amplitude ratios $A_{i,j}/A_{ref,j}$ of all events j for each station i of the SWATH-D network, relative to station ZS.D017 (black rectangle). (a) Z, (b) R and (c) T component. Minor amplitude variations are explained by site-effects and different noise levels.*

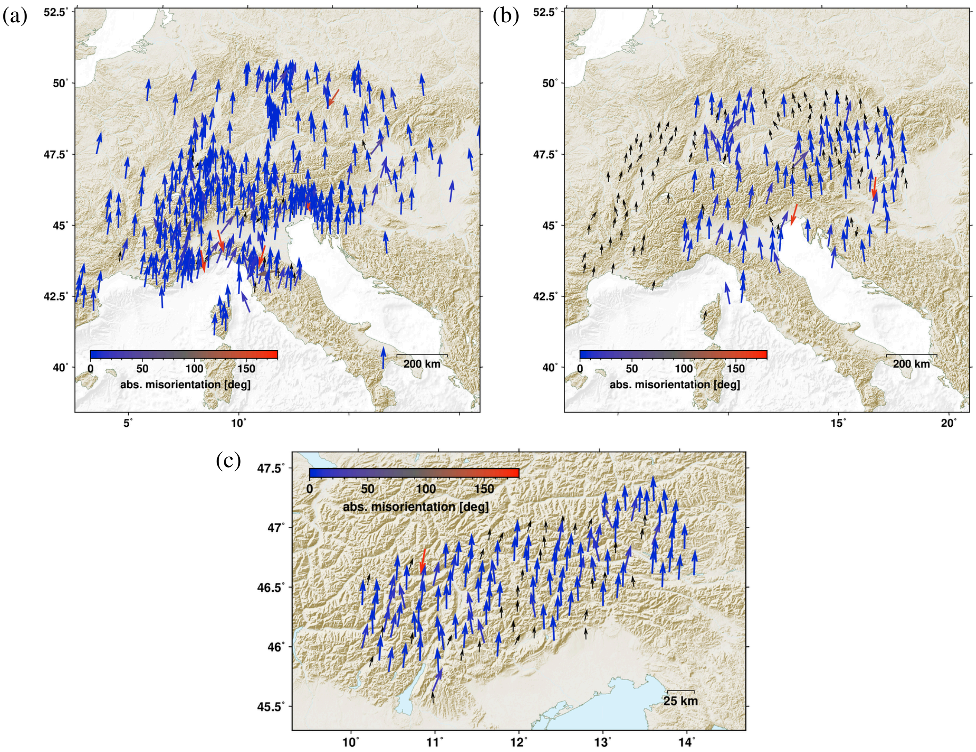

Figure 8: *Automatically generated maps showing the obtained sensor orientations ($o_N = 0° - \alpha_c$) of the (a) permanent, (b) temporary, and (c) SWATH-D AlpArray stations. The orientations of the horizontal components of all stations are indicated by the vectors. The colors indicate the absolute misorientations. Tiny black arrows denote stations where less than five events could be used to obtain the results.*

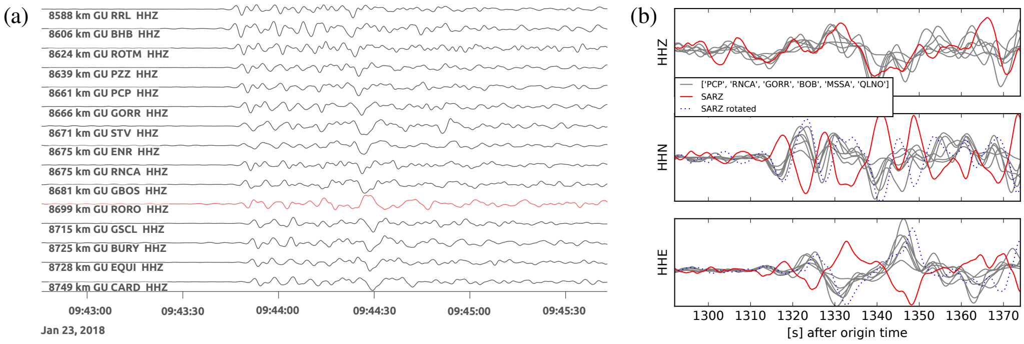

Figure 9: *(a) M 7.9, 2018-01-23 09:32:03.970 Gulf of Alaska. P-phase onsets on vertical channels of GU network, bandpass filtered at 0.05-0.4 Hz. GU.RORO shows opposite polarity. (b) S-phase of the same event on horizontal and vertical channels of IV.SARZ and neighboring stations. The polarities of the HHN and HHE channels of IV.SARZ are reversed. The blue dotted line depicts the traces of IV.SARZ reoriented by the correction angle (Table 3).*

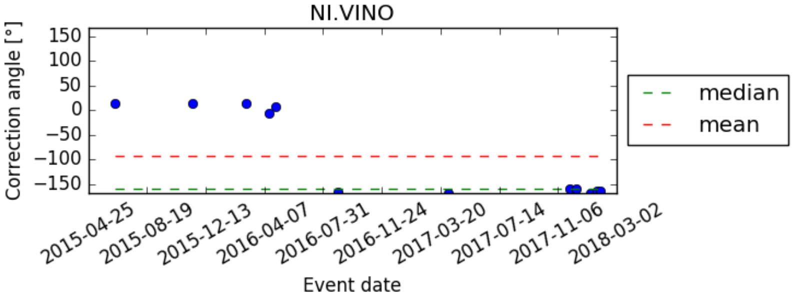

Figure 10: *Correction angle over time for NI.VINO showing a temporal change in summer 2016.*

CHAPTER 5

Orientations of Broadband Stations of the KOERI Seismic Network (Turkey) from Two Independent Methods: P- and Rayleigh-Wave Polarization

Büyükakpinar, P., Aktar, M., **Petersen, G.M.**, and Köseoğlu, A. (2021)

Published in Seismological Research Letters, vol. 92 (3), pp. 1512-1521.
https://doi.org/10.1785/0220200362

The following chapter contains the accepted manuscript (AM) of the above publication. Please refer to the citation to get access to the final, formatted publication. The supplementary material for this publication can be downloaded at https://doi.org/10.1785/0220200362.

Orientations of Broadband Stations of the KOERI Seismic Network (Turkey) from Two Independent Methods: P- and Rayleigh-Wave Polarization

Pınar Büyükakpınar[1], Mustafa Aktar, Gesa Maria Petersen, Ayşegül Köseoğlu

[1]Kandilli Observatory and Earthquake Research Institute, Regional Earthquake-Tsunami Monitoring Center, Boğaziçi University, İstanbul, Turkey

ABSTRACT

The correct orientation of seismic sensors is critical for studies such as full moment tensor inversion, receiver function analysis, and shear wave splitting. Therefore, the orientation of horizontal components needs to be checked and verified systematically. This study relies on two different waveform based approaches to assess the sensor orientations of the broadband network of the Kandilli Observatory and Earthquake Research Institute (KOERI). The network is an important backbone for seismological research in the Eastern Mediterranean Region and provides a comprehensive seismic data set for the North Anatolian Fault. In recent years, this region became a worldwide field laboratory for continental transform faults. A systematic survey of the sensor orientations of the entire network, as presented here, facilitates related seismic studies. We apply two independent orientation tests, based on the polarization of P-waves and Rayleigh-waves to 123 broadband seismic stations, covering a period of 15 years (2004-2018). For 114 stations we obtain stable results with both methods. Approximately 80% of the results agree with each other within 10°. Both methods indicate that about 40% of the stations are misoriented by more than 10°. Among these, 20 stations are misoriented by more than 20°. We observe temporal changes of sensor orientation which coincide with maintenance work or instrument replacement. We provide time-dependent sensor misorientation correction values for the KOERI network as supplementary material.

INTRODUCTION

Three-component seismograms recorded by broadband sensors are essential for the study of earthquake source processes and structural properties of the subsurface. Most applications use the ray-based coordinate system (radial and transverse components), which is obtained by rotating the seismograms of the horizontal components (conventionally oriented NS and EW) for an event. A reliable rotation requires the correct estimation of the back-azimuth determined from source and receiver coordinates and a known orientation of the sensors which might deviate from NS and EW convention. The misorientation of the horizontal sensor components is a common problem in seismic networks as has been reported by many detailed observations worldwide (e.g. Laske, 1995; Niu and Li, 2011; Rueda and Mezcua, 2015; Ojo *et al.*, 2019; Petersen *et al.*, 2019). In practice, the geographical north is routinely determined from the magnetic north using a magnetic compass, with a precision of about ±5° (e.g. Vecsey *et al.*, 2017). In Polar regions, as well as in volcanic areas, the fluctuations of the magnetic field are inevitable and supplementary checks are usually applied. More often, the error is anthropogenic, resulting from either magnetic material in nearby buildings or the improper use of the magnetic compass. Misorientations may further be introduced by transferring the determined north line to the sensor location (Ringler *et al.*, 2013). Tools such as a gyrocompass, sun-shot jig, and GPS can be used to increase the accuracy of the sensor orientation (e.g. Ringler *et al.*, 2013). Time-dependent changes of the sensor orientation have been observed and attributed e.g. to field-visits without proper reorientation, switches in the polarity of vertical or horizontal components, or animal activity (e.g. Rueda and Mezcua, 2015; Petersen *et al.*, 2019).

The misorientation of the sensors may lead to wrong interpretations in many applications, such as full moment tensor inversion, anisotropy, shear-wave splitting, the polarization of seismic waves, and receiver function studies, which rely heavily on the component rotation (Ekström and Busby, 2008; Zahradník and Custódio, 2012; Wang *et al.*, 2016). For this reason, the correct orientation of horizontal components should be a part of data quality assessment before any processing and interpretation. Tilted vertical components are less common and therefore generally assumed as correct in most orientation studies (Ekström and Busby, 2008; Niu and Li, 2011).

Sensor orientations have previously been studied for various networks worldwide. Laske (1995) used long-period surface waves to show that 4 of 37 stations from Geoscope and International Deployment of Accelerometers (IDA) networks had misorientation of more than 3°. Laske and Masters (1996) also analyzed the polarization of long-period surface waves and reported that 12 of the 76 stations operated by GEOSCOPE (G), IDA/IRIS (II), and IRIS/USGS (IU) are misaligned, sometimes by more than 5°. Yoshizawa *et al.* (1999) used the polarization of lower-mantle P-waves and found significant deviations from the N-S direction for 4 Global Seismic Network (GSN) stations. Larson (2000) and Larson and Ekström (2002) used the polarization of intermediate-period surface waves and showed similar sensor misorientations in the order of 10° for 10 GSN stations. Likewise, Schulte-Pelkum *et al.*

(2001) estimated that at least 10 GSN stations were misoriented by more than 10°, based on particle motion of long-period P waves. Ekström and Busby (2008) reported that 10.3% of the backbone and transportable stations of the USArray were misoriented by 7° or more. Niu and Li (2011) evaluated the CEArray (>1000 stations) with a signal to noise ratio-weighted-multi-event method. They estimated that one-third of stations had misorientations larger than 8°. Rueda and Mezcua (2015) have used 10 years of data to quantify the misorientation of the Spanish Broadband National Network stations using the Rayleigh-wave polarization method. They found that 15 of 47 stations had significant misorientations of more than 15°. Ojo *et al.* (2019) analyzed the orientation of 1075 African seismic stations. In their study, three independent waveform-based methods were simultaneously applied, namely P-wave particle motion based on the principal component analysis (PCA), minimization of the P-wave energy on the transverse component, and measuring intermediate-period Rayleigh wave arrival. They found that 251 stations were misaligned by more than 10°. Braunmiller *et al.* (2020) have recently demonstrated that approximately 75% of the Iranian National Seismic Network (INSN) and 59% of the Iranian Seismological Center (IRSC) are oriented within 15° of true North, using P-wave energy minimization on the transverse component. Furthermore, they observe temporary variations for 36 out of 121 stations. As a result of the increasing number of seismic stations, automated station quality assessment is inevitable. Petersen *et al.* (2019) developed the python-based toolbox “AutoStatsQ”, which includes a test to identify sensor misorientations using Rayleigh-wave polarization analysis. They analyzed over 750 stations of the AlpArray seismic network and the smaller SWATH-D seismic array and identified sensor misorientations of more than 20° for about 5% of the stations. Lastly, Zeng *et al.* (2020) have recently indicated that 80 stations and 49 stations of CHINArray have misorientation by 5°-20° and >20° or other malfunctioning problems, respectively. They have also shown that large sensor alignment errors could adversely affect the results of many seismic studies such as receiver function, anisotropy, and ambient noise.

In this study, we assess the orientation of the horizontal components of the broadband stations of the seismic network operated by the Kandilli Observatory and Earthquake Research Institute (KOERI; Fig. 1). After an introduction into the methodology of both applied orientation tests, we present the orientation estimates for all stations and discuss methodological limitations. We provide all results in a table to allow the reader to apply corrections before performing further seismological studies.

METHOD AND DATA

In this study, we use two independent methods to obtain the apparent arrival direction of teleseismic waves from the polarization of two wave types, P and Rayleigh waves. The apparent arrival directions are compared to the theoretical direction obtained from event and source location. Deviations between theoretical and apparent arrival direction are explained by misoriented horizontal components of the seismic sensors. Since the two methods use different parts of the seismogram and different frequency bands, the results obtained by the two methods are considered independent. Data are limited to broadband waveforms recorded between 2004 and 2018 by the KOERI network. The sensors include GURALP 3T, 3ESP, 3ESPC, 6T, 40T seismometers, with long period corner varying between 30 s to 360 s.

Figure 2 summarizes the procedure used in this study. The blue solid lines represent the geographical coordinates (North and East). The blue dashed line represents the theoretical direction of the incoming ray. The angle (φ) between the incoming ray and the geographic north is called the theoretical back-azimuth angle. Since this angle is obtained directly from the event-station coordinates, without using the waveforms, it is independent of the sensor orientation. The back-azimuth angle can also be obtained from waveform analysis using the polarization of particle motions. A sensor misorientation directly influences this apparent back-azimuth angle (φ’). In Figure 2, the black solid lines represent the actual and therefore possibly erroneous orientation of horizontal components of a sensor. If the sensor is not correctly oriented to the North, the apparent back-azimuth is not the same as the one obtained from the station-event location. The difference between the theoretical and the apparent back-azimuth angles is defined as the sensor deviation angle ($\theta_0 = \varphi - \varphi'$), assuming as positive in the clockwise direction.

Note that the approach described above is based on the a priori assumption that the deviations between the theoretical and apparent back-azimuth values are only caused by the sensor misorientation. In reality, however, many other factors may also lead to an erratic bending of the ray path from its direct trajectory and deviate the particle motion from its direction. A dipping layer below the station or 3D complexities can perturb the results. Similarly, any type of anisotropy along the ray path, either at lower crust or upper mantle layers, can also result in deviations of the polarization of the seismic waves. The best way to test the degree of validity of the primary assumption is to repeat the tests for events from various back-azimuths and distances. If the same sensor deviation angle is found for different ray paths, it can safely be assumed that the sensor misorientation is the main cause of the deviation. In practice, however, earthquakes are not distributed evenly in all azimuthal directions. In the P wave polarization analysis we use a large number of events, mainly from two azimuthal ranges (blue stars in Fig. 3). In the Rayleigh wave polarization analysis, we use a relatively homogeneous distribution of large earthquakes (red stars in Fig. 3). Detailed descriptions of the two methods are given in the following paragraphs.

P-wave polarization method

In the P-wave polarization analysis, we use first arrivals from distant events to estimate the direction of the incoming wave. This part of the waveform is entirely composed of P-wave, therefore the particle motions are aligned with the radial direction. The polarization angle of this initial part of the seismogram gives directly the apparent back-azimuth angle (Niu and Li 2011; Ojo *et al.*, 2019). The P-wave time window is chosen as the first 8 seconds after the arrival time, which is estimated theoretically and then validated visually for each teleseismic events. The polarization of particle motion on the horizontal plane is estimated by applying a principal component analysis (PCA) to the covariance matrix of the horizontal components. The direction of the eigenvector corresponding to the highest eigenvalue equals the preferred direction of particle motion, in other words, the direction of the incoming radial ray.

The direction estimation is not based on a single event only, but on a collection of a large number of events, with an epicentral distance of 30°-90° and with magnitude ≥5.5. All waveforms are low-pass filtered using a two-pole Butterworth filter with a cut-off frequency of 0.3 Hz. Filtering is applied both in forward and reverse directions to preserve the phase content of both components. Approximately 100,000 waveforms were visually analyzed for the whole network and a total of 9313 waveforms with a high signal-to-noise ratio were selected for further analysis.

For the P-wave based analysis of the KOERI network, we use two specific azimuth directions, which provide extensive data for a stable application of the PCA (Fig. 3, blue stars). These are Japan (back-azimuth 45°N-55°N, BAZ_1) and the Java Trenches (back-azimuth 90°N-110°N, BAZ_2). In order to increase the accuracy of the approach, we use events within a narrow back-azimuth range of 6° for each station, thus guaranteeing nearly the same ray path for all waveforms that are jointly processed.

For most stations, the P-wave polarization analysis is done only for these two directions and the final sensor deviation angle is determined by taking the mean of these two independent results (see Table S1 available in the supplemental material to this article). If the estimates of these two azimuths are close, we can safely assume that the sensor misorientation is the main cause for the deviation. Otherwise, other factors described above may likely influence the deviations of particle motion. In order to illustrate the procedure, the particle motion and the result of PCA are shown in Figure 4a and 4b, for station KO.SVAN. The two subplots show the particle motion for the two different back-azimuth ranges. In both directions, a composite wave is obtained by concatenating all of the P-wave arrivals from a large number of different events (92 and 34 events). The black dashed lines show the direction of motion obtained from the PCA, which gives the apparent back-azimuth (φ'). The red line shows the true\theoretical back-azimuth (φ) computed from source and receiver coordinates using the SAC2000 package (Goldstein *et al.*, 2003). In the case of the station KO.SVAN, the sensor deviation angle is found to be 8.4° ±1.9 and 12.2° ±1.9 for BAZ_1 and BAZ_2, respectively which gives the mean of 10.3°.

Rayleigh-wave polarization method

The second method uses the polarization of Rayleigh-waves to estimate the apparent back-azimuth of the teleseismic waves. Rayleigh waves are theoretically observed on radial and vertical components with a phase shift of 90°. Assuming a correctly oriented sensor and hence a correct radial component, the Hilbert-transformed radial component should resemble the vertical component. The test is implemented in the python-based toolbox AutoStatsQ (Petersen *et al.*, 2019; https://github.com/gesape/AutoStatsQ, last accessed September 2020), which is based on the seismological python library Pyrocko (Heimann *et al.*, 2017). The tool selects time windows of 660 s length assuming a maximum propagation velocity of V_R=4 km/s. All waveforms are band-pass filtered between 100 s and 30 s, and the instrument response is removed. For each event, the Hilbert-transformed radial component is rotated in steps of 1° and cross-correlated with the vertical component. The rotation angle resulting in the highest correlation of the two components corresponds to the orientation correction angle. 69 azimuthally well-distributed events are selected from a teleseismic distance >30°, with Mw≥6.9 and depth<35km (red stars in Fig. 3). In order to improve the accuracy, only events showing a sufficiently high maximum value of the cross-correlation coefficients (>0.85) are used. An average of 16 events is finally used for each station. To avoid any bias due to single outliers, the median of the independent estimates per event is chosen as the final orientation error for each station (Petersen *et al.*, 2019).

Figure 4c shows the estimated orientation error for the single events at the station KO.SVAN. The events are sorted according to their back-azimuth to check the validity of the initial assumptions of horizontal layers and isotropy. The azimuthal variation of the sensor deviation angle does not show any sinusoidal pattern which may be interpreted with simple geometrical considerations. It is observed that for this particular station the median of the sensor deviation angle for 36 events is 9.0°. The mean (6.4°) and the standard deviation (8.0°) are influenced between 80° and 110° range, where significantly different orientations angles around -10° to -15° are obtained. To avoid such bias we used the median value obtained from azimuthally distributed earthquakes. Note that the median sensor deviation angle found for this station is similar to the result obtained from the P wave-polarization which therefore confirms both methods.

RESULTS

The sensor deviation angle is estimated for a total of 123 broadband stations operated by the KOERI network. For most of these stations (114 of 123), it was possible to determine the sensor orientation using both the P-wave and the Rayleigh-wave approaches. This redundancy provided a double-check mechanism for all values obtained in this study. Figure 5 summarizes the results of both methods. Since the network is much denser in the Marmara Region (NW Turkey), an additional detailed map of this region is included (Fig. 5a for the whole KOERI network and Fig. 5b for the Marmara Region). Blue and red arrows show the estimated orientation of the sensors, obtained from P wave and Rayleigh-wave methods respectively. The orientation results of both methods agree well with differences of ≤5° for 55% and ≤10° for 80% of the stations. Since 10° corresponds approximately to the sensitivity range of the methods, we assume that the values estimated by either method are close to the true orientation error of the sensor. For 18 stations, the orientation error obtained by both methods differs by 10-20°, which may be attributed to some basic methodological differences, such as the frequency band used. Some discussions about the possible causes of the disagreement between the two methods are included at the end of this section. For 5 stations the difference between both methods exceeds 20°.

For the 91 stations where the two methods agree well (≤10°), we use the average of the two sensor deviation angles and present the final orientation of the sensors (θ_0) in Table S1. For 53 of 91 stations, the sensor deviation angle is less than 10°. We assume that these station orientations are good enough for most subsequent seismological studies and therefore we do not propose a complementary test. On the other hand, a rotation correction is strongly recommended before applying any processing for the 20 stations that have an average sensor deviation angle >20° (Table 1).

The data used for testing covers a period of 15 years, starting from the initial installation of broadband sensors of the KOERI network in 2004. This gives an opportunity to check whether there are changes of orientation during the operating time of the network. 18 stations show temporal variations of the sensor orientation during the course of the operational period in one of the two analysis methods. Both methods show time shifts at stations KO.BGKT, KO.PTK, and KO.YAYX (see Supplementary Table S1). In these three cases, the time interval where the modification took place is found to coincide with maintenance operations where the sensor was either removed from its initial position for repair or replaced. It was therefore easy to determine the exact date of the orientation change by referring to the field notes of maintenance technicians.

At this stage, it is useful to focus on possible explanations about why the results of the two methods may deviate from each other. The basic difference between the two methods lies in the use of waveforms, namely the time window selected and the frequency band utilized. These differences are less relevant in a setting where the a priori assumptions described above (purely horizontal layering and no anisotropy) are fully valid. However, in a situation where there is some deviation from the ideal conditions, the way the two methods respond is quite different. Since the Rayleigh-wave approach uses low frequencies, it is less sensitive to small-scale perturbations of the underlying structure. Furthermore, since it is restricted to only large events, data from all azimuths need to be included and the final result is an intermediate solution that satisfies all azimuths. The P-wave method however takes advantage of much smaller events and uses much higher frequencies. It has the potential of producing stable results for very narrow azimuth angles. In fact, this study used only two directions, which provide the largest number of events (Japan and Java Trenches). In both regions, the data was sufficient enough to focus the test to a very narrow angle of ±3° and thus, avoid any blurring effects due to azimuth fluctuations. However, the use of higher frequencies makes the P-wave approach more sensitive to crustal complexities, which may be desirable or not depending on the purpose. To summarize, one can say that the Rayleigh-wave approach provides a robust solution nearly valid for all azimuths, while the P-wave method provides greater accuracy for narrow angles and therefore helps to detect azimuth variations. This is well illustrated in the case of the station KO.LEF. Figure 6 shows the orientation error estimated at several different azimuths using both P-wave and Rayleigh-wave methods. Clearly, although the amplitude of scattering is comparable for both methods, the P-wave approach reveals a periodicity, while the Rayleigh approach remains blind to it. A first-order interpretation of the azimuthal periodicity is the presence of a 3D geological structure, which deviates the incoming ray from its direct path. In fact, any velocity changes near the station may provide a faster path, which would deviate from the direct line and follow an alternative path, for the ray which is bent. Accordingly, the particle motion would not align with the source-receiver direction. In this situation, the sensor deviation angle would be azimuth dependent. For simple structures such as a single dipping layer or a single anisotropic layer, the orientation estimates show a well-defined sinusoidal periodicity (Wang *et al.*, 2016). This type of structural irregularities is not uncommon in tectonically active zones such as Turkey where geological formations are strongly perturbed by recent tectonic movements. For the station KO.LEF, the result of the P-wave method is clearly much closer to a sinusoidal pattern as compared to the Rayleigh-wave method. This can be explained by the fact that the P-wave approach uses more events for each azimuth interval and therefore achieves much higher accuracy. Additionally, the P wave polarization method uses a higher frequency band (<0.3 Hz) compared to the Rayleigh wave analysis (<0.03 Hz) and therefore the results are far more sensitive to crustal-scale anomalies. A close inspection of Figure 5 shows that a considerable number of stations aligned along the Black Sea Coast have a nearly identical type of disagreement between the two methods. A similar behavior is also observed for the stations West of the Lake Van. It would be interesting to know whether this type of regional trends may be related to a single common feature, such as the two large Transform Faults located nearby in both cases (the North Anatolian Fault for Black Sea stations and the East Anatolian Fault for Lake Van, respectively). However, it is too early to draw a final conclusion, since a similar behavior is not observed in other parts of the same Transform Faults.

In general, for cases where the results from P-wave and Rayleigh methods differ more than 10°, it would be useful to make a detailed study of the azimuth variation using the P-wave approach. Our attempt in this context did not provide satisfactory results except for the station KO.LEF. This may be due to either higher structural complexity or simply to the insufficient number of the events from all azimuth angles. In future, as more data will be available we expect to obtain a more complete understanding of the effect of the azimuthal variation. In the present situation, we do not suggest a correction value for these ambiguous stations and recommend further in-situ test for assessing the true sensor orientation.

DISCUSSION & CONCLUSIONS

This study provides a first-order estimation of the orientation for broadband stations operated by the KOERI network, for the entire operating time of 15 years. Results show that for more than 40% of the stations, the orientation error exceeds the acceptable limit of <10°, and a rotation correction is strongly recommended.

The determination of the sensor orientation based solely on waveform data is not a simple task and uncertainties are inherent in the methods. Both methods that were applied in this study to estimate the sensor orientation are based on simplifying assumptions (horizontal geometry, isotropy). The violation of these assumptions influences the two methods differently. The final result is a trade-off between resolution (i.e. frequency) and robustness, which in this study are represented by the P-wave and the Rayleigh-wave methods, respectively. We have therefore based our final conclusions on the joint interpretation of the results of both approaches.

In some cases, the increased resolution of the P-wave approach reveals useful details about the azimuthal distribution of the orientation error. In particular, a sinusoidal pattern is observed in the azimuth distribution (KO.LEF station), which can be attributed to simple structures such as a single dipping layer or single layer anisotropy.

The most reliable but time consuming way of determining the sensor orientation is to measure it directly at the station site, using an astronomically determined geographical north. We have validated some of our results by in-situ measurements at selected stations using a magnetic compass. For comparison, the two polarization methods indicate that stations KO.ADVT and KO.CTKS are misoriented by 37.5° and -30.9°, respectively. The field measurements revealed that they were misaligned by 45° and -36°. Taking into account the measurement uncertainties of the magnetic compass and the standard deviations of both methods, these values are in good agreement (Table 1). Field observations also show that the main source of orientation error is the inadequate usage of the compass during the initial installation. Magnetic disturbances caused by the iron reinforcement of concrete buildings at the station sites cause considerable measurement difficulties. During the validation in the field, the magnetic north is determined at a sufficiently long distance from the station site, where disturbances can be assumed to be minimal. Then the inferred direction of the magnetic north was extrapolated into the interior of the building using geodetic tools. The magnetic to geographic conversion is applied using the actual value of the declination angle.

Worldwide experience shows that although many studies about sensor orientations indicate significant errors, sensor orientations are not always routinely checked and reported. The sensor orientation study presented here is, to our knowledge, the first one for the KOERI network. One main goal of this study is therefore to provide the users of the network with a reference correction table, which can be used in future studies.

DATA AND RESOURCES

Seismic data used in this study are free and open access to users via the International Federation of Digital Seismograph Networks (FDSN) client code (KO; https://doi.org/10.7914/SN/KO) in the databases of the Boğaziçi University Kandilli Observatory and Earthquake Research Institute (KOERI; http://eida.koeri.boun.edu.tr). Some of the figures were prepared using the Generic Mapping Tools version 5.2.1 (v.5.2.1; http://www.soest.hawaii.edu/gmt/, Wessel *et al.,* 2013). The MATLAB code to evaluate the sensor misorientation from P-wave polarization was developed by Mustafa Aktar and Pınar Büyükakpınar, and can be requested from the corresponding authors. The Python-based AutoStatsQ toolbox was used to estimate the sensor misorientation, using Rayleigh-wave polarization (Petersen *et al.,* 2019; https://github.com/gesape/AutoStatsQ). For topography in Figures 1 and 5, ETOPO1 data (Amante and Eakins 2009) and SRTM-3 data (Farr *et al.,* 2007) were used. Seismic data were analyzed with the Seismic Analysis Code (SAC; Goldstein *et al.,* 2003). All websites were last accessed in December 2020. The supplemental material for this article includes a table for sensor orientations of the KOERI broadband network.

ACKNOWLEDGMENTS

This study was supported by Boğaziçi University Research Fund(BAP) with Grant Number 15683 (19T04P1). The authors are thank-ful to D. Kalafat, H. Özener, K. Kekovalı, E. Zor, A.Ö. Konca, Ö.Necmioğlu, S. Tunç, Ö. Çok, and M. Jamalreyhani for constructive comments on this work. The authors thank P. Niemz for proofreading and helpful discussions. G. Petersen is funded by the DeutscheForschungsgemeinschaft (DFG) Project 362440331, a subproject of Schwerpunktprogramm (SPP) "Mountain Building Processes in 4D" (Project 313806092). The authors thank Editor-in-Chief Allison Bent, Guest Editor Susana Custódio as well as Jochen Braunmiller, and one anonymous reviewer for their valuable comments and suggestions that helped us to improve the article.

REFERENCES

Amante, C., Eakins, B.W., 2009. ETOPO1 1 Arc-Minute Global Relief Model: Procedures, Data Sources and Analysis. NOAA Technical Memorandum NESDIS NGDC-24, 19 pp.

Braunmiller, J., J. Nabelek, and A. Ghods (2020). Sensor Orientation of Iranian Broadband Seismic Stations from P-Wave Particle Motion, *Seismol. Res. Lett.* **91,** 1660–1671, doi: 10.1785/0220200019.

Ekström, G., and R. W. Busby (2008). Measurements of seismometer orientation at USArray transportable array and backbone stations, *Seismol. Res. Lett.* **79,** no. 4, 554–561.

Farr, T. G., P. A. Rosen, E. Caro, R. Crippen, R. Duren, S. Hensley, M.Kobrick, M. Paller, E. Rodriguez, L. Roth, *et al.* (2007). The Shuttle Radar Topography Mission, *Rev. Geophys.* **45,** no. 2, 1–33.

Goldstein, P., D. Dodge, M. Firpo, and L. Minner (2003). SAC2000: Signal processing and analysis tools for seismologists and engineers, in The IASPEI International Handbook of Earthquake and Engineering Seismology, E. H. K. Lee, H. Kanamori, P. C. Jennings, and C. Kisslinger (Editors), Vol. 81, Chapter 85.5, Academic Press, San Diego, California, 1613–1620.

Heimann, S., M. Kriegerowski, M. Isken, S. Cesca, S. Daout, F. Grigoli, C. Juretzek, T. Megies, N. Nooshiri, A. Steinberg, *et al*. (2017). Pyrocko—An open-source seismology toolbox and library, v.0.3, GFZ Data Services, doi: 10.5880/GFZ.2.1.2017.001.

Kandilli Observatory And Earthquake Research Institute, Bosphorus Univ. (2001). *Bogazici University Kandilli Observatory And Earthquake Research Institute* [Data set]. International Federation of Digital Seismograph Networks, https://doi.org/10.7914/SN/KO.

Larson, E. W. F. (2000). Measuring refraction and modeling velocities of surface waves, Ph.D. thesis, Harvard University, Cambridge, Massachusetts.

Larson, E. W. F., and G. Ekström (2002). Determining surface wave arrival angle anomalies, *J. Geophys. Res.* **107,** no. B6, ESE-7, doi: 10.1029/2000JB000048.

Laske, G. (1995). Global observation of off-great-circle propagation of long-period surface waves, *Geophys. J. Int.* **123,** 245–259.

Laske, G., and G. Masters (1996). Constraints on global phase velocity maps from long-period polarization data, *J. Geophys. Res.* **101,** 16059–16075.

Niu, F., and J. Li (2011). Component azimuths of the CEArray stations estimated from P-wave particle motion, *Earthq. Sci.* **24,** 3–13, doi: 10.1007/s11589-011-0764-8.

Ojo, O. A., L. Zhao, and X. Wang (2019). Estimations of sensor misorientation for broadband seismic stations in and around Africa, *Seismol. Res. Lett.* **90,** no. 6, 2188–2204.

Petersen, G. M., S. Cesca, M. Kriegerowski, and the AlpArray Working Group (2019). Automated Quality Control for Large Seismic Networks: Implementation and Application to the AlpArray Seismic Network. *Seismol. Res. Lett.* **90,** no. 3, 1177–1190, doi: 10.1785/0220180342.

Ringler, A. T., C. R. Hutt, K. Persefield, and L. S. Gee (2013). Seismic station installation orientation errors at ANSS and IRIS/USGS stations, *Seismol. Res. Lett.* **84,** no. 6, 926–931, doi: 10.1785/0220130072.

Rueda, J., and J. Mezcua (2015). Orientation analysis of the Spanish Broadband National Network using Rayleigh-wave polarization, *Seismol. Res. Lett.* **86,** no. 3, 929–940.

Schulte-Pelkum, V., G. Masters, and P. M. Shearer (2001). Upper mantle anisotropy from long-period P-polarization, *J. Geophys. Res.* **106,** no. B10, 21, 917–21, 934.

Vecsey, L., J. Plomerová, P. Jedlicka, H. Munzarová, V. Babuska, and the AlpArray Working Group (2017). Data quality control and tools in passive seismic experiments exemplified on the Czech broadband seismic pool MOBNET in the AlpArray collaborative project, *Geosci. Instrum. Method Data Syst.* **6,** 505–521.

Wang, X., Q. F. Chen, J. Li, and S. J. Wei (2016). Seismic sensor misorientation measurement using P-wave particle motion: An application to the NECsaids array, *Seismol. Res. Lett.* **87,** no. 4, 901–911, doi: 10.1785/0220160005.

Wessel, P., W. H. F. Smith, R. Scharroo, J. F. Luis, and F. Wobbe (2013). Generic Mapping Tools: Improved version released, *Eos Trans.* AGU **94,** 409–410.

Yoshizawa, K., K. Yomogida, and S. Tsuboi (1999). Resolving power of surface wave polarization data for higher-order heterogeneities, *Geophys. J. Int.* **138,** 205–220, doi: 10.1046/j.1365-246x.1999.00861.x.

Zahradník, J. and S. Custódio (2012). Moment tensor resolvability: Application to Southwest Iberia. *Bull. Seismol. Soc. Am.*, **102**, 1235-1254, doi: 10.1785/0120110216.

Zeng, S., Y. Zheng, F. Niu, and S. Ai (2020). Measurements of Seismometer Orientation of the First Phase CHINArray and Their Implications on Vector-Recording-Based Seismic Studies, *Bull. Seismol. Soc. Am.* **XX**, 1–14, doi: 10.1785/0120200129.

Pınar Büyükakpınar[1]

Ayşegül Köseoğlu[4]

Kandilli Observatory and Earthquake Research Institute, Regional Earthquake-Tsunami Monitoring Center, Boğaziçi University, İstanbul, Turkey

pinar.buyukakpinar@boun.edu.tr

koseogla@boun.edu.tr

Mustafa Aktar[2]

Kandilli Observatory and Earthquake Research Institute, Geophysics Department, Boğaziçi University, İstanbul, Turkey

aktar@boun.edu.tr

Gesa Maria Petersen[3]

Helmholtz Centre Potsdam German Research Centre for Geosciences – GFZ, Potsdam, Germany

Also at: University of Potsdam, Institute of Geosciences, Potsdam, Germany

gesap@gfz-potsdam.de

Table 1. Results of sensor deviation angles θ_0 estimated from P and Rayleigh wave polarization methods for stations with θ_0>20°.

No	Network	Station Code	θ_0 (P-wave)	θ_0 (Rayleigh-wave)	θ_0
1	KO	ADVT[*]	37.0°±2.9	38.0°±6.0	37.5°
2	KO	BGKT[†]	-24.2°±1.6	-23.5°±6.8	-23.9°
3	KO	BODT	-30.3°±2.0	-21.0°±9.5	-25.7°
4	KO	CAVI	25.6°±1.8	17.0°±7.5	21.3°
5	KO	CTKS[‡]	-31.8°±4.6	-30.0°±8.0	-30.9°
6	KO	CTYL	45.0°±0.7	45.5°±7.5	45.3°
7	KO	GEDZ	23.5°±3.0	20.5°±3.0	22.0°
8	KO	GEMT	30.9°±1.8	25.0°±5.0	28.0°
9	KO	GULA	28.9°±4.1	28.0°±7.6	28.5°
10	KO	KARO	-21.7°±1.9	-20.0°±7.9	-20.9°
11	KO	KARS	24.3°±6.3	16.5°±4.9	20.4°
12	KO	KLYT§	-160.3°±1.9	-157.0°±7.9	-158.7°
13	KO	KRBG	35.2°±0.9	33.0°±6.0	34.1°
14	KO	LADK	-19.2°±3.9	-22.0°±7.8	-20.6°
15	KO	PTK	23.7°±1.3	27.0°±8.6	25.4°
16	KO	RSDY	-26.6°±4.0	-22.5°±10.6	-24.6°
17	KO	SLVT	-67.7°±5.9	-58.0°±5.7	-62.9°
18	KO	YAYX	27.4°±4.6	25.0°±5.5	26.2°
19	KO	YER	20.6°±9.1	22.5°±6.8	21.6°
20	KO	YLV	21.6°±4.8	23.0°±3.9	22.3°

[*] In situ measurement θ_0=45° .

[†] Date interval (30 September 2009–17 June 2015).

[‡] In situ measurement θ_0=-36°.

§Polarity reversal for the date interval (30 September 2009–07 July 2018).

Figure 1. Map showing the location of broadband stations (black triangles) used in the study operated by KOERI network.

Figure 2. The diagram shows the sketch of a sensor alignment. The dashed line represents the incoming ray. The angle φ between the geographic north and the incoming ray is the theoretical back-azimuth. The apparent back-azimuth angle φ′ is obtained from a polarization analysis. North (N′) and east (E′) components deviate by $\theta_0 = \varphi - \varphi'$ from the geographic coordinates, implying an erroneous orientation of the horizontal components.

Figure 3. Teleseismic events used in the sensor orientations analysis. Blue stars show the location of the events used for the P-wave polarization method. The two groups are referred to as BAZ_1 and BAZ_2 for NE (45°-55°) SE quadrants (90°-110°), respectively. Red stars show the events used in the Rayleigh-wave polarization method.

Figure 4. The P wave particle motion recorded at KO.SVAN station for 92 events from BAZ_1 (a) and 34 events from BAZ_2 directions (b). Black dashed lines show the mean apparent back-azimuth obtained from P wave particle motion from multiple events (blue lines) using the principal component analysis. Red line shows the mean theoretical back-azimuth for the group of events calculated by the station and earthquake location parameters. In the case of a correctly oriented sensor, black and red lines (mean apparent and theoretical back-azimuth lines) overlap. The sensor deviation angle for the station is 8.4°±1.9 and 12.2°±1.9 for BAZ_1 and BAZ_2, respectively. The lower figure (c) shows the Rayleigh-wave polarization results (median 9.0°, mean 6.4°±8.0) for the same station obtained from 36 events. The gray area indicates the standard deviation around the mean. Mean and standard deviation are influenced by the back-azimuthal range between 80° and 110° while the median value of the Rayleigh wave method and the result of the P wave method show comparable results.

Figure 5. The sensor deviation angles determined in this study for the KOERI network (a) and Marmara Region (b). Blue arrows and red arrows show the deviation relative to geographic north obtained from two methods, P-wave and Rayleigh-wave, respectively. Both methods agree well with each other for 80% of the stations (≤10°). For some stations (e.g. KO.LEF), the results differ between both methods which may point to a common regional origin (e.g. anisotropy or 3D structure, see also Fig. 6).

Figure 6. The extended polarization analysis of the P-wave (a) and Rayleigh-wave (b) for different azimuthally distributed events at the KO.LEF station. Blue stars show the average sensor deviation angle over many events in a narrow zone within 6° for P-wave analysis while the stars indicate single events for Rayleigh wave analysis. The results obtained using the P-wave method show a distinct sinusoidal pattern, hinting at crustal-scale features. The mean of this sinusoidal pattern (1.2° ±3.8) gives the estimated orientation for the sensor. The Rayleigh wave method results are more scattered around a median value of 4.0° (mean 4.4° ±8.0). The gray area shows the standard deviation around the mean.

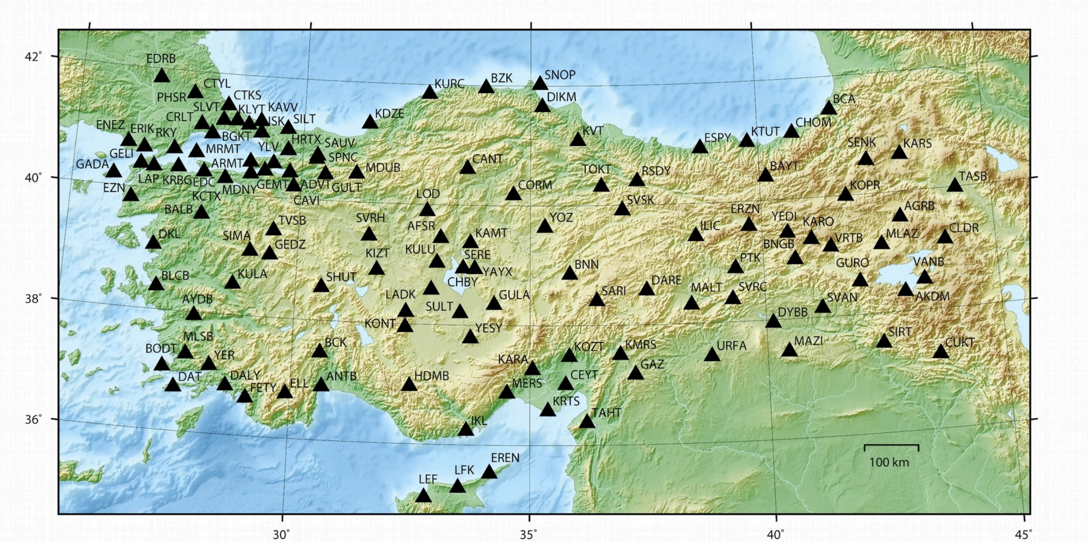

Figure 1. Map showing the location of broadband stations (black triangles) used in the study operated by KOERI network.

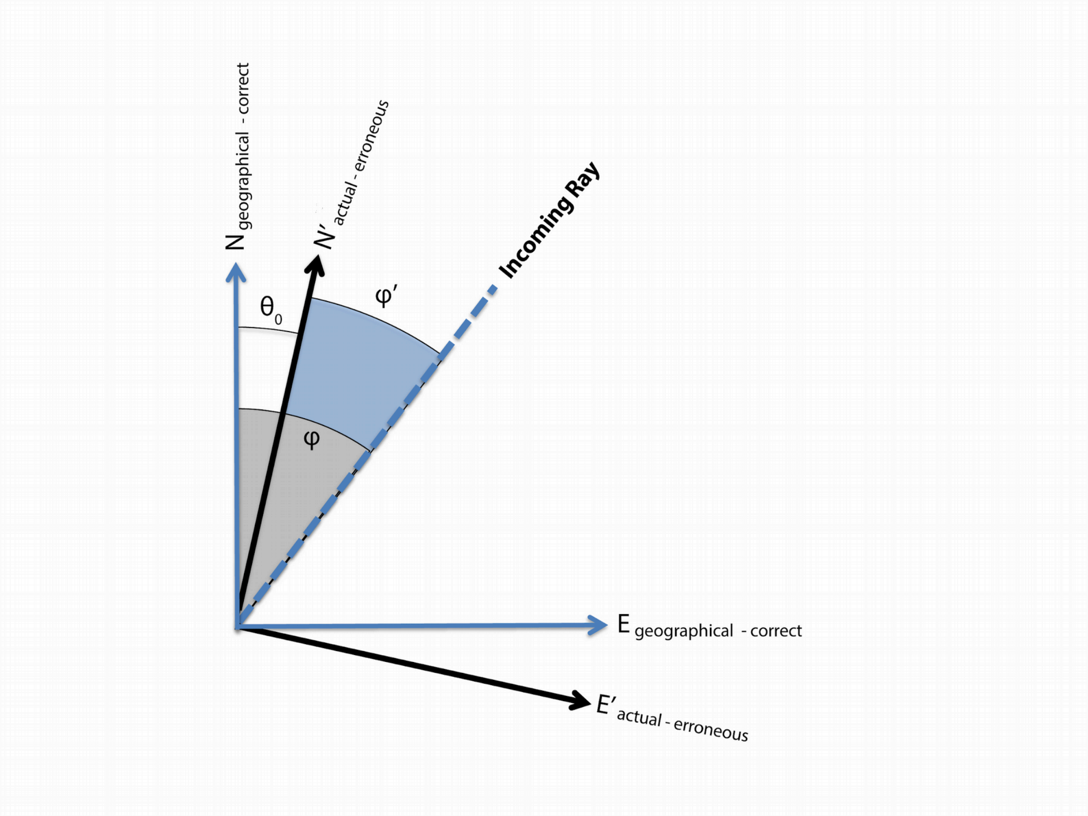

Figure 2. The diagram shows the sketch of a sensor alignment. The dashed line represents the incoming ray. The angle φ between the geographic north and the incoming ray is the theoretical back-azimuth. The apparent back-azimuth angle φ′ is obtained from a polarization analysis. North (N′) and east (E′) components deviate by $\theta_0 = \varphi - \varphi'$ from the geographic coordinates, implying an erroneous orientation of the horizontal components.

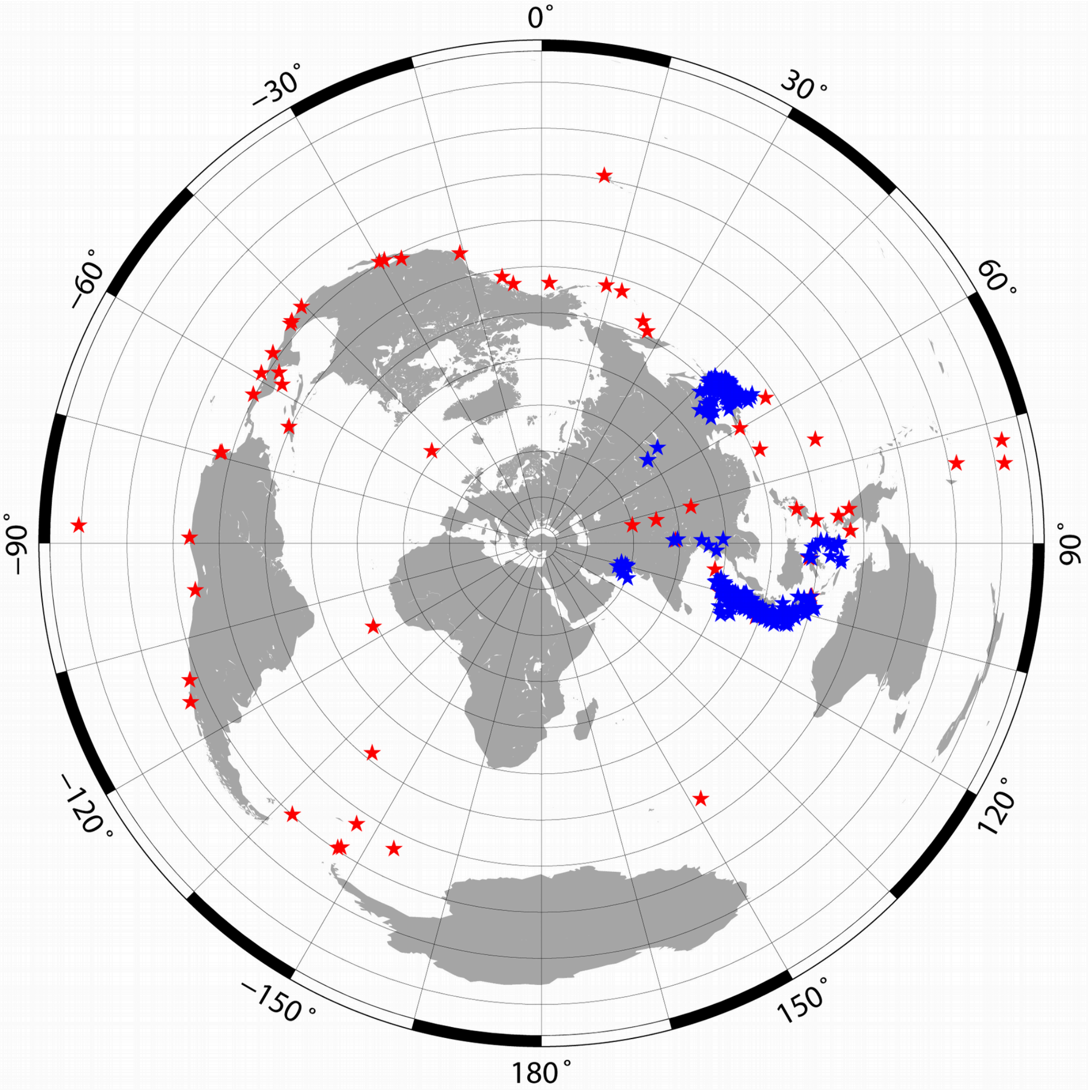

Figure 3. Teleseismic events used in the sensor orientations analysis. Blue stars show the location of the events used for the P-wave polarization method. The two groups are referred to as BAZ_1 and BAZ_2 for NE (45°-55°) SE quadrants (90°-110°), respectively. Red stars show the events used in the Rayleigh-wave polarization method.

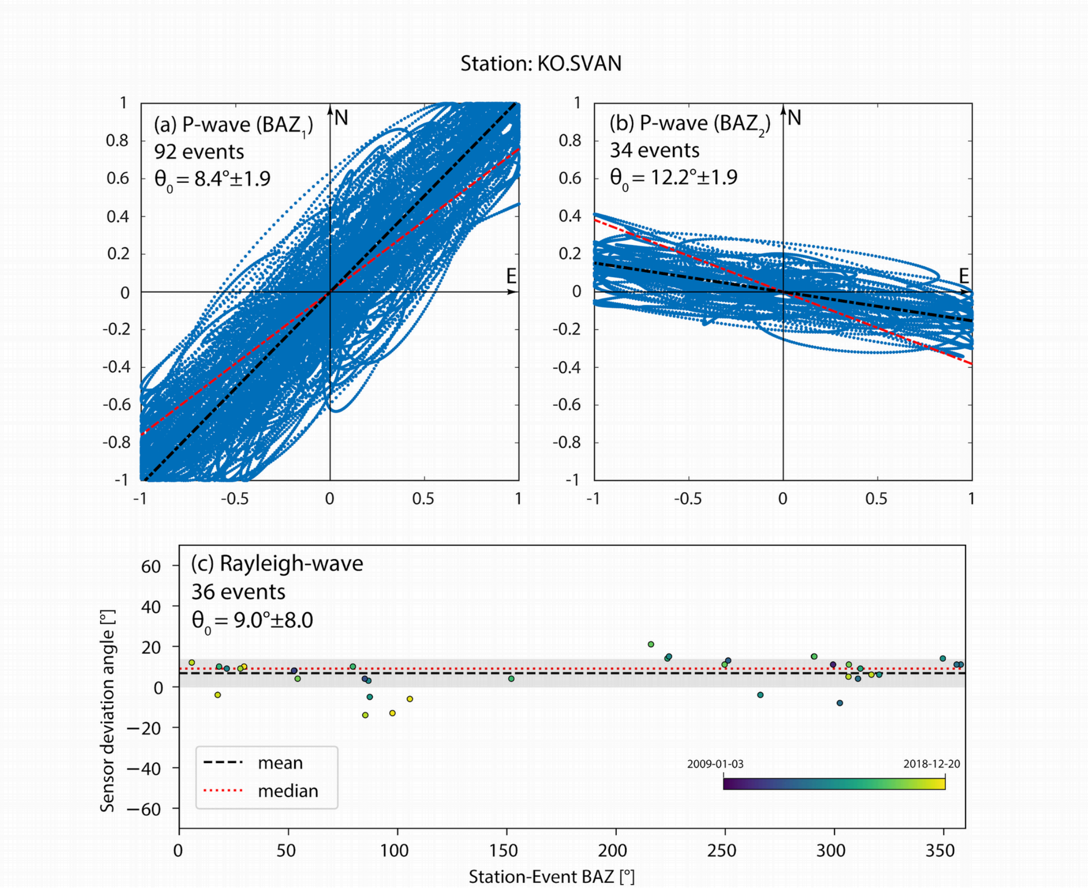

Figure 4. The P wave particle motion recorded at KO.SVAN station for 92 events from BAZ$_1$ (a) and 34 events from BAZ$_2$ directions (b). Black dashed lines show the mean apparent back-azimuth obtained from P wave particle motion from multiple events (blue lines) using the principal component analysis. Red line shows the mean theoretical back-azimuth for the group of events calculated by the station and earthquake location parameters. In the case of a correctly oriented sensor, black and red lines (mean apparent and theoretical back-azimuth lines) overlap. The sensor deviation angle for the station is 8.4°±1.9 and 12.2°±1.9 for BAZ$_1$ and BAZ$_2$, respectively. The lower figure (c) shows the Rayleigh-wave polarization results (median 9.0°, mean 6.4°±8.0) for the same station obtained from 36 events. The gray area indicates the standard deviation around the mean. Mean and standard deviation are influenced by the back-azimuthal range between 80° and 110° while the median value of the Rayleigh wave method and the result of the P wave method show comparable results.

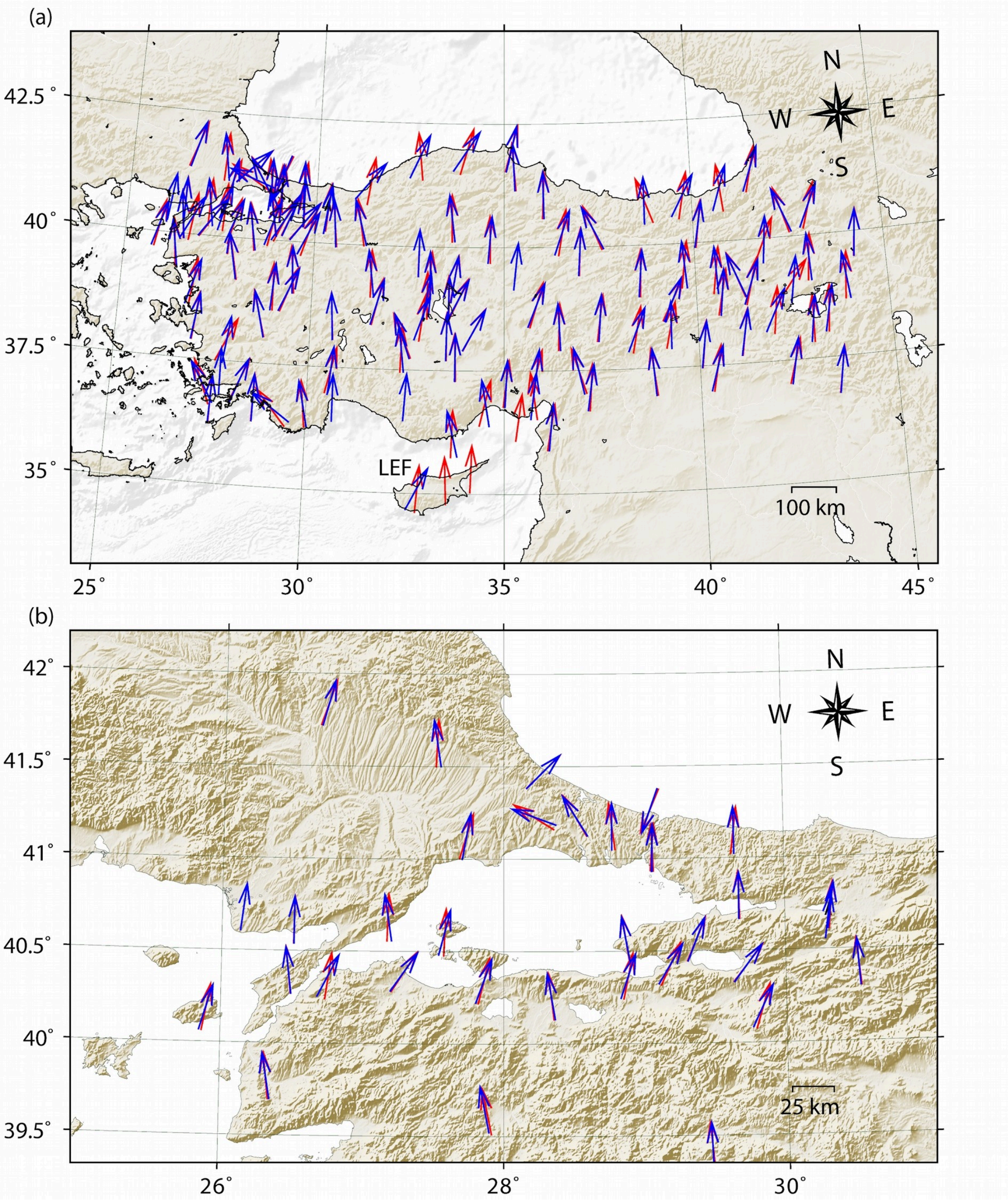

Figure 5. The sensor deviation angles determined in this study for the KOERI network (a) and Marmara Region (b). Blue arrows and red arrows show the deviation relative to geographic north obtained from two methods, P-wave and Rayleigh-wave, respectively. Both methods agree well with each other for 80% of the stations (≤10°). For some stations (e.g. KO.LEF), the results differ between both methods which may point to a common regional origin (e.g. anisotropy or 3D structure, see also Fig. 6).

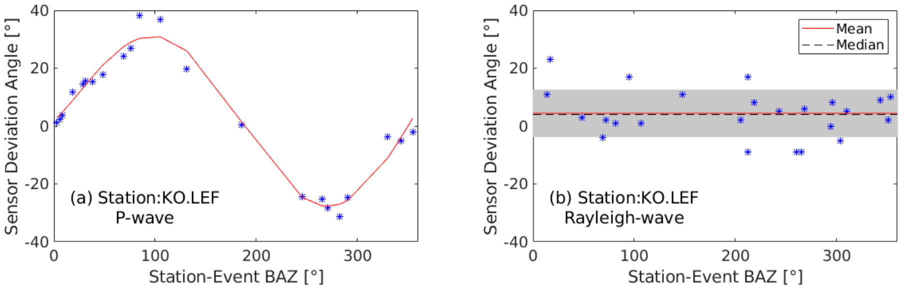

Figure 6. The extended polarization analysis of the P-wave (a) and Rayleigh-wave (b) for different azimuthally distributed events at the KO.LEF station. Blue stars show the average sensor deviation angle over many events in a narrow zone within 6° for P-wave analysis while the stars indicate single events for Rayleigh wave analysis. The results obtained using the P-wave method show a distinct sinusoidal pattern, hinting at crustal-scale features. The mean of this sinusoidal pattern (1.2° ±3.8) gives the estimated orientation for the sensor. The Rayleigh wave method results are more scattered around a median value of 4.0° (mean 4.4° ±8.0). The gray area shows the standard deviation around the mean.

CHAPTER 6

Regional centroid MT inversion of small to moderate earthquakes in the Alps using the dense AlpArray seismic network: challenges and seismotectonic insights

Petersen, G.M., Cesca, S., Heimann, S., Niemz, P., Dahm, T., Kühn, D., Kummerow, J.,
Plenefisch, T., AlpArray Working Group (2021)

Published in Solid Earth, vol. 12, pp. 1233–1257.
https://doi.org/10.5194/se-12-1233-2021

The supplementary material for this publication can be downloaded at https://doi.org/10.5194/se-12-1233-2021.

Solid Earth, 12, 1233–1257, 2021
https://doi.org/10.5194/se-12-1233-2021

Solid Earth

Regional centroid moment tensor inversion of small to moderate earthquakes in the Alps using the dense AlpArray seismic network: challenges and seismotectonic insights

Gesa Maria Petersen[1,2], Simone Cesca[1], Sebastian Heimann[1], Peter Niemz[1,2], Torsten Dahm[1,2], Daniela Kühn[1,3], Jörn Kummerow[4], Thomas Plenefisch[5], and the AlpArray and AlpArray-Swath-D working groups+

[1]GeoForschungsZentrum Potsdam, Potsdam, Germany
[2]University of Potsdam, Institute of Geosciences, Potsdam, Germany
[3]NORSAR, Applied Seismology, Kjeller, Norway
[4]Institute of Geological Sciences, Freie Universität Berlin, Berlin, Germany
[5]Federal Institute for Geosciences and Natural Resources (BGR), Hanover, Germany
+For further information regarding the team, please visit the link that appears at the end of the paper.

Correspondence: Gesa Maria Petersen (gesap@gfz-potsdam.de)

Received: 5 February 2021 – Discussion started: 16 February 2021
Revised: 28 April 2021 – Accepted: 2 May 2021 – Published: 2 June 2021

Abstract. The Alpine mountains in central Europe are characterized by a heterogeneous crust accumulating different tectonic units and blocks in close proximity to sedimentary foreland basins. Centroid moment tensor inversion provides insight into the faulting mechanisms of earthquakes and related tectonic processes but is significantly aggravated in such an environment. Thanks to the dense AlpArray seismic network and our flexible bootstrap-based inversion tool *Grond*, we are able to test different setups with respect to the uncertainties of the obtained moment tensors and centroid locations. We evaluate the influence of frequency bands, azimuthal gaps, input data types, and distance ranges and study the occurrence and reliability of non-double-couple (DC) components. We infer that for most earthquakes ($M_\mathrm{w} \geq 3.3$) a combination of time domain full waveforms and frequency domain amplitude spectra in a frequency band of 0.02–0.07 Hz is suitable. Relying on the results of our methodological tests, we perform deviatoric moment tensor (MT) inversions for events with $M_\mathrm{w} > 3.0$. Here, we present 75 solutions for earthquakes between January 2016 and December 2019 and analyze our results in the seismotectonic context of historical earthquakes, seismic activity of the last 3 decades, and GNSS deformation data. We study regions of comparably high seismic activity during the last decades, namely the Western Alps, the region around Lake Garda, and the eastern Southern Alps, as well as clusters further from the study region, i.e., in the northern Dinarides and the Apennines. Seismicity is particularly low in the Eastern Alps and in parts of the Central Alps. We apply a clustering algorithm to focal mechanisms, considering additional mechanisms from existing catalogs. Related to the N–S compressional regime, E–W-to-ENE–WSW-striking thrust faulting is mainly observed in the Friuli area in the eastern Southern Alps. Strike-slip faulting with a similarly oriented pressure axis is observed along the northern margin of the Central Alps and in the northern Dinarides. NW–SE-striking normal faulting is observed in the NW Alps, showing a similar strike direction to normal faulting earthquakes in the Apennines. Both our centroid depths and hypocentral depths in existing catalogs indicate that Alpine seismicity is predominantly very shallow; about 80 % of the studied events have depths shallower than 10 km.

1 Introduction

The Alpine mountains and surrounding areas are known for their complex tectonic setting with a highly heterogeneous lithospheric structure (e.g., Handy et al., 2010, 2015; Schmid et al., 2004; Hetényi et al., 2018). The mountain range was

Published by Copernicus Publications on behalf of the European Geosciences Union.

tectonically shaped by the interaction of the Adriatic microplate and the European plate in several stages of convergence between Europe and Africa (e.g., Schmid et al., 2004, 2008; Handy et al., 2010; Hetényi et al., 2018). Geological studies show that the Adriatic plate is the upper plate in the subduction of the Alpine Tethys in the Alps, while it is the lower plate of the thrust systems in the Apennines and the Dinarides (e.g., Schmid et al., 2008; Handy et al., 2015). The terranes of the Mesozoic Tethys ocean between Europe and Africa were compressed, rotated, faulted, and stacked during the Alpine orogenesis (e.g., Handy et al., 2010). Along a distance of approximately 700 km between NW Italy and Slovenia, the Northern Alps and the Southern Alps are separated by the Periadtriatic line or fault system (e.g., Handy et al. (2005); see also Fig. 1). Reversals in the subduction polarities have been proposed at the transition to both the Apennines and the Dinarides, while the geometry and orientation of the slab is still controversial (e.g., Hetényi et al., 2018; Handy et al., 2010, 2015; Mitterbauer et al., 2011; Schmid et al., 2004). GPS measurements show that the Adriatic microplate is rotating counterclockwise relative to Europe around an Euler pole located in the Western Alps or western Po plain (D'Agostino et al., 2008; Weber et al., 2010). Velocity anomalies in the crust and the upper mantle reflect the complexity of the crustal structure and the geodynamic setting (e.g., Diehl et al., 2009; Fry et al., 2010; Molinari et al., 2015; Kästle et al., 2018; Lu et al., 2020; Qorbani et al., 2020).

Seismic activity across the Alps is typically characterized by low- to moderate-magnitude earthquakes. However, large damaging earthquakes have occurred in the past, such as the 1356 Basel earthquake (Meyer et al., 1994) or the 1976 Friuli earthquake (M_w 6.45, Poli and Zanferrari, 2018). Recent seismic activity in the eastern Southern Alps is caused by the N–S convergence (2–3 mm yr^{-1}) between the Adriatic Plate and Eurasia, which is accommodated by the ENE-trending, SSE-verging thrust front of the eastern Alps and by the NW–SE-trending right-lateral Dinaric strike-slip fault systems in western Slovenia (Moulin et al., 2016; Poli and Zanferrari, 2018). The wider Alpine region, including parts of the Dinarides and the Apennines, stretches across Switzerland, Austria, Liechtenstein, France, Italy, Germany, Slovenia, and Croatia. Most of these countries have national earthquake observatories, research institutes or universities that routinely monitor the regional seismicity. The Swiss Seismological Service (SED) and the Slovenian Environment Agency (ARSO) provide annual reports containing mainly first-motion-based focal mechanisms (e.g., Diehl et al., 2018; Ministrstvo za okolje in prostor Agencija RS za okolje, 2020), while for example INGV (Italy), GEOFON (Germany), EM-RCMT (European-Mediterranean Regional Centroid-Moment Tensors; Pondrelli, 2002), SISMOAZUR (France), and GCMT (Lamont-Doherty Earth Observatory of Columbia University, USA) provide moment tensor (MT) solutions in online bulletins for magnitudes above 3.5 or larger (see the data and code availability section for more information).

The region can be characterized by compartments with varying tectonic movement in close proximity, as described by many studies of local seismic activity. Focal mechanism in the SW Alps indicate predominantly N–S-to-NNW–SSE-striking normal faulting (e.g., Nicolas et al., 1998; Sue et al., 2000), while in the W Alps strike-slip earthquakes have been observed and explained as a consequence of regional NW–SE compression and NE–SW extension (Maurer et al., 1997). In the central Alps, Marschall et al. (2013) observe strike-slip faulting in central Switzerland. NW–SE-striking normal faulting is reported for SE Switzerland (e.g., Marschall et al., 2013; Diehl et al., 2018). Reiter et al. (2018) provide focal mechanism solutions from P (primary) and S (secondary) polarities and amplitude ratios for the Central to Eastern Alps. They report strike-slip mechanisms and oblique strike-slip mechanisms in the Brenner–Inntal transfer zone (see Brenner and Inntal fault in Fig. 1), and normal faulting is seen with a strike direction parallel to the Giudicarie fault system. Within this fault system, E–W-to-NE–SW-striking thrust faulting with strike-slip components were described by Viganò et al. (2008). The Italian MT dataset provides extensive mechanisms for N Italy. Within the Lake Garda region and in the eastern Southern (eS) Alps close to Friuli thrust faulting with ENE–WSW to ESE–WNW strike direction is dominant (Pondrelli et al., 2006; Anselmi et al., 2011; Bressan et al., 1998). East of Friuli and in the northern Dinarides, both (oblique) thrust and strike-slip faulting is observed (Pondrelli et al., 2006; Moulin et al., 2016). This overview is not complete by far but provides a small glimpse into the complex seismic and tectonic activity that is not simply dominated by the main active deformation fronts at the southern and northern margin of the Alps but that also occurs in smaller fault systems across the entire region.

To study the orogenesis of the Alps and related processes like recent seismic activity, mantle dynamics, plate motion, and surface processes, the AlpArray initiative was established. In this initiative, more than 35 European institutes joined resources to operate the AlpArray Seismic Network (AASN) (Hetényi et al., 2018), consisting of more than 600 temporary (AlpArray Seismic Network, 2015) and regional permanent stations with an average spacing of < 60 km (Fig. 1). For comparison, in summer 2011, before the AASN planning period started and first additional permanent stations were set up, there were 234 stations in the same area (Hetényi et al., 2018). The AASN is complemented by the dense Swath-D network in the eastern Alps (Heit et al., 2017). The permanent stations of the AlpArray are part of existing European regional networks (RD, GU , CZ, ST, G, CH, OE, MN, HU, GE, RF, FR, IV, BW, SX, NI, TH, OX; see data and code availability). The dense AASN allows for studying regional seismicity in new, greater detail and provides the opportunity to perform centroid moment tensor (CMT) inversions with a constant station coverage over the entire re-

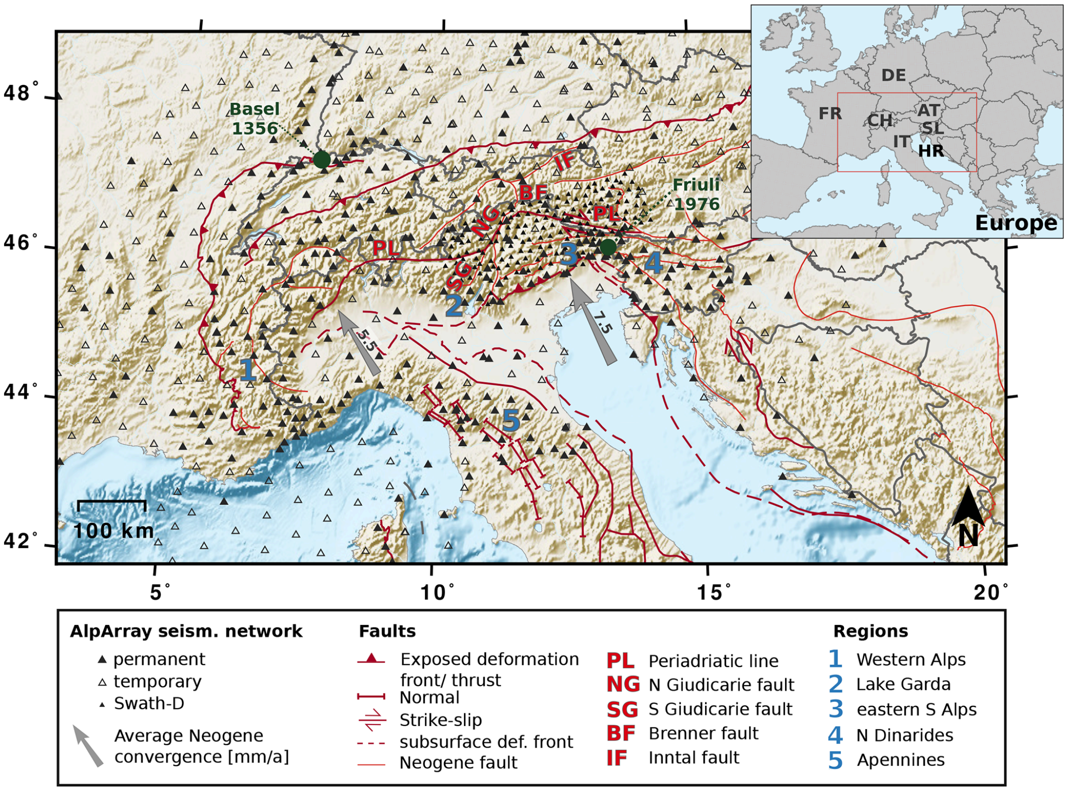

Figure 1. Study area and AlpArray seismic network. Subregions that are discussed in greater detail in this study are numbered. Arrows indicate average Neogene (20–0 Ma) Adria–Europe convergence rates from Le Breton et al. (2017). Exposed and subsurface faults simplified from Schmid et al. (2004, 2008), Handy et al. (2010, 2015), and Patacca et al. (2008). Topographic data from SRTM-3 (Farr et al., 2007) and ETOPO1 (Amante and Eakins, 2009) datasets. The inset shows the location of the study area in Central Europe (red rectangle): FR is France, DE is Germany, IT is Italy, SW is Switzerland, AT is Austria, SL is Slovenia, and HR is Croatia.

gion. In contrast, many of the previous studies focus on specific regions or seismic sequences within the Alps, and therefore do not provide a broad overview. Furthermore, many of these studies relied on first-motion polarities. First-motion-based approaches can be used even for small earthquakes when no surface wave energy is observed. However, the obtained mechanism is only representative for the very first moment of the fracturing process. This might introduce discrepancies when comparing first-motion solutions to MT solutions (Scott and Kanamori, 1985; Guilhem et al., 2014). The instability of take-off angles of shallow earthquakes may introduce significant errors in the polarity readings (Hardebeck and Shearer, 2002). Additionally, first-motion solutions of small earthquakes are often only based on few polarities, which makes it difficult to assess uncertainties.

Despite the limited resolution, first-motion polarity approaches are often used in the Alps, where MT inversion is particularly challenging. First, earthquake magnitudes are generally small to moderate, requiring waveform modeling at relatively high frequencies and local distances. Furthermore, structural heterogeneities, site effects, and topographic effects hinder full waveform MT inversions based on 1-D velocity profiles when considering frequencies above 0.1 Hz. Signal-to-noise ratios (SNR) vary significantly across the region due to densely populated areas and environmental conditions (weather and wind, rivers, rock falls, avalanches, etc.). Each study or observatory reporting focal mechanisms uses different inversion tools, input data, and distance and frequency ranges. Furthermore, uncertainties are not routinely discussed, which makes it difficult to evaluate published solutions. Uncertainties can be assessed, e.g., by performing a grid search over parameters like strike, dip, rake, and depth (Stich et al., 2003; Cesca et al., 2010) or using independent bootstrap chains in the inversions with varying weighting of the input data from different stations (e.g., Heimann et al., 2018; Kühn et al., 2020, and this study). The latter approach provides uncertainties of all inversion parameters (e.g., MT components, centroid location) and helps to identify trade-offs between these parameters.

Studies of focal mechanisms in the Alps have mainly considered double-couple (DC) solutions. Here, based on the dense seismic network, we also attempt to consider non-DC components. The decomposition of the moment tensor allows for studying the seismic source in more detail, including not only pure tectonic dislocations represented by the DC but also volumetric changes and tensile faulting (e.g., Vavryčuk, 2015).

In this study, we predominately target small to moderate earthquakes ($M_w > 3.0$) that occurred in the Alps or surrounding areas between January 2016 and December 2019, based on the operation time of most of the temporary broadband stations of the AASN. While the temporarily densified network provides a great amount of input data to the single MT inversions, the short time span limits the number of observed earthquakes. We test various setups and input types to establish workflows for a homogeneous and consistent list of MT solutions for the Alps (see Supplement). We attempt to lower the magnitude threshold for inversions compared to routinely reported solutions by optimizing the used methods and by combining different input data types (e.g., time domain full waveforms and frequency domain amplitude spectra). Using the AASN and the bootstrap inversion framework *Grond* (Heimann et al., 2018; Dahm et al., 2018; Kühn et al., 2020) allows for determining the most suitable setups for source inversions of small to moderate earthquakes within the study area.

After an introduction into the inversion method, we describe the methodological tests that were performed to assess inherent methodological uncertainties. At the same time, we propose guidelines for MT inversion of small to moderate earthquakes in complex tectonic settings. Subsequently, we present the MT solutions that were obtained for the Alpine region and discuss these with respect to mechanisms, spatial patterns, and centroid depths. We discuss different tectonic areas in the Alps systematically, including observations of seismicity, faulting mechanisms, and GNSS deformation data.

2 Methodology

2.1 Moment tensor inversion using *Grond*

We use the open-source software *Grond* for MT inversions (Heimann et al., 2018; Kühn et al., 2020). In a Bayesian bootstrap-based probabilistic joint inversion scheme, solution uncertainties are retrieved along with the best-fitting CMT solution (see also Dahm et al., 2018). We simultaneously invert for the six independent moment tensor components, for the seismic moment, for the centroid location, and for the origin time. The objective function is set up in a flexible way to combine different input data types as a weighted sum. In our study, we use combinations of time domain full waveforms, time domain cross-correlations, and frequency domain amplitude spectra as an input for the inversion. Following the studies of Zahradník and Sokos (2018) and Dahal and Ebel (2020), we implemented envelopes of time domain waveforms. The misfits of the different input data are combined using an L1 or L2 norm. We assign the same weighting to each input data type. The misfit values of single stations within one input data type group are weighted to account for different epicentral distances (Heimann, 2011). Without applying such a weighting, summed misfits are always dominated by the closest stations which have the highest amplitudes. In the case of using time domain full waveforms or cross-correlation fitting procedures, we allow for small time shifts to compensate for errors in the velocity models. To avoid the mismatching of phases, these time shifts were set to be well below a quarter of the dominant wavelength. Time shifts are regulated by a penalty function with an empirically chosen maximum of 0.05.

Precalculated Green's function databases are used for rapidly computing synthetic data (Heimann et al., 2019). In our case, we used regional velocity profiles from the CRUST2.0 Earth model database (see https://igppweb.ucsd.edu/~gabi/crust2.html, last access: June 2020; Bassin et al., 2000), which we choose according to the earthquake epicenter location. The Green's function databases were calculated with the orthonormal propagator algorithm QSEIS (Wang, 1991). *Grond* selects the appropriate time window, corrects the recorded waveforms for the instrument response, and rotates to ZRT coordinate system. Filters are applied and, if specified, waveform attributes as spectra or envelopes are calculated. The inversion is performed in parallel bootstrap chains (here, 100 for normal inversions and 500 for method testing), where individual bootstrap weights are applied to the single-station-component input data type combinations. Bootstrapping is applied for two reasons. Firstly, to avoid distortions due to a few high misfit values resulting from a low SNR at single stations, incorrect transfer functions, or malfunctioning stations. Secondly, the bootstrap chains are used to access model parameter uncertainties and trade-offs between the inversion parameters. Each bootstrap chain performs an entirely independent optimization. Along with the best solution with the lowest misfit, *Grond* provides a defined number (here, 10) of best solutions of each bootstrap chain, which we call the ensemble of solutions.

Figure 2 presents a selection of plots provided by the inversion software to assess the solution robustness, in this case for the 14 June 2019 thrust-faulting earthquake in northern Italy (M_w 3.9). Figure 2a shows the fuzzy MT, which is an illustration of the MT uncertainty. It is composed of the superimposed P radiation pattern of the ensemble of solutions from the bootstrap chains. If the variability of the ensemble solutions is small, and hence the uncertainties are small (as seen here), the fuzzy plot has clearly separated black and white quadrants. The red lines indicate the solution with the lowest misfit. Other plots show the station distribution (Fig. 2b) and the decomposition of the best deviatoric MT solution into the DC and the CLVD component (Fig. 2c). Figure 2d shows the distribution of the centroid locations obtained from all ensemble solutions, and Fig. 2e depicts the resolution of the six independent MT components in the form of probability density functions. As is typical for shallow events inverted using surface waves, the m_{nd} and

m_{ed} components are not as well resolved as the other components (Cesca and Heimann, 2018; Bukchin et al., 2010; Valentine and Trampert, 2012). Finally, Fig. 2f shows examples of waveform and frequency spectra fits of Z, R, and T component traces at three stations.

The selection and joint inversion of waveform attributes can improve the stability and goodness of solutions. In the following, we want to point out advantages and drawbacks of the waveform-based input data types, which are used in the subsequent methodological tests: time domain (TD), frequency domain (FD), cross-correlation, and envelopes.

2.1.1 TD full waveform fitting

In the time domain, the misfit between a selected time window of a seismic trace and a synthetic trace in a defined frequency range is computed as the normalized sum of sample misfits. Time shifts are allowed and regulated with a penalty function. For regional MT inversion, surface waves are commonly considered in full waveform approaches (e.g., Ritsema and Lay, 1995; Minson and Dreger, 2008; Sokos and Zahradnik, 2008; Dahm et al., 2018). The frequency band is magnitude dependent. While at low frequencies effects of the velocity model and topography are minor, at higher frequencies the SNR is usually better. At regional distances, magnitude-dependent frequency bands below 0.1 Hz are often used to consider Rayleigh waves and Love waves, which have particularly simple waveforms at this distance range (Ritsema and Lay, 1995). However, in the case of very shallow sources, the resolution of the m_{xz} and m_{yz} components of the MT are limited when using surface waves (Bukchin et al., 2010; Valentine and Trampert, 2012; Cesca and Heimann, 2018, see also Fig. 2). Relying on time domain fitting only, time shifts, noisy data, or distorted amplitudes can hinder finding stable initial inversion solutions. It has proven to be helpful to combine time domain full waveform fitting with other input data types like frequency domain amplitude spectra, which are often less affected by these issues.

2.1.2 FD amplitude spectra fitting

Real-valued amplitude spectra of recorded Love and Rayleigh waves carry all information necessary to resolve the geometry of the MT, while neglecting the phase information and dispersion (e.g., Mendiguren, 1977). This means that two MT solutions with common nodal planes but opposite polarities model the amplitude spectra equally well and that additional information from first-motion polarity readings or time domain waveform fitting is needed to resolve this ambiguity (e.g., Cesca et al., 2010; Heimann, 2011). The misfit is computed as the misfit between amplitude spectra of recorded and synthetic waveforms in a selected frequency range and time window. Compared to fitting full waveforms in the time domain, more conservative, less exact time windows can be selected. Cesca et al. (2010, 2013) propose a multistep approach to stepwise combine the fitting of amplitude spectra and displacement waveforms to subsequently obtain point source parameters, the centroid location, and kinematic source parameters. Compared to full waveform fitting, amplitude spectra inversion methods are less sensitive to trace misalignments and phase shifts resulting from coarse or erroneous velocity models (Cesca et al., 2010, 2013; Domingues et al., 2013). In the subsequent tests, we do not use a stepwise inversion but use amplitude spectra and time domain full waveforms or cross-correlated waveforms simultaneously.

2.1.3 Cross-correlation waveform fitting

In the cross-correlation-based fitting of full waveforms, the amplitudes of recorded and synthetic traces are normalized. The inversion searches for the maximum cross-correlation value for the selected time window in time domain, basically fitting the phase shift (Stähler and Sigloch, 2014; Kühn et al., 2020). Cross-correlations help to constrain the centroid location and centroid time in a joint inversion. We allow for small time shifts, regulated with a penalty function, to compensate for imprecise velocity models. Time shifts need to be small compared to the frequency range in order to avoid mismatching phases. Due to the amplitude normalization, this method is sensitive to patterns in the waveforms, while it is not influenced by gain errors or site effects. Magnitudes cannot be resolved. Cabieces et al. (2020) used cross-correlation fitting in their MT inversion for ocean bottom stations, where absolute amplitudes could not be modeled due to the unknown coupling to the ground. When using cross-correlations to fit time domain waveforms, frequency bands and time windows need to be selected carefully to avoid mismatching phases.

2.1.4 Envelope fitting

In our study, we compute the waveform envelopes by convolving the squared time series using the fast Fourier transform with a Hanning taper. This smoothens and therefore simplifies the waveforms. Hensch et al. (2019) used non-smoothed envelopes in the same inversion routine in combination with amplitude spectra, spectral ratios, and time domain waveforms. Envelopes, especially smoothed ones, are less influenced by small un-modeled time shifts or noisy data compared to full waveforms. Fitting envelopes of seismic waveforms can be helpful in the case of using high-frequency bands, simplified velocity models, and increased noise levels. Zahradník and Sokos (2018) stress that due to the simplification of the waveforms, the results of envelope-based inversions have a limited precision and results need an even more careful inspection of uncertainties and resolution. However, if body waves are considered, envelopes can especially help to constrain P- and S-phase arrivals and thus the centroid time and location. Since the envelopes are based

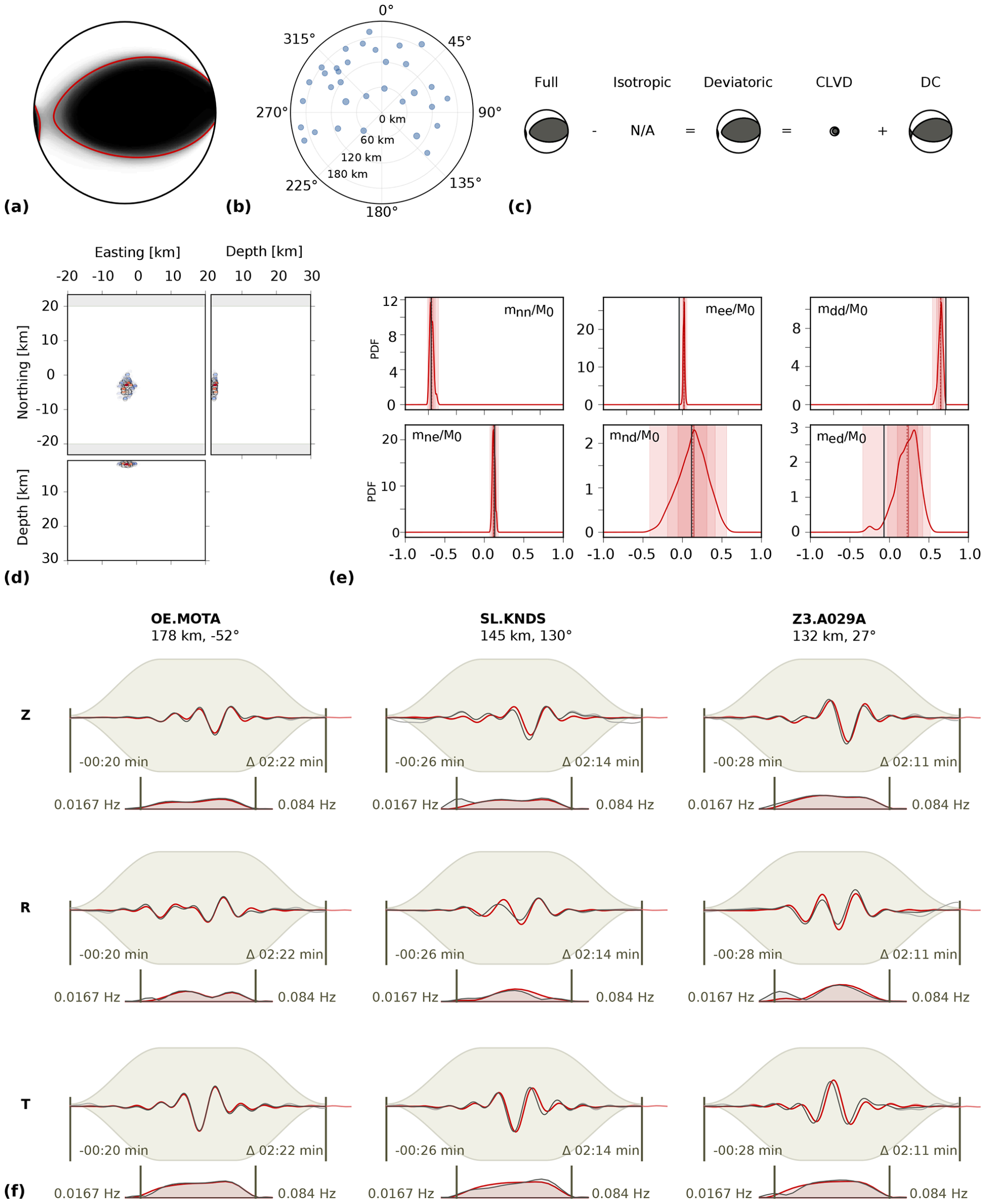

Figure 2. Example of an MT inversion result, 14 June 2019, M_w 3.9, NE Italy. **(a)** Fuzzy beach ball illustrating the MT solution uncertainty. **(b)** Station distribution around the epicenter. **(c)** Decomposition of the best MT solution into DC and CLVD component. **(d)** Resolution of the centroid depth, easting, and northing relative to the starting position. **(e)** Probability density functions (PDFs) showing the resolution of the six independent MT components m_{xy} normalized by the seismic moment M_0. **(f)** Examples of waveform and spectral fits at three stations and three components. Red and black lines indicate synthetic and recorded waveform data, respectively. The beige-shaded area represents the time window and taper function. Station name, azimuth, and distance to the epicenter are indicated above each column. Numbers within the panels describe the time window and the frequency band.

on absolute amplitudes, they need to be combined with a method providing polarity information. Zahradník and Sokos (2018) and Dahal and Ebel (2020) have shown that envelopes can be used to derive focal mechanisms for $M < 4$ events in the case of unfavorable settings like sparse networks, for which full waveform fitting is not feasible. In both studies, the envelopes are combined with P polarities of one or more nearby stations to resolve the polarity ambiguity.

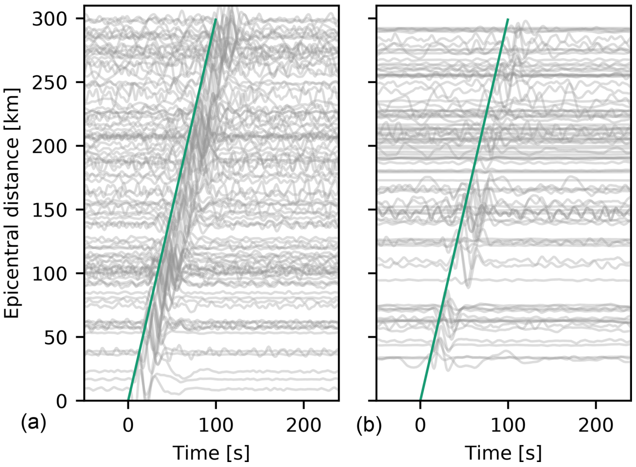

Figure 3. Vertical component seismograms of permanent AASN stations, sorted by distance: **(a)** 6 March 2017, M_W 4.1, Switzerland; **(b)** 27 October 2017, M_W 3.6, France. Time is in seconds after origin time. Waveforms are bandpass-filtered between 0.02 and 0.07 Hz. Rayleigh waves dominate the seismograms in this frequency range with an average phase velocity of 3 km s^{-1} (green line).

2.2 Methodological tests

We perform methodological tests using recorded seismograms and synthetic data to investigate the resolution capacities, requirements, and limits of MT inversions in the Alpine region. We use subsets of representative earthquakes that occurred between 2016 and 2019 in the Alps. The tests are particularly computationally demanding, as every single inversion of each test is run in 500 bootstrap chains. The number of events in each test depends on the number of tested parameters. The proposed tests can be used as a guideline for assessing the feasibility of MT inversions in other study areas with moderate seismicity.

We benefit from the large seismic network and use more than 80 stations at distances of up to 400 km for the largest events (Fig. 3). For earthquakes with moderate magnitudes between M_W 3.5–3.9, we mostly rely on 20 to 50 stations within a radius of 200 km. The number of available stations depends on the magnitude and the epicenter location within the network. Furthermore, the SNR and quality of the individual stations is variable in time and space. Before the inversions, we applied the toolbox *AutoStatsQ* to identify seismic stations with misorientations, metadata errors, or gain problems (Petersen et al., 2019).

2.2.1 Double-couple, deviatoric, and full moment tensor inversions

We study the stability and resolvability of non-DC components by performing full, deviatoric, and pure DC MT inversions for a subset of 32 earthquakes of the AlpArray dataset. We consider these earthquakes representative as they cover a large magnitude range (M_W 3.2–4.2), are distributed across the entire study area, and are comprised of different types of mechanisms. We use a passband of 0.02–0.07 Hz and fit time domain full waveforms and frequency domain amplitude spectra simultaneously. We compared the pure DC, the deviatoric, and the full MT obtained for each earthquake with respect to the fit of the recorded data and to the uncertainties of MT components and centroid locations. Subsequently, we statistically evaluate those solutions, for which a low misfit between synthetic and observed waveforms was achieved with all three inversion types. Four events with Kagan angles > 60° between full and deviatoric solutions were removed since they were not well resolved.

The isotropic source component of the seismic moment tensor resolves volumetric changes, including processes like explosions, cavity collapses, fluid movement, or ruptures on nonplanar faults (e.g., Sileny and Hofstetter, 2002; Ford et al., 2009; Miller et al., 1998; Minson and Dreger, 2008). The CLVD component is often described as the residual radiation to the best DC without geological interpretation (Dahm and Krüger, 2014), it is however required for a mathematically complete decomposition (Vavryčuk, 2015). Large CLVD components are often explained by noisy data, a simplified or incorrect velocity model, neglected 3-D wave effects, or insufficient station coverage (e.g., Panza and Saraò, 2000; Cesca et al., 2006) but can also be interpreted physically in combination with an isotropic component of the same sign as a product of tensile faulting (Vavryčuk, 2015). Non-DC components are also used as an indicator of anthropogenic seismicity (Dahm et al., 2013; Cesca et al., 2013; Lizurek, 2017).

Despite frequent geological interpretations which propose fluid movements or tensile processes, various studies show that resolving non-DC components in MT inversions is particularly difficult. Seismic noise and inaccurate Green's functions may result in large non-DC components. Trade-offs between hypocenter location or depth and isotropic component have been observed (e.g., Dufumier and Rivera, 1997; Panza and Saraò, 2000; Křížová et al., 2013; Kühn et al., 2020). Non-DC components must therefore be evaluated carefully with respect to tectonic processes (Lizurek, 2017). Methodological tests based on observed data and synthetic tests can help to identify which non-DC components can be considered statistically significant (see also Panza and Saraò, 2000).

Figure 4a and b show the ratio of DC and non-DC components of the full and deviatoric MT inversions of our test dataset. The deviatoric inversions result in 0 %–40 % CLVD components for 70 % of the events and in CLVD components of > 50 % for 19 % of the events. In the case of full MT inversions, we find significant isotropic components of > 30 % in the case of one-third of the earthquakes. Figure 4c indicates that the non-CLVD components of the test events scatter significantly. It is clearly visible that many events with shallow depths (dark colors) are located in the upper-right and lower-left quadrants of the Hudson plot, indicating isotropic and CLVD components of opposite signs. Cesca and Heimann (2018) showed that for shallow depths, isotropic and CLVD components often appear indistinguishable. Further below, we discuss this observation comparing forward calculated synthetic waveforms for one example event.

The DC component is representing the purely tectonic shear dislocation (e.g., Miller et al., 1998; Julian et al., 1998; Cesca et al., 2013); therefore, it is crucial to resolve this component unambiguously. We compare the DC component that we obtain from the decomposition of the deviatoric and the full MT with the pure DC inversion result by computing the smallest rotation angle (Kagan angle, Kagan, 1991) between them to assess the stability of the DC components (Fig. 5). Rotations below 30° are generally accepted as representing very similar mechanisms, while a Kagan angle $\ll 60°$ is still described as corresponding (Pondrelli et al., 2006; d'Amico et al., 2011). A total of 70 % of the earthquakes have a very stable DC, with Kagan angles below 30° between the three solutions. In the case of about 10 % of the events, a Kagan angle $\geq 60°$ is found. These larger deviations result predominantly from large non-DC components in the full inversion result (in $>$ 70 % of these events). In these cases, the CLVD combined with the isotropic component shows orientations similar to the DC component of the pure DC and the deviatoric inversion result. Therefore, the resulting focal sphere is similar, while the DC component deviates from the pure DC inversion result. Overall, the results of this test indicate that the DC component is in most cases very well resolved, independently of allowing for a CLVD and an isotropic component.

In the following, we present a more detailed analysis of an exemplary earthquake with a significant non-DC components: 28 May 2019, M_w 3.9, close to Lake Geneva, France (Fig. 6a). Figure 6b depicts the MT decompositions of the MTs obtained with a pure DC inversion, a deviatoric inversion, and a full MT inversion. All three inversions were performed using the same inversion setup (full waveforms and amplitude spectra; Z, R, and T components; 73 stations; 0.02–0.07 Hz). The DC component is similar for all inversion types, but the deviatoric and full inversion results indicate significant non-DC components.

To investigate whether the resolved non-DC components are unambiguous, we forward model synthetic waveforms of the three MT solutions recorded at fictional receivers in 250 km distance in azimuthal steps of 1° (Fig. 6a). We use a bandpass filter of 0.02–0.1 Hz, which is even wider than the frequency range used in the MT inversion (0.02–0.07 Hz) to assess the similarity of the entire modeled surface wave trains. By cross-correlating the forward modeled waveforms, we find that the full and deviatoric sources produce very similar waveforms on all seismometer components in all back-azimuthal directions (Fig. 6d). Furthermore, the maximum amplitudes between the deviatoric and full solution differ only slightly. This indicates that the non-DC component can be comparably well represented by a CLVD or by a combination of an isotropic plus a CLVD component.

A comparison of the forward modeled waveforms from a pure DC solution with a full or deviatoric solution shows very high correlations in all azimuthal directions on the T components (Fig. 6d, lower panel). Neither the CLVD nor the isotropic component is influencing the transversal Love wave. On R and Z components, the resulting waveforms show cross-correlations below 0.9 in strike-direction only (Fig. 6d, upper and middle panel). This indicates that in the case of this event, without any station covering this ray path direction, we cannot resolve the difference between a pure DC MT and a full or deviatoric one.

The true azimuthal coverage of seismic stations is much denser to the NE and E than in the strike direction (Fig. 6a). Forward modeling the waveforms of the 73 used stations results in a similar but less well-resolved pattern compared to Fig. 6d. The uneven azimuthal distribution and the lack of stations in strike directions hinders the unambiguous identification of non-DC components.

This example shows that whenever we investigate large non-DC components in a deviatoric or full MT inversion, one must assess the resolution and the validity of the results. The synthetic tests indicate that including full waveforms of body waves at higher frequencies in the inversion clearly helps to improve the resolution of non-DC components. However, due to the station spacing, the relatively high noise level, and the low resolution of crustal velocity models, we cannot use higher frequencies for most events in this study. Following our findings, we report deviatoric MT inversions in the result section and only perform inversions for the full MT in the case of large non-DC components for comparison.

2.2.2 Frequency ranges and input data type

In previous studies, dependencies of the MT inversion results on the inverted frequency band have been observed and multistep inversion workflows including several frequency bands were proposed (e.g., Barth et al., 2007). In order to find the best combination of frequency ranges and time domain or frequency domain input types for the MT inversion, we selected a subgroup of 13 earthquakes recorded by the AlpArray stations. These test events span a magnitude range of M_w 3.3 to 4.1 and are therefore considered representative. We perform MT inversions using different combinations of input data types (Figs. 7 and S1 in the Supplement): time domain full waveforms (td), frequency domain amplitude spectra (fd), cross-correlations of time domain full waveforms (cc), waveform envelopes, and combinations thereof. The input data are filtered using nine different bandpass filters with passbands between 0.01 and 0.7 Hz (Figs. 7 and S1). We compare the uncertainties of the resolved MTs in order to find the most appropriate parameter settings for our study and future MT studies in the Alps or similar settings.

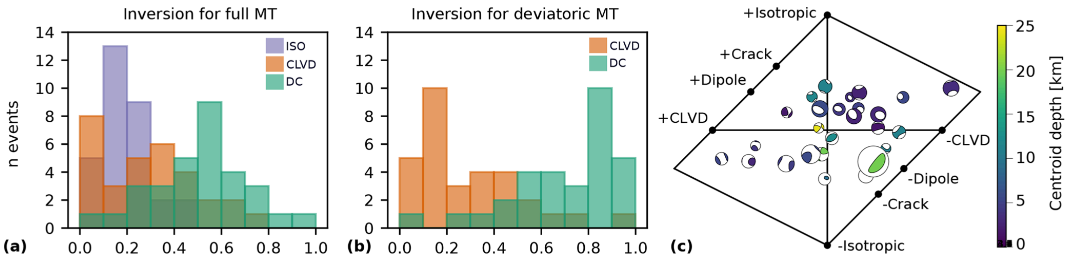

Figure 4. Histograms showing the decomposition of the full **(a)** and deviatoric **(b)** MT inversion results into isotropic (ISO), compensated linear vertical dipole (CLVD) and double couple (DC). Each bar of 10 % width (x axis) indicates for how many test earthquakes (y axis) the proportion of decomposition is found. For example, an isotropic component of 10 %–20 % is found for 13 test events in the full MT inversion. **(c)** Hudson plot showing non-DC components of individual events. Four events with Kagan angles > 60° between full and deviatoric solutions were removed, since they were not well resolved. Color represents depth, and beach ball size represents magnitude.

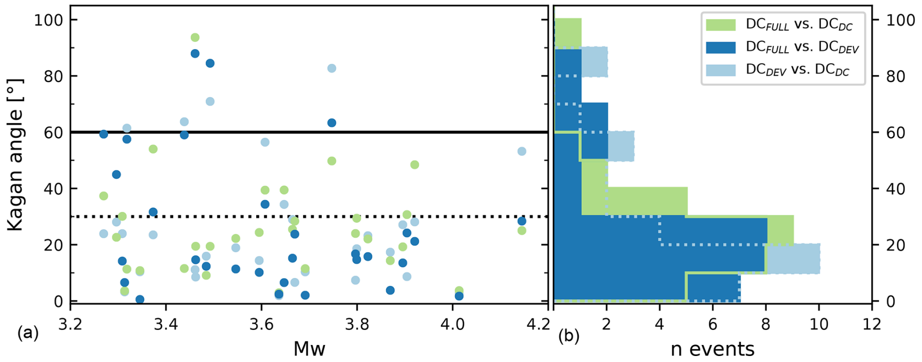

Figure 5. (a) Kagan angle between DC of pure double-couple, deviatoric and full MT solutions for 30 earthquakes, M_w 3.3–4.5. The dashed and solid lines indicate Kagan angles of 30 and 60°, respectively, indicating levels of high agreement and corresponding mechanisms. **(b)** Histograms showing the distribution of Kagan angles between the DC of pure DC, deviatoric, and full MT inversion solutions.

In Fig. 7, we show the results for three exemplary events. The color intensity of each focal sphere represents the summed standard deviations of the six MT components derived from the ensemble of solutions of the bootstrap chains. Intense colors represent stable solutions with low uncertainties. The first event is a M_w 4.1 earthquake in Switzerland. Due to the high magnitude, the MT inversion results are stable over frequency bands ranging from 0.01–0.03 Hz up to 0.01–0.10 Hz for all input data types. The MT is not well resolved when filtering using a passband of 0.03–0.1 Hz or higher. A similar behavior is observed for the second example, a M_w 3.9 normal faulting event close to Lake Geneva. The MT is very well resolved using bandpass filters covering the intermediate passbands between 0.02 and 0.1 Hz. In contrast to the first event and corresponding to the lower magnitude, the resolution is worse when frequencies between 0.01–0.02 Hz are included, while the frequency band between 0.03–0.1 Hz still leads to satisfying results. In general, the higher the frequency band, the lower the stability of the ensemble of solutions due to the simplified 1-D velocity model, site effects, and increased noise levels.

In the case of the third example (Fig. 7), a M_w 3.6 earthquake from France, the MT solutions vary substantially. This illustrates the need for a careful selection of appropriate methods and frequency ranges and the analysis of the uncertainties of MT inversions. For both the higher-frequency ranges (from 0.03–0.1 Hz and higher) and the lowest-frequency bands (0.01–0.03 and 0.02–0.05 Hz) surface waves have insufficient SNRs. Stable results for most input types are obtained in the frequency band 0.02–0.07 Hz, in which surface waves are more distinct. A visual inspection of the recorded waveforms of various events with magnitudes of M_w 3.4–3.9 confirms that surface waves have highest SNRs for periods between 0.02 and 0.05 Hz. Extending the passband to 0.02–0.07 Hz helps to avoid mismatching monochrome phases in the inversion process.

Comparing the different input data types for all 13 test events, we find that a combination of frequency domain amplitude spectra and time domain full waveform fitting (tdfd in Fig. 7) provides more stable results than relying on time domain waveform fitting alone. The high uncertainties of the frequency domain amplitude spectra fitting alone (fd) result from the unresolved polarity. The geometry of the nodal planes can still be determined. For most events, the other combinations (tdcc, tdfccc, fdcc) provide more stable results compared to using only time domain full waveforms (td).

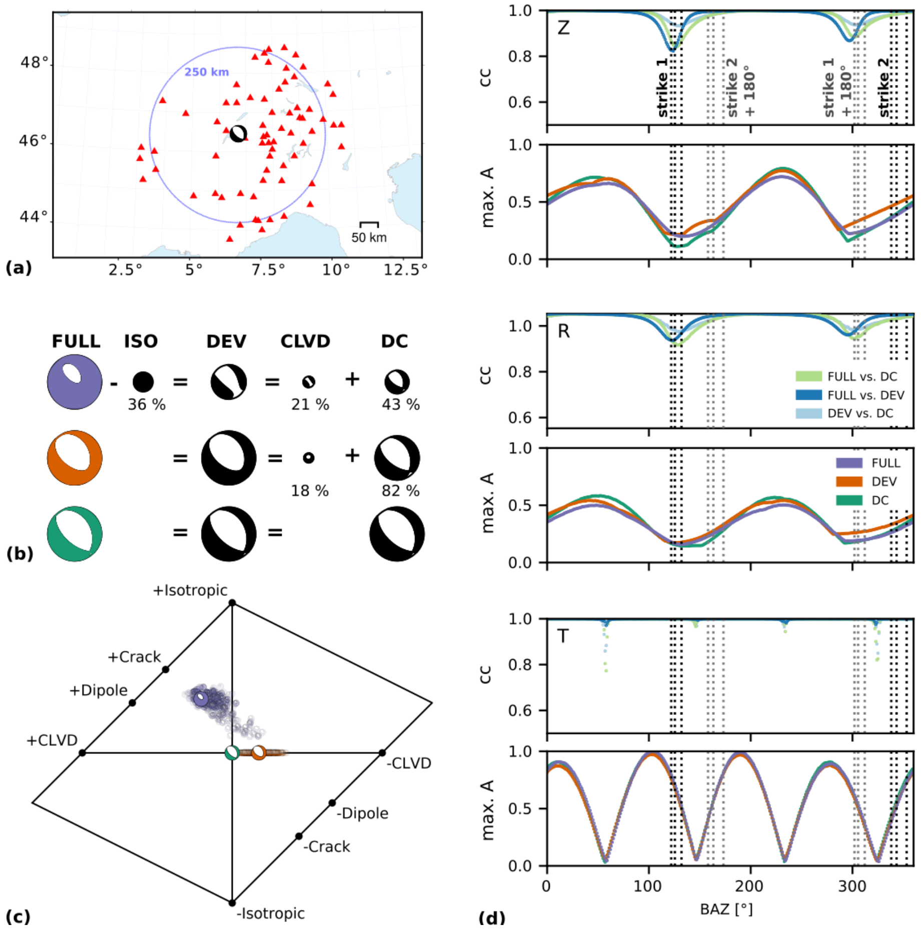

Figure 6. Earthquake close to Lake Geneva (France–Switzerland border region), M_w 3.9, 28 May 2019, 08:48:06 UTC. **(a)** Seismic network used for the MT inversions (73 broadband sensors, red triangles) and synthetic network (circle of blue dots, in 1° steps). **(b)** Decomposition of the full (purple), deviatoric (orange), and pure DC (green) MT inversion solution with the smallest misfit. **(c)** Hudson plots showing the ensemble of solutions for the full and the deviatoric MT inversions; colors are as in **(b)**. Larger symbols depict the best solutions of **(b)**. **(d)** For the three MT solutions (full, deviatoric and DC) synthetic data were forward-computed for the fictional network shown in **(a)**. For each component (Z, R, T), the first row shows the maximum cross-correlation values of the three synthetic traces at each station (BP filter 0.02–0.1 Hz). The second row shows the maximum absolute amplitude at each back-azimuth, normalized over the three solutions. The dashed lines indicate the strike 1 and 2 directions of the two nodal planes of full, deviatoric, and DC solutions and their 180° equivalent.

However, compared to the tdfd combination, they do not further improve the stability of the solution.

In addition to the presented tests of input data types, we tested waveform envelopes (Fig. S1). In order to resolve the polarity of the mechanisms, the envelopes are combined with time domain full waveforms or cross-correlation fitting of waveforms at nearby stations. This is a reasonable setting for weak events, where full waveforms may be of such low amplitudes that they can only be fitted at closer stations while envelopes of more distant stations may still be of use. We find that in the case of intermediate- or large-magnitude test events ($M_\mathrm{w} \geq 3.6$), the resulting MT is well recovered, although uncertainties are larger than with a time domain–frequency domain combination. In the case of smaller events, where time domain–frequency domain combinations might fail, the envelopes may stabilize the inversion. The applicability of the combination of envelopes and nearby time domain traces depends on the data quality of the closest stations and on the careful selection of the frequency range and the smoothing of the waveform envelopes.

Following the results of our methodological tests, we routinely use a combination of frequency domain amplitude spectra and time domain full waveform fitting in a frequency band of 0.02–0.07 Hz for earthquakes with $M_\mathrm{w} > 3.5$. In the case of smaller-magnitude earthquakes, we additionally perform inversions using a frequency range of 0.03–0.10 Hz. We observe that in the case of low-magnitude earthquakes the initial local magnitudes can differ significantly from our moment magnitude estimates. Furthermore, the availability of stations with a good SNR depends not only on the event

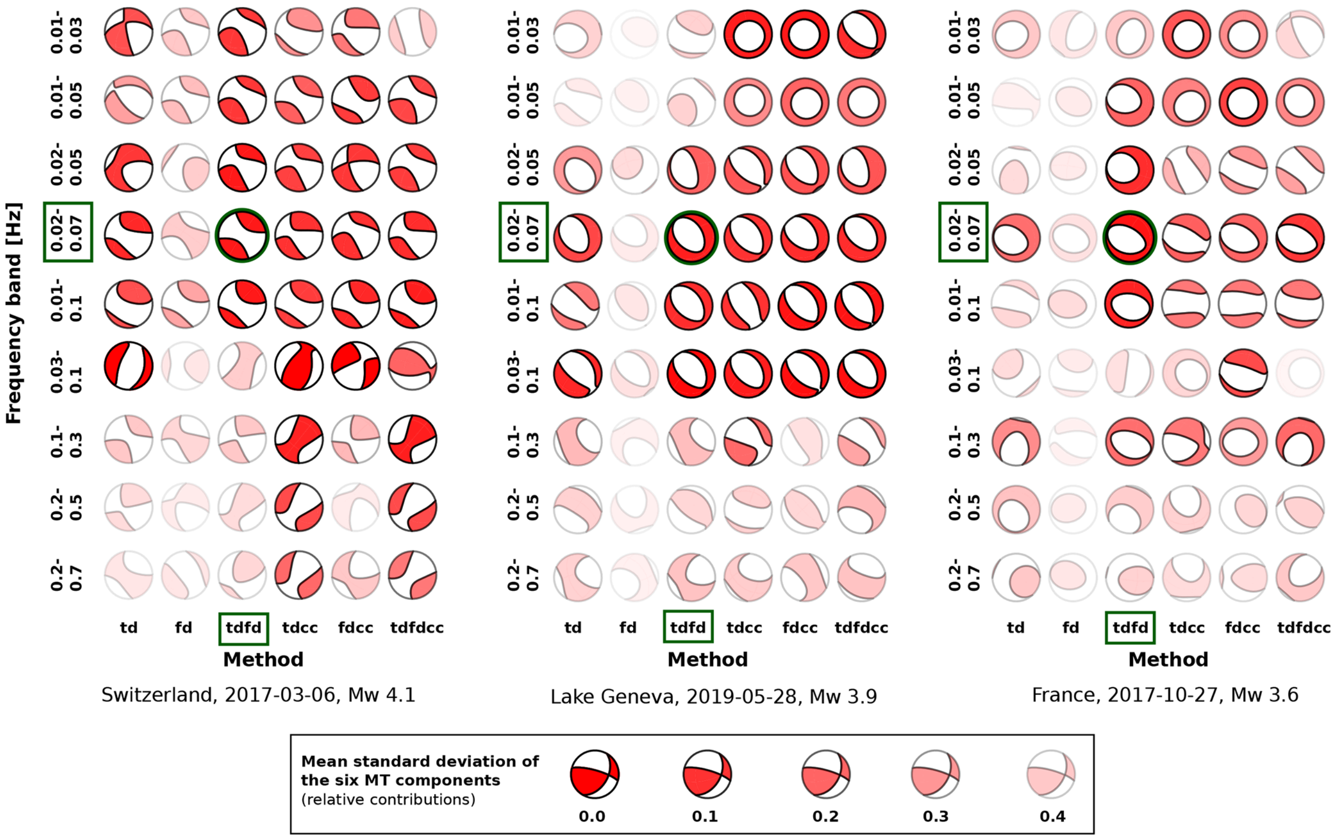

Figure 7. Testing of input data types and frequency ranges for three earthquakes with magnitudes between M_w 3.6 and 4.1. Abbreviations are as follows: td is time domain full waveforms; fd is frequency domain amplitude spectra; cc is cross-correlation fitting of full waveforms; tdfd, tdcc, fdcc, and tdfdcc are combinations of these. Color intensity represents summed uncertainty of MT components. A combination of fd and td in a frequency band between 0.02–0.07 Hz yields the best results for $M_w > 3.3$ (marked in green).

magnitude but also on noise conditions and damping along the travel path. It is therefore necessary to adapt the approach to the individual earthquakes, but the two frequency ranges constitute reasonable guidelines.

2.2.3 Station coverage

The dense AASN provides an excellent azimuthal distribution of seismic stations for moderate to large earthquakes in the Alps. We take advantage of the large number of stations in the AASN to investigate how the stability of the deviatoric MT inversion is influenced by gaps in the azimuthal station distribution around an earthquake. This allows simulating uncertainties of MT solutions in the marginal areas of the AASN, but the results also apply to other locations and networks (e.g., close to subduction zones). Most generally, within the AASN larger event-station distances can be taken into account for larger magnitude earthquakes and therefore both the number of stations and the azimuthal station coverage increases. In contrast, individual malfunctioning stations may already result in large azimuthal gaps for low magnitude earthquakes located within the AASN. In theory, the DC components of a moment tensor can be resolved from a single station using 3-component data (Dufumier and Cara, 1995). However, such an analysis requires high data quality and exact knowledge about velocity structures and path effects. In practice, single-station approaches are mostly avoided as they often result in unstable solutions (Dufumier and Cara, 1995).

Figure 8 shows the fuzzy MTs (right panels) for decreasing azimuthal coverage of seismic stations (left panels) for three exemplary events. In the case of the largest event (M_w 4.1), the solution is very stable when seismic stations cover at least an azimuthal range of 90°. In the case of an even smaller coverage, the mechanism rotates slightly depending on the azimuthal direction of the remaining stations. In the case of the M_w 3.9 event, the uncertainties of the solutions increase with decreasing station coverage. Two examples in which the inversions were done with stations covering only an azimuthal range of 45° show significant differences between the resulting focal mechanisms. When only considering the fuzziness of the two focal mechanism plots, both ensembles of solutions seem to be well resolved and stable. This indicates that

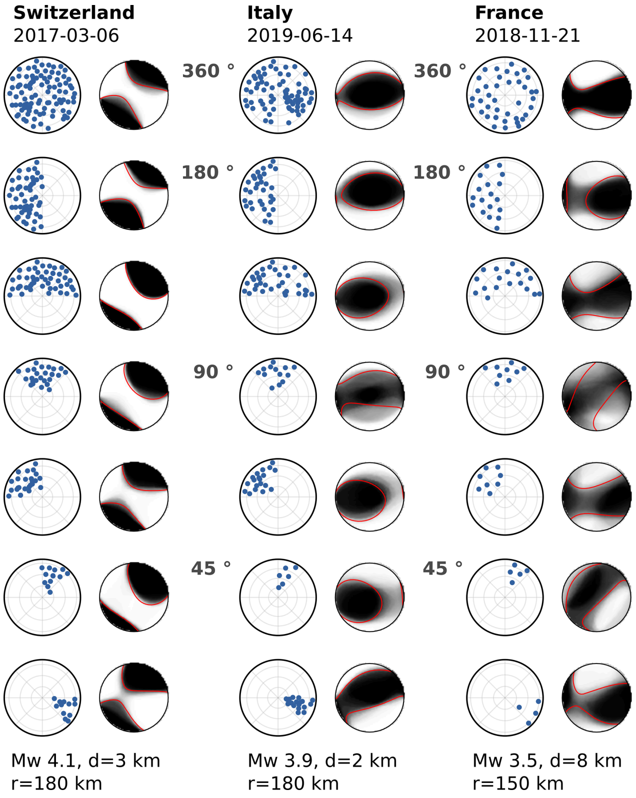

Figure 8. Resolution of the deviatoric MT depending on the azimuthal station coverage for three earthquakes with magnitude M_w, centroid depth d, and event-station radius r given below each column (left, middle, and right panels). The station coverage (blue dots in the first, third, and fifth columns) decreases from top to bottom as indicated in between the event columns. The fuzzy MTs show the solution stability (Sect. 2.1 and Fig. 2). They are composed of the superimposed P radiation pattern of the ensemble of solutions from the bootstrap chains.

the amount and variability of input data are not sufficient to resolve the MT unambiguously.

Furthermore, we observe a clear trend of increasing non-DC components with decreasing azimuthal coverage. We find a non-DC component below 10 % for a coverage of 180° but 40 % for the smallest tested coverage for the M_w 3.9 event.

For the smallest earthquake (M_w 3.5), the resulting MT solutions vary even more. In the case of the inversions with a station coverage of 90°, the variability among the ensembles of solutions is high and depends on the location of the 90° quadrant covered with stations. When only considering the dominant DC components of the deviatoric moment tensors, we observe the same general correlation between coverage and resolution. It is worth noticing that even with a small number of stations covering a small azimuthal range, it is possible to resolve a MT under favorable geometrical conditions. When stations are located in strike direction and cover both tensional and compressional quadrants, they may resolve the MT correctly even when covering only 45° (Fig. 8, M_w 3.5 event, fifth row and last row).

We conclude that in the case of larger earthquakes with a high SNR and a sufficient number of stations at different epicentral distances even a limited azimuthal coverage does not necessarily pose a problem, but lower-magnitude earthquakes usually require a better azimuthal station coverage. In regard to a semi-automated MT inversion workflow, we implemented an optional minimum station distribution threshold. Based on our results, and since we do not assume any a priori known strike direction, we limit the inversions to earthquakes with an azimuthal coverage above 90° but thoroughly evaluate all results with a coverage below 180°.

3 Results

3.1 CMT solutions for the Alpine region, 2016–2019

Based on our methodological tests, we use a combination of time domain full waveforms and frequency domain amplitude spectra as input data for the centroid MT inversion for earthquakes larger than M_w 3.0. We choose a frequency range of 0.02 to 0.07 Hz for a first inversion of each event. Depending on the event magnitude, the maximum epicentral distance varies between 80 and 300 km. In the case of poor fits, we slightly increase the frequency bands (0.03–0.1 Hz for $M_\mathrm{w} < 3.$) for smaller events and decrease it for the larger events (0.02–0.05 Hz for $M_\mathrm{w} > 4.2$). Deviatoric inversions were generally favored over full moment tensors since we demonstrated that the isotropic and CLVD components can often not be distinguished reliably. In addition, no volume changes are expected to accompany small earthquakes in the seismotectonic setting of the Alps. We obtained deviatoric MT solutions for 75 earthquakes occurring between January 2016 and December 2019 in the wider Alpine region for which we determine moment magnitudes between M_w 3.1 to 4.8 (Fig. 9, Table S1 in the Supplement). While we were able to compute stable MTs for most Alpine earthquakes from regional catalogs with local magnitudes larger M_l 3.3, we resolved only 13 MTs for earthquakes with local magnitudes between M_l 3.1 and 3.3, corresponding to one-third of the events in this magnitude range compared to the GEOFON catalog. Low SNR in the tested frequency bands covering frequencies between 0.02 and 0.5 Hz and fewer available stations hindered successful inversions for the other small earthquakes. Furthermore, we realized that a station spacing of about 60 km is not sufficient for small earthquakes ($M_\mathrm{w} < 3.3$) in case a part of the data is rejected due to quality issues.

For about 40 % of our own MT solutions for 2016 to 2019, no MT solutions were available from regional observatories (INGV, GEOFON, EM-RCMT, SISMOAZUR, SED, ARSO). For the other earthquakes, we obtain similar MT solutions, with a median deviation Kagan angle of 21° (mean

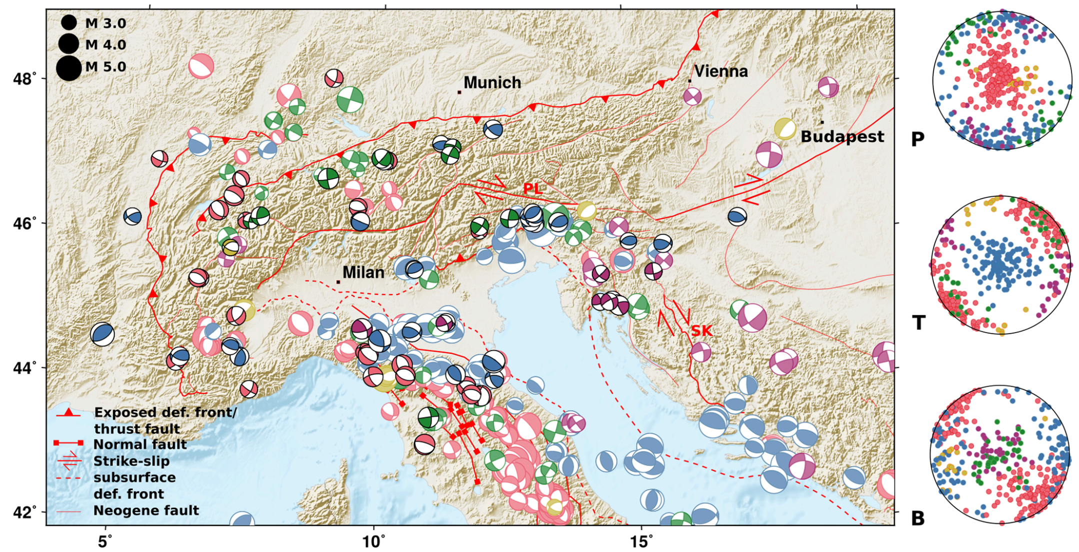

Figure 9. Moment tensor inversion results from January 2016 to December 2019 (focal spheres with black lines) along with MTs from 1983–2015 from bulletins of GCMT, GEOFON, INGV, SED, EM-RCMT, and ARSO (lighter colors). Similar colors represent clusters of comparable mechanisms obtained from a clustering approach based on the smallest rotation between the mechanisms (see text). Red and orange colors correspond to dominant normal faulting mechanisms in a cluster. Thrust faulting is indicated in blue, and strike-slip faulting earthquakes are colored in green and purple. Exposed and subsurface faults are simplified from Schmid et al. (2004, 2008), Handy et al. (2010, 2015), and Patacca et al. (2008). "PL" marks the Periadriatic line, and SK marks the Split–Karlovac Fault. (right) Pressure (P), tension (T), and null (B) axis of all focal mechanisms. Topographic data from SRTM-3 (Farr et al., 2007) and ETOPO1 (Amante and Eakins, 2009) datasets.

of 24°). For the largest events, the deviation is 15°. In the following, we jointly analyze our results with approximately 350 moment tensors of earthquakes that occurred before 2016, as reported by GCMT, GEOFON, INGV, EM-RCMT, SED, and ARSO (Fig. 9). Whenever more than one MT solution is available from the different bulletins, we prioritize local institutes (INGV for Italian earthquakes, SED for earthquakes in Switzerland, ARSO for Slovenia), unless they indicate high uncertainties. Furthermore, EM-RCMT with great experience for the Mediterranean and surrounding areas is favored over GEOFON solutions and over GCMT.

We used a clustering algorithm (Cesca, 2020) based on the Kagan angles between all focal mechanisms obtained in this study and reported in the catalogs to define classes of similar mechanisms (Fig. 9). The clustering tool uses the DBSCAN clustering algorithm (Ester et al., 1996), which relies on two parameters, the maximum acceptable similarity distance (eps) between two events, here eps = 0.14, and the minimum number of neighboring items (nmin), here nmin = 6. We choose a rather large eps value to emphasize patterns of general similarity between mechanisms. In a second step, we assign all remaining earthquakes to the cluster to which they have the smallest rotation angle.

Within the Alps, we observe four dominant groups of focal mechanisms (Fig. 9). Roughly E–W-striking thrust faulting is observed in the eastern Southern Alps (northern Italy) and at the central southern margin of the mountain range (blue focal spheres). A group of similar strike-slip-faulting earthquakes are aligned parallel to the northern deformation front of the Alps (green focal spheres, Fig. 9). A second group of strike-slip mechanisms is situated in the transition of the Alps to the Dinarides and in the northern Dinarides (purple and green focal spheres). NW–SE-striking normal faulting events are found in the NW Alps (red focal spheres), while mechanisms are more heterogeneous in the SW Alps.

3.2 Distribution of centroid depths

The resolved centroid depths within the Alps range from about 2 to 15 km, pointing to a shallow seismic activity within the mountain range. A total of 80 % of the studied events have depths shallower than 10 km. A comparison of our inverted centroid depths to the depths published in the event catalogs is limited for two reasons. First, the event depths were fixed in some of the published moment tensor inversion results, and second the depth estimates differ significantly among the different catalogs. We find a good correspondence with less than 3 km difference for > 60 % of the events to at least one of the published solutions. For another 26 %, we report differences between 3 and 5 km.

In Fig. 10, we display the depth distribution of mechanisms depicted in Fig. 9 sorted by faulting type. In the left panels, the focal mechanisms derived from the aforementioned bulletins are shown, while our own centroid solutions are provided in the right panels. While the depth in the catalogs may be partly fixed during the inversion, the centroid depth is determined during the MT inversion in our approach.

Uncertainties of our solutions are mostly in the range of 1 to 3 km. Many events within the Alpine mountain range are shallower than 10 km (Fig. 10d–f). While we obtained depths below 5 km for all normal faulting events in the NW Alps, depths of up to 15 km are observed for thrust-faulting events occurring between 2016 and 2019 in the eastern Southern Alps.

Centroid depths in the Apennines can be significantly larger. Thrust and normal faulting events are roughly separated into two NW–SE-running bands, with more thrust events in the NE and more normal faulting events in the SW part. Normal faulting and strike-slip events occur predominantly at shallower depths (< 20 km) than the thrust-faulting events with depths of often 30–50 km.

4 Discussion

4.1 Dominant mechanisms and the regional stress regime

The distribution of our mechanisms coincide well with long-term seismological and tectonic observations. The moment tensor solutions obtained from small to moderate earthquakes during 4 years with an enhanced station density in the course of the AlpArray project allows for identifying multiple seismotectonic domains. The faulting styles of these domains are in agreement with those derived from longer-term moment tensor catalogs (Fig. 9). Furthermore, new solutions for regions of sparse seismicity like the northern Central Alps provide new insights into recent activity. Thrust faulting related to the N–S compression between the European plate and the Adriatic plate is mainly observed in the eastern Southern Alps, strike-slip faulting is observed in the northern Dinarides and along the northern Alps and normal faulting is observed in the NW Alps (Fig. 9).

The orientations of P and T axes of the moment tensor solutions across the Alps provide information on local deformation regimes. Their distribution across the mountain belt points out both local and regional heterogeneities (Fig. 11). In addition to the direct interpretation of P and T axes, we apply a stress inversion approach based on the minimization of the seismic energy released on unfavorably oriented faults (Cesca et al., 2016) in volumes of comparably high seismic activity (Fig. S2). Stress inversion results provide the orientations of the most compressive (σ_1), the intermediate (σ_2), the least compressive principle stresses (σ_3), and the relative stress magnitude $R = (\sigma_1 - \sigma_2)/(\sigma_1 - \sigma_3)$. A homogeneous stress field is assumed within the selected rock volume and time period for each subregion.

In the following, we describe the patterns of P and T axes, as well as the local stress regimes in the different seismotectonic domains, which were inferred from the moment tensor solutions. In doing so, we first concentrate on the typical N–S compressional regime in the central to eastern Southern Alps (Region 2 and 3 in Fig. 1), before we focus on the transition to the strike-slip regime in the northern Dinarides (Region 4 in Fig. 1). Subsequently, the deformation regime in the Western Alps (Region 1 in Fig. 1) is discussed. Additionally, we discuss the findings for the neighboring northern Apennine mountain range (Region 5 in Fig. 1).

At the southern margin of the central Southern Alps, we observe predominantly thrust mechanisms with NNW–SSE-to-NW–SE-oriented P axes in the central Alps, close to Lake Garda, to NNE–SSW-oriented P axes further east (Fig. 11a, features d and e). Our stress inversion results confirm dominating compression from the central to eastern Southern Alps with sub-horizontal σ_1 orientation (Fig. S2), which is in agreement with the stress map of the Mediterranean and Central Europe (Heidbach et al., 2016). Seismic activity at thrust faults originating from the N–S convergence of the Adriatic and Eurasian plates in the Southern Alps are well known and have been described by various studies (e.g., Pondrelli et al., 2006; Anselmi et al., 2011; Poli and Zanferrari, 2018). According to Cheloni et al. (2014), the SE Alpine thrust front absorbs about 70 % of the convergence between the continental plates. In the transition from the Southern Alps to the northern Dinarides a rotation of the P axes from NW–SE to NNE–SSW is observed (Fig. 11a, features a–c). Despite increased uncertainties due to the relatively low number of available MT solutions, we observe a similar rotation of σ_1. Although less distinct, this rotation can also be seen when looking at the stress direction obtained from thrust MTs in Heidbach et al. (2016). The changes in the orientation of the thrust mechanisms may be attributed to the bending of the southern thrust front of the Alps and to the transition to the strike-slip fault systems in the Dinarides.

The transition from dominant thrust faulting close to Friuli to the strike-slip events to the east and in the northern Dinarides was also described by Pondrelli et al. (2006) and is mapped by the change from a sub-vertical to an almost horizontal σ_3 direction (Fig. S2). Moulin et al. (2016) describe right-lateral motion ($3.8 \pm 0.6\,\mathrm{mm\,yr^{-1}}$) on three main Dinaric faults and suggest that the system of NW–SE-oriented right-lateral strike-slip faults might be the northeastern boundary of the Adriatic microplate.

The W Alps show more heterogeneous faulting compared to the Southern Alps and the northern Dinarides. We obtained four new MT solutions indicating NW–SE-striking normal faulting east of Lake Geneva in the NW Alps, in agreement with the orientation of T axis at a high angle to the bending of the orogen described by Delacou et al. (2004). Our MT solutions and the catalog solutions show normal faulting, thrust faulting, and some oblique strike-slip faulting events in the W to SW Alps (Region 1 on Fig. 1). Despite the small number of moment tensors, we can also infer a rotation of the T axes in the southwestern Alps. In contrast to the northwestern Alps, where the tensional axis points at an extension along the mountain belt, the T axes of the focal mechanisms are oriented roughly perpendicular to the Alpine arc

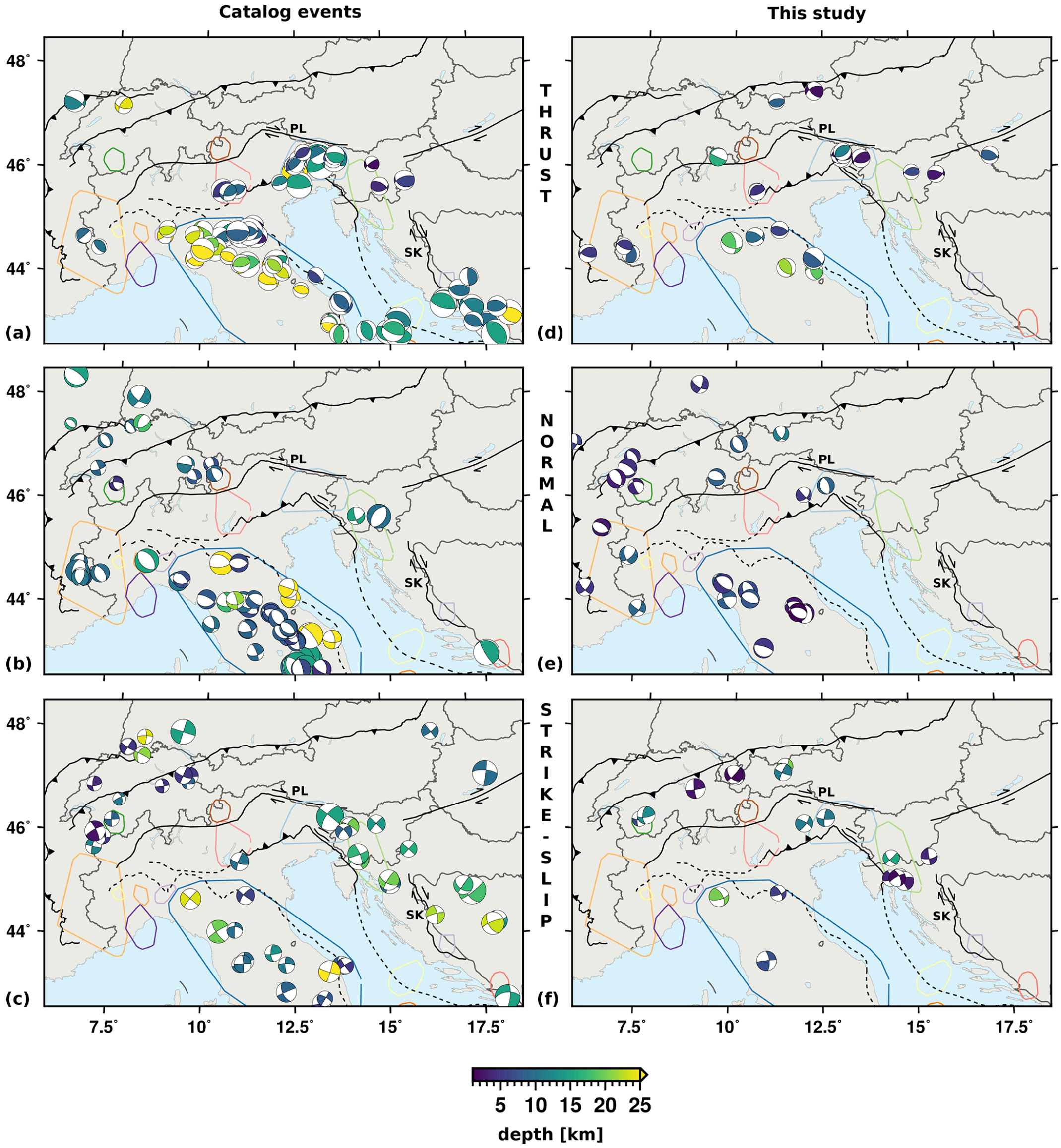

Figure 10. **(a–c)** Catalog depths of earthquakes shown in Fig. 9. Depths may be fixed in some catalogs. **(d, e)** Centroid depths of MT solutions in this study. Earthquakes are sorted according to their mechanisms: **(a, d)** thrust-faulting events, **(b, e)** normal faulting events, and **(c, f)** strike-slip events. Exposed and subsurface faults (solid and dashed lines) are simplified from Schmid et al. (2004, 2008), Handy et al. (2010, 2015), and Patacca et al. (2008). PL marks the Periadriatic line, and SK marks the Split–Karlovac Fault. The outlines of spatial clusters of increased seismic activity from Fig. 12a are indicated for orientation.

(Fig. 11b, features f and g). The stress inversion results indicate an extensional regime in the Western Alps with a subvertical σ_1 orientation. However, across the large region the uncertainties of the stress inversion are relatively high. This is in agreement with the co-existing thrust faulting, normal faulting, and strike-slip faulting also shown by Delacou et al. (2004) and Heidbach et al. (2016).

Along the Apennines, thrust faulting is dominant at the northern arc, while normal faulting earthquakes are dominant southwest of the ridge of the Apennines. The NW–SE orientations of the T axes of the normal faulting events are perpendicular to the elongation of the mountain belt as also described by Pondrelli et al. (2006). The vertical σ_1 direction and the NE–SW-oriented, horizontal σ_3 direction confirm an extensional stress regime (Fig. S2). In contrast, a compressional regime is observed along the NE arc of the Apennines with P axes of the thrust-faulting events oriented NW–SE to NE–SW (Fig. 11).

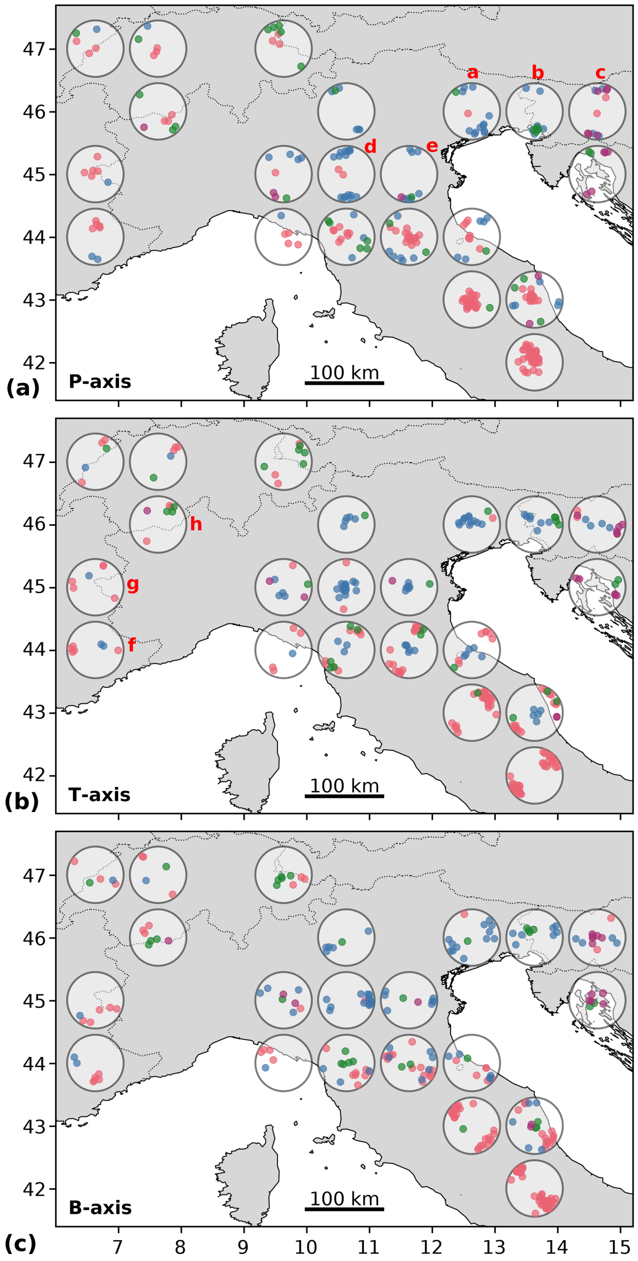

Figure 11. Regional distribution of **(a)** P, **(b)** T, and **(c)** B axes of focal mechanisms presented in Fig. 9. Colors correspond to mechanism classes as shown in Fig. 9. Only areas with more than five events in a latitude–longitude grid of 1° × 1° are shown. Areas a to h mark features that are discussed in the text.

4.2 CMT solutions in the seismotectonic context

Since only a few focal mechanisms are available for large parts of the Alps, we additionally take into account recent seismicity (Fig. 12a, c and d), historical large earthquakes (Fig. 12b), and GNSS data (Fig. 12e and f) to analyze our results in the seismotectonic context and draw a more detailed picture of the seismic and tectonic activity in the study area. To emphasize areas of significant seismic activity (Fig. 12a), we cluster the earthquakes in the seismicity catalogs by INGV, GEOFON, and GCMT according to their epicentral locations using the DBSCAN clustering algorithm (Ester et al., 1996) implemented in the Python package *scikit-learn* (Pedregosa et al., 2011). The merged catalog comprises more than 50 000 earthquakes with $M_1 > 2.0$ (1983–2017). The recent seismic activity can be traced back to historical times. Figure 12b shows historical earthquakes from the European Archive of Historical Earthquake Data 1000-1899 (AHEAD; Locati et al., 2014; Rovida and Locati, 2015) based on the SHARE European Earthquake Catalogue (SHEEC; Stucchi et al., 2013) and the ISC-GEM catalog (Storchak et al., 2013, 2015; Bondár et al., 2015; Di Giacomo et al., 2015, 2018) with $M_\mathrm{w} > 5.5$.

In general, the seismicity along the southern margin of the Alpine mountains is higher than along its northern counterpart. Apart from the large cluster of seismicity in the Apennines, we identify five dominant clusters and several smaller ones mainly located at the margins of the Alps (Fig. 12a). The largest seismicity clusters correspond to the numbered regions shown in Fig. 1. To avoid confusion with the mechanism-based clustering we here continue writing region (R) when referring to these clusters of epicenters. We focus on the analysis of the largest clusters, for which we were able to obtain multiple moment tensor solutions between 2016 and 2019. Following the Alpine arc from west to east, the first cluster is located in the Western Alps at the French–Italian border (R1 in Figs. 12a and 1), and two smaller clusters are found in the region around Lake Garda in the central Southern Alps (R2) and north of it. Two more clusters of high seismicity are situated in the eastern Southern Alps in the border region between Italy (Friuli) and Slovenia (R3), and in the northern Dinarides (R4). Figure 12a indicates dominant faulting styles for each cluster, namely thrust faulting for regions 2 and 3 around Lake Garda and in the eastern Southern Alps and strike-slip faulting in the northern Dinarides (R4). In the epicentral cluster of the Apennines (R5), two representative mechanisms reflect the separation of dominant normal and thrust-faulting earthquakes SW and NE of the ridge, respectively. Due to the heterogeneous faulting in the Western Alps, we assign no representative mechanism.

The cluster of high seismicity in the eastern Southern Alps (Fig. 12a) is located close to the epicenter of the 1976 Friuli earthquake (M_b 6.0; Pondrelli et al., 2001). The observed E–W-striking thrust events map the regional dominant stress field (Fig. 9), evolving from the underthrusting of the Friuli Plain beneath the Alps (e.g., Cipar, 1980). Focal mechanism solutions of the 1976 mainshock and aftershocks show similar thrust mechanisms, partly with a small strike-slip component, and are associated with the complex Periadriatic overthrust system (e.g., Cipar, 1980; Bressan et al., 1998; Pondrelli et al., 2001, 2006; Poli and Zanferrari, 2018; Slejko, 2018). Only a few tenths of kilometers to the west

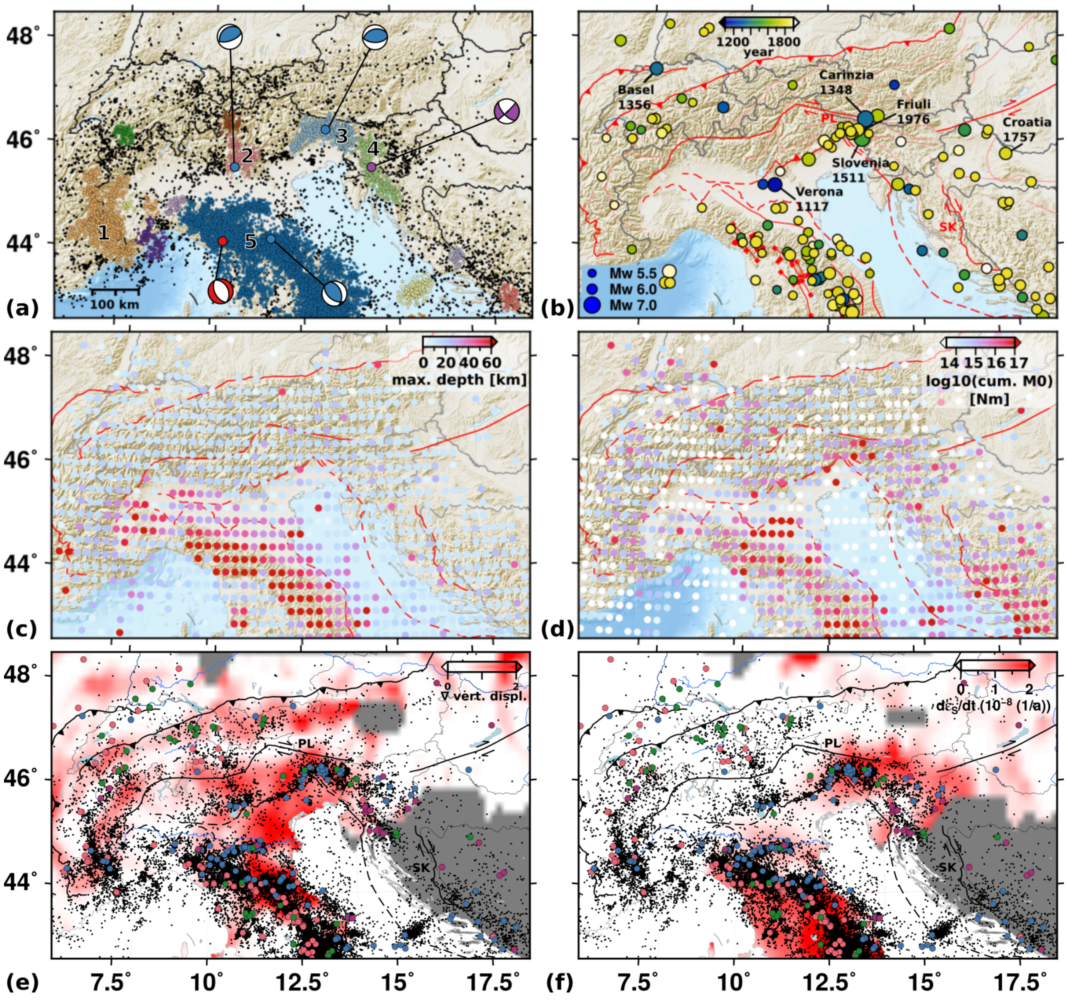

Figure 12. Characteristics of recent and historical seismicity and strain from GNSS data. **(a)** Seismic activity between 1978 and 2017; $M_\mathrm{l} > 2.0$; from GEOFON, INGV, and GCMT catalogs; and colored according to epicentral clusters of seismicity. Representative MTs from Fig. 9. Numbers refer to regions (1) W Alps, (2) Lake Garda, (3) eastern S Alps, (4) N Dinarides, and (5) Apennines. **(b)** Historical earthquakes with $M_\mathrm{W} > 5.5$ from the European Archive of Historical Earthquake Data 1000–1899 (AHEAD) (Locati et al., 2014; Rovida and Locati, 2015; Stucchi et al., 2013) and ISC-GEM catalog (1906–2016) (Storchak et al., 2013, 2015; Bondár et al., 2015; Di Giacomo et al., 2015, 2018). **(c, d)** Maximum event depth and the cumulative seismic moment on a grid with a spacing of 0.25° × 0.25° latitude and longitude. **(e, f)** Absolute value of the spatial gradient of the relative uplift rate as a proxy for vertical strain rates and observed GNSS shear strain rate (second invariant of strain tensor); both are obtained from GNSS data of the EUREF WG on European Dense Velocities (Brockmann et al., 2019). Black dots indicate seismicity, $M_\mathrm{l} > 2.0$. Events with MT solutions are color-coded as in Fig. 9. Exposed and subsurface faults (solid and dashed lines) are simplified from Schmid et al. (2004, 2008), Handy et al. (2010, 2015), and Patacca et al. (2008). PL marks the Periadriatic line, and SK marks the Split–Karlovac Fault. Topographic data are from the SRTM-3 (Farr et al., 2007) and ETOPO1 (Amante and Eakins, 2009) datasets.

of the Friuli area we observe strike-slip faulting (Fig. 9). Anselmi et al. (2011) report the occurrence of both thrust and strike-slip faulting for this area, mostly in agreement with an E–W to ENE–WSW minimum horizontal stress reported by Montone et al. (2004). Large historical events are reported along the southern margin of the Alps between Lake Garda (R2), the eastern Southern Alps (R3), and the transition to the northern Dinarides (R4) (Verona 1117, Slovenia 1511, and Carinthia 1348, all $M_\mathrm{w} \geq 6.7$). Similar high-seismicity and cumulative seismic moments during the last decades (Fig. 12d) are observed here. Within the seismicity cluster close to Lake Garda, Italy, the observed thrust mechanisms are typical for earthquakes located in the Giudicarie region close to the Ballino–Garda fault that runs through Lake Garda (Viganò et al., 2008).

Less frequent large historical earthquakes with magnitude estimates between M_w 5 and 6 are reported in the Western Alps and the Dinarides (R2 and 4). Within the last decades, earthquakes with $4 < M_\mathrm{l} < 5$ are observed across a wider part of the Western and Southern Alps, but magnitudes rarely exceed M_l 3.5 in large areas of the Central to NE Alps. The Eastern Alps north of the Periadriatic line and the area between the seismically active regions in the Western Alps and the Central Alps have particularly low seismicity rates (Fig. 12a). While at least three large earthquakes occurred in the eastern part of Switzerland in historical times, seismicity in this region appears to be relatively low in recent years (Fig. 12a and b).

The observed depth ranges of our MT solutions (Fig. 10) are in accordance with the maximum depths in the long-term seismic catalogs of GCMT, INGV and GEOFON, including $> 50\,000$ earthquakes with $M_l > 2.0$ (Fig. 12c). While the Moho depth increases gradually from less than 30 km at the northern margin of the Alps to above 50 km in the central part of the orogen (Spada et al., 2013), we do not observe any gradual change in the event depth. The catalogs and our own centroid depths show that seismicity is shallow across most of the Alps with rare deeper events (< 30 km) at the southern margin, where the Moho is at about 40 km depth (Spada et al., 2013). These few deeper events are located above the Moho. Maximum depths of above 60 km are observed in the Apennines.

The joined interpretation of seismicity, GNSS data, and MT solutions shows how the overall spatial distribution of faulting styles in the study area can be interpreted in the regional tectonic regime. Figure 12e and f present the spatial gradient of the uplift rates and the horizontal strain rates, computed from the GNSS data of the EUREF WG on European Dense Velocities (http://pnac.swisstopo.admin.ch/divers/dens_vel/index.html, last access: December 2020, Brockmann et al., 2019). Please refer to the Supplement for additional methodological information. Following Keiding et al. (2015), we use the spatial derivative of the uplift rate as a proxy of vertical strain rates (Fig. 12e).

Within the Alpine mountain range, the GNSS data show a consistent uplift relative to the surrounding areas (Fig. S3). Figure 12e and f emphasize the relation between recent seismic activity and both high spatial gradients of the uplift rate (Fig. 12e) and the shear strain rate (Fig. 12f) across large parts of the study area. The largest gradients of the uplift rate, high shear strain rates, and highest seismicity rates are observed in the eastern Southern Alps (R3 in Fig. 12a) and in the Apennines (R5 in Fig. 12a). The distribution of the cumulative seismic moment (Fig. 12d) agrees particularly well with the distribution of shear strain rates (Fig. 12f). We observe typically E–W-striking thrust faulting in the eastern Southern Alps, as also described in many previous studies (e.g., Pondrelli et al., 2006; Poli and Zanferrari, 2018). High horizontal velocities point to the shortening and crustal thickening in the eastern Southern and Eastern Alps due to the convergence of Adriatic and European plate (Fig. S3), in accordance with Serpelloni et al. (2016) and Sternai et al. (2019). Southeast of this area, at the transition to the northern Dinarides (Regions 3–4), the uplift gradients are low, while increased shear strain rates agree with our dominant strike-slip mechanisms (see also Serpelloni et al., 2016) and right-lateral motion on the Dinaric strike-slip faults (Moulin et al., 2016).

While there is no significant shear strain in the Western and Central Alps, we depict two subparallel bands of moderate spatial gradients of the uplift rate running roughly along the northern and the southern margin of the Alps. These two bands result from the overall relative uplift of the Alps and also have higher seismicity rates compared to the central Alpine belt. In the SW Alps, the largest events cluster in the transition area between relative uplift and subsidence, indicated by the band of increased spatial gradient of the uplift in Fig. 12e. Normal faulting events are dominant. Intraplate shear strain rates are relatively low in the entire Western and Central Alps.

The Adriatic plate, which is the upper plate in the Alpine subduction zone, rotates counterclockwise relative to Europe around an Euler pole located in the western Po plain or Western Alps (D'Agostino et al., 2008; Weber et al., 2010; Le Breton et al., 2017). The rotation results in varying convergence rates across the Alps. Le Breton et al. (2017, 2021) infer a rotation of about 5.25° during the last 20 Myr resulting in convergence rates ranging from 5.5 mm yr^{-1} in the NW Adria (Western Alps) to 7.5 mm yr^{-1} in the NE Adria (eastern Southern Alps) (Fig. 1). In comparison, kinematic reconstructions of Van Hinsbergen et al. (2020) involve less convergence but a higher rotation of Adria relative to Europe (10°), leading to 2.5 mm yr^{-1} convergence in the NW Adria to 6.25 mm yr^{-1} in the NE Adria. Recent GPS data indicate little to no horizontal movement in the Western Alps but more than 2 mm yr^{-1} NNW-ward movement of Adria in the eastern Southern Alps (see Fig. S3), which is in agreement with increased seismicity rates. The Western Alps are closer to the location of the Euler pole of the rotation of the Adriatic plate, and therefore convergence rates are lower. Recent GPS measurements and the computed horizontal strain rates even indicate the absence of convergence (D'Agostino et al., 2008, and Fig. S3). Therefore, the uplift pattern of the Western and Central Alps (Figs. 12e and S3) and the seismicity clusters in the W Alps need to be attributed to other mechanisms. Sternai et al. (2019) propose that isostatic adjustment to deglaciation and erosion and mantle-related processes such as slab detachment or asthenospheric upwelling may jointly explain the observed uplift pattern. The assumption of a stress or strain field that is not dominantly effected by the convergence of Europe and Africa was also proposed by Delacou et al. (2004) based on focal mechanisms and stress inversion in the Western Alps. Our moment tensor solutions indicating normal and strike-slip faulting, as well as the P and T axes, match these observations from GNSS data.

The seismic activity along the northern margin of the Alps is in agreement with the increased gradient of uplift in this area. However, the occurrence of strike-slip faulting earthquakes described in this study can hardly be explained by vertical strain, especially on favorably oriented faults. However, pre-existing faults may be unfavorably oriented, the stress field may be heterogeneous and local anomalies may not be resolved by the sparse GNSS network. Rather low seismicity is further observed in the eastern Po plain, where high spatial gradients of the uplift rate are observed. The high absolute gradient here can be attributed to the relative subsidence of the sediments in the Po plain (see Fig. S3) (Carminati and Martinelli, 2002) but not to a tectonic uplift which would likely be accompanied by seismic activity.

5 Conclusions

Centroid moment tensor inversion provides insight into faulting mechanisms of earthquakes and related tectonic processes. In this study, we used the AlpArray seismic network to analyze the mechanisms of earthquakes occurring from 2016 to end of 2019. Thanks to the flexible inversion tool *Grond*, we were able to test different inversion setups in order to derive guidelines for MT inversions in complex tectonic settings such as the Alps. These guidelines and the proposed tests can, on the one hand, facilitate future studies of faulting mechanisms in the Alps and, on the other hand, help to derive workflows to obtain reliable moment tensors in other dense networks or complex study regions. We evaluated the results with respect to their uncertainties and parameter trade-offs. For subsets of events, we tested various frequency bands, distance ranges, and different input data types comprising time domain full waveforms, frequency domain amplitude spectra, time domain cross-correlation fitting, waveform envelopes and combinations of these. In the case of our study area, for most earthquakes with magnitudes larger M_w 3.3, we find that a combination of time domain full waveforms and frequency domain amplitude spectra in a frequency band of 0.02–0.07 Hz is most suitable. The dense deployment of the AASN is ideal to study the effect of (manually introduced) azimuthal gaps. While a higher azimuthal station coverage is favorable in general, we find that a small number of stations with little azimuthal coverage may be sufficient depending on the location of the stations with respect to the strike direction of the fault. Performing CMT inversions constraining the solutions to a pure double-couple MT, a deviatoric MT, or a full MT, indicates that for the specific Alpine context with a dense network DC components are reliably resolved independent of the applied constraint. While allowing for non-DC components reduces the overall misfit, the CLVD and the isotropic components cannot be distinguished unambiguously. We propose performing similar tests prior to MT inversions for other study areas, when earthquake magnitudes are small, the crustal structure is complex, the number of stations is limited, or other factors might hinder straightforward inversions.

Relying on the results of the methodological tests, we performed deviatoric MT inversions for events with $M_\mathrm{w} \geq 3.1$. We present 75 solutions with reasonably low uncertainties occurring between 2016 and 2019. With four years of acquisition of small to moderate earthquakes in the course of the AlpArray project, we are able to identify seismotectonic domains that are representative in faulting styles of those derived from long-term seismic observations. We compare the derived MT solutions to historical earthquakes, recent seismicity, published focal mechanisms, and GNSS deformation data. Our moment tensor results indicate that while the Alps represent a rather heterogeneous study area, the region is characterized by compartments of different tectonic movement in close proximity. Typical ENE–WSW-to-E–W-striking thrust faulting is observed in the Friuli area in the eastern Southern Alps related to the N–S convergence of the Eurasian and Adriatic plate (Pondrelli et al., 2006; Poli and Zanferrari, 2018) and counterclockwise rotation of Adria relative to Europe (e.g., D'Agostino et al., 2008; Le Breton et al., 2017). Strike-slip faulting with similarly oriented P axes is observed parallel to the northern margin of the Central Alps and in the northern Dinarides, which is in agreement with right-lateral strike-slip faults and high shear strain rates. In contrast, NW–SE-striking normal faulting events with NE–SW-oriented T axes are observed in the NW Alps. Faulting styles in the SW Alps are more heterogeneous, with a majority of events related to an extensional stress regime. Simultaneous observations of low horizontal strain rates and normal faulting earthquakes are in agreement with studies proposing that relatively high uplift rates in the Western Alps are attributed to processes other than the Europe–Adria convergence. Based on a clustering of epicenters, we identify five main seismically active regions, namely the Western Alps, the region around Lake Garda, the eastern Southern Alps, the northern Dinarides, and the Apennines. Areas of high seismicity are mostly located in the proximity of the southern margin of the Alps, where significant vertical or horizontal strain rates are reported. Maximum observed magnitudes coincide with regions of increased seismicity and significant historical earthquakes but rarely exceed M_w 5.0. In contrast, seismicity is particularly low in the Eastern Alps and in parts of the Central Alps. The depths inferred from our moment tensor inversions and the depths in seismic catalogs indicate that the seismic activity in the Alpine mountain ranges is predominantly shallow with only few events in depth greater than 15 km in the eastern Southern Alps. Significantly deeper earthquakes are observed in the Apennines.

Code and data availability. The moment tensor inversions were performed using the free and open-source inversion tool *Grond* (Heimann et al., 2018). Figures were plotted using pyrocko (Heimann et al., 2019) and GMT (Wessel et al., 2013).

The topographic data for the maps were taken from the SRTM-3 (Farr et al., 2007) and ETOPO1 (Amante and Eakins, 2009) (NOAA National Geophysical Data Center 2009: ETOPO1 1 Arc-Minute Global Relief Model. NOAA National Centers for Environmental Information. Last access: December 2020).

Seismic catalogs are from the following sources: earthquake information and focal mechanisms are provided by the below-mentioned institutes. Swiss Seismological Service (SED) (Deichmann et al., 2004, 2006, 2008, 2009, 2010, 2011, 2012; Baer et al., 2005, 2007; Diehl et al., 2013, 2014, 2015, 2018; Diehl, 2020);

Slovenian Environment Agency (ARSO) (Ministrstvo za okolje in prostor Agencija RS za okolje, 2018, 2019, 2020);

INGV (Italy) (Scognamiglio et al., 2006), http://terremoti.ingv.it/en (last access: December 2020);

GEOFON (Germany) event locations were obtained from the GEOFON program of the GFZ German Research Center for Geosciences using data from the GEVN partner networks: https://geofon.gfz-potsdam.de/eqinfo/list.php (last access: December 2020);

EM-RCMT (European-Mediterranean Regional Centroid-Moment Tensors) http://rcmt2.bo.ingv.it/ (last access: December 2020), (Pondrelli, 2002);

SISMOAZUR (France) http://sismoazur.oca.eu/focal_mechanism_emsc (last access: December 2020) provide MTs obtained using FMNEAR (Delouis, 2014);

GCMT (Lamont-Doherty Earth Observatory of Columbia University, USA) https://www.globalcmt.org/ (last access: December 2020) (Dziewonski et al., 1981; Ekström et al., 2012).

Permanent seismic networks are as follows. The permanent stations of the AlpArray are part of existing European regional networks (RD – RESIF, 2018, GU – University Of Genova, 1967, CZ – Institute Of Geophysics, 1973, ST – Geological Survey – Provincia Autonoma Di Trento, 1981, G – Institut De Physique Du Globe De Paris (IPGP) and Ecole Et Observatoire Des Sciences De La Terre De Strasbourg (EOST), 1982, CH – Swiss Seismological Service, 1983, OE – ZAMG, 1987, MN – MedNet Project Partner Institutions, 1990, HU – Kövesligethy Radó Seismological Observatory, 1992, GE – GEOFON Data Centre, 1993, RF – University Of Trieste, 1993, FR – RESIF, 1995, IV – INGV Seismological Data Centre, 2006, BW – Department Of Earth And Environmental Sciences, Geophysical Observatory, University Of Munchen, 2001, SX – Leipzig University, 2001, NI – OGS and University Of Trieste, 2002, TH – Jena, 2009, OX – OGS, 2016).

Supplement. The supplement related to this article is available online at: https://doi.org/10.5194/se-12-1233-2021-supplement.

Team list. The complete member list of the AlpArray Working Group can be found at http://www.alparray.ethz.ch and the complete list of the Swath-D Working Group can be found at https://doi.org/10.14470/MF7562601148.

Author contributions. GMP, SC, and TD conceptualized the study. GMP performed the moment tensor inversions, conceptualized and developed the methodological tests, prepared the figures, and wrote the original draft of the manuscript. SC, TD, JK, and TP developed the general project idea and acquired the funding. SC, SH, DK, and TD supervised the study. SH developed the moment tensor inversion and the software tools used in this study (Heimann et al., 2018, 2019). SH, SC, TD, and PN contributed to methodological developments. SH and PN helped to visualize the results. TD and TP performed stress field inversions. GMP, SC, and TD validated the results. The AlpArray Working Group provided access to the seismic data of the temporary network and additional background information. All co-authors reviewed and edited the manuscript.

Competing interests. The authors declare that they have no conflict of interest.

Special issue statement. This article is part of the special issue “New insights into the tectonic evolution of the Alps and the adjacent orogens”. It is not associated with a conference.

Acknowledgements. We like to thank the three anonymous reviewers for constructive comments that helped to improve the manuscript. Eline Le Breton is thanked for providing helpful information for the geological and tectonic background. Peter Niemz is currently funded by the BMBF (German Federal Ministry of Education and Research) project SECURE (grant agreement no. 03G0872A).

Financial support. This research has been supported by the German Science Foundation DFG From Top to Bottom – Seismicity, Motion Patterns and Stress Distribution in the Alpine Crust (project number 362440331), a subproject of “SPP 2017: Mountain Building Processes in 4D” (project number 313806092).

The article processing charges for this open-access publication were covered by the Helmholtz Centre Potsdam – GFZ German Research Centre for Geosciences.

Review statement. This paper was edited by Emanuel Kästle and reviewed by three anonymous referees.

References

AlpArray Seismic Network: AlpArray Seismic Network (AASN) temporary component, Other/Seismic Network, AlpArray Working Group, https://doi.org/10.12686/alparray/z3_2015, 2015.

Amante, C. and Eakins, B.: ETOPO1 1 Arc-Minute Global Relief Model: Procedures, Data Sources and Analysis, NOAA Technical Memorandum NESDIS NGDC-24, National Geophysical Data Center, NOAA, https://doi.org/10.7289/V5C8276M, 2009.

Anselmi, M., Govoni, A., De Gori, P., and Chiarabba, C.: Seismicity and velocity structures along the south-Alpine thrust front of the Venetian Alps (NE-Italy), Tectonophysics, 513, 37–48, 2011.

Baer, M., Deichmann, N., Braunmiller, J., Husen, S., Fäh, D., Giardini, D., Kästli, P., KRadolfer, U., and Wiemer, S.: Earthquakes in Switzerland and surrounding regions during 2004, Ecl. Geolog. Helvet., 98, 407–418, 2005.

Baer, M., Deichmann, N., Braunmiller, J., Clinton, J., Husen, S., Fäh, D., Giardini, D., Kästli, P., Kradolfer, U., and Wiemer, S.: Earthquakes in Switzerland and surrounding regions during 2006, Swiss J. Geosci., 100, 517–528, 2007.

Barth, A., Wenzel, F., and Giardini, D.: Frequency sensitive moment tensor inversion for light to moderate magnitude earthquakes in eastern Africa, Geophys. Res. Lett., 34, L15302, https://doi.org/10.1029/2007GL030359, 2007.

Bassin, C., Laske, G., and Masters, G.: The current limits of resolution for surface wave tomography in North America, EOS Trans AGU, 81, F897, 2000.

Bondár, I., Engdahl, E. R., Villaseñor, A., Harris, J., and Storchak, D.: ISC-GEM: Global instrumental earthquake catalogue (1900–2009), II. Location and seismicity patterns, Phys. Earth Planet. Inter., 239, 2–13, 2015.

Bressan, G., Snidarcig, A., and Venturini, C.: Present state of tectonic stress of the Friuli area (eastern Southern Alps), Tectonophysics, 292, 211–227, 1998.

Brockmann, E., Lutz, S., Zurutuza, J., Caporali, A., Lidberg, M., Völksen, C., Sánchez, L., Serpelloni, E., Bitharis, S., Pikridas, C., Fotiou, A., Mathis, E., Sánchez Sobrino, J., Valdés Péres De Vargas, M., Vernant, P., Baron, A., Westerhaus, M., Legrand, J., Kreemer, C., Gianniou, M., Nykiel, G., Figurski, M., Kenyeres, A., and Kurt, A.: Towards a Dense Velocity Field in Europe as a basis for Maintaining the European Reference Frame, in: 27th IUGG Assembly, Montreal, 2019.

Bukchin, B., Clévédé, E., and Mostinskiy, A.: Uncertainty of moment tensor determination from surface wave analysis for shallow earthquakes, J. Seismol., 14, 601–614, 2010.

Cabieces, R., Buforn, E., Cesca, S., and Pazos, A.: Focal parameters of earthquakes offshore Cape St. Vincent using an amphibious network, Pure Appl. Geophys., 177, 1761–1780, https://doi.org/10.1007/s00024-020-02475-3, 2020.

Carminati, E. and Martinelli, G.: Subsidence rates in the Po Plain, northern Italy: the relative impact of natural and anthropogenic causation, Eng. Geol., 66, 241–255, https://doi.org/10.1016/S0013-7952(02)00031-5, 2002.

Cesca, S.: Seiscloud, a tool for density-based seismicity clustering and visualization, J Seismology, 24, 443–457, https://doi.org/10.1007/s10950-020-09921-8, 2020.

Cesca, S. and Heimann, S.: Challenges in regional moment tensor resolution and interpretation, in: Moment Tensor Solutions, edited by: D'Amico, S., Springer Natural Hazards. Springer, Cham, 163–181, https://doi.org/10.1007/978-3-319-77359-9_7, 2018.

Cesca, S., Buforn, E., and Dahm, T.: Amplitude spectra moment tensor inversion of shallow earthquakes in Spain, Geophys. J. Int., 166, 839–854, 2006.

Cesca, S., Heimann, S., Stammler, K., and Dahm, T.: Automated procedure for point and kinematic source inversion at regional distances, J. Geophys. Res.-Solid, 115, B06304, https://doi.org/10.1029/2009JB006450, 2010.

Cesca, S., Rohr, A., and Dahm, T.: Discrimination of induced seismicity by full moment tensor inversion and decomposition, J. Seismol., 17, 147–163, 2013.

Cesca, S., Grigoli, F., Heimann, S., Dahm, T., Kriegerowski, M., Sobiesiak, M., Tassara, C., and Olcay, M.: The M_W 8.1 2014 Iquique, Chile, seismic sequence: a tale of foreshocks and aftershocks, Geophys. J. Int., 204, 1766–1780, 2016.

Cheloni, D., D'Agostino, N., and Selvaggi, G.: Interseismic coupling, seismic potential, and earthquake recurrence on the southern front of the Eastern Alps (NE Italy), J. Geophys. Res.-Solid, 119, 4448–4468, https://doi.org/10.1002/2014JB010954, 2014.

Cipar, J.: Teleseismic observations of the 1976 Friuli, Italy earthquake sequence, Bull. Seismol. Soc. Am., 70, 963–983, 1980.

D'Agostino, N., Avallone, A., Cheloni, D., D'anastasio, E., Mantenuto, S., and Selvaggi, G.: Active tectonics of the Adriatic region from GPS and earthquake slip vectors, J. Geophys. Res.-Solid, 113, B12413, https://doi.org/10.1029/2008JB005860, 2008.

Dahal, N. R. and Ebel, J. E.: Method for Determination of Focal Mechanisms of magnitude 2.5–4.0 Earthquakes Recorded by a Sparse Regional Seismic Network, Bull. Seismol. Soc. Am., 110, 715–726, https://doi.org/10.1785/0120190170, 2020.

Dahm, T. and Krüger, F.: Moment tensor inversion and moment tensor interpretation, in: New Manual of Seismological Observatory Practice 2 (NMSOP-2), edited by: Bohrmann, P., GFZ German Research Centre for Geosciences, Potsdam, 1–37, https://doi.org/10.2312/GFZ.NMSOP-2_IS_3.9, 2014.

Dahm, T., Becker, D., Bischoff, M., Cesca, S., Dost, B., Fritschen, R., Hainzl, S., Klose, C. D., Kühn, D., Lasocki, S., Meier, T., Ohrnberger, M., Rivalta, E., Wegler, U., and Husen, S.: Recommendation for the discrimination of human-related and natural seismicity, J. Seismol., 17, 197–202, 2013.

Dahm, T., Heimann, S., Funke, S., Wendt, S., Rappsilber, I., Bindi, D., Plenefisch, T., and Cotton, F.: Seismicity in the block mountains between Halle and Leipzig, Central Germany: centroid moment tensors, ground motion simulation, and felt intensities of two $M \approx 3$ earthquakes in 2015 and 2017, J. Seismol., 22, 985–1003, https://doi.org/10.1007/s10950-018-9746-9, 2018.

d'Amico, S., Orecchio, B., Presti, D., Gervasi, A., Zhu, L., Guerra, I., Neri, G., and Herrmann, R.: Testing the stability of moment tensor solutions for small earthquakes in the Calabro-Peloritan Arc region (southern Italy), Bollettino di Geofisica Teorica ed Applicata, 52, 283–298, https://doi.org/10.4430/bgta0009, 2011.

Deichmann, N., Baer, M., Braunmiller, J., Cornou, C., Fäh, D., Giardini, D., Gisler, M., Huber, S., Husen, S., Kästli, P., Kradolfer, U., Mai, M., Maraini, S., Oprsal, I., Schler, T., Schorlemmer, D., Wiemer, S., Wössner, J., and Wyss, A.: Earthquakes in Switzerland and surrounding regions during 2003, Eclog. Geolog. Helvet., 97, 447–458, 2004.

Deichmann, N., Baer, M., Braunmiller, J., Husen, S., Fäh, D., Giardini, D., Kästli, P., Kradolfer, U., and Wiemer, S.: Earthquakes in Switzerland and surrounding regions during 2005, Eclog. Geolog. Helvet., 99, 443–452, 2006.

Deichmann, N., Baer, M., Clinton, J., Husen, S., Fäh, D., Giardini, D., Kästli, P., Kradolfer, U., and Wiemer, S.: Earthquakes in Switzerland and surrounding regions during 2007, Swiss J. Geosci., 101, 659–667, 2008.

Deichmann, N., Clinton, J., Husen, S., Haslinger, F., Fäh, D., Giardini, D., Kästli, P., Kradolfer, U., Marschall, I., and Wiemer, S.: Earthquakes in Switzerland and surrounding regions during 2008, Swiss J. Geosci., 102, 505, https://doi.org/10.1007/s00015-009-1339-8, 2009.

Deichmann, N., Clinton, J., Husen, S., Edwards, B., Haslinger, F., Fäh, D., Giardini, D., Kästli, P., Kradolfer, U., Marschall, I., and Wiemer, S.: Earthquakes in Switzerland and surrounding regions during 2009, Swiss J. Geosci., 103, 535–549, 2010.

Deichmann, N., Clinton, J., Husen, S., Edwards, B., Haslinger, F., Fäh, D., Giardini, D., Kästli, P., Kradolfer, U., and Wiemer, S.: Earthquakes in Switzerland and surrounding regions during 2010, Swiss J. Geosci., 104, 537–547, 2011.

Deichmann, N., Clinton, J., Husen, S., Edwards, B., Haslinger, F., Fäh, D., Giardini, D., Kästli, P., Kradolfer, U., and Wiemer, S.: Earthquakes in Switzerland and surrounding regions during 2011, Swiss J. Geosci., 105, 463–476, 2012.

Delacou, B., Sue, C., Champagnac, J.-D., and Burkhard, M.: Present-day geodynamics in the bend of the western and central Alps as constrained by earthquake analysis, Geophys. J. Int., 158, 753–774, https://doi.org/10.1111/j.1365-246X.2004.02320.x, 2004.

Delouis, B.: FMNEAR: Determination of focal mechanism and first estimate of rupture directivity using near-source records and a linear distribution of point sources, Bull. Seismol. Soc. Am., 104, 1479–1500, 2014.

Department Of Earth And Environmental Sciences, Geophysical Observatory, University Of Munchen: BayernNetz [Data set], International Federation of Digital Seismograph Networks, Other/Seismic Network, https://doi.org/10.7914/SN/BW, 2001.

Diehl, T., Husen, S., Kissling, E., and Deichmann, N.: High-resolution 3-DP-wave model of the Alpine crust, Geophys. J. Int., 179, 1133–1147, 2009.

Diehl, T., Deichmann, N., Clinton, J., Husen, S., Kraft, T., Plenkers, K., Edwards, B., Cauzzi, C., Michel, C., Kästli, P., Wiemer, S., Haslinger, F., Fäh, D., Kradolfer, U., and Woessner, J.: Earthquakes in Switzerland and surrounding regions during 2012, Swiss J. Geosci., 106, 543–558, 2013.

Diehl, T., Clinton, J., Kraft, T., Husen, S., Plenkers, K., Guilhelm, A., Behr, Y., Cauzzi, C., Kästli, P., Haslinger, F., Fäh, D., Michel, C., and Wiemer, S.: Earthquakes in Switzerland and surrounding regions during 2013, Swiss J. Geosci., 107, 359–375, 2014.

Diehl, T., Deichmann, N., Clinton, J., Kästli, P., Cauzzi, C., Kraft, T., Behr, Y., Edwards, B., Guilhem, A., Korger, E., Hobiger, M., Haslinger, F., Fäh, D., and Wiemer, S.: Earthquakes in Switzerland and surrounding regions during 2014, Swiss J. Geosci., 108, 425–443, 2015.

Diehl, T., Clinton, J., Deichmann, N., Cauzzi, C., Kästli, P., Kraft, T., Molinari, I., Böse, M., Michel, C., Hobiger, M., Haslinger, F., Fäh, D., and Wiemer, S.: Earthquakes in Switzerland and surrounding regions during 2015 and 2016, Swiss J. Geosci., 111, 221–244, 2018.

Diehl, T. E. A.: Earthquakes in Switzerland and surrounding regions during 2017 and 2018 (in prep.), Swiss J. Geosci., 111, 221–244, 2020.

Di Giacomo, D., Bondár, I., Storchak, D. A., Engdahl, E. R., Bormann, P., and Harris, J.: ISC-GEM: Global Instrumental Earthquake Catalogue (1900–2009), III. Re-computed MS and mb, proxy MW, final magnitude composition and completeness assessment, Phys. Earth Planet. Inter., 239, 33–47, https://doi.org/10.1016/j.pepi.2014.06.005, 2015.

Di Giacomo, D., Engdahl, E. R., and Storchak, D. A.: The ISC-GEM Earthquake Catalogue (1904–2014): status after the Extension Project, Earth Syst. Sci. Data, 10, 1877–1899, https://doi.org/10.5194/essd-10-1877-2018, 2018.

Domingues, A., Custodio, S., and Cesca, S.: Waveform inversion of small-to-moderate earthquakes located offshore southwest Iberia, Geophys. J. Int., 192, 248–259, 2013.

Dufumier, H. and Cara, M.: On the limits of linear moment tensor inversion of surface wave spectra, Pure Appl. Geophys., 145, 235–257, 1995.

Dufumier, H. and Rivera, L.: On the resolution of the isotropic component in moment tensor inversion, Geophys. J. Int., 131, 595–606, 1997.

Dziewonski, A., Chou, T.-A., and Woodhouse, J. H.: Determination of earthquake source parameters from waveform data for studies of global and regional seismicity, J. Geophys. Res.-Solid, 86, 2825–2852, 1981.

Ekström, G., Nettles, M., and Dziewoński, A.: The global CMT project 2004–2010: Centroid-moment tensors for 13,017 earthquakes, Phys. Earth Planet. Inter., 200, 1–9, 2012.

Ester, M., Kriegel, H.-P., Sander, J., and Xu, X.: A density-based algorithm for discovering clusters in large spatial databases with noise, KDD-96 Proc., 96, 226–231, 1996.

Farr, T. G., Rosen, P. A., Caro, E., Crippen, R., Duren, R., Hensley, S., Kobrick, M., Paller, M., Rodriguez, E., Roth, L., Seal, D., Shaffer, S., Shimada, J., Umland, J., Werner, M., Oskin, M., Burbank, D., and Alsdorf, D.: The Shuttle Radar Topography Mission, Rev. Geophys., 45, RG2004, https://doi.org/10.1029/2005RG000183, 2007.

Ford, S. R., Dreger, D. S., and Walter, W. R.: Identifying isotropic events using a regional moment tensor inversion, J. Geophys. Res.-Solid, 114, B01306, https://doi.org/10.1029/2008JB005743, 2009.

Fry, B., Deschamps, F., Kissling, E., Stehly, L., and Giardini, D.: Layered azimuthal anisotropy of Rayleigh wave phase velocities in the European Alpine lithosphere inferred from ambient noise, Earth Planet. Sc. Lett., 297, 95–102, 2010.

GEOFON Data Centre: GEOFON Seismic Network, Other/Seismic Network, Deutsches GeoForschungsZentrum GFZ, https://doi.org/10.14470/TR560404, 1993.

Geological Survey – Provincia Autonoma Di Trento: Trentino Seismic Network, International Federation of Digital Seismograph Networks, Other/Seismic Network, Trento, https://doi.org/10.7914/SN/ST, 1981.

Guilhem, A., Hutchings, L., Dreger, D., and Johnson, L.: Moment tensor inversions of $M \sim 3$ earthquakes in the Geysers geothermal fields, California, J. Geophys. Res.-Solid, 119, 2121–2137, 2014.

Handy, M., Babist, J., Wagner, R., Rosenberg, C., and Konrad, M.: Decoupling and its relation to strain partitioning in continental lithosphere: insight from the Periadriatic fault system (European Alps), Geol. Soc. Lond. Spec. Publ., 243, 249–276, 2005.

Handy, M. R., Schmid, S. M., Bousquet, R., Kissling, E., and Bernoulli, D.: Reconciling plate-tectonic reconstructions of Alpine Tethys with the geological–geophysical record of spreading and subduction in the Alps, Earth-Sci. Rev., 102, 121–158, 2010.

Handy, M. R., Ustaszewski, K., and Kissling, E.: Reconstructing the Alps–Carpathians–Dinarides as a key to understanding switches in subduction polarity, slab gaps and surface motion, Int. J. Earth Sci., 104, 1–26, 2015.

Hardebeck, J. L. and Shearer, P. M.: A new method for determining first-motion focal mechanisms, Bull. Seismol. Soc. Am., 92, 2264–2276, 2002.

Heidbach, O., Custodio, C., Kingdon, A., Mariucci, M. T., Montone, P., Müller, B., Pierdominici, S., Rajabi, M., Reinecker, J., Reiter, K., Tingay, M., Williams, J., and Ziegler, M.: Stress map of the Mediterranean and Central Europe 2016, GFZ Data Services, https://doi.org/10.5880/WSM.Europe2016, 2016.

Heimann, S.: A Robust Method To Estimate Kinematic Earthquake Source Parameters, PhD thesis, Universität Hamburg, Hamburg, available at: http://ediss.sub.uni-hamburg.de/volltexte/2011/5357/pdf/Dissertation.pdf (last access: December 2020), 2011.

Heimann, S., Isken, M., Kühn, D., Sudhaus, H., Steinberg, A., Vasyura-Bathke, H., Daout, S., Cesca, S., and Dahm, T.: Grond – A probabilistic earthquake source inversion framework, https://doi.org/10.5880/GFZ.2.1.2018.003, 2018.

Heimann, S., Vasyura-Bathke, H., Sudhaus, H., Isken, M. P., Kriegerowski, M., Steinberg, A., and Dahm, T.: A Python framework for efficient use of pre-computed Green's functions in seismological and other physical forward and inverse source problems, Solid Earth, 10, 1921–1935, https://doi.org/10.5194/se-10-1921-2019, 2019.

Heit, B., Weber, M., Tilmann, F., Haberland, C., Jia, Y., and Pesaresi, D.: The Swath-D seismic network in Italy and Austria, Other/Seismic Network, GFZ Data Services, https://doi.org/10.14470/mf7562601148, 2017.

Hensch, M., Dahm, T., Ritter, J., Heimann, S., Schmidt, B., Stange, S., and Lehmann, K.: Deep low-frequency earthquakes reveal ongoing magmatic recharge beneath Laacher See Volcano (Eifel, Germany), Geophys. J. Int., 216, 2025–2036, 2019.

Hetényi, G., Molinari, I., Clinton, J., Bokelmann, G., Bondár, I., Crawford, W. C., Dessa, J.-X., Doubre, C., Friederich, W., Fuchs, F., Giardini, D., Gráczer, Z., Handy, M. R., Herak, M., Jia, Y., Kissling, E., Kopp, H., Korn, M., Margheriti, L., Meier, T., Mucciarelli, M., Paul, A., Pesaresi, D., Piromallo, C., Plenefisch, T., Plomerová, J., Ritter, J., Rümpker, G., Šipka, V., Spallarossa, D., Thomas, C., Tilmann, F., Wassermann, J., Weber, M., Wéber, Z., Wesztergom, V., Živčić, M., AlpArray Seismic Network Team, AlpArray OBS Cruise Crew, and AlpArray Working Group: The AlpArray seismic network: a large-scale European experiment to image the Alpine orogen, Surv. Geophys., 39, 1009–1033, 2018.

INGV Seismological Data Centre: Rete Sismica Nazionale (RSN), Other/Seismic Network, Istituto Nazionale di Geofisica e Vulcanologia (INGV), Italy, https://doi.org/10.13127/SD/X0FXnH7QfY, 2006.

Institut De Physique Du Globe De Paris (IPGP) and Ecole Et Observatoire Des Sciences De La Terre De Strasbourg (EOST): GEOSCOPE, French Global Network of broad band seismic stations, Institut de physique du globe de Paris (IPGP), Other/Seismic Network, Université de Paris, Paris, https://doi.org/10.18715/GEOSCOPE.G, 1982.

Institute Of Geophysics, A. O. S. O. T. C. R.: Czech Regional Seismic Network, Other/Seismic Network, International Federation of Digital Seismograph Networks, https://doi.org/10.7914/SN/CZ, 1973.

Jena, F. S. U.: Thüringer Seismologisches Netz (TSN), Other/Seismic Network, International Federation of Digital Seismograph Networks, Jena, https://doi.org/10.7914/SN/TH, 2009.

Julian, B. R., Miller, A. D., and Foulger, G.: Non-double-couple earthquakes 1. Theory, Rev. Geophys., 36, 525–549, 1998.

Kagan, Y.: 3-D rotation of double-couple earthquake sources, Geophys. J. Int., 106, 709–716, 1991.

Kästle, E. D., El-Sharkawy, A., Boschi, L., Meier, T., Rosenberg, C., Bellahsen, N., Cristiano, L., and Weidle, C.: Surface wave tomography of the Alps using ambient-noise and earthquake phase velocity measurements, J. Geophys. Res.-Solid, 123, 1770–1792, 2018.

Keiding, M., Kreemer, C., Lindholm, C., Gradmann, S., Olesen, O., and Kierulf, H.: A comparison of strain rates and seismicity for Fennoscandia: depth dependency of deformation from glacial isostatic adjustment, Geophys. J. Int., 202, 1021–1028, https://doi.org/10.1093/gji/ggv207, 2015.

Kövesligethy Radó Seismological Observatory – Geodetic And Geophysical Institute, Research Centre For Astronomy And Earth Sciences, Hungarian Academy Of Sciences (MTA CSFK GGI KRSZO): Hungarian National Seismological Network, Other/Seismic Network, Deutsches GeoForschungsZentrum GFZ, https://doi.org/10.14470/UH028726, 1992.

Křížová, D., Zahradník, J., and Kiratzi, A.: Resolvability of isotropic component in regional seismic moment tensor inversion, Bull. Seismol. Soc. Am., 103, 2460–2473, 2013.

Kühn, D., Heimann, S., Isken, M. P., Ruigrok, E., and Dost, B.: Probabilistic Moment Tensor Inversion for Hydrocarbon-Induced Seismicity in the Groningen Gas Field, The Netherlands, Part 1: Testing, Bull. Seismol. Soc. Am., 110, 2095–2111, https://doi.org/10.1785/0120200099, 2020.

Le Breton, E., Handy, M. R., Molli, G., and Ustaszewski, K.: Post-20 Ma motion of the Adriatic Plate: New constraints from surrounding orogens and implications for crust-mantle decoupling, Tectonics, 36, 3135–3154, https://doi.org/10.1002/2016TC004443, 2017.

Le Breton, E., Brune, S., Ustaszewski, K., Zahirovic, S., Seton, M., and Müller, R. D.: Kinematics and extent of the Piemont–Liguria Basin – implications for subduction processes in the Alps, Solid Earth, 12, 885–913, https://doi.org/10.5194/se-12-885-2021, 2021.

Leipzig University: SXNET Saxon Seismic Network, Other/Seismic Network, International Federation of Digital Seismograph Networks, Leipzig, https://doi.org/10.7914/SN/SX, 2001.

Lizurek, G.: Full moment tensor inversion as a practical tool in case of discrimination of tectonic and anthropogenic seismicity in Poland, Pure Appl. Geophys., 174, 197–212, 2017.

Locati, M., Rovida, A., Albini, P., and Stucchi, M.: The AHEAD portal: a gateway to European historical earthquake data, Seismolog. Res. Lett., 85, 727–734, 2014.

Lu, Y., Stehly, L., Brossier, R., Paul, A., and Group, A. W.: Imaging Alpine crust using ambient noise wave-equation tomography, Geophys. J. Int., 222, 69–85, 2020.

Marschall, I., Deichmann, N., and Marone, F.: Earthquake focal mechanisms and stress orientations in the eastern Swiss Alps, Swiss J. Geosci., 106, 79–90, 2013.

Maurer, H., Burkhard, M., Deichmann, N., and Green, A.: Active tectonism in the central Alps: contrasting stress regimes north and south of the Rhone Valley, Terra Nova, 9, 91–94, 1997.

MedNet Project Partner Institutions: Mediterranean Very Broadband Seismographic Network (MedNet), Other/Seismic Network, Istituto Nazionale di Geofisica e Vulcanologia (INGV), https://doi.org/10.13127/SD/fBBBtDtd6q, 1990.

Mendiguren, J. A.: Inversion of surface wave data in source mechanism studies, J. Geophys. Res., 82, 889–894, 1977.

Meyer, B., Lacassin, R., Brulhet, J., and Mouroux, B.: The Basel 1356 earthquake: which fault produced it?, Terra Nova, 6, 54–63, 1994.

Miller, A. D., Foulger, G., and Julian, B. R.: Non-double-couple earthquakes 2. Observations, Rev. Geophys., 36, 551–568, 1998.

Ministrstvo za okolje in prostor Agencija RS za okolje: Potresi v letu 2016, Earthquakes in 2016, ARSO POTRESI, ISSN 1318-4792, 2018.

Ministrstvo za okolje in prostor Agencija RS za okolje: Potresi v letu 2017, Earthquakes in 2017, ARSO POTRESI, ISSN 1318-4792, 2019.

Ministrstvo za okolje in prostor Agencija RS za okolje: Potresi v letu 2018, Earthquakes in 2018, ARSO POTRESI, ISSN 1318-4792, 2020.

Minson, S. E. and Dreger, D. S.: Stable inversions for complete moment tensors, Geophys. J. Int., 174, 585–592, 2008.

Mitterbauer, U., Behm, M., Brückl, E., Lippitsch, R., Guterch, A., Keller, G. R., Koslovskaya, E., Rumpfhuber, E.-M., and Šumanovac, F.: Shape and origin of the East-Alpine slab constrained by the ALPASS teleseismic model, Tectonophysics, 510, 195–206, 2011.

Molinari, I., Verbeke, J., Boschi, L., Kissling, E., and Morelli, A.: Italian and Alpine three-dimensional crustal structure imaged by ambient-noise surface-wave dispersion, Geochem. Geophy. Geosy., 16, 4405–4421, 2015.

Montone, P., Mariucci, M. T., Pondrelli, S., and Amato, A.: An improved stress map for Italy and surrounding regions (central Mediterranean), J. Geophys. Res.-Solid, 109, B10410, https://doi.org/10.1029/2003JB002703, 2004.

Moulin, A., Benedetti, L., Rizza, M., Jamšek Rupnik, P., Gosar, A., Bourles, D., Keddadouche, K., Aumaître, G., Arnold, M., Guillou, V., and Ritz, J.-F.: The Dinaric fault system: Large-scale structure, rates of slip, and Plio-Pleistocene evolution of the transpressive northeastern boundary of the Adria microplate, Tectonics, 35, 2258–2292, https://doi.org/10.1002/2016TC004188, 2016.

Nicolas, M., Bethoux, N., and Madeddu, B.: Instrumental seismicity of the Western Alps: a revised catalogue, Pure Appl. Geophys., 152, 707–731, 1998.

OGS – Istituto Nazionale Di Oceanografia E Di Geofisica Sperimentale: North-East Italy Seismic Network, Other/Seismic Network, International Federation of Digital Seismograph Networks, https://doi.org/10.7914/SN/OX, 2016.

OGS – Istituto Nazionale Di Oceanografia E Di Geofisica Sperimentale – and University Of Trieste: North-East Italy Broadband Network, Other/Seismic Network, International Federation of Digital Seismograph Networks, https://doi.org/10.7914/SN/NI, 2002.

Panza, G. F. and Saraò, A.: Monitoring volcanic and geothermal areas by full seismic moment tensor inversion: Are non-double-couple components always artefacts of modelling?, Geophys. J. Int., 143, 353–364, 2000.

Patacca, E., Scandone, P., Di Luzio, E., Cavinato, G. P., and Parotto, M.: Structural architecture of the central Apennines: Interpretation of the CROP 11 seismic profile from the Adriatic coast to the orographic divide, Tectonics, 27, TC3006, https://doi.org/10.1029/2005TC001917, 2008.

Pedregosa, F., Varoquaux, G., Gramfort, A., Michel, V., Thirion, B., Grisel, O., Blondel, M., Prettenhofer, P., Weiss, R., Dubourg, V., Vanderplas, J., Passos, A., Cournapeau, D., Brucher, M., Perrot, M., and Duchesnay, E.: Scikit-learn: Machine Learning in Python, J. Mach. Learn. Res., 12, 2825–2830, 2011.

Petersen, G. M., Cesca, S., Kriegerowski, M., and the AlpArray Working Group: Automated Quality Control for Large Seismic Networks: Implementation and Application to the AlpArray Seismic Network, Seismolog. Res. Lett., 90, 1177–1190, https://doi.org/10.1785/0220180342, 2019.

Poli, M. and Zanferrari, A.: The seismogenic source of the 1976 Friuli earthquakes: a new seismotectonic model for the Friuli area, Bollettino di Geofisica Teorica ed Applicata, 59, 463–480, https://doi.org/10.4430/bgta0209, 2018.

Pondrelli, S.: European-Mediterranean Regional Centroid-Moment Tensors Catalog (RCMT) [Data set], Istituto Nazionale di Geofisica e Vulcanologia (INGV), https://doi.org/10.13127/rcmt/euromed, 2002.

Pondrelli, S., Ekström, G., and Morelli, A.: Seismotectonic re-evaluation of the 1976 Friuli, Italy, seismic sequence, J. Seismol., 5, 73–83, 2001.

Pondrelli, S., Salimbeni, S., Ekström, G., Morelli, A., Gasperini, P., and Vannucci, G.: The Italian CMT dataset from 1977 to the present, Phys. Earth Planet. Inter., 159, 286–303, 2006.

Qorbani, E., Zigone, D., Handy, M. R., Bokelmann, G., and AlpArray-EASI working group: Crustal structures beneath the Eastern and Southern Alps from ambient noise tomography, Solid Earth, 11, 1947–1968, https://doi.org/10.5194/se-11-1947-2020, 2020.

Reiter, F., Freudenthaler, C., Hausmann, H., Ortner, H., Lenhardt, W., and Brandner, R.: Active seismotectonic deformation in front of the Dolomites indenter, Eastern Alps, Tectonics, 37, 4625–4654, 2018.

RESIF: RESIF-RLBP French Broad-band network, RESIF-RAP strong motion network and other seismic stations in metropolitan France [Data set], Other/Seismic Network, RESIF – Réseau Sismologique et géodésique Français, https://doi.org/10.15778/RESIF.FR, 1995.

RESIF: CEA/DASE broad-band permanent network in metropolitan France [Data set], Other/Seismic Network, RESIF – Réseau Sismologique et géodésique Français, https://doi.org/10.15778/RESIF.RD, 2018.

Ritsema, J. and Lay, T.: Long-period regional wave moment tensor inversion for earthquakes in the western United States, J. Geophys. Res.-Solid, 100, 9853–9864, 1995.

Rovida, A. and Locati, M.: Archive of historical earthquake data for the European-Mediterranean area, in: Perspectives on European Earthquake Engineering and Seismology, Springer, Cham, 359–369, 2015.

Schmid, S. M., Fügenschuh, B., Kissling, E., and Schuster, R.: Tectonic map and overall architecture of the Alpine orogen, Eclog. Geolog. Helvet., 97, 93–117, 2004.

Schmid, S. M., Bernoulli, D., Fügenschuh, B., Matenco, L., Schefer, S., Schuster, R., Tischler, M., and Ustaszewski, K.: The Alpine-Carpathian-Dinaridic orogenic system: correlation and evolution of tectonic units, Swiss J. Geosci., 101, 139–183, 2008.

Scognamiglio, L., Tinti, E., and Quintiliani, M.: Time Domain Moment Tensor (TDMT), Istituto Nazionale di Geofisica e Vulcanologia (INGV) [Data set], https://doi.org/10.13127/TDMT, 2006.

Scott, D. R. and Kanamori, H.: On the consistency of moment tensor source mechanisms with first-motion data, Phys. Earth Planet. Inter., 37, 97–107, 1985.

Serpelloni, E., Vannucci, G., Anderlini, L., and Bennett, R. A.: Kinematics, seismotectonics and seismic potential of the eastern sector of the European Alps from GPS and seismic deformation data, Tectonophysics, 688, 157–181, 2016.

Sileny, J. and Hofstetter, R.: Moment tensor of the 1999 Dead Sea calibration shot: Limitations in the isotropic source retrieval without a detailed earth model, Tectonophysics, 356, 157–169, 2002.

Slejko, D.: What science remains of the 1976 Friuli earthquake?, Bollettino di Geofisica Teorica ed Applicata, 59, 327–350, 2018.

Sokos, E. N. and Zahradnik, J.: ISOLA a Fortran code and a Matlab GUI to perform multiple-point source inversion of seismic data, Comput. Geosci., 34, 967–977, 2008.

Spada, M., Bianchi, I., Kissling, E., Agostinetti, N. P., and Wiemer, S.: Combining controlled-source seismology and receiver function information to derive 3-D Moho topography for Italy, Geophys. J. Int., 194, 1050–1068, https://doi.org/10.1093/gji/ggt148, 2013.

Stähler, S. C. and Sigloch, K.: Fully probabilistic seismic source inversion – Part 1: Efficient parameterisation, Solid Earth, 5, 1055–1069, https://doi.org/10.5194/se-5-1055-2014, 2014.

Sternai, P., Sue, C., Husson, L., Serpelloni, E., Becker, T. W., Willett, S. D., Faccenna, C., Di Giulio, A., Spada, G., Jolivet, L., Valla, P., Petit, C., Nocquet, J.-M., Walpersdorf, A., and Castelltort, S.: Present-day uplift of the European Alps: Evaluating mechanisms and models of their relative contributions, Earth-Sci. Rev., 190, 589–604, https://doi.org/10.1016/j.earscirev.2019.01.005, 2019.

Stich, D., Ammon, C. J., and Morales, J.: Moment tensor solutions for small and moderate earthquakes in the Ibero-Maghreb region, J. Geophys. Res.-Solid, 108, 2148, https://doi.org/10.1029/2002JB002057, 2003.

Storchak, D. A., Di Giacomo, D., Bondár, I., Engdahl, E. R., Harris, J., Lee, W. H., Villaseñor, A., and Bormann, P.: Public release of the ISC–GEM global instrumental earthquake catalogue (1900–2009), Seismolog. Res. Lett., 84, 810–815, https://doi.org/10.1785/0220130034, 2013.

Storchak, D. A., Di Giacomo, D., Engdahl, E., Harris, J., Bondár, I., Lee, W. H., Bormann, P., and Villaseñor, A.: The ISC-GEM global instrumental earthquake catalogue (1900–2009): introduction, Phys. Earth Planet. Inter., 239, 48–63, https://doi.org/10.1016/j.pepi.2014.06.009, 2015.

Stucchi, M., Rovida, A., Capera, A. G., Alexandre, P., Camelbeeck, T., Demircioglu, M., Gasperini, P., Kouskouna, V., Musson, R., Radulian, M., Sesetyan, K., Vilanova, S., Baumont, D., Bungum, H., Fäh, D., Lenhardt, W., Makropoulos, K., Martinez Solares, J., Scotti, O., Živčić, M., Albini, P., Batllo, J., Papaioannou, C., Tatevossian, R., Locati, M., Meletti, C., Viganò, D., and Giardini, D.: The SHARE European earthquake catalogue (SHEEC) 1000–1899, J. Seismol., 17, 523–544, 2013.

Sue, C., Martinod, J., Tricart, P., Thouvenot, F., Gamond, J.-F., Fréchet, J., Marinier, D., Glot, J.-P., and Grasso, J.-R.: Active deformation in the inner western Alps inferred from comparison between 1972 – classical and 1996 – GPS geodetic surveys, Tectonophysics, 320, 17–29, 2000.

Swiss Seismological Service – SED – At ETH Zurich: National Seismic Networks of Switzerland, Other/Seismic Network, ETH Zürich, Zurich, https://doi.org/10.12686/sed/networks/ch, 1983.

University Of Genova: Regional Seismic Network of North Western Italy, Other/Seismic Network, International Federation of Digital Seismograph Networks, Genova, https://doi.org/10.7914/SN/GU, 1967.

University Of Trieste: Friuli Venezia Giulia Accelerometric Network, Other/Seismic Network, International Federation of Digital Seismograph Networks, Trieste, https://doi.org/10.7914/SN/RF, 1993.

Valentine, A. P. and Trampert, J.: Assessing the uncertainties on seismic source parameters: Towards realistic error estimates for centroid-moment-tensor determinations, Phys. Earth Planet. Inter., 210, 36–49, 2012.

Van Hinsbergen, D. J., Torsvik, T. H., Schmid, S. M., Maţenco, L. C., Maffione, M., Vissers, R. L., Gürer, D., and Spakman, W.: Orogenic architecture of the Mediterranean region and kinematic reconstruction of its tectonic evolution since the Triassic, Gondwana Res., 81, 79–229, https://doi.org/10.1016/j.gr.2019.07.009, 2020.

Vavryčuk, V.: Moment tensor decompositions revisited, J. Seismol., 19, 231–252, 2015.

Viganò, A., Bressan, G., Ranalli, G., and Martin, S.: Focal mechanism inversion in the Giudicarie–Lessini seismotectonic region (Southern Alps, Italy): insights on tectonic stress and strain, Tectonophysics, 460, 106–115, 2008.

Wang, R.: A simple orthonormalization method for stable and efficient computation of Green's functions, Bull. Seismol. Soc. Am., 89, 733–741, 1991.

Weber, J., Vrabec, M., Pavlovčič-Prešeren, P., Dixon, T., Jiang, Y., and Stopar, B.: GPS-derived motion of the Adriatic microplate from Istria Peninsula and Po Plain sites, and geodynamic implications, Tectonophysics, 483, 214–222, https://doi.org/10.1016/j.tecto.2009.09.001, 2010.

Wessel, P., Smith, W. H., Scharroo, R., Luis, J., and Wobbe, F.: Generic mapping tools: improved version released, Eos Trans. Am. Geophys. Union, 94, 409–410, 2013.

Zahradník, J. and Sokos, E.: Fitting waveform envelopes to derive focal mechanisms of moderate earthquakes, Seismolog. Res. Lett., 89, 1137–1145, 2018.

ZAMG – Zentralanstalt Für Meterologie Und Geodynamik: Austrian Seismic Network, Other/Seismic Network, International Federation of Digital Seismograph Networks, https://doi.org/10.7914/SN/OE, 1987.

CHAPTER 7

Clusty, the waveform-based network similarity clustering toolbox: concept and application to image complex faulting offshore Zakynthos (Greece)

Petersen, G.M., Niemz, P., Cesca, S., Mouslopoulou, V. and Bocchini, G.M. (2021)

Published in Geophysical Journal International, vol. 224, issue 3, pp. 2044-2059.
https://doi.org/10.1093/gji/ggaa568

The supplementary material for this publication can be downloaded at https://doi.org/10.1093/gji/ggaa568.

Geophysical Journal International

Geophys. J. Int. (2021) **224,** 2044–2059
doi: 10.1093/gji/ggaa568
Advance Access publication 2020 November 25
GJI Seismology

Clusty, the waveform-based network similarity clustering toolbox: concept and application to image complex faulting offshore Zakynthos (Greece)

G.M. Petersen,[1,2] P. Niemz ,[1,2] S. Cesca,[1] V. Mouslopoulou[3] and G.M. Bocchini [4]

[1] *GFZ German Research Centre for Geosciences, Potsdam, Germany. E-mail: gesap@gfz-potsdam.de*
[2] *Institute of Geosciences, University of Potsdam, Potsdam, Germany*
[3] *National Observatory of Athens, Institute of Geodynamics, Athens* 11810, *Greece*
[4] *Ruhr University of Bochum, Institute of Geology, Mineralogy and Geophysics, Germany*

Accepted 2020 November 23. Received 2020 November 10; in original form 2020 July 30

SUMMARY

Clusty is a new open source toolbox dedicated to earthquake clustering based on waveforms recorded across a network of seismic stations. Its main application is the study of active faults and the detection and characterization of faults and fault networks. By using a density-based clustering approach, earthquakes pertaining to a common fault can be recognized even over long fault segments, and the first-order geometry and extent of active faults can be inferred. Clusty implements multiple techniques to compute a waveform based network similarity from maximum cross-correlation coefficients at multiple stations. The clustering procedure is designed to be transparent and parameters can be easily tuned. It is supported by a number of analysis visualization tools which help to assess the homogeneity within each cluster and the differences among distinct clusters. The toolbox returns graphical representations of the results. A list of representative events and stacked waveforms facilitate further analyses like moment tensor inversion. Results obtained in various frequency bands can be combined to account for large magnitude ranges. Thanks to the simple configuration, the toolbox is easily adaptable to new data sets and to large magnitude ranges. To show the potential of our new toolbox, we apply Clusty to the aftershock sequence of the M_w 6.9 25 October 2018 Zakynthos (Greece) Earthquake. Thanks to the complex tectonic setting at the western termination of the Hellenic Subduction System where multiple faults and faulting styles operate simultaneously, the Zakynthos data set provides an ideal case-study for our clustering analysis toolbox. Our results support the activation of several faults and provide insight into the geometry of faults or fault segments. We identify two large thrust faulting clusters in the vicinity of the main shock and multiple strike-slip clusters to the east, west and south of these clusters. Despite its location within the largest thrust cluster, the main shock does not show a high waveform similarity to any of the clusters. This is consistent with the results of other studies suggesting a complex failure mechanism for the main shock. We propose the existence of conjugated strike-slip faults in the south of the study area. Our waveform similarity based clustering toolbox is able to reveal distinct event clusters which cannot be discriminated based on locations and/or timing only. Additionally, the clustering results allows distinction between fault and auxiliary planes of focal mechanisms and to associate them to known active faults.

Key words: Persistence, memory, correlations, clustering; Seismicity and tectonics; Fractures, faults, and high strain deformation zones.

1 INTRODUCTION

The world-wide increasing number of seismic stations, even deployed in areas of moderate seismicity, significantly lowers earthquake detection thresholds. This enables seismologists to study spatial and temporal seismicity patterns in great detail. In general, earthquakes occur along pre-existing faults. Both, the extent and the stress state of seismogenic faults are of interest for structural studies and for seismic hazard assessment at local, regional or global scale. The association of seismic events to faults is a major but also challenging task. Depending on the location of active faults, fault identification may involve field investigations (i.e. mapping, trenching, etc.), aerial investigations (analysis of satellite images or air-born lidar) or seismic-reflection/bathymetric data. Following large-magnitude earthquakes ($M_w > 6$), the geometry of the fault associated with the main rupture, as well as its slip distribution, is often estimated using seismological and geodetic tools (e.g. Koper *et al.* 2011; Yokota *et al.* 2011; Grandin *et al.* 2015; Cirella *et al.* 2020).

Moment tensor inversion represents a powerful tool to identify earthquake faulting mechanisms. Focal mechanisms obtained for seismic sequences are often used to obtain insight into the faulting style and the extent of an active fault (e.g. Örgülü & Aktar 2001; Serpetsidaki *et al.* 2010; Asano *et al.* 2011; Herrmann *et al.* 2011) or the geometry of multiple faults (e.g. Cesca *et al.* 2017). Although moment tensor inversion provides valuable insights, it has several limitations that complicate the identification of active faults. First, robust moment tensor inversions require a detailed knowledge of velocity structures and station instrumentation. Furthermore, the quality of moment tensor solutions strongly depends on the radiated frequencies: for lower magnitude events moment tensor inversion is often not feasible. In these cases, the signal to noise ratio is only sufficient at higher frequencies which cannot be modelled using simple 1-D velocity models. Finally, the causative fault plane cannot be distinguished from the auxiliary plane of the moment tensor (MT) without additional geological (e.g. fault geometry) or geophysical constraints (e.g. GPS displacements or aftershock distributions).

The clustering of earthquakes into groups of similar events is another approach to analyse the observed seismicity regarding underlying seismogenic processes. The clustering analysis can be based on various parameters such as: (1) spatial and/or temporal distributions (e.g. Frohlich 1987; Shearer *et al.* 2005; Ansari *et al.* 2009; Ouillon & Sornette 2011; Mouslopoulou & Hristopulos 2011; Mesimeri *et al.* 2019; Czecze & Bondár 2019); (2) the smallest rotation between moment tensors (e.g. Cesca 2020); (3) *P* and *S* polarities (e.g. Shelly *et al.* 2016) or (4) waveform similarities, as for example in Tsujiura (1983), Maurer & Deichmann (1995), Shearer *et al.* (2003), Barani *et al.* (2007), Trugman & Shearer (2017), Ruscic *et al.* (2019), Abramenkov *et al.* (2020) and in this study.

The clustering based on waveform similarity favours fault mapping by considering locations and mechanisms, since waveforms are inherently sensitive to both. Waveform similarity is generally assessed by cross-correlating waveforms of earthquakes at one or multiple stations. Very high waveform similarities (i.e. >0.9–0.95) are attributed to so-called repeaters (e.g. Geller & Mueller 1980; Igarashi *et al.* 2003; Baisch *et al.* 2008; Han *et al.* 2014). According to Geller & Mueller (1980) repeaters are located at distances smaller than a quarter of the dominant wavelength, however, also larger spatial separation was reported (e.g. Arrowsmith & Eisner 2006). Similar waveforms, observed at multiple stations, imply similar focal mechanisms and travel paths (locations and depths, e.g. Maurer & Deichmann 1995). Thus, the identification of clusters of similar events can shed light on the fault geometry and on the faulting style. In favourable conditions, waveform similarity studies can help to identify faults and map their geometries (e.g. Tsujiura 1983; Maurer & Deichmann 1995; Shearer *et al.* 2003). The waveform similarity based clustering approach is independent from the uncertainty of the hypocentral locations, therefore it can be applied even when hypocentral locations are poorly constraint. Only at a later stage of this study, when fault planes are inferred from the clusters, the location uncertainties are considered. Waveform similarity is also used to identify groups of events for relative relocation methods (e.g. Shearer *et al.* 2005; Trugman & Shearer 2017). High waveform similarities among a small magnitude foreshock or afterhock with a larger main shock with a known focal mechanism can be used to infer a similar mechanism for the weaker event. Such analyses can also be used for a more advanced declustering of a catalogue, not only relying on occurrence times (Barani *et al.* 2007), as well as for determining event pairs for an empirical green's function analysis.

Here we use a density-based clustering approach, which allows grouping earthquakes with a wide range of magnitudes, locations and focal mechanisms. End members of a density-cluster are not required to be as similar as neighbouring events, if they are connected via multiple events with gradually changing locations or mechanisms. Consequently, we are able to assign individual earthquakes assumed to be produced along an elongated fault into a single cluster.

Here, we introduce a new open-source, user-friendly and highly adaptable waveform clustering toolbox, named *Clusty*. The toolbox allows correlating and clustering hundreds to few thousands of events recorded by a network of stations based on what we refer to as the *network similarity* of the event pairs. We implemented different approaches to combine the waveform similarities computed for multiple stations across a network, allowing a comparison of the clustering methods and their results. In the development of the code we put emphasis not only on computational efficiency and the stability of results, but also on a broad range of analysis and plotting tools. Apart from the resulting catalogue of clustered events and accompanying plots, Clusty provides a list of representative events, i.e. one event for each cluster that is most similar to the rest of the cluster. The representative events can be used to perform moment tensor inversions aiming for a representative focal mechanism for each cluster.

In this study we apply the clustering toolbox to the aftershock sequence of the 25 October 2018 M_w 6.9 Zakynthos (Greece) earthquake (Chousianitis & Konca 2019; Cirella *et al.* 2020; Ganas *et al.* 2020; Karakostas *et al.* 2020; Mouslopoulou *et al.* 2020; Sokos *et al.* 2020). The data set includes >2300 events with $M \geq 2.8$ recorded at 33 stations from 25/10/2018 to 14/11/2019. The catalogue is available in Mouslopoulou *et al.* (2020). Zakynthos is located in the proximity of the western termination of the Hellenic subduction zone. The region is known for its high seismic activity and a great variety of faulting mechanisms (Mouslopoulou *et al.* 2020). Serpetsidaki *et al.* (2010) studied another seismic sequence offshore Zakynthos in April 2006 and emphasized the importance of the identification of active faults for regional seismic hazard assessment. Our waveform-based clustering analysis provides a better understanding of the geometries and kinematics of the faults involved in the 2018–2019 aftershock sequence. Further, we associate moment tensors inverted for representative events to the individual clusters. The identification of different waveforms excited by spatially clustered earthquakes provides evidence for the presence of various faulting styles on neighbouring faults, an outcome that is in agreement with the local geology (Mouslopoulou *et al.* 2020) and the regional stress field (Konstantinou *et al.* 2017).

We use the Zakynthos application to assess the stability of the clustering results, using different clustering settings, frequency ranges and discuss limits and opportunities of the toolbox. In Section 2, we describe the work-flow of the clustering toolbox Clusty. We applied our toolbox to the Zakynthos Earthquake aftershock case study and present the results of the clustering analysis in Section 3. We discuss both, the methods and the application with respect to the clustering results, inferred fault geometries and methodological limitations in Section 4.

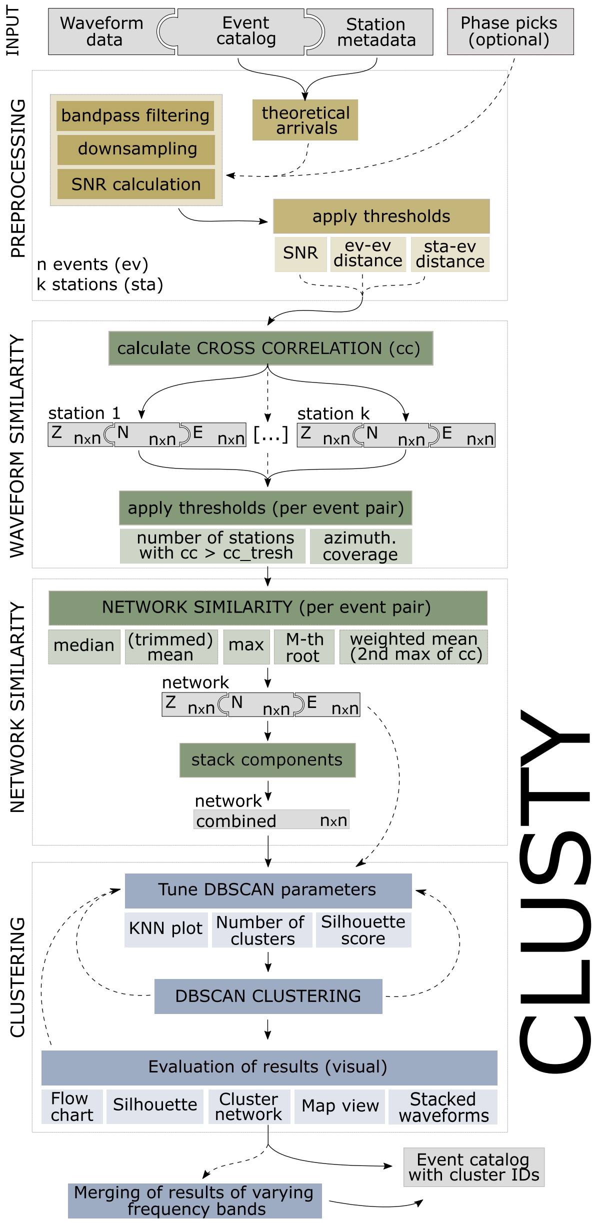

Figure 1. Schematic workflow diagram for the waveform-based network similarity clustering toolbox *Clusty*.

2 METHODOLOGY: THE CLUSTY NETWORK SIMILARITY CLUSTERING TOOLBOX

Clusty is a flexible, efficient and user-friendly *python* toolbox dedicated to seismic cluster analysis based on waveform similarity across a network of stations. It is based on the seismological *python* library Pyrocko (Heimann *et al.* 2017) and is running on Linux systems including desktop and server environments.

The general workflow is sketched in Fig. 1. As input Clusty requires an earthquake catalogue, waveform data and station metadata. If phase picks are not available, it is possible to compute theoretical arrival times using a chosen 1-D velocity model and *cake*, a tool implemented in *Pyrocko* to solve ray theory problems for layered earth models (Heimann *et al.* 2017). The user can either select a fixed time window for each phase or use our empirical relations (i.e. for surface waves: $[t_{\mathrm{onset}} - 10s,\ t_{\mathrm{onset}} + (3/f_{\mathrm{min}}) + 10s]$ and for body waves: *P*: $[t_P - 2,\ t_S]$, S: $[t_S - 2,\ 1.5(t_S - t_P)]$). Clusty preprocesses the waveforms, that is downsampling and bandpass filtering, and applies thresholds for inter-event distances (either epicentral (in this study) or hypocentral), event-to-station distances and signal-to-noise ratio (SNR). While none of these thresholds are strictly required, we recommend using them for computational efficiency. Distance-based thresholds should be set conservatively to avoid rejecting event pairs or station-event-pairs due to mislocated events. A minimum station–event distance is recommended as the clustering method assumes a station–event distance that is large compared to the event–event distance.

The workflow can be quickly adjusted to three channel or single channel data. For all event pairs passing the thresholds, Clusty computes the maximum cross-correlation coefficient (*cc*) at each station and for each component. For computational efficiency, this step runs in parallel on a user-defined number of cores on the CPU. Only event-pairs, that exceed an additional *cc* threshold (e.g. >0.7) at a minimum number of stations (e.g. >5), with a minimum azimuthal station coverage (e.g. $>60^\circ$) are considered in the subsequent analysis. However, it is important to notice that once these conditions are satisfied, all stations which passed the primary SNR and distance thresholds (and not only those passing the *cc* threshold) will be considered for the network similarity computation to assure that the statistics are not biased. The *cc* threshold does not represent a measure of the minimum similarity among events in the later applied clustering process. It only assures higher computational efficiency.

By applying the above mentioned thresholds, we reduced the number of calculated cross-correlations in our test data set from more than 378 million (45 stations, 3 components, 2367 events) to about 5 million. The pre-processing of the waveforms and the calculation of the *cc* values is the computationally most expensive step within Clusty. In the frequency band of 0.05–0.20 Hz (allowing a downsampling to 10 Hz) it takes about 4 hr on a cluster using 16 cores. All further steps within Clusty require only a few minutes on a single core. A memory saving option is available, so that Clusty can also be used on personal computers.

The *cc* values of the event pairs at each station are combined to a network similarity for each component using one of the methods described below. Subsequently, the components can be combined or analysed individually, for example to compare the results obtained from horizontal and vertical components. The network similarity matrix is then used as input for the clustering algorithm DBSCAN (Ester *et al.* 1996, see Section 2.2). The choice of appropriate clustering parameters is often difficult and sometimes subjective. To overcome these difficulties we implemented tools for testing various sets of clustering parameters and compare them using multiple analysis plots (see Section 2.3).

To analyse earthquakes with a broad range of magnitudes, the entire workflow can be repeated using different frequency bands. The resulting cluster labels can be harmonized with respect to a defined reference frequency band to create a joint cluster result catalogue. The user can run *Clusty* in one flow, but tuning the settings of the network similarity computation and the clustering parameters is a crucial point in this analysis. Therefore all steps can be run separately and repeated (e.g. computation of *cc*, network similarity, clustering, plotting of the results).

Settings for the toolbox like frequency filters, downsampling, SNR thresholds to retain or reject events as well as the choice of methods to compute the network similarity can be defined in a configuration file. We provide an example configuration file in the git repository including information on the settings used for this study (https://git.pyrocko.org/clusty/clusty, last accessed October 2020). Clusty returns several figures to evaluate and present the results together with the output from the cluster analysis (i.e. clustering matrices and event-cluster identification). In addition, Clusty can provide stacked waveforms for each cluster as well as a list of representative events for subsequent studies.

2.1 Network similarity computation

The network similarity *nsim* of two events with index i and j (event pair ij) across a network of stations s with components c can be computed based on the maximum cross-correlation coefficients $cc_{ij,c,s}$ using a variety of methods implemented within the clustering toolbox to allow an easy comparison of different techniques. The network similarity of each event-pair is a value between 0 and 1, with 1 being the highest correlation.

For each pair of events i, j the maximum, the mean or the median of the $cc_{ij,c,s}$ value of all stations s (separate components c) can, among other methods, be used as a measure for network similarity. These three methods are computationally very efficient. However, the mean of the *cc* values of all stations is generally prone to outliers especially when calculated from a small sample of events, while the maximum of the *cc* values can be distorted in case of highly correlated monotonous noise or band-limited stations, for example due to high near-surface attenuation (Aster & Scott 1993). Moreover, the maximum-method is based on the *cc* value of a single station and cannot separate two different mechanisms which may radiate similar, highly correlated waveforms in the particular direction of the station. Therefore Aster & Scott (1993) suggest using the median of the *cc* values of all stations as best practice to determine the degree of similarity between two events. Consequently, the maximum value should only be used for testing, to adjust time windows and select appropriate bandpass filters or in cases where only single stations close to the epicentre have a sufficient SNR (Ruscic *et al.* 2019). For smaller magnitudes only the closest stations are expected to record an event, therefore it helps to use the mean or median of those stations that comply with the given SNR threshold.

For the same reason Maurer & Deichmann (1995) introduced an asymmetrically trimmed mean for the computation of the network similarity $nsim_{ij,c}$ across a total number of M stations: For each event pair the lowest k per cent of the *cc* values are removed before the mean is computed:

$$nsim_{ij,c} = \frac{1}{M - kM} \sum_{s=1}^{M-kM} cc_{ij,c,s}, \quad (1)$$

where $cc_{ij,c,s}$ is sorted by descending *cc* value. Lower *cc* values between events at some stations do not necessarily imply weaker correlation of the events in regard to mechanism and location but can also be caused by other influences, such as variable site effects or noise conditions (Akuhara & Mochizuki 2014).

The network similarity of an event pair can also be computed as a weighted sum of the *cc* values at all stations. The weights $w_{ij,c,s}$ are the absolute differences between the first and the second maximum of the according cross-correlation function (Shelly *et al.* 2016):

$$nsim_{ij,c} = \sum_{s=1}^{M} cc_{ij,c,s}\ w_{ij,c,s}. \quad (2)$$

The use of a weighted sum limits the influence of poorly correlated records from distant or noisy stations and stabilizes the computation. However, we recommend to use a threshold for a required *cc* value at a minimum number of stations. Further, the resulting weights should be analysed along with the network similarity to avoid that the result is dominated by few stations only.

Another approach to combine the *cc* values of all stations is a composite correlation measure computed as the Mth root of the product of the *cc* values (Stuermer *et al.* 2011):

$$nsim_{ij,c} = [\prod_{s=1}^{M} (cc_{ij,c,s})]^{-M}. \quad (3)$$

Stuermer *et al.* (2011) combined P and S *cc* values extracted from the same single component trace in the product. When using three component data, we first compute the Mth root of the product for each component c separately, and then combine the obtained network similarities in a consecutive step.

The network similarity matrices $nsim_{ij,c}$ are computed for the different components c (e.g. Z, N and E) separately and subsequently combined as a weighted sum:

$$nsim_{ij} = \sum_{c=1}^{C} nsim_{ij,c}\ \omega_c. \quad (4)$$

The weighting of the components ω_c is defined in the configuration file. A component-based weighting allows compensating site-effects, which can lead to complex horizontal traces. The weighting can also compensate for variations in waveforms originating from different mechanisms that affect horizontal and vertical components differently. By comparing the results of independent phases (e.g. P and S or Love and Rayleigh) and components (i.e. Z, N and E) one can learn about the sensitivity of the waveforms in regard to different faulting types.

2.2 Event clustering

For the clustering algorithm input, the network similarity matrix (with 1 being the highest correlation) is converted into a distance matrix (with 0 corresponding to identical events). To avoid confusion with the spatial distance we hereafter refer to it as the similarity-distance. At the current version of the clustering toolbox, the density-based DBSCAN algorithm (Ester *et al.* 1996), as implemented in the python package *scikit-learn* (Pedregosa *et al.* 2011), is used for clustering. Other clustering algorithms, such as OPTICS (Ankerst *et al.* 1999) or k-means (Lloyd 1982) can be added by the user depending on the clustering targets.

Clusters derived using the DBSCAN algorithm can have any shape and the number of clusters is not predefined. Further, the algorithm allows for unclustered events (a noise class). Following the definitions of Ester *et al.* (1996), events belonging to one cluster are either core events or border events. Core events have at least a minimum number of neighbouring events (*MinPts*) within the similarity-distance *Eps*. Events at the border of the cluster (border events) are connected to at least one core point, but have less then *MinPts* neighbouring events within the similarity-distance *Eps*. Clusters are formed based on the concept of density reachability. An event i is considered directly density-reachable from a core event j, if it is within the similarity-distance *Eps*. Further the events i and j are density-connected if they are density-reachable through one or more density-connected core events.

The DBSCAN clustering procedure starts with the selection of an arbitrary event of the data set. All events that are density-reachable from this very first event (with respect to *Eps* and *MinPts*) are retrieved. A cluster is only formed if there is at least one core event. If not, DBSCAN visits the next point of the database. This process is continued until all points have been processed (Ester *et al.* 1996). Events not lying within similarity-distance *Eps* of any other event are assigned to a noise class (unclustered). *Eps* and *MinPts* need to be tuned by the user according to the data set.

2.3 Tuning of the clustering parameters and graphical analysis of clustering results

Our clustering toolbox provides several analysis plots that facilitate the tuning of the clustering parameters and the evaluation of the stability of the clusters. Further, these plots provide detailed insight into the clustering results. The plotting tools can also be used to analyse, compare and choose multiple target frequency bands to include surface waves for larger, distant events and body waves for smaller, local events. The graphical output is generated using GMT (Wessel *et al.* 2013) and the python plotting packages *matplotlib* (Hunter 2007) and *plotly* (Plotly Technologies Inc. 2015). The plots presented in this section illustrate the analysis that was performed to obtain optimal clustering settings and stable results for the application to the aftershock sequence of the 25 October 2018 Zakynthos M_w 6.9 earthquake in Greece.

Clusty allows the user to run the entire clustering process for different DBSCAN parameters (*Eps* and *MinPts*) in parallel to compare the results. As mentioned above, the input similarity-distance matrix for DBSCAN is computed from the cross-correlations of waveforms. Therefore the similarity-distance radius (*Eps*) is directly related to the underlying physical process and a rough first estimate of *Eps* can be made based on expected similarities. However, the expected *cc* values, and consequently, the optimal *Eps* value may vary depending on the length of the considered waveform time windows, the frequency content as well as on site and noise conditions at the stations. An *Eps* of 0.1 implies that a pair of connected events has at least a network similarity of 0.9. Depending on the chosen method for the network similarity computation, waveform cross-correlation values at single stations can be smaller if other stations with higher values compensate for it. *Eps* needs to be adjusted to the purpose of the clustering. Using a small *Eps* value allows finding very similar events or repeaters. However, in this case other events are omitted, which would still be considered similar when clustering is performed using a higher *Eps* for fault identification and tracing.

Ester *et al.* (1996) suggested a *k*-nearest neighbour (*k*-NN) plot (Fig. 2a) to choose the *Eps* parameter. Therein, the average similarity-distance of every sample to its *k* nearest neighbours (here corresponding to the *MinPts* parameter) is calculated and plotted in an ascending order to visually find a 'knee', that corresponds to the optimal *Eps* value for the given data set (Ester *et al.* 1996). In Fig. 2(a), the sorted similarity-distances of the *k*th nearest neighbours are shown for *MinPts* values from 5 to 8. For *MinPts* 5, significant gradient changes are seen for *Eps* values of 0.16 and 0.21 (red arrows in Fig. 2a). For increased *MinPts* values these gradient changes are observed for larger *Eps* values. However, we prefer smaller *Eps* values, because otherwise we observe rather unstable and heterogeneous clusters in our application (Fig. 2b and following paragraphs). Therefore, we suggest three additional metrics to constrain a range of appropriate DBSCAN clustering parameters for fault tracing purposes: (1) the silhouette score, (2) the number of clusters and (3) the total number of clustered events. These metrics reflect the ensemble of all clusters, while the influence of different parameter sets onto single clusters can be analysed using more sophisticated analysis tools, introduced hereafter. Fig. 2(b) shows these metrics for *Eps* values between 0.01 and 0.30 and *MinPtS* values of 5 and 8. The trends of the three curves are similar for both *MinPts* values. The silhouette score is a measure of the homogeneity of all clusters (Rousseeuw 1987), here neglecting the unclustered events. It is the mean of the silhouette coefficients of all clustered events. The silhouette coefficient of a single event expresses how similar that event is compared to the other events within the same cluster and compared to the events of the nearest other cluster. The silhouette coefficient is defined as:

$$s = (\overline{icd} - \overline{ncd})/max(\overline{icd}, \overline{ncd}), \tag{5}$$

where $\overline{ncd}$ is the mean nearest cluster similarity-distance for each event and $\overline{icd}$ is the mean intracluster similarity-distance (Rousseeuw 1987). The silhouette coefficient ranges between –1 and 1, where 1 corresponds to a cluster of identical events, that are completely different from events belonging to other clusters. Coefficients between –1 and 0 indicate that the similarity-distance of an event with respect to events of other clusters is smaller than the average similarity-distance to events of its own cluster. We use the implementation of *scikit-learn* (Pedregosa *et al.* 2011) to calculate the silhouette coefficients. The silhouette score in Fig. 2(b) is largest at very low *Eps* values, when only highly similar earthquakes are assigned to one or few clusters. Thereafter, the silhouette score decreases with increasing *Eps* value, so in fact we are visually searching for local maxima or changes in the gradient of the curve, but not for the global maximum. The shift between the two lines for *MinPts* 5 and 8 (grey and black, respectively) in Fig. 2(b) is the result of an increased number of earthquakes required per cluster for higher *MinPts* values. The first cluster can therefore only be found for a slightly higher *Eps* value in case of a higher *MinPts* value. In both curves a local maximum is seen at an *Eps* value of 0.06. Several minor changes in the gradient are observed between 0.10 and 0.14, followed by a major gradient change at 0.15 (black arrow in Fig. 2b). Below *Eps* 0.15, the silhouette score is relatively stable on a low level. By decreasing the *Eps* only by 0.01 or 0.02 we obtain significantly higher silhouette scores, thus more homogeneous clusters (Fig. 2b), a prerequisite for a reliable identification of active faults. The total number of clusters and the number of clustered events decreases with increasing *MinPts*, resulting from a higher required number of earthquakes to form a cluster. The number of clustered events increases rapidly until an *Eps* value of 0.13 (*MinPts* 5, green arrow in Fig. 2b) and 0.16 (*MinPts* 8) and shows a smaller gradient afterwards. Local maxima of the number of clusters are found for 0.10 and 0.13 (blue arrow in Fig. 2b) for *MinPts* 5 and 0.13 for *MinPts* 8. For larger *Eps* values single clusters collapse into larger, more heterogeneous ones, as can be seen in the flow diagram (Fig. 3).

The flow diagram helps to assess the stability of the clustering results. It allows a comprehensive comparison of clustering results obtained using different clustering parameters (Fig. 3) or waveform frequency filters (Fig. S1). Fig. 3 shows the flow diagram of clustering results obtained for an *Eps* range of 0.06–0.30. The width of the connecting bands between two clusters obtained with two sets of parameters is proportional to the number of common events. In this way, the diagram reflects conserved quantities as well as the splitting or merging of clusters (Fig. 3). In Fig. 3 the small clusters in the lower part of the diagram remain stable over a wide range of *Eps* values. The two largest and distinct green and light blue (3 and 5) clusters collapse into one heterogeneous cluster when *Eps*

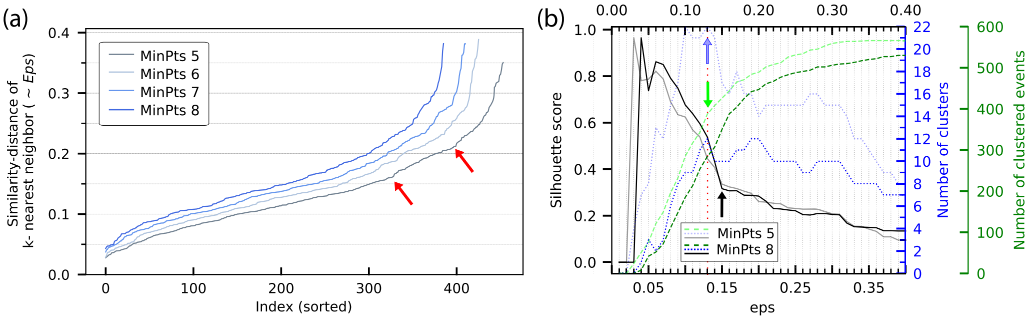

Figure 2. Selection of the DBSCAN clustering parameters. (a) The *k*-nearest neighbour plot (here for *MinPts* of 5–8) helps selecting *Eps* by identify a 'knee' (gradient changes, red arrows). (b) Silhouette score (black solid lines), number of clusters (blue dotted lines) and total number of clustered events (green dashed lines) for *Eps* values between 0.01 and 0.4 and *MinPts* values of 5 (lighter colours) and 8 (darker colours). Arrows mark features discussed in the text for *MinPts* 5. Blue: max. number of clusters, green: gradient change in number of clustered events, black: gradient change in silhouette score. Red dotted line indicates the *Eps* value used in the application to the Zakynthos data set (0.13).

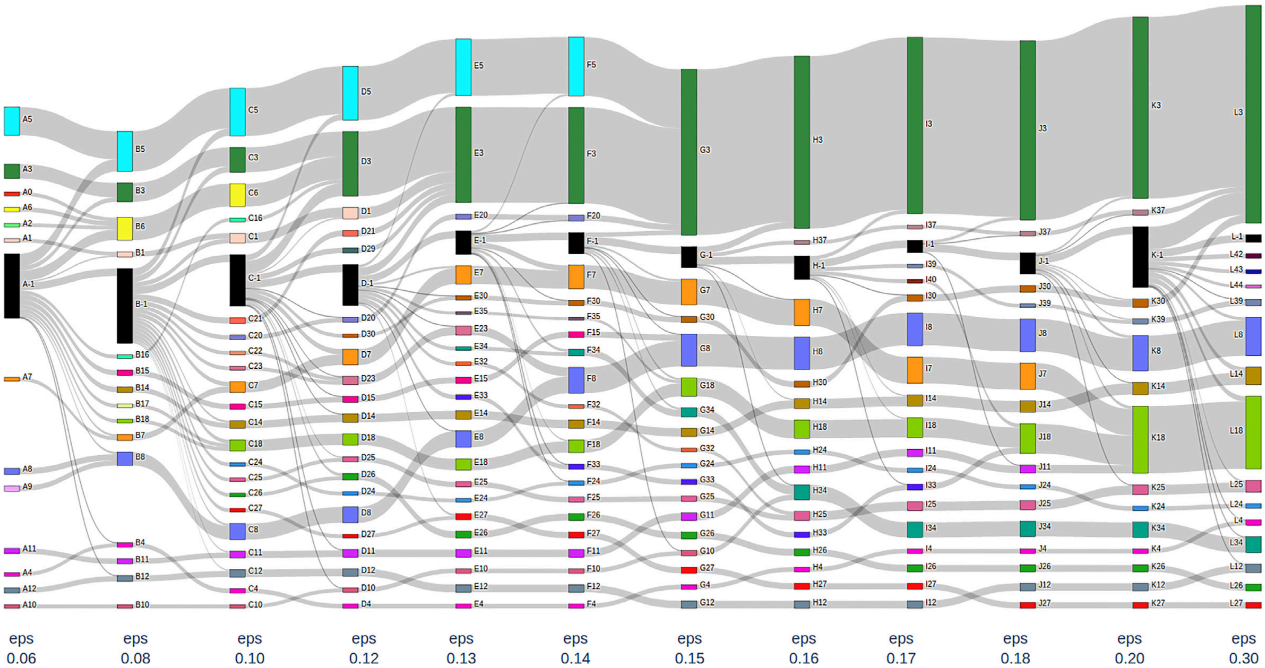

Figure 3. Screenshot of the interactive flow diagram for a comparison of clustering results obtained with *Eps* values between 0.06 and 0.30, *MinPts* 5 (0.05–0.2 Hz). Black represents the noise cluster (here reduced in size to emphasize the clustered events). Same colours represent the same cluster. The size of the clusters varies depending on the required similarity (Eps value), the block size is proportional to the number of events within the cluster. The grey bands connect clusters obtained with different clustering parameters which share at least one event. The thickness of the grey bands is proportional to the number of shared events. This representation allows evaluating the stability of cluster results when changing clustering parameters.

increases from 0.14 to 0.15. For *Eps* values as small as 0.06 only few small clusters are found. For *Eps* = 0.30 large clusters with clearly distinguishable event types (when using a smaller *Eps*) collapse into one cluster.

When using multiple clustering settings, the resulting clusters as well as their labels will differ. Therefore, we implemented a function that provides harmonized cluster labels across the different clustering results. The harmonization of labels can lead to a discontinuous cluster label numbering but assures that labels are persistent.

Finally, we introduce two more visualization tools to analyse the clustering parameters and control the clustering results: the silhouette coefficient plot (Figs 4a–c) and the event-connectivity plot (Figs 4d–f). Both depict the homogeneity and the connectivity within each cluster or among different clusters, respectively.

The silhouette coefficient plot (Figs 4a–c) shows how similar each event is to the events in its own cluster compared to the events of the most similar cluster (Rousseeuw 1987). Each coloured block represents the events of one cluster, sorted by their silhouette coefficient. The silhouette plot helps to find appropriate *Eps* and *MinPts* settings and the optimal number of clusters by evaluating the similarity of events within each cluster. The connectivity plot (Figs 4d–f) provides a complementary visualization of the similarity between events as well as between clusters. Within this force-directed projection (Fruchterman & Reingold 1991) the relative distance between events or clusters of events represent their similarity. When choosing *Eps*=0.06 (Figs 4a and d) only a few, very similar events are clustered. However, the visualization of the connectivity (Fig. 4d) shows that there are many more clusters of similar events. This

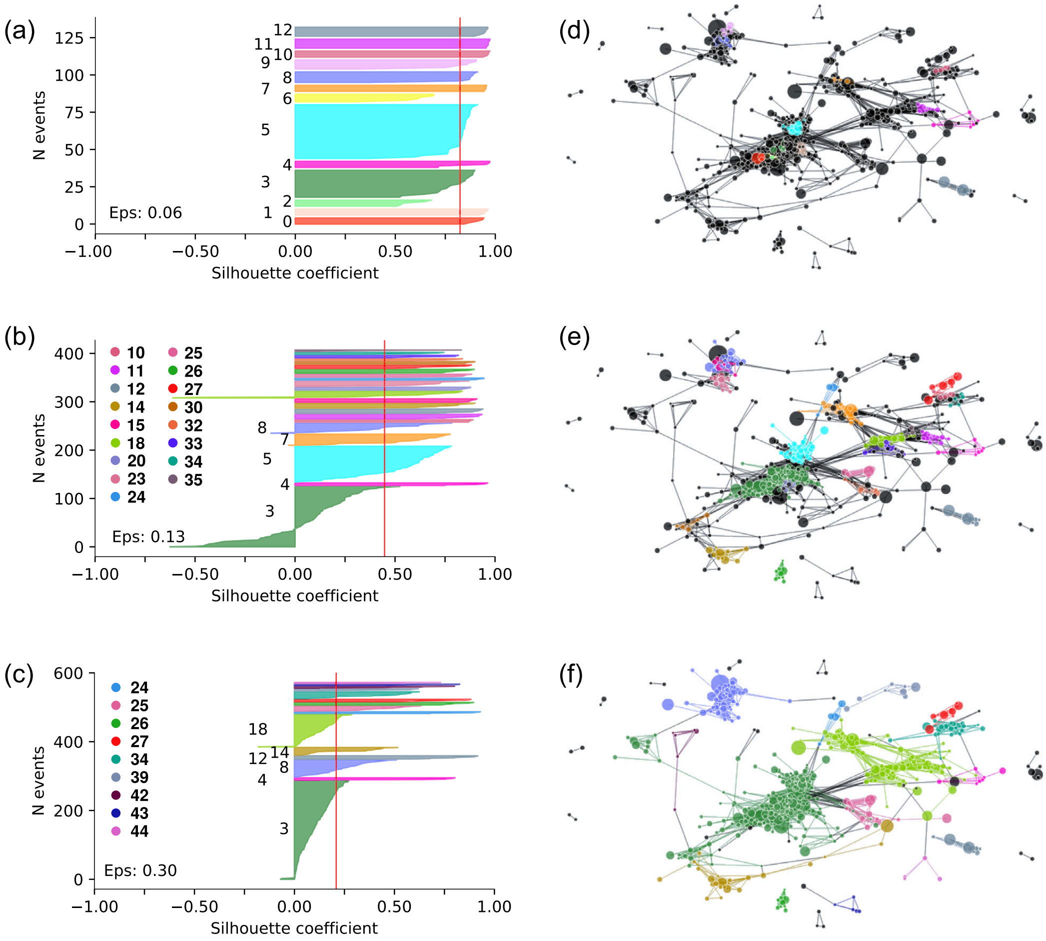

Figure 4. Example for silhouette coefficient plots (a–c) and connectivity plots (d–f), obtained for the Zakynthos data set with *Eps* values 0.06, 0.13 and 0.3, *MinPts* = 5. The numbers next to the clusters in (a–c) indicate the cluster label. The red vertical line is the silhouette score (mean of silhouette coefficients) of the clustered events. The connectivity plots (d–f) provide an additional visualization of the similarity of events within the same cluster as well as among different clusters. Events are coloured according to their cluster as in (a–c). Unclustered events are shown in black. In this projection the relative distance between events or clusters represents their similarity. The absolute locations within the projection have no meaning.

cannot be seen from the silhouette plot alone (Fig. 4a). By increasing *Eps* to 0.13 (Figs 4b and e) all clusters are well separated and homogeneous, except for cluster 3 and 18. For *Eps*=0.30 (Figs 4c and f) the central clusters collapse into one. In the latter case, the silhouette plot indicates that the clusters are generally more heterogeneous and larger. We want to stress the importance of the analysis of both, the similarity between separated clusters as well as among the events that belong to the same cluster, before interpreting the results. The user can get insights into the quality of the performed clustering analysis by comparing the presented plots for a range of parameters.

Clusty provides maps and waveform plots as final graphical output along with the catalogue of clustered events (for examples, see also Section 3). Station-wise waveform plots display all aligned waveforms per cluster and component. The waveform plots provide another direct visualization to evaluate the similarity of waveforms. We would like to point out that the clustering algorithm, the plots to evaluate the stability of the results (flow diagram, silhouette and connectivity plots) and the final maps may be used independently with any other distance matrix provided by the user. For example, these distance matrices could be based on Kagan angles or spatial distances.

3 APPLICATION: OFFSHORE AFTERSHOCK SEQUENCE OF THE *M* 6.9 ZAKYNTHOS EARTHQUAKE, GREECE

3.1 Study area

The study area is located at the western margin of the Hellenic Subduction System (HSS), along which the oceanic lithosphere of the African Plate is subducted beneath the continental lithosphere of the Eurasian Plate with a NE dipping slab (Fig. 5). Within the study area, faults of varying geometries and slip movements (Mouslopoulou *et al.* 2020) accommodate the northward kinematic transition from convergence to strike-slip (i.e. Pérouse *et al.* 2017; Sachpazi *et al.*

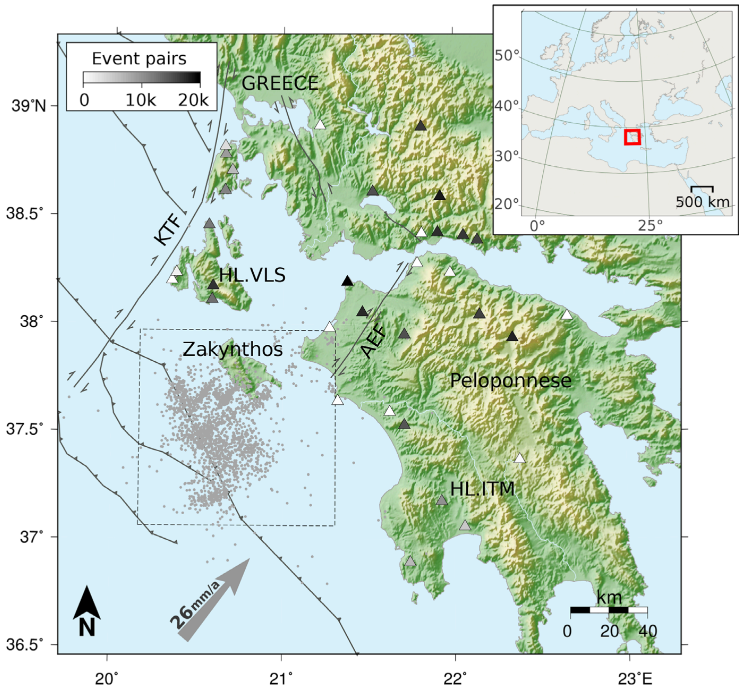

Figure 5. Study area and station network. Triangles indicate seismic stations. Colour intensity depicts the contribution of each station to the clustering result (number of clustered event pairs for which the station was used). The dashed square outlines the extent of Figs 6(a) and 7. The grey arrow indicates the relative movement of the African Plate with respect to stable Eurasia (Pérouse *et al.* 2017). Active regional faults from Basilic *et al.* (2013), topography from SRTM (Farr *et al.* 2007). KTF, Kefalonia Transform Fault; AEF, Achaia-Elia Fault.

2000). Although all types of faulting (thrust, normal and strike-slip) may occur (Konstantinou *et al.* 2017; Mouslopoulou *et al.* 2020), thrust faulting appears to prevail south and southwest of Zakynthos (Papadimitriou *et al.* 2013; Wardell *et al.* 2014), while strike-slip faulting is dominant to the northwest (Louvari *et al.* 1999; Sachpazi *et al.* 2000), onshore Peloponnese (Feng *et al.* 2010; Stiros *et al.* 2013) and in the offshore area between Zakynthos and Peloponnese (Kokkalas *et al.* 2013; Haddad *et al.* 2020; Mouslopoulou *et al.* 2020). Normal faulting is accommodated in the shallower sections of the crust (above 15 km), often at high angles to the prevailing strike of the mapped thrust/strike-slip faults (Mouslopoulou *et al.* 2020).

The study region is characterized by intense seismic activity and strong main shocks ($M > 6$, Papazachos & Papazachou 2003). On 25 October 2018, a magnitude M_w 6.9 earthquake struck southwest of Zakynthos (Chousianitis & Konca 2019; Cirella *et al.* 2020; Ganas *et al.* 2020; Karakostas *et al.* 2020; Mouslopoulou *et al.* 2020; Sokos *et al.* 2020). It occurred after a 4-yr-long phase of seismic unrest which was probably triggered by a slow-slip event (Mouslopoulou *et al.* 2020) and was followed by strong aftershock activity, which is still ongoing (Mouslopoulou *et al.* 2020; Sokos *et al.* 2020). The complex moment tensor of the main shock, with a significant non-double couple component, was attributed to subevents of thrust faulting and moderately dipping right lateral strike-slip faulting, in accordance with the African–Eurasian Plate motion (Cirella *et al.* 2020; Mouslopoulou *et al.* 2020; Sokos *et al.* 2020). While seismological results alone cannot clearly discriminate between a splay-thrust and a subduction-thrust fault scenario for the main candidate earthquake fault, the scenario of a splay-thrust fault is supported by published seismic-reflection and bathymetric data (Mouslopoulou *et al.* 2020) and the recording of a minor tsunami that suggests rupture of the sea-bed (Cirella *et al.* 2020).

Our study is based on the catalogue of the aftershock sequence reported by Mouslopoulou *et al.* (2020). It consists of ≥2300 events ($M_\mathrm{w} \geq 2.8$), including about 80 double-couple solutions showing a large variability of thrust, normal and strike-slip mechanisms. This hints at the activation of a complex fault system, in accordance with local fault diversity (e.g. Konstantinou *et al.* 2017; Mouslopoulou *et al.* 2020). Thanks to the complex tectonic setting, together with the multitude of activated faults, we consider the Zakynthos data set an ideal case study for our clustering analysis tool. The waveform data of the networks HA, HC, HL, HP, HT, MN (University Of Athens 2008; Technological Educational Institute Of Crete 2006; National Observatory Of Athens, I. O. G. 1997; University Of Patras, G. D. 2000; Aristotle University Of Thessaloniki Seismological Network 1981; MedNet Project Partner Institutions 1990) used in this study was obtained using the pyrocko fdsn client to access the databases of the National Observatory of Athens Seismic Network (NOA, http://www.gein.noa.gr/en/), GEOFOrschungsNetz (GEOFON; https://geofon.gfz-potsdam.de/), Observatories and Research Facilities for European Seismology (ORFEUS; https://www.orfeus-eu.org/), Incorporated Research Institutions for Seismology (IRIS; https://www.iris.edu/hq/) and Instituto Nazionale di Geofisica e Vulcanologia (INGV; http://webservices.ingv.it).

3.2 Results

Here, we present the clustering results for the Zakynthos data set obtained using a 30 per cent-trimmed mean for the calculation of the network similarity from waveforms of the seismic stations presented in Fig. 5. Vertical (HHZ) and horizontal (HHN and HHE) components were combined with weightings of 0.4, 0.3 and 0.3, respectively. Only event-pairs with *cc* values ≥0.7 and an SNR ≥ 2 at more than five stations, covering a minimum azimuthal range of 60°, are considered. We discuss the choice of the network similarity computation method and the DBSCAN clustering parameters (here: Eps 0.13, MinPts 5, primary frequency band 0.05–0.20 Hz, time window 80 s) in Section 4.

We used four different frequency bands to account for surface waves (0.02–0.15 Hz and 0.05–0.20 Hz) and body waves (0.1–0.5 Hz and 0.2–1.0 Hz). The overall patterns of clustered events are similar in all four frequency bands. Considering the stability and homogeneity as well as the total number of clustered events, the frequency band 0.05–0.20 Hz provides the best results. Using this frequency band, the clustering toolbox grouped 387 of 2361 (16 per cent) earthquakes with $M_w > 2.8$ into 22 clusters (Fig. 6a). 75 per cent of the events in the catalogue were rejected because they did not meet the quality thresholds (SNR, min. number of available traces) described above. Despite the small number of events compared to the total number of events in the catalogue, we consider the clustered events representative for the entire aftershock sequence as they cover 70 per cent of the cumulative moment.

The results of the primary frequency band are combined with the other, secondary frequency bands, mainly to account for smaller events with a low SNR at low frequencies. About 50 events were added to the clustering results, resulting in a total of approximately 430 clustered events. For each cluster, we computed deviatoric MTs (Fig. 6a) for one representative event using the probabilistic full waveform inversion framework Grond (Heimann *et al.* 2018), following the approach described in Mouslopoulou *et al.* (2020). The inversion includes 101 bootstrap chains with different weightings of the station-component-based misfits. The ten best MTs of each bootstrap chain, referred to as the ensemble of solutions, are used to analyse the uncertainties of the best solution obtained in the inversion.

Fig. 7 shows the temporal activity and moment release of the clusters. 84 per cent of the cumulative seismic moment of the aftershocks is released within the first month of the sequence. The central clusters (3, green; 4, pink; 5, light blue and 20, blue) are activated soon after the main shock. Our representative mechanisms (Fig. 6a) as well as the MT solutions of Mouslopoulou *et al.* (2020) for events belonging to the central clusters (3, 4, 5, 20 in Fig. S2) indicate predominantly thrust faulting. The thrust clusters 3 and 5 release 50 per cent of the cumulative seismic moment of the 1-yr aftershocks sequence or 70 per cent of the cumulative seismic moment of the clustered events (Fig. 7, inset). The proximity to the main shock, the time of initiation and the thrust nature of these events collectively suggest that they may be directly triggered by slip during the main shock. This is further supported by the representative mechanisms of cluster 3 and 5, which resemble the geometry resolved for the thrust part of the main shock by Sokos *et al.* (2020) and Mouslopoulou *et al.* (2020), possibly reflecting slip on the same (or neighbouring) fault. The representative mechanism of cluster 4 (Fig. 6a) shows a shallowly dipping (<10°) fault plane, however, its slip mechanism cannot be resolved unambiguously.

Following the rupture of the thrust clusters 3 and 5, and within hours of the main event, several strike-slip faults were activated north and south of the main shock's epicentre (Fig. 7), contributing significantly (12 per cent) to the total moment release of the aftershock sequence (Fig. 7, inset). West of the island of Zakynthos, we observe two NE–SW elongated seismicity clusters, which are associated with strike-slip faulting: overlapping clusters 11, 18 and 35 and the isolated cluster 7 (Fig. 6a). The small strike-slip cluster 24 abuts against the cluster 5 which is associated with thrust faulting. Due to the vicinity of these two clusters, the smaller strike-slip cluster cannot be detected based on spatio-temporal clustering. While the strike-slip clusters 7 and 24, which are located to the east and to the west of cluster 5, respectively, are active within the first ten days after the main shock, the activity of the overlapping strike-slip clusters 11, 18 and 35 starts two months later (Fig. 7). Cluster 33, which overlaps spatially with cluster 11, 18 and 35, in contrast is active within the first days after the main shock and shows a more oblique mechanism (Fig. 6). South of the main shock, three spatially and temporally overlapping strike-slip clusters (8, 15, 23) show a similar elongation in NE–SW direction (Fig. 6a). There, the activity starts within the first week after the main shock. The mechanisms of the three representative events of these clusters, together with the solutions from Mouslopoulou *et al.* (2020) (Fig. S2) indicate strike-slip on NS or EW striking fault planes, incompatible with the distribution of hypocentres. The latest cluster in the aftershock sequence is cluster 27 (red cluster in Figs 6a and 7), located to the south of the main shock. It is associated with a thrust slip on a NW–SE striking plane. The cluster consists of eight highly similar events.

4 DISCUSSION

In the introduction we briefly described the problem of the identification of active seismic faults and two related seismic methods, MT inversions and clustering of earthquakes based on selected precomputed features. Unlike the clustering of seismic events by their moment tensor, the clustering based on waveform similarities, which we propose here, is able to resolve closely located faults of different mechanisms without the limitation to larger magnitudes. Spatial clustering analysis is not limited by the magnitude, either, but is not able to resolve differences in the faulting mechanism. The clustering approach upon waveform similarity reflects the sensitivity of mechanism, location and depth, thus, providing a tool for the identification of active faults. Following a discussion on the methodological implementation, we review how a joint analysis of the clustering results and MT solutions for representative events can help to identify and describe active faults.

4.1 Discussion Part I: On the methodological implementation

The clustering toolbox presented here is dedicated to the study of active faults based on the waveform similarities of event pairs across a network of seismic stations. Compared to a single station approach, the network similarity has several advantages. By taking into account spatially distributed stations, a larger portion of the seismic radiation pattern is considered. Therefore a network similarity allows distinguishing mechanisms which cannot be distinguished in single station approaches. Especially in narrow frequency bands, it is possible to achieve high correlations at single stations that are excited by different faulting mechanisms. Further, even for a single high quality station noise conditions may vary temporarily and data gaps are likely. Using multiple stations in our network similarity approach assures the most efficient use of the available data.

We tested all methods for the network similarity computation (Section 2) by applying them to the aftershock sequence of the 25 October 2018, Zakynthos Earthquake. We observe that the network similarity based on the highest *cc* value across the network cannot resolve small differences between clusters of similar location and mechanism. The other methods implemented in the toolbox, that is median, mean, trimmed mean, the weighted sum and the composite

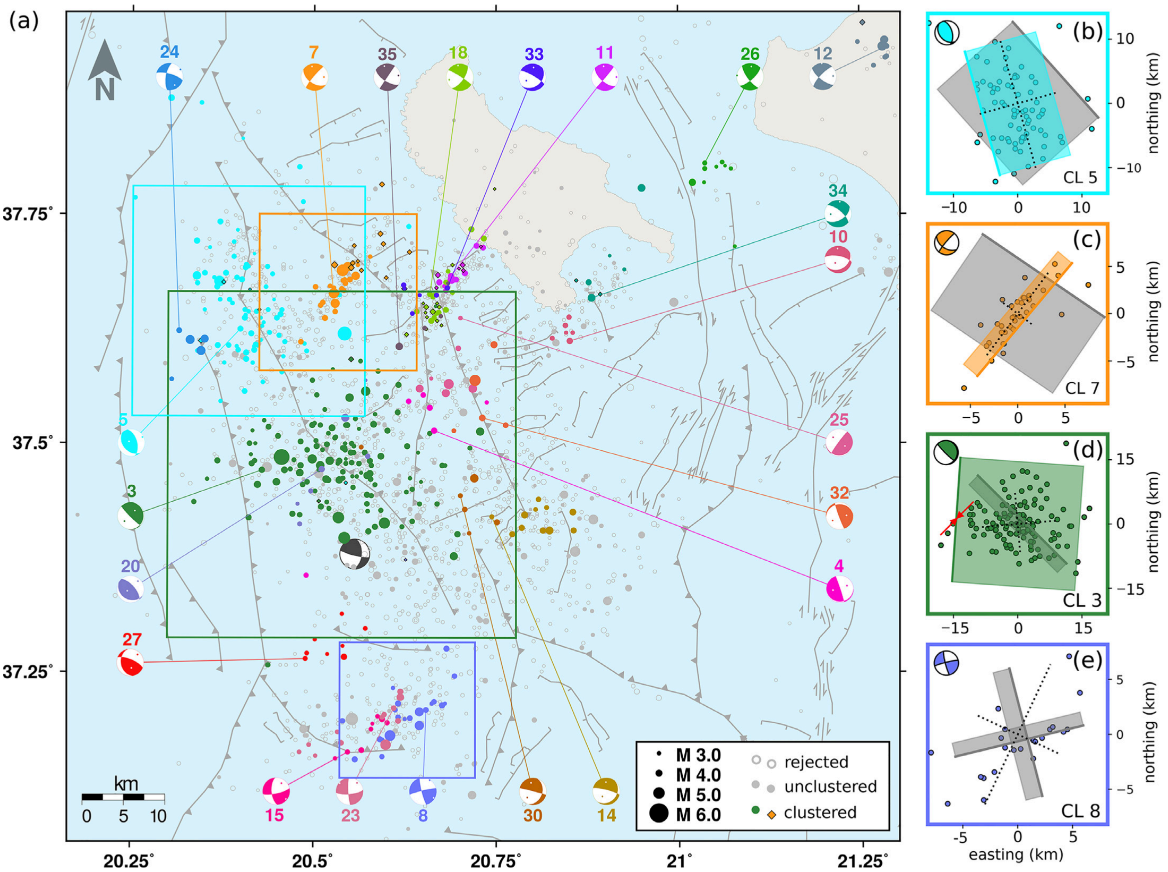

Figure 6. (a) Combined waveform-based clustering results for the aftershock sequence of the 25 October 2018, M_w 6.9 earthquake offshore Zakynthos, Greece (black MT). Clusters and representative MTs are colour-coded. Cluster label numbers are discontinuous due to harmonization of different *Eps* values and frequency bands (see Figs 3 and 4). Open grey circles represent events rejected from the clustering analysis due to selection criteria. The primary frequency band results (0.05–0.20 Hz) are shown as dots, diamonds refer events added to the clusters using the secondary frequency ranges. For the four largest clusters surface projections of the nodal planes of the representative MTs are shown in (b)–(e). Causative planes are coloured. For cluster 3 the strike angle is poorly resolved in the MT solution. The red arrows show the slip direction on the shallow nodal plane (green rectangle). Dashed lines depict the principle axes of principle component analyses of epicentres (see Section 4). Offshore faults are compiled and reinterpreted by Mouslopoulou *et al.* (2020) from bathymetric data and seismic-reflection profiles provided by Kokkalas *et al.* (2013), Wardell *et al.* (2014) and EMODnet Bathymetry Consortium (2018).

correlation measure (see Section 2.1), return comparable results after slightly adjusting the clustering parameters. For the sake of clarity, we only refer to the 30 per cent-trimmed mean network similarity when discussing the choice of the clustering parameters and the clustering results.

In the methodological section, we introduced the density-based DBSCAN clustering algorithm (Ester *et al.* 1996; Pedregosa *et al.* 2011). DBSCAN does not require that all events within one cluster are (highly) similar to all other events. Instead, it is sufficient that events within one cluster are connected by more similar events. Events with small differences in waveforms due to gradual changes in site effects, faulting mechanism or the travel path (location) can still belong to the same cluster if there are other connecting events in between them. Consequently, this approach is not only able to identify repeaters (e.g. Figs 4a, d and 8) (Geller & Mueller 1980), but allows grouping of events located on elongated faults. In our clustering toolbox we allow for unclustered events: If an event is not exhibiting a high similarity to any cluster of events, it is assigned to the noise class. In contrast, for instance the *k*-means clustering algorithm assigns every event to one of the given clusters without allowing for a noise class (Lloyd 1982). Therefore, we do not recommend using *k*-means for fault mapping purposes. Furthermore, in contrast to density-based clustering algorithms like DBSCAN, centroid-based clustering like *k*-means require a predefined number of clusters. Another common density-based clustering algorithm is OPTICS (Ankerst *et al.* 1999). Contrary to DBSCAN, which has a fixed radius *Eps*, OPTICS can handle varying cluster densities. However, for the fault tracing, we intend to have fixed criteria in regard to the required similarity of events and therefore use a fixed search radius. Thus, we rely on DBSCAN that assures that the event similarities, which result from physical processes and interevent distances, are comparable between the clusters. However, since our toolbox is set-up in a modular fashion, more methods can easily be implemented.

Clusty is applicable to different seismological scales since it directly uses waveforms and does not require precomputed features, such as moment tensors, characteristic functions, polarities or amplitude ratios. Potential applications range from acoustic emissions in laboratory or mining experiments to sequences of regional seismicity. Days to weeks long swarm activity as well as yearlong seismic sequences can be analysed. The flexibility in combining results from different frequency bands allows to investigate events with a large range of magnitudes. Thanks to the output of representative events of each cluster and stacked waveforms (optional),

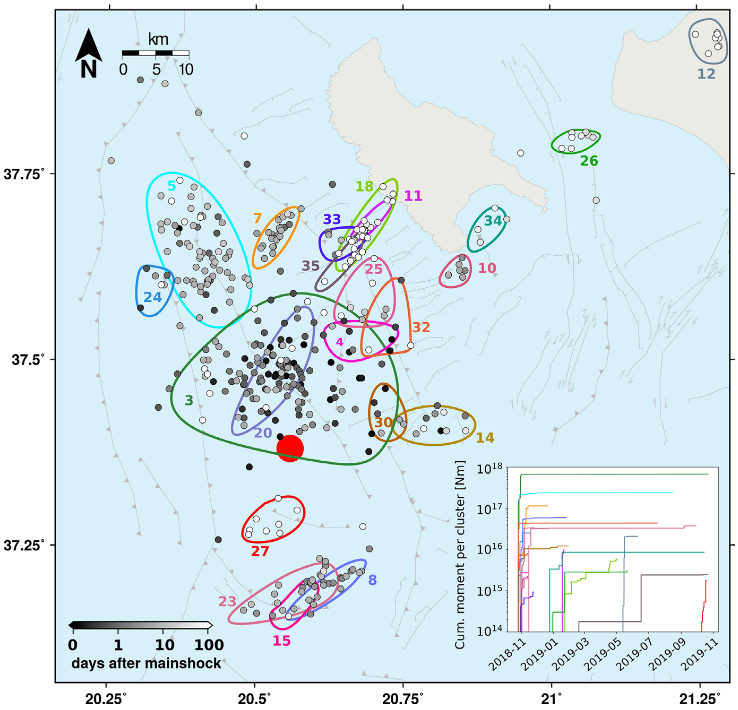

Figure 7. Spatial and temporal distribution of earthquake clusters during the Zakynthos aftershock sequence. The origin time of the clustered earthquakes are relative to the main shock. Contours of clusters and cluster labels for orientation and comparison to Fig. 6(a). The red dot indicates the main shock epicentre. Offshore faults are adopted from Mouslopoulou *et al*. (2020). Inset: Cumulative seismic moment of clusters over time.

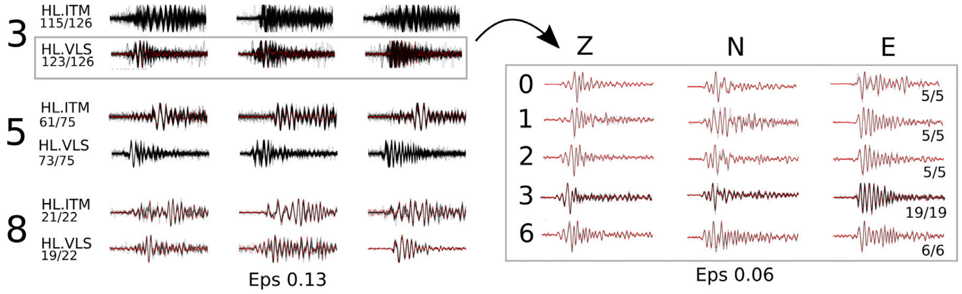

Figure 8. Aligned waveforms of the events in the two thrust clusters 3 and 5 and in the strike-slip cluster 8 at stations HL.ITM and HL.VLS (left-hand panel). See Fig. 5 for station locations. Numbers below the station name indicate the number of stacked traces versus the number of events within the clusters. Differences arise from waveform quality thresholds or missing data. When lowering the *Eps* to 0.06, cluster 3 splits up into smaller, more homogeneous subclusters (right-hand panel).

further analyses, such as subsequent moment tensor inversion, is facilitated.

The clustering toolbox returns several analysis plots to calibrate the settings for each study and to avoid black-box like usage. The DBSCAN parameter *Eps* should always be carefully adjusted. Larger values result in larger and more heterogeneous clusters. In contrast, low *Eps* values result in a higher similarity within the single clusters at the cost of a smaller number of clustered events, eventually losing information on the fault orientation. This trade-off needs to be considered when choosing an *Eps* value. We recommend testing different *Eps* values in parallel, for example from 0.05 to 0.30, and inspect what can be learned with respect to event clusters. We chose the *Eps* value of 0.13 for the cluster analysis after the joint consideration of the analysis tools as presented in Section 2. By testing different *MinPts* values, we find that the parameter does not significantly influence the observed pattern of earthquake clustering. To allow for smaller clusters to be included in the results, we set *MinPts* to 5.

Fig. 8 (left-hand panel) shows the aligned waveforms of clusters 3, 5 and 8 at two stations located north and east of the epicentral region (Fig. 5). The stacked waveforms of cluster 3 are clearly more diffuse than those of the other clusters. When lowering the *Eps* to 0.06 the large cluster 3 splits up into multiple homogeneous subclusters (right-hand part of Fig. 8 and see also Fig. 3). While the homogeneity within the subclusters is much higher, this approach substantially reduces the total number of clustered events (40 in 5 subclusters versus 126 in one cluster), showing a trade-off which was previously described.

4.2 Discussion Part II: On the application to the Zakynthos sequence

By applying the clustering toolbox to the aftershock sequence of the Zakynthos Earthquake, we are able to assign about 430 events to 22 distinct clusters. This is five times the number of aftershocks (∼80) that were clustered using the Kagan angle in Mouslopoulou *et al.* (2020). The increased number of clustered events enables a more precise characterisation of seismic patterns. Contrary to other clustering approaches that use event locations and/or times (e.g. Mouslopoulou & Hristopulos 2011; Ouillon & Sornette 2011; Karakostas *et al.* 2020), here we are able to distinguish events that are located close to each other but have different focal mechanisms and, thus, are expected to excite different waveforms, as seen for thrust cluster 5 and strike-slip cluster 24. Karakostas *et al.* (2020) identify 8 clusters for the same aftershock sequence based on event locations. We identify several additional small clusters (e.g. 24, 14 and 30), extending the insight into the complex fault system. Spatial or temporal clustering cannot separate events in complex faulting patterns as seen for the southernmost strike-slip clusters 8, 15, and 23. Cluster 33 overlaps spatially with clusters 11, 18 and 35, but the waveform similarity clearly separates these event groups, which are also separated temporally by 2 months.

Location errors need to be taken into account in the analysis of structures inferred from the clustering results. Earthquake (re-)location offshore Zakynthos is challenging due to the effects of a non-homogeneous velocity model, large azimuthal gaps and a sparse station coverage (e.g. Karastathis *et al.* 2015; Sachpazi *et al.* 2016). The locations and their uncertainties in the catalogue of Mouslopoulou *et al.* (2020) that we use here, were obtained using NonLinLoc (Lomax *et al.* 2000, 2009). The clustered events in this study have median uncertainties of 1.8 km and 2.7 km in horizontal and vertical direction, respectively (95 per cent confidence interval: 3.8 and 4.5 km). Due to the location errors, we do not consider any small structures (<10 km) in our analysis of fault planes.

Moment tensor solutions for representative events or for stacked waveforms of all events in a cluster enable the interpretation of the seismicity clusters with respect to faulting styles and fault orientations. Using stacked waveforms for each cluster can facilitate moment tensor inversion if the SNR of single events is too low otherwise. However, stacked waveforms need a particularly careful checking due to possible artefacts. For the application to the Zakynthos aftershock sequence the magnitudes of the representative events (M_w 3.5–4.6) allow for full waveform moment tensor inversions. In case of cluster 3, we report the moment tensor for the event with the second highest silhouette coefficient, because its magnitude is significantly larger (M_w 4.6 versus 3.9), providing a more stable MT result. Since Clusty is based on the Pyrocko python package, subsequent MT inversions using the probabilistic inversion framework Grond (Heimann *et al.* 2018) are facilitated.

The representative MTs show a wide variety of faulting types including thrusts, strike-slips and few normal faults. In general, our results are consistent with the MT solutions from Mouslopoulou *et al.* (2020) (Fig. 6a and Fig. S2). The *P* axes of their MTs are oriented NE–SW in general agreement with the regional compression.

For 15 of our 22 clusters, there is at least one MT available from Mouslopoulou *et al.* (2020, Fig. S2). Our representative MT solutions and MTs from Mouslopoulou *et al.* (2020) for events that belong to our clusters differ by a Kagan angle <30° for >50 per cent of the clusters and by <40° for 12 of our 15 clusters, respectively, implying homogeneous clusters. A Kagan angle of 30° is often used as a threshold for similar focal mechanisms in literature (e.g. Lee *et al.* 2014), while an angle ≪60° still indicates a good correspondence (Pondrelli *et al.* 2006; d'Amico *et al.* 2011). The large clusters 3 and 5 have increased mean Kagan angles of 40 and 55°, respectively. The variations of mechanisms in clusters 3 and 5 might primarily reflect varying dips of thrust fault planes.

For cluster 3, Mouslopoulou *et al.* (2020) report oblique strike-slip MTs for four earthquakes besides the predominant thrust mechanism. The oblique strike-slip and thrust mechanisms within this cluster cannot be distinguished, even when the *Eps* value is as low as 0.06. In our clustering approach we use a broader frequency band (0.05–0.20 Hz) compared to the MT inversions by Mouslopoulou *et al.* (2020). Repeating the MT inversion for all events for which solutions are reported by Mouslopoulou *et al.* (2020) in a broader frequency band (0.02–0.07 Hz), we obtain thrust mechanisms with minor oblique components. Kagan angles between our representative event for cluster 3 and our own MT solutions for the events that were also reported by Mouslopoulou *et al.* (2020) result in a mean angle of 25°, indicating similar event mechanisms. We assume that the narrower bandwidth used by Mouslopoulou *et al.* (2020), along with the unfavourable station distribution along the coast, results in two possible mechanisms that could not be distinguished in the MT inversion in the case of these four events.

Varying fault plane dip angles could be attributed to listric thrust faults offshore Zakynthos (Kokinou *et al.* 2005; Papoulia & Makris 2010; Kokkalas *et al.* 2013). Cluster 3 was active immediately after the main shock (Fig. 7). As the cluster is located within the main shock rupture area (Sokos *et al.* 2020), its heterogeneity may be linked to the complexity of the main shock, which possibly involves two overlapping events (Mouslopoulou *et al.* 2020; Sokos *et al.* 2020). The main shock itself does not belong to any of the clusters. Its waveforms are different probably because of its larger magnitude (and lower corner frequency) and/or because of its rupture complexity.

Strike-slip clusters are activated to the south and to the north of the M_w 6.9 epicentre few days after the main shock (and after the activation of the dominant thrust clusters 3 and 5). Activity on these distinct faults may have been triggered by stress perturbations imposed by the main shock and aftershock activity. The overlapping strike-slip clusters 11, 18, 35 southwest of the island of Zakynthos are activated two months after the main shock.

The identification and tracing of fault planes cannot be automated in this study. Increased vertical uncertainties of the hypocentres in the studied catalogue inhibit the direct fitting of fault planes into clouds of clustered events. Instead, we use their epicentral locations, geological constraints, and the projection of the two nodal planes of the representative MTs onto the surface (Figs 6b–e) to distinguish the fault plane from the auxiliary plane. The nodal planes are centred at the mean cluster location. The area of the nodal planes is estimated using an empirical relation to the cumulative seismic moment magnitude of the cluster following Wells & Coppersmith (1994). Local magnitudes are converted to moment magnitudes using an empirical relation derived from the MT solutions of Mouslopoulou *et al.* (2020). Since we only analyse event clusters with a moderate cumulative moment, we assume that a square-shaped fault model is representative for the fault plane (Delouis *et al.* 2009). We compare the projected planes and the epicentre distribution to distinguish the fault plane from the auxiliary plane. Additionally, we apply a Principle Component Analysis (PCA, Jolliffe 2002; Shearer *et al.* 2003) to each cluster by determining the eigenvectors ($\boldsymbol{v}_1$, $\boldsymbol{v}_2$) and eigenvalues (λ_1, λ_2) of the covariance matrix of the epicentres within each cluster. The length of the axes (dotted lines in Figs 6b–e) is

Table 1. Results of the joint interpretation of the clustering analysis and the representative MTs (nodal plane orientation) for clusters containing ≥10 earthquakes (n_{ev}). Time period is activity in days after the main shock. Interpreted fault planes in bold type. TF, thrust fault; SSF, strike-slip fault; NF, normal fault.

Cluster label	n_{ev}	Time period	$ML_{\max}$	cum. moment (Nm)	Nodal planes (strike/dip/rake)	Mechanism
3	126	0–23	5.9	1.3e+18	134/84/83, **4/8/138**	TF
5	75	0–47	5.7	4.7e+17	138/37/68, **344/55/105**	TF
14	11	0–74	4.6	2.6e+16	284/80/-70, 39/22/-152	NF
7	24	3–20	5.3	2.3e+17	124/51/-9, **219/82/-140**	SSF
8	22	5–67	5.2	1.2e+17	256/84/7, 165/82/173	SSF
23	12	7–27	5.1	6.9e+16	84/72/-8, 176/81/-162	SSF
11	10	83–87	4.7	2.1e+16	131/63/3, **40/87/153**	SSF
18	15	87–187	4.1	1.3e+16	302/83/-23, **35/66/-173**	SSF
12	10	199–226	4.9	4.3e+16	128/70/-14, 223/75/-159	SSF

estimated from the 95 per cent confidence interval. When using epicentres (2-D case), the eigenvector of the largest eigenvalue can be interpreted as the strike direction of the fault, while the smaller eigenvalue can provide insight into the dip of the fault. For steep faults we expect $\lambda_1 >> \lambda_2$, while $\lambda_1 \approx \lambda_2$ represents a low-angle dip.

We test the results of Clusty against structural fault mapping offshore Zakynthos by focusing on prominent seismicity patterns: (1) the central thrust clusters 3 and 5 north of the M_{w} 6.9 epicentral area and (2) the large strike-slip clusters 7 and 8 north and south of the epicentral area. Figs 6(b) and (d) show the central clusters 3 and 5. The representative MT for cluster 3 has one steeply dipping (84°) SE–NW striking nodal plane and one shallowly dipping (<10°), NS striking plane. Due to the shallow dip angle of the latter and the unfavourable station distribution, it is difficult to resolve the strike angle of this nodal plane: among the ensemble of MT solutions having a small misfit the strike direction of the low-angle dipping nodal plane varies between NNW and N. Despite the limited resolution of the strike angle, both, the orientation of the *P*- and *T*-axis and the NE-ward slip of the shallow nodal plane (red arrow in Fig. 6d), are distinct and in agreement with the tectonic setting. Considering the broad scatter of the epicentres and the regional tectonic setting we identify the shallowly dipping nodal plane as the fault plane (coloured nodal plane in Fig. 6d). It has a similar orientation as the fault planes that Cirella *et al.* (2020) and Ganas *et al.* (2020) inferred for the main shock by jointly considering geodetic and seismic data. However, in contrast to our representative MT of cluster 3, the main shock mechanism has a large strike-slip component (Cirella *et al.* 2020; Ganas *et al.* 2020; Mouslopoulou *et al.* 2020; Sokos *et al.* 2020). The PCA supports the identification of the causative plane, as both PCA axes have a similar length, which indicates a low dip angle. However, in this case of two axes of similar length the PCA cannot resolve the strike direction of the fault plane. For cluster 5, both nodal planes (striking NNW and SE) could explain the scatter of events. A mapped thrust fault coincides with the NNW strike direction and ENE dip direction of the first nodal plane as well as with the major axis from the PCA (Fig. 6b). The identification of the causative plane is further supported by the regional tectonic setting. (Fig. 6a). The lack of seismic activity between the two large thrust clusters (3 and 5) may reflect a locked patch on an otherwise creeping fault plane (Moreno *et al.* 2011) or a rupture on two fault segments with deviating geometries, as seen in Fig. 6(a). However, it may also reflect a bias from the short observational period (∼1 yr).

For cluster 7, the SW striking nodal plane of the representative MT clearly coincides with the elongated epicentre distribution. This makes the selection of the fault plane unambiguous, also when relying on the PCA results (Fig. 6c). Cluster 8 is an example of a more complex fault system. The two steeply dipping nodal planes strike in SSE and WSW direction while the cluster is elongated in NE–SW direction, as indicated by the PCA (Fig. 6e). Consequently, an unambiguous identification of the fault plane is not possible. Considering similar observations for the clusters 15 and 23 we propose that this deviation is not caused by limitations in the analysis or a systematic bias in epicentre locations. Instead, it may be attributed to multiple strike-slip faults forming a bookshelf structure (en-echelon). Sokos *et al.* (2020) decompose their main shock moment tensor into one major strike-slip segment and a thrust segment. Similar to our finding for clusters 8, 15 and 23, they describe that the N10°E striking nodal plane of the strike-slip subevent is not in accordance with the alignment of the aftershocks.

The strike-slip faults associated with clusters 7 and 8 (north and south of the epicentral area) have not been constrained geologically using the available bathymetric data, possibly due to their subtle signature on the seabed and the limited resolution of the bathymetric data. Seismic-reflection data are not available for these regions. In addition to the mapped normal faults south of Zakynthos, we identify strike-slip clusters (11, 18, 35) which are oriented parallel to cluster 7 (Fig. 6a). This possibly implies the presence of NE–SW trending strike-slip faults north and south of the M_{w} 6.9 epicentral area, providing an example of how the toolbox Clusty can enhance or complement available tectonic information on active faults which might be of importance for seismic hazard scenarios.

Additional identified fault planes from the cluster analysis are presented in Table 1. The analysis demonstrated here depends on the availability of both, a sufficient number of cluster members with reliable event locations, and representative MTs. This prevents a fault plane identification for small clusters. If MTs are not available or cannot be computed, the clusters of earthquakes can still be compared to mapped faults, possibly providing additional information on activated faults and on the faulting style.

In summary, we show how our new waveform-based network similarity clustering toolbox Clusty helps to better constrain the geometries and kinematics of earthquake sequences that rupture multiple faults. We applied our toolbox onto the western-end of the HSS in the eastern Mediterranean, a complex tectonic setting where all types of faulting occur simultaneously. However, Clusty is applicable on other multifault systems globally, including subduction terminations (e.g. Mouslopoulou *et al.* 2019), closely spaced faults in narrow rift basins (Nicol *et al.* 2006) or fault intersections (Mouslopoulou *et al.* 2007). In ongoing studies we use it to analyse acoustic emission activity from a mine-scale experiment as well as low magnitude seismicity in areas where moment tensor inversion meets its methodological limits.

5 CONCLUSIONS

The open source toolbox Clusty clusters earthquakes based on the waveform similarity across a seismic network. Thanks to comprehensive analysis tools, and the flexible choice of methods, the toolbox provides an easily tunable workflow and produces transparent results. Based on the analysis plots (i.e. flow diagram, silhouette score plot, connectivity plots), the user can visually inspect the results and select the most appropriate settings such as frequency bands, the quality thresholds and DBSCAN clustering parameters (*Eps* and *MinPts*). Besides the clustered catalogue and its graphical representation, Clusty provides a list of representative events and optionally stacked waveforms for each cluster to facilitate subsequent analyses such as moment tensor inversions and fault plane identifications. The modular setup of the toolbox allows an easy adaption to a broad range of applications e.g. local swarm like activity or regional long-term seismic patterns. The toolbox is open-source and can be downloaded at https://git.pyrocko.org/clusty/clusty. We applied the clustering toolbox to a seismic sequence following the magnitude M_w 6.9 Zakynthos Earthquake, Greece. We show how clustering parameters can be selected using the analysis plots provided by the toolbox. As a result we identify 22 clusters comprising more than 430 events that represent >70 per cent of the cumulative seismic moment released during the investigated time period. Relying on full waveform analysis, we can distinguish closely located events with different faulting styles. Moment tensor inversions for representative events of each cluster complement the clustering analysis of the seismic sequence. We show how our waveform-based clustering approach can be used to discriminate the fault plane from the auxiliary planes. Using 1 yr of seismic activity, we are able to associate clusters of events to individual faults and shed light onto the complex fault system in the study region. Thrust faulting is observed in two large clusters that are activated immediately after the main shock and remain active during the entire observation period, although the largest portion of the seismic moment from these clusters is released within the first days after the main shock. We suggest that these events are closely related to the M_w 6.9 earthquake and possibly occur on the same fault plane, accommodating subduction-related strain. However, the main shock itself does not show a high waveform similarity compared to these clusters. Clusty suggests the presence of strike-slip faults north and south of the main shock, in areas which are poorly resolved by seismic-reflection data. The results are broadly compatible with the geometry and kinematics of offshore faults mapped using seismic-reflection profiles and bathymetric data.

ACKNOWLEDGEMENTS

We like to thank the Editor, an anonymous reviewer and J. Zahradnik for constructive comments that helped to improve the manuscript. GMP is funded by DFG project ‘From Top to Bottom - Seismicity, Motion Patterns and Stress Distribution in the Alpine Crust’ (Project Number 362440331), a subproject of ‘SPP 2017: Mountain Building Processes in 4D’ (Project Number 313806092). PN is currently funded by the BMBF (German Federal Ministry of Education and Research) project SECURE (grant agreement No. 03G0872A).

6 DATA AVAILABILITY

The code for the toolbox is open-source and can be accessed at https://git.pyrocko.org/clusty/clusty. The event catalog used in this study can also be downloaded from the git repository (database last accessed in November 2019). The waveform data is freely available via the FDSN services (see section 3.1).

REFERENCES

Abramenkov, S., Shapiro, N.M., Koulakov, I. & Abkadyrov, I., 2020. Clustering of long-period earthquakes beneath Gorely Volcano (Kamchatka) during a degassing episode in 2013, *Geosciences,* **10**(6), 230.

Akuhara, T. & Mochizuki, K., 2014. Application of cluster analysis based on waveform cross-correlation coefficients to data recorded by ocean-bottom seismometers: results from off the Kii Peninsula, *Earth, Planets Space,* **66**(1), 80.

Ankerst, M., Breunig, M.M., Kriegel, H.-P. & Sander, J., 1999. Optics: ordering points to identify the clustering structure, in *Proceedings of the 1999 ACM SIGMOD International Conference on Management of Data,* SIGMOD ’99, pp. 49–60, Association for Computing Machinery, New York, NY, USA.

Ansari, A., Noorzad, A. & Zafarani, H., 2009. Clustering analysis of the seismic catalog of Iran, *Comput. Geosci.,* **35**(3), 475–486.

Aristotle University Of Thessaloniki Seismological Network, 1981. Permanent regional seismological network operated by the Aristotle University of Thessaloniki. International Federation of Digital Seismograph Networks, https://doi.org/10.7914/SN/HT.

Arrowsmith, S.J. & Eisner, L., 2006. A technique for identifying microseismic multiplets and application to the valhall field, north sea, *Geophysics,* **71,** V31–V40.

Asano, Y., *et al.*, 2011. Spatial distribution and focal mechanisms of aftershocks of the 2011 off the Pacific coast of Tohoku Earthquake, *Earth, Planets Space,* **63**(7), 669–673.

Aster, R.C. & Scott, J., 1993. Comprehensive characterization of waveform similarity in microearthquake data sets, *Bull. seism. Soc. Am.,* **83**(4), 1307–1314.

Baisch, S., Ceranna, L. & Harjes, H.-P., 2008. Earthquake cluster: what can we learn from waveform similarity?, *Bull. seism. Soc. Am.,* **98**(6), 2806–2814.

Barani, S., Ferretti, G., Massa, M. & Spallarossa, D., 2007. The waveform similarity approach to identify dependent events in instrumental seismic catalogues, *Geophys. J. Int.,* **168**(1), 100–108.

Basilic, R., *et al.*, 2013. The European Database of Seismogenic Faults (EDSF) compiled in the framework of the Project SHARE. http://diss.rm.ingv.it/share-edsf/, doi: 10.6092/INGV.IT-SHARE-EDSF.

Cesca, S., 2020. Seiscloud, a tool for density-based seismicity clustering and visualization, *J. Seismol.,* **24**(1), doi:10.1007/s10950-020-09921-8.

Cesca, S., *et al.*, 2017. Complex rupture process of the Mw 7.8, 2016, Kaikoura earthquake, New Zealand, and its aftershock sequence, *Earth planet. Sci. Lett.,* **478,** 110–120.

Chousianitis, K. & Konca, A.O., 2019. Intraslab deformation and rupture of the entire subducting crust during the 25 October 2018 Mw 6.8 Zakynthos earthquake, *Geophys. Res. Lett.,* **46**(24), 14 358–14 367.

Cirella, A., *et al.*, 2020. The 2018 Mw 6.8 Zakynthos (Ionian Sea, Greece) earthquake: seismic source and local tsunami characterization, *Geophys. J. Int.,* **221**(2), 1043–1054.

Czecze, B. & Bondár, I., 2019. Hierachical cluster analysis and multiple event relocation of seismic event clusters in Hungary between 2000 and 2016, *J. Seismol.,* **23,** 1313–1326.

d’Amico, S., Orecchio, B., Presti, D., Gervasi, A., Zhu, L., Guerra, I., Neri, G. & Herrmann, R., 2011. Testing the stability of moment tensor solutions for small earthquakes in the Calabro-Peloritan Arc region (southern Italy), *Boll. Geof. Teorica. Appl.,* **52**(2), doi:10.4430/bgta0009.

Delouis, B., Charlety, J. & Vallée, M., 2009. A method for rapid determination of moment magnitude Mw for moderate to large earthquakes from the near-field spectra of strong-motion records (MWSYNTH), *Bull. seism. Soc. Am.,* **99**(3), 1827–1840.

EMODnet Bathymetry Consortium, 2018. EMODnet Digital Bathymetry (DTM 2018), Tech. rep., EMODnet Bathymetry Consortium.

Ester, M., Kriegel, H.-P., Sander, J., Xu, X., *et al.*, 1996. A density-based algorithm for discovering clusters in large spatial databases with noise, in *KDD'96: Proceedings of the Second International Conference on Knowledge Discovery and Data Mining,* August 1996, pp. 226–231.

Farr, T.G., *et al.*, 2007. The shuttle radar topography mission, *Rev. Geophys.,* **45**(2), doi:10.1029/2005RG000183.

Feng, L., Newman, A.V., Farmer, G.T., Psimoulis, P. & Stiros, S.C., 2010. Energetic rupture, coseismic and post-seismic response of the 2008 MW 6.4 Achaia-Elia Earthquake in northwestern Peloponnese, Greece: an indicator of an immature transform fault zone, *Geophys. J. Int.,* **183**(1), 103–110.

Frohlich, C., 1987. Aftershocks and temporal clustering of deep earthquakes, *J. geophys. Res.,* **92**(B13), 13 944–13 956.

Fruchterman, T.M. & Reingold, E.M., 1991. Graph drawing by force-directed placement, *Softw.: Pract. Experience,* **21**(11), 1129–1164.

Ganas, A., *et al.*, 2020. The 25 October 2018 Mw= 6.7 Zakynthos earthquake (Ionian Sea, Greece): a low-angle fault model based on GNSS data, relocated seismicity, small tsunami and implications for the seismic hazard in the west Hellenic Arc, *J. Geodyn.,* **137,**.

Geller, R.J. & Mueller, C.S., 1980. Four similar earthquakes in central California, *Geophys. Res. Lett.,* **7**(10), 821–824.

Grandin, R., Vallée, M., Satriano, C., Lacassin, R., Klinger, Y., Simoes, M. & Bollinger, L., 2015. Rupture process of the Mw= 7.9 2015 Gorkha earthquake (Nepal): insights into Himalayan megathrust segmentation, *Geophys. Res. Lett.,* **42**(20), 8373–8382.

Haddad, A., Ganas, A., Kassaras, I. & Lupi, M., 2020. Seismicity and geodynamics of western Peloponnese and central Ionian Islands: insights from a local seismic deployment, *Tectonophysics,* **778,** 228353.

Han, L., Wu, Z., Li, Y. & Jiang, C., 2014. Cross-correlation coefficients for the study of repeating earthquakes: an investigation of two empirical assumptions/conventions in seismological interpretation practice, *Pure appl. Geophys.,* **171**(3–5), 425–437.

Heimann, S., *et al.*, 2017. Pyrocko - an open-source seismology toolbox and library, V. 0.3. GFZ Data Services. https://doi.org/10.5880/GFZ.2.1.2017.001.

Heimann, S., Isken, M., Kühn, D., Sudhaus, H., Steinberg, A., Daout, S., Cesca, S., Bathke, H. & Dahm, T., 2018. Grond: a probabilistic earthquake source inversion framework. V. 1.0. GFZ Data Services. https://doi.org/10.5880/GFZ.2.1.2018.003.

Herrmann, R.B., Malagnini, L. & Munafó, I., 2011. Regional moment tensors of the 2009 L'Aquila earthquake sequence, *Bull. seism. Soc. Am.,* **101**(3), 975–993.

Hunter, J.D., 2007. Matplotlib: a 2D graphics environment, *Comput. Sci. Eng.,* **9**(3), 90–95.

Igarashi, T., Matsuzawa, T. & Hasegawa, A., 2003. Repeating earthquakes and interplate aseismic slip in the northeastern Japan subduction zone, *J. geophys. Res.,* **108**(B5), doi:10.1029/2002JB001920.

Jolliffe, I.T., 2002. *Principal Component Analysis, Springer Series in Statistics,* 2nd edn, Springer-Verlag.

Karakostas, V., Kostoglou, A., Chorozoglou, D. & Papadimitriou, E., 2020. Relocation of the 2018 Zakynthos, Greece, aftershock sequence: spatiotemporal analysis deciphering mechanism diversity and aftershock statistics, *Acta Geophys.,* **68,** 1263–1294.

Karastathis, V., Mouzakiotis, E., Ganas, A. & Papadopoulos, G., 2015. High-precision relocation of seismic sequences above a dipping Moho: the case of the January-February 2014 seismic sequence on Cephalonia island (Greece), *Solid Earth,* **6**(1), 173.

Kokinou, E., Kamberis, E., Vafidis, A., Monopolis, D., Ananiadis, G. & Zelilidis, A., 2005. Deep seismic reflection data from offshore western Greece: a new crustal model for the Ionian Sea, *J. Petrol. Geol.,* **28**(2), 185–202.

Kokkalas, S., Kamberis, E., Xypolias, P., Sotiropoulos, S. & Koukouvelas, I., 2013. Coexistence of thin-and thick-skinned tectonics in Zakynthos area (western Greece): Insights from seismic sections and regional seismicity, *Tectonophysics,* **597,** 73–84.

Konstantinou, K., Mouslopoulou, V., Liang, W.-T., Heidbach, O., Oncken, O. & Suppe, J., 2017. Present-day crustal stress field in Greece inferred from regional-scale damped inversion of earthquake focal mechanisms, *J. geophys. Res.,* **122**(1), 506–523.

Koper, K.D., Hutko, A.R., Lay, T., Ammon, C.J. & Kanamori, H., 2011. Frequency-dependent rupture process of the 2011 Mw 9.0 Tohoku earthquake: comparison of short-period p wave backprojection images and broadband seismic rupture models, *Earth, Planets Space,* **63**(7), 16.

Lee, S.-J., Liu, Q., Tromp, J., Komatitsch, D., Liang, W.-T. & Huang, B.-S., 2014. Toward real-time regional earthquake simulation II: real-time online earthquake simulation (ROS) of Taiwan earthquakes, *J. Asian Earth Sci.,* **87,** 56–68.

Lloyd, S., 1982. Least squares quantization in PCM, *IEEE Trans. Inform. Theory,* **28**(2), 129–137.

Lomax, A., Virieux, J., Volant, P. & Berge-Thierry, C., 2000. Probabilistic earthquake location in 3D and layered models, in *Advances in Seismic Event Location,* pp. 101–134, Springer.

Lomax, A., Michelini, A. & Curtis, A., 2009. Earthquake location, direct, global-search methods, in *Encyclopedia of Complexity and System Science,* pp. 1–33, Springer.

Louvari, E., Kiratzi, A. & Papazachos, B., 1999. The Cephalonia transform fault and its extension to western Lefkada Island (Greece), *Tectonophysics,* **308**(1–2), 223–236.

Maurer, H. & Deichmann, N., 1995. Microearthquake cluster detection based on waveform similarities, with an application to the western Swiss Alps, *Geophys. J. Int.,* **123**(2), 588–600.

MedNet Project Partner Institutions, 1990. Mediterranean very broadband seismographic network (MedNet). Istituto Nazionale di Geofisica e Vulcanologia (INGV), https://doi.org/10.13127/SD/fBBBtDtd6q.

Mesimeri, M., Karakostas, V., Papadimitriou, E. & Tsaklidis, G., 2019. Characteristics of earthquake clusters: application to western Corinth Gulf (Greece), *Tectonophysics,* **767,** 228160.

Moreno, M., *et al.*, 2011. Heterogeneous plate locking in the South-Central Chile subduction zone: building up the next great earthquake, *Earth Planet. Sci. Lett.,* **305**(3–4), 413–424.

Mouslopoulou, V. & Hristopulos, D.T., 2011. Patterns of tectonic fault interactions captured through geostatistical analysis of microearthquakes, *J. geophys. Res.,* **116**(B7), doi:10.1029/2010JB007804.

Mouslopoulou, V., Nicol, A., Little, T. & Walsh, J., 2007. Displacement transfer between intersecting regional strike-slip and extensional fault systems, *J. Struct. Geol.,* **29**(1), 100–116.

Mouslopoulou, V., Saltogianni, V., Nicol, A., Oncken, O., Begg, J., Babeyko, A., Cesca, S. & Moreno, M., 2019. Breaking a subduction-termination from top to bottom: the large 2016 Kaikōura Earthquake, New Zealand, *Earth planet. Sci. Lett.,* **506,** 221–230.

Mouslopoulou, V., Bocchini, G.M., Cesca, S., Saltogianni, V., Bedford, J.R., Petersen, G.M., Gianniou, M. & Oncken, O., 2020. Earthquake-swarms, slow-slip and fault-interactions at the western-end of the Hellenic Subduction System precede the Mw 6.9 Zakynthos Earthquake, Greece, *Geochem., Geophys., Geosyst.,* doi:10.1029/2020GC009243.

National Observatory Of Athens, I. O. G., 1997. National Observatory of Athens Seismic Network. International Federation of Digital Seismograph Networks, https://doi.org/10.7914/SN/HL.

Nicol, A., Walsh, J., Berryman, K. & Villamor, P., 2006. Interdependence of fault displacement rates and paleoearthquakes in an active rift, *Geology,* **34**(10), 865–868.

Örgülü, G. & Aktar, M., 2001. Regional moment tensor inversion for strong aftershocks of the August 17, 1999 Izmit earthquake (Mw= 7.4), *Geophys. Res. Lett.,* **28**(2), 371–374.

Ouillon, G. & Sornette, D., 2011. Segmentation of fault networks determined from spatial clustering of earthquakes, *J. geophys. Res.,* **116**(B2), doi:10.1029/2010JB007752.

Papadimitriou, E., Gospodinov, D., Karakostas, V. & Astiopoulos, A., 2013. Evolution of the vigorous 2006 swarm in Zakynthos (Greece) and probabilities for strong aftershocks occurrence, *J. Seismol.,* **17**(2), 735–752.

Papazachos, B. & Papazachou, C., 2003, *The Earthquakes of Greece,* Ziti Publication (In Greek), pp. 356.

Papoulia, J. & Makris, J., 2010. Tectonic processes and crustal evolution on/offshore western Peloponnese derived from active and passive seismics, *Bull. Geol. Soc. Greece,* **43**(1), 357–367.

Pedregosa, F., *et al.*, 2011. Scikit-learn: machine learning in Python, *J. Mach. Learn. Res.,* **12,** 2825–2830.

Pérouse, E., *et al.*, 2017. Transition from collision to subduction in Western Greece: the Katouna–Stamna active fault system and regional kinematics, *Int. J. Earth Sci.,* **106**(3), 967–989.

Plotly Technologies Inc., 2015, *Collaborative Data Science,* Plotly Technologies Inc., https://plot.ly.

Pondrelli, S., Salimbeni, S., Ekström, G., Morelli, A., Gasperini, P. & Vannucci, G., 2006. The Italian CMT dataset from 1977 to the present, *Phys. Earth planet. Inter.,* **159**(3–4), 286–303.

Rousseeuw, P.J., 1987. Silhouettes: a graphical aid to the interpretation and validation of cluster analysis, *J. Comput. Appl. Math.,* **20,** 53–65.

Ruscic, M., Bocchini, G.M., Becker, D., Meier, T. & van Keken, P., 2019. Variable spatio-temporal clustering of microseismicity in the Hellenic Subduction Zone as possible indicator for fluid migration, *Lithos,* **346,** 105154.

Sachpazi, M., *et al.*, 2000. Western Hellenic subduction and Cephalonia Transform: local earthquakes and plate transport and strain, *Tectonophysics,* **319**(4), 301–319.

Sachpazi, M., *et al.*, 2016. Slab segmentation controls the interplate slip motion in the SW Hellenic subduction: new insight from the 2008 Mw 6.8 Methoni interplate earthquake, *Geophys. Res. Lett.,* **43**(18), 9619–9626.

Serpetsidaki, A., Sokos, E., Tselentis, G.-A. & Zahradnik, J., 2010. Seismic sequence near Zakynthos Island, Greece, April 2006: identification of the activated fault plane, *Tectonophysics,* **480**(1–4), 23–32.

Shearer, P., Hauksson, E. & Lin, G., 2005. Southern California hypocenter relocation with waveform cross-correlation, Part 2: results using source-specific station terms and cluster analysis, *Bull. seism. Soc. Am.,* **95**(3), 904–915.

Shearer, P.M., Hardebeck, J.L., Astiz, L. & Richards-Dinger, K.B., 2003. Analysis of similar event clusters in aftershocks of the 1994 Northridge, California, earthquake, *J. geophys. Res.,* **108**(B1), doi:10.1029/2001JB000685.

Shelly, D.R., Hardebeck, J.L., Ellsworth, W.L. & Hill, D.P., 2016. A new strategy for earthquake focal mechanisms using waveform-correlation-derived relative polarities and cluster analysis: Application to the 2014 Long Valley Caldera earthquake swarm: a new strategy for focal mechanisms, *J. geophys. Res.,* **121**(12), 8622–8641.

Sokos, E., Gallovič, F., Evangelidis, C.P., Serpetsidaki, A., Plicka, V., Kostelecký, J. & Zahradník, J., 2020. The 2018 Mw 6.8 Zakynthos, Greece, earthquake: dominant strike-slip faulting near subducting slab, *Seismol. Res. Lett.,* **91**(2A), 721–732.

Stiros, S., Moschas, F., Feng, L. & Newman, A., 2013. Long-term versus short-term deformation of the meizoseismal area of the 2008 Achaia–Elia (MW 6.4) earthquake in NW Peloponnese, Greece: evidence from historical triangulation and morphotectonic data, *Tectonophysics,* **592,** 150–158.

Stuermer, K., Kummerow, J. & Shapiro, S.A., 2011. Waveform similarity analysis at Cotton Valley, Texas, in *Proceedings of the SEG Technical Program Expanded Abstracts 2011,* San Antonio , Society of Exploration Geophysicists, pp. 1669–1673.

Technological Educational Institute Of Crete, 2006. Seismological Network of Crete. International Federation of Digital Seismograph Networks, https://doi.org/10.7914/SN/HC.

Trugman, D.T. & Shearer, P.M., 2017. GrowClust: a hierarchical clustering algorithm for relative earthquake relocation, with application to the Spanish Springs and Sheldon, Nevada, earthquake sequences, *Seismo. Res. Lett.,* **88**(2A), 379–391.

Tsujiura, M., 1983. Characteristic frequencies for earthquake families and their tectonic implications: evidence from earthquake swarms in the Kanto District, Japan, *Pure Appl. Geophys.,* **121**(4), 573–600.

University Of Athens, 2008. Seismological Laboratory. International Federation of Digital Seismograph Networks, https://doi.org/10.7914/SN/HA.

University Of Patras, G. D., 2000. PSLNET, permanent seismic network operated by the University of Patras, Greece. International Federation of Digital Seismograph Networks, https://doi.org/10.7914/SN/HP.

Wardell, N., Camera, L., Mascle, J., Nicolich, R., Marchi, M. & Barison, E., 2014. The structural framework of the Peloponnese continental margin from Zakynthos to Pylos from seismic reflection and morpho-bathymetric data, *Boll. Geof. Teorica Appl.,* **55**(2), 343–367.

Wells, D.L. & Coppersmith, K.J., 1994. New empirical relationships among magnitude, rupture length, rupture width, rupture area, and surface displacement, *Bull. seism. Soc. Am.,* **84**(4), 974–1002.

Wessel, P., Smith, W.H., Scharroo, R., Luis, J. & Wobbe, F., 2013. Generic mapping tools: improved version released, *EOS, Trans. Am. geophys. Un.,* **94**(45), 409–410.

Yokota, Y., Koketsu, K., Fujii, Y., Satake, K., Sakai, S., Shinohara, M. & Kanazawa, T., 2011. Joint inversion of strong motion, teleseismic, geodetic, and tsunami datasets for the rupture process of the 2011 Tohoku earthquake, *Geophys. Res. Lett.,* **38**(7), doi:10.1029/2011GL050098.

SUPPORTING INFORMATION

Supplementary data available at *GJI* online:

Figure S1 Screenshot of interactive flow diagram for a comparison of clustering results obtained in four different frequency bands, targeting surface waves and body waves. The diagram was produced using the waveform-similarity based clustering toolbox Clusty and data from the 2018/2019 Zakynthos aftershock sequence. Each colour refers to one cluster of earthquakes. The width of connecting bands is proportional to the number of shared events between the results obtained in the different frequency bands.
Figure S2 Moment tensor solutions from Mouslopoulou *et al.* (2020) along with the estimated extent of our clusters, for comparison. MTs of events that were grouped into clusters in our study are coloured according to the cluster they belong to. Offshore faults are adopted from Mouslopoulou *et al.* (2020).

CHAPTER 8

Discussion

In this chapter, I discuss the major findings of this thesis. **Instead of repeating the discussions and conclusions of the single publications, I herein focus on the research questions and objectives that were formulated in chapter 2.** These research questions concern mainly two aspects of seismic source studies in the Alps between 2016 and 2019: (1) The challenges and benefits from working with an outstanding large seismic network like the AASN and (2) addressing the challenges of source studies in a study area with low to moderate magnitude earthquakes, high relief differences and a heterogeneous crustal structure.

8.1 Challenges and opportunities of large seismic networks

Altogether, the AASN and Swath-D comprise more than 700 seismic stations [Heit et al., 2021; Hetényi et al., 2018; AlpArray Seismic Network, 2015]. The even spacing of about 60 km across the AASN and of about 15 km in the Swath-D implies a significant densification of the regional networks [Hetényi et al., 2018; Heit et al., 2021], even in seismically not very active regions. Dealing with such an extensive dataset bears new opportunities for many seismological studies, but also poses new challenges.

8.1.1 Facing data and metadata quality issues

Most generally, the increasing amount of seismic data due to world-wide growing networks as well as large temporary installations leads to a variety of new problems, especially when processing the data routinely using automated procedures like for example machine learning approaches [e.g. Cauzzi et al., 2021]. Accordingly, tools to perform automated (meta-)data quality checks experience an increasing demand.

Seismological analysis such as moment tensor inversion rely on correctly reported station meta data, sensor orientations and low waveform noise levels. When running first CMT inversions in 2017, I found that a significant number of stations could not successfully be used in the inversion. Wrong amplitude gain factors and misoriented stations resulted in increased misfits and unstable inversions. A careful analysis of data and metadata was needed to identify, report and correct malfunctioning stations or metadata.

In the case of the AASN and the Swath-D, long-term PSDs are provided for many stations by the network operators [e.g. Fuchs et al., 2016; Molinari et al., 2016; Govoni et al., 2017; Vecsey et al., 2017]. PSDs provide characterizations of the noise conditions at a seismic station in time periods of days to years. The necessity to assess the data quality of the AASN prior to seismic analysis is confirmed by the study of Kolínský et al. [2019], who removed on average 19% of the AlpArray stations prior to their analysis of Rayleigh wave arrival angles. They followed multiple steps to check the waveform quality including checks for data gaps, visual inspections, comparisons of group velocity dispersion curves, wavefront maps to check phase arrival times and beamforming to check the consistency among neighboring stations [Kolínský et al., 2019].

In order to systematically check all stations of the AASN, I developed the *AutoStatsQ* toolbox presented in chapter 4 [Petersen et al., 2019]. Compared to the noise PSDs, which rely on continuous data of several weeks or months, I follow a different approach using teleseismic earthquakes. This allows using the polarization of incoming Rayleigh waves to check sensor orientations. Additionally, using events with different travel paths avoids bias from large-scale crustal structures which may effect amplitude gains or apparent azimuths when using events from one direction. The reliability of all implemented tests depends on the data availability of azimuthally well distributed teleseismic events. I identified a number of issues covering misoriented sensors, interchanged and locked components, wrong gain factors in the metadata and other errors in the transfer functions.

In the second study in chapter 5, I applied the orientation test to the Turkish KOERI network. The KOERI network covers the Eastern Mediterranean Region, including the North Anatolian fault, and is therefore of great importance for seismic studies. In addition to the Rayleigh-wave polarization test of the *AutoStatsQ* toolbox we used a P-wave polarization method. The P-wave polarization approach relies on particle motions of first arrivals of a large number of distant events located in two azimuthal directions. Time windows of each event are manually checked. Due to the large number of events, the uncertainties are relatively small with standard deviations often below 3°. In contrast, the Rayleigh wave approach in *AutoStatsQ* uses a smaller number of evenly distributed earthquakes. The test is fully automated and hence less time consuming. However, we observe increased standard deviations of 5-8°, as only one event of every azimuthal direction is used and structures along the travel paths may bias the backazimuth estimates. The comparison with the results from the P-wave polarization indicates that we solve the problem of increased uncertainties by using the median instead of the mean of the results from the different directions. We find that the results of both approaches agree well within 10° for 80 % of the stations.

In addition to the two studies which are included as chapters of this thesis, *AutoStatsQ* was used by both network operators and scientists who wanted to check seismic stations prior to further analysis. GEOFON recently included the possibility to detect quality problems of data and metadata using *AutoStatsQ* [Quinteros et al., 2021]. Heit et al. [2021] used the *AutoStatsQ* toolbox to check the orientation of the Swath-D network and found three sensors with >20° misorientation. Evangelidis et al. [2021] followed our approach to test the sensor orientations of the seismic networks of Greece and Cyprus. Cambaz et al. [2021] applied the toolbox in a second study to the KOERI network. In addition, I used the tool to investigate gain problems and sensor orientations prior to single and multi station analyses in Mayotte where only few remote stations are available [Cesca, 2020]. ORFEUS (Observatories & Research Facilities for European Seismology) recently started coordinating workshops on data and metadata quality, where I presented *AutoStatsQ* in September 2020 and February 2021. Furthermore, I recently received the positive respond that future developments of *AutoStatsQ* will be supported by the ORFEUS Software Development Grant to integrate the tool into ORFEUS work flows.

The tests in *AutoStatsQ* are designed for application to broad band stations. Relying on Rayleigh waves for the orientation test, it cannot be applied to short period stations where the frequency content of the Rayleigh waves are significantly below the lower corner frequency of the instrument. Additional tests relying on body waves are currently implemented (see outlook in chapter 9).

The *AutoStatsQ* toolbox uses waveform data to detect gain problems. However, gain errors are often (not always) introduced by wrong transfer functions. Tests to check the consistency and completeness of the metadata of a network are currently not implemented in *AutoStatsQ*. Such checks could comprise for example comparing channel names of waveform data and meta data and checking the dip and azimuth angles of the components. P. Kolinsky (University of Vienna, ORFEUS quality workshop 2021) additionally suggests to check poles and zeros against a database of all sensors that are used on a regular basis. Compared to downloading and processing all waveform data, the metadata checks would be faster. Yet, following this approach alone, errors in the waveform data could not be detected. Therefore, the metadata checks would not replace the tests currently included in *AutoStatsQ*, but would be performed additionally. Among other recently developed and publicly available tools is, for example, the Seismic Data (and metadata) Amplitude Anomaly Score (*sdaas*, https://github.com/rizac/sdaas, last access Feb. 2021). This program detects anomalies in the waveform amplitudes of seismic data using a pre-trained isolation forest model. The tool can detect suspicious amplitude gains with a rating between 0 and 1, while it does not provide correction factors like *AutoStatsQ*. Additional tests, e.g. on sensor orientations, are not implemented. Other new data and metadata testing approaches within the ORFEUS community are currently under development for example by P. Kolinsky (University of Vienna) and L. Vecsey (Czech Academy of Sciences). I am in contact with these researchers to share our experiences towards the development of consistent data and metadata checks (see also outlook in chapter 9).

The various applications of *AutoStatsQ* to the AASN and other networks have shown that regular checks of seismic stations are needed in order to avoid bias in seismological studies due to wrong gains or orientations.

8.1.2 Opportunities for source studies in the Alps

The temporarily densified network allows lowering the detection threshold of small magnitude earthquakes and provides the opportunity to perform high quality MT inversions for moderate earthquakes in the entire study area with a constant good azimuthal station coverage (chapter 6, Petersen et al. [2021a]). In general, CMT inversion in the Alps is challenging due to three main factors: (1) Seismicity in the Alps is low to moderate with Mw>4.0 events mainly occurring in the SE Alps and the neighboring areas in the N Dinarides and N Apennines [e.g. Faenza et al., 2009]. (2) High topographic relief differences between the Alpine foreland, mountains and valleys exist, and (3) the crustal structure is extremely complex with subducted, accreted and tilted blocks, which lead to significant heterogeneities in the subsurface velocities [e.g. Handy et al., 2010; Hetényi et al., 2018; Diehl et al., 2009; Molinari et al., 2015; Kästle et al., 2018].

Moment tensor solutions for earthquakes with magnitudes above Mw 4.0 or Mw 3.5 are provided by regional research institutes in online bulletins and yearly reports (see also Introduction, chapter 1). Due to the rather low seismicity in the Alpine mountains, these comprise only few MT solutions per year. As an example, INGV published two MT solutions for Alpine earthquakes in 2018 [Scognamiglio et al., 2006]. In the same year, GEOFON published only a single MT solution for earthquakes in the Alps (https://geofon.gfz-potsdam.de/eqinfo/list.php, last access March 2021) and the reports on earthquakes in Switzerland contain two MT solutions for 2018 [Diehl et al., 2021].

In our study, we addressed the challenges of source studies of Alpine earthquakes with magnitudes below Mw 4.0 in order to increase the number of available CMT solutions in the study region. In theory, two approaches can be followed. Either the forward modeling of synthetic waveforms can be improved to better fit the observed waveforms at higher frequencies, or features of the observed waveforms can be extracted to simplify the input data of the inversion.

The first approach depends on the availability of detailed crustal velocity models, which are not yet available for the Alps. Ideally, these would be 3-D models including topography and with a high resolution to forward model path effects of P and S phases in frequency ranges »0.1 Hz. Wang and Zhan [2020] have recently shown that 3-D velocity models can significantly improve the amplitude and phase fits of Ml$\geq$3.5 events in California. The recent publications by Kühn et al. [2020] and Dost et al. [2020] show that full moment tensor solutions can be computed for earthquakes with Mw$\geq$2.0 when representative (1-D) velocity models are available and the seismic network is sufficiently dense. They used 15 stations located within 10 km distance, complemented by more distant stations, and show that variations in the velocity model can result in shifts in the centroid location, rotated mechanisms and unstable CLVD components [Kühn et al., 2020]. Similar tests on our own CMT inversions of regional Alpine earthquakes (Mw>3.3) using surface waves indicate that these are not strongly influenced by changes in the velocity model. However, when testing higher frequencies (>0.1 Hz), the forward modeled P and S phases do not match the complex recorded ones. Furthermore, the station spacing of more than 50 km in the AASN is much larger than that of comparable studies on small earthquakes [e.g. Kühn et al., 2020]. At the time of writing this thesis, improved velocity models are being computed for the Swath-D and other regions by other projects within the AlpArray initiative (see Outlook chapter 9).

In my thesis, I relied on the second approach to handle the challenges of MT inversion for small earthquakes and tested many options to combine the time domain full waveforms in the CMT inversion with extracted waveform features. Following the examples by Cesca et al. [2010, 2013] and Domingues et al. [2013], I combined the time domain full waveforms with amplitude spectra. Amplitude spectra are less sensitive to trace misalignments and phase shifts, which may result from simplified velocity models. Additionally, I tested cross-correlation based fitting approaches [e.g. Stähler and Sigloch, 2014; Kühn et al., 2020] of the full time domain waveforms, which are not disturbed by mismodeled amplitudes [e.g. Cabieces et al., 2020] as amplitudes are normalized. Furthermore I followed the ideas of Zahradník and Sokos [2018] and Dahal and Ebel [2020] and implemented simplified and smoothed waveform envelopes, although the simplification results in a limited precision. In Petersen et al. [2021a] I combined all these input data types in various ways and investigated their ability to resolve the focal mechanisms of test events in multiple frequency bands between 100 s and 0.7 Hz. In chapter 6 I showed how more than 50 stations were used to study the effect of large azimuthal gaps. These tests require a large number of stations in different distances as provided by the AASN. In addition, the dense network allowed us to study the azimuthal dependency of the resolution of non-DC components. The developed guide lines allow to invert for most earthquakes with magnitudes Mw$\geq$3.3 and some additional smaller ones. Thanks to the AlpArray seismic network, our methodological tests and the developed guidelines, we were able to report MT solutions for 75 earthquakes in the Alps and neighboring regions. For 40 % of these earthquakes, no solutions were provided by the regional research centers and institutes.

For earthquakes with magnitudes below Mw 3.3 the SNR of surface waves is at limit. The decrease of the SNR (or even the excitation) of surface waves with decreasing magnitudes may be related to the smaller source dimensions [Wyss and Brune, 1968]. Most often, we can only use a few seismic stations within a distance of less than 100 km and in some cases the surface waves are not distinct enough for MT inversion. Within the average station spacing of 60 km significant changes in the topography and the subsurface structure of the Alpine mountain belt hinder forward modeling body waves (>0.1 Hz) sufficiently well, even when relying on extracted waveform features. However, in areas of low to moderate seismic activity like the Alps, lower magnitude earthquakes are important to consider when studying active faults [compare also Ebel, 2008; Brodsky, 2019; Ross et al., 2019], as discussed in section 8.3.

8.2 Seismic source processes in the Alps and their link to tectonic state

Relying on the results of the quality control and the tests of inversion set-ups, moment tensor solutions for 75 earthquakes with magnitudes Mw$\geq$3.1 were obtained (see also chapter 6, Petersen et al. [2021a]). Due to the limited time span of the temporary installation of the seismic network, I additionally collected moment tensor solutions of various available catalogs since the 1970ies. These joined catalogs from INGV, GEOFON, EM- RCMT, SISMOAZUR, SED and ARSO comprise about 330 earthquakes. Most of these earthquakes are located in the Apennines, the SE Alps and in the Northern Dinarides. Significantly less solutions are available across the Alps (see also Fig. 9 in Petersen et al. [2021a], chapter 6). While many other publications focus on local features in the Alps, I decided to study the bigger picture across the entire mountain range and neighboring regions, analyzing the seismic activity and dominant faulting mechanisms as well as deformation regimes (chapter 6).

Due to the previously discussed challenges of MT inversion for small earthquakes (i.e. unmodeled path effects, low SNR of surface waves) the total number of MT solutions to study a large region like the Alps is rather small. However, 75 earthquakes (Mw$\geq$3.1) for the years 2016-2019 imply an increase of 40 % compared to the number of events in the joined catalogs for the same time period. In a highly complex region like the Alps the number of available MT solutions limit the study of single faults or fault systems. Even when considering the published MT solutions of the last decades, many empty spots on the map remain and detailed studies of single faults are not possible. In order to study the deformation regimes across the entire mountain belt, I compared spatial patterns of pressure and tension axis and performed stress inversions using my own MT inversion results as well as published MT solutions. Additionally including the seismic activity of the past decades, historical large events and strain data, allows identifying and characterizing different seismo-tectonic domains of the Alps.

I identified clusters of increased seismic activity, namely in the eastern Southern Alps, the Lake Garda region in the central Southern Alps, the Western Alps, as well as the Northern Dinarides and the Northern Apennines in the vicinity of the Alps. In contrast, seismicity is particularly low in the Eastern Alps and in parts of the Central Alps, as also described by low values of seismic hazard on regional hazard maps [Giardini et al., 2014]. Compared to the Apennines, seismicity can be described as low across the entire Alps, except for the eastern Southern Alps.

The orientation of P and T axis of the MT solutions across the mountain range indicate varying dominant deformation regimes from extensional regimes in the Western Alps to compressional regimes in the eastern Southern Alps. These deformation regimes are in agreement with observations from geological and tectonic studies. The N-S convergence of Africa and Europe led to the subduction of the European plate underneath the Adriatic micro plate and to the counter-clockwise rotation of the Adriatic micro plate relative to Europe [D'Agostino et al., 2008; Le Breton et al., 2017; Le Breton et al., 2021]. Since Neogene the rotation has resulted in higher convergence rates in the eastern Southern Alps than in the Western Alps [Le Breton et al., 2017; Le Breton et al., 2021; Van Hinsbergen et al., 2020]. This in agreement with higher recent measurements from GPS data [e.g. D'Agostino et al., 2008] as well as higher seismicity rates in the eastern Southern Alps [Petersen et al., 2021a].

Typical ENE-WSW to E-W striking thrust faulting, related to the convergence of Adria and Europe and the resulting underthrusting of the Friuli Plain beneath the Alps [Cipar, 1980] is mainly observed in the Southern Alps and has been reported in publicly available earthquake catalogs as well as in many studies on the 1976 Friuli earthquake and ongoing seismic activity [e.g. Pondrelli et al., 2001, 2006; Slejko, 2018; Poli and Zanferrari, 2018; Bressan et al., 1998]. The distribution of devastating historical earthquakes points at the increased seismic hazard in the SE Alps. Strike-slip faulting with similarly oriented P-axis compared to the thrust events in the SE Alps is observed in the northern Dinarides as well as along the northern margin of the Alps. The strike-slip faulting earthquakes in the northern Dinarides are in agreement with the right-lateral strike-slip faults [Moulin et al., 2016] and support the assumption of a distributed activity of faults, rather than a single major structure, as recently proposed by Grützner et al. [2021]. The dominant normal faulting events in the NW Alps point at an extensional regime, supported by the absence of significant horizontal strain and relatively high uplift rates. Extensional patterns of focal mechanisms in the W Alps have been described in various studies [e.g. Sue et al., 1999, 2007]. The stress map of the Mediterranean and Central Europe shows similarly oriented tensional axes [Heidbach et al., 2016]. Recent GPS measurement indicate very little horizontal movement in the Alps. Therefore, the high uplift rates need to be attributed to other causes then the N-S convergence [Sternai et al., 2019].

While our study of CMT solutions in the Alps provides an overview of dominant regional faulting patterns and seismotectonic activity across the mountain range, the number of MT solutions alone does not allow studying single faults in greater detail. The number of earthquakes with moment tensor solutions is in many regions too small to perform stable stress inversions and to characterize local patterns in detail.

8.3 Why small earthquakes matter: Inclusion of earthquakes with Mw<3 to study active faults

I have discussed above that CMT inversion of earthquakes with low magnitudes in the Alps is a challenging task. Especially in study areas where few Mw>4 events per year or in the case of limited monitoring periods, including earthquakes with low magnitudes can be crucial to identify and characterize active faults and fault systems [e.g. Ross et al., 2019]. The extent and the stress state of seismogenic faults is of major interest for seismic hazard assessment. Following the Gutenberg-Richter law, decreasing the lower bound of the earthquakes taken into account by one or two magnitude units, respectively, will increase the number of earthquakes by a factor of ten or even 100 [Gutenberg and Richter, 1944]. Thus, seismic fault studies can benefit greatly from lowering the magnitude threshold of the considered set of events. Additionally, small earthquakes may pose a significant hazard, when located at shallow depth [Briseghella et al., 2019] or acting as triggers for landslides or avalanches [Pérez-Guillén et al., 2014].

To map the extent, geometry and orientation of a seismic fault based on seismicity, earthquakes that occur on the same fault need to be identified. Approaches to find clusters of events can rely on obtained focal mechanisms [e.g. Cesca, 2020], locations [e.g. Ouillon and Sornette, 2011] or directly on waveforms [Shearer et al., 2003]. A clustering of earthquakes based on focal mechanisms requires the possibility to compute these in the first place. For small magnitude earthquakes focal mechanisms are often obtained from first motion polarity readings, in case a sufficient number of stations records distinct phase onsets. However, these mechanisms are only representative for the very first moment of the rupture process and the instability of the take-off angles of shallow events may introduce significant errors [Hardebeck and Shearer, 2002].

The clustering of earthquakes based on their locations is often applied to study seismogenic processes and to group events pertaining to the same fault. Ouillon and Sornette [2011] use a spatial clustering approach to identify active faults and fault patches in California. They infer the existence of a deformation zone around the faults rather than smooth faults planes. Mouslopoulou and Hristopulos [2011] study clusters of relocated events and propose the interaction of several neighboring faults. Location based clustering approaches assume that closely located earthquakes belong to the same fault. The measure of closeness is herein relative and defined with respect to the distribution of all events that are considered. Differences between waveforms of earthquakes in the same cluster are not taken into account and therefore the existence of multiple different faulting mechanisms within one location-based cluster can remain undetected. In the case of a complex fault system with multiple faults in close proximity (*bookshelf structures, en-echelon structures*), a location-based approach is therefore not sufficient.

We developed the clustering toolbox *Clusty* to respond to the necessity of including waveforms recorded across a seismic network in the clustering of earthquakes (Chapter 7). Seismic waveforms are sensitive to location and mechanism, therefore this clustering approach helps fault characterization. Maurer and Deichmann [1995] studied micro earthquake clusters in the Swiss Alps using a waveform-similarity clustering approach and confirmed that the active fault planes of two clusters correspond to mapped structures in the study area. Shearer et al. [2003] compute waveform cross-correlations to study >14000 aftershocks of the 1994 Northridge Mw 6.7 earthquake in California. Based on relocations they infer the extent and orientation of possible fault planes and suggest a complex aftershock activity. In the development of the waveform-based network similarity clustering toolbox *Clusty*, we follow these approaches and include a number of different options to compute the network similarity from the waveform similarities obtained at multiple seismic stations. These options are based on the work of Aster and Scott [1993]; Maurer and Deichmann [1995]; Shelly et al. [2016] and Stuermer et al. [2011]. By taking into account the waveform similarity on a network of stations instead of a single station, a larger portion of the radiation pattern is considered. Further, this allows comparing earthquakes even when parts of the stations have data gaps. By offering a number of different methods to compute the network similarity, it is possible to compare results to other studies and to compare the stability of results obtained from the different methods. The design of the clustering tool is flexible and transparent in order to facilitate its application to a large number of different data sets. The tool follows an automated work-flow, which does not require any manual preprocessing of the input waveform data. The user of the toolbox benefits from a large number of graphical output, which allows assessing not only the final results, but also allows for evaluating the similarity of earthquakes within a cluster and among different clusters. In our opinion to evaluate both is necessary to avoid a black box-like usage of any clustering algorithm. Therefore multiple settings can (and should always) be tested at the same time.

As a test data set for our toolbox we chose the aftershock sequence of the Zakynthos 2018 Mw 6.8 earthquake, which comprises >2300 earthquakes (Mw $\geq$2.8) in a complex and heterogeneous study area [Mouslopoulou et al., 2020]. We showed that the density-based (chain-like) clustering approach helps to recognize earthquakes on a common fault even over long fault segments, when gradual changes of the waveforms occur due to location differences [Petersen et al., 2021b]. The first-order geometry and extent of active faults can be inferred from the extent of the clusters. For each cluster, I performed CMT inversions of representative events. The joint analysis of the representative mechanism and the distribution of earthquakes belonging to the same cluster sheds light on the geometry of the active fault plane and helps to distinguish fault plane and auxiliary plane. Based on our clustering analysis, we propose the existence of conjugated strike-slip faults located to the south of the study area and reveal event clusters, which cannot be discriminated based on the event locations alone.

The clustering toolbox was developed with the seismotectonic setting of the Alps in mind. To study the state, orientation and extent of active faults, a sufficient number of earthquakes that map this fault is needed. As the seismic activity is rather low, we need to rely on small magnitude events for this purpose. Multiple co-located faults of different orientation and mechanisms are plausible in the Alpine setting with a heterogeneous crustal structure. Therefore we implemented a waveform-based clustering toolbox rather than relying on the locations and the few mechanisms for larger events alone. Future applications to the earthquakes in the Alps are based on enhanced seismicity catalogs, which are currently developed in the course of the AlpArray initiative. In the outlook in chapter 9 I discuss in detail the ongoing work. I expect that *Clusty* can enhance the knowledge on active faults and provide insight into ongoing seismo-tectonic processes in the Alpine mountain belt. *Clusty* allows for combining various frequency bands, which will help to include micro earthquakes in the analysis of the Alpine seismicity.

8.4 Towards a semi-automated work flow of source studies in the Alps

One aim of this thesis was the development of a reliable and replicable work flow to study source processes in the Alps. In our research questions, I raise the issue of an automation of such a work flow. Fully automated determinations of source mechanisms and their fast distribution have been addressed since the beginning of fast data transfer via the Internet [Kawakatsu, 1995; Pasyanos et al., 1996]. Providing fast and reliable MT solutions is of great importance to quickly estimate the potential damage of large earthquakes and their tsunami potential [e.g. Kanamori and Rivera, 2008]. Furthermore, an automation of inversion approaches is required in the case of large numbers of earthquakes for which manual adjustments of inversion set-ups would result in excessive work loads [e.g. Trifu et al., 2000]. Nowadays, automated CMT solutions are determined by a variety of regional to global data centers and provided in online bulletins, mostly focusing on moderate to large earthquakes (Mw>4.0). Recently developed approaches automatize not only the inversion procedure itself, using a fixed configuration, but also the selection of inversion settings like for example the station weighting based on noise levels and the selection of frequency ranges with a high SNR [Vackář et al., 2017]. Approaches are developed and improved for regional and local seismic activity [e.g. Bernardi et al., 2004; Clinton et al., 2006; Vackář et al., 2017; Niksejel et al., 2020], but also for mining-induced seismicity with magnitudes below Ml 2.0 [Sen et al., 2013].

Large magnitude events are rarely observed in the Alps and additionally the total number of earthquakes for which a MT inversion is feasible is limited. Therefore, a very fast and fully automated approach is not strictly required. However, guidelines developed towards an automation are interesting, because they reflect a high degree of generalization. This provides reproducible work flows and lowers the workload for subsequent MT inversions in the study area. Further, the testing procedure itself, which was performed to find appropriate inversion set-ups (chapter 6, Petersen et al. [2021a]), may serve as a guideline for other study areas.

Concerning the presented full work flow from quality control to the study of faulting mechanisms and active faults, several steps are automated. The quality control toolbox *AutoStatsQ* was presented in chapter 4 [Petersen et al., 2019]. The toolbox is highly automated and does not require any manual preprocessing. It is applicable to large seismic networks as well as single stations. In the future, I plan to extend the toolbox so that it will update the quality checks, whenever a large teleseismic event occurs and raise warning if changes are detected (see outlook, chapter 9).

The implemented checks are independent of the target earthquake of the MT inversion. Therefore an additional check of the SNR of the waveform data is needed in the CMT inversion, as part of the utilized CMT inversion tool *Grond* [Heimann et al., 2018]. I implemented the option to use automatically selected precomputed Green's function databases [Heimann et al., 2019], based either on the location of single seismic stations or on the earthquake epicenter. Our methodological tests (chapter 6) provide guidelines for the selection of input data types as well as frequency and distance ranges, which is helpful towards automation. However, in the case of high misfits, these settings need to be adjusted reflecting varying station availability and noise levels. Compared to our relatively wide frequency range, Barth et al. [2007] follow another approach and perform their MT inversions in parallel in multiple narrow frequency bands (8 mHz) between 0.01 and 0.029 Hz. They compare the variance of the different solutions and observe rotations between the solutions as well as varying uncertainties. By relying on a wider frequency band instead, I avoid the danger of mismatching phases and cover a larger range of magnitudes that can be inverted for with the same setting. As we study lower magnitude earthquakes, SNRs are low at the frequency band of 0.01-0.03 Hz. Other approaches towards automated MT inversions propose an automated selection of a subset of close and well distributed seismic stations to accelerate the inversions [Jian et al., 2018]. I do not follow similar approaches in our study because I want to use as many stations as possible in the inversions to obtain reliable solutions. I therefore select stations based on the quality checks conducted beforehand, the SNR of the waveforms and a maximum distance estimate based on the methodological tests. In chapter 6 [Petersen et al., 2021a] I additionally discuss the influence of gaps in the azimuthal distribution of seismic stations. In order to avoid running MT inversions when the number of stations or the azimuthal coverage is insufficient, I implemented an optional check on the distribution of seismic stations. Finally, *Grond* [Heimann et al., 2018; Kühn et al., 2020] provides the user with uncertainties by running all inversions in multiple independent bootstrap-chains. I assessed the stability of the CMT solutions manually and evaluated whether adjustments are needed.

In order to include smaller earthquakes into the analysis of active faults we presented the toolbox *Clusty* in chapter 7 [Petersen et al., 2021b]. This tool is easily applicable to new datasets and provides a semi-automated work flow. Figures and output are generated automatically, but the user has to select the appropriate clustering settings. The selection of clustering parameters is facilitated by the option to run different settings in parallel. Analysis plots are provided to choose the appropriate set-up among the parallel runs. This cannot be automated further. The final choice of settings depends on the aim of the study, e.g. finding earthquakes of a general agreement in mechanism or repeaters, as well as on the geological setting. Subsurface heterogeneities define how much waveforms of neighboring earthquakes change.

To sum it up, the methodological steps presented in this thesis comprise quality control, CMT inversions and waveform based clustering. The two toolboxes for quality control and clustering are designed as automated as possible, keeping in mind high flexibility and user-friendliness. The CMT inversion work flow is not automated, but the methodological tests provide guidelines for inversions in the Alps and serve concepts for optimizing inversion set-ups in other study areas.

CHAPTER 9

Outlook

The AlpArray seismic network was a temporary densification of the regional networks in the Alpine area. Operation times of the majority of stations has ended by the time this thesis is finalized. While some stations may remain as new permanent installations, future earthquakes in the Alps will not be reported by such a large and dense network.

The first part of the thesis dealt with the development of a toolbox for automated quality control of seismic metadata and waveform data, *AutoStatsQ*. In the two publications I applied the tool to the AlpArray seismic network and the KOERI network. The results of the two studies were published and network operators informed so that future studies can hopefully rely on higher quality datasets. The *AutoStatsQ* tool has proven to be helpful to a wide community of users for checks of single stations, small local networks, as well as large regional networks with several hundreds of stations. As pointed out in the Discussion, it is currently used by the world-wide network operator GEOFON [Quinteros et al., 2021] among others and further applications to other seismic networks are in preparation (e.g. AFAD). The tool was developed and published in 2019 and has been maintained since then. New functionalities were added with ongoing testing. These new features comprise a check for significant timing errors in the order of > 2s and the possibility to check gains and orientations in a second interactive mode using body waves. This can also be applied for short period stations, but needs further testing. L. Vecsey (Czech academy of Sciences) recently presented a new methodology to obtain sensor orientations with greater precision at the ORFEUS data quality workshop. In this approach, Rayleigh waves recorded at multiple closely located stations are used to determine the orientation of the horizontal components of a single station. By including several stations in the analysis of each station, the result is obtained relative to a dynamic backazimuth instead of a fixed, theoretical backazimuth. This prevents bias of the result due to travel paths deviating from the theoretical backazimuth. A precision of 1-2 degrees can be achieved (L. Vecsey, pers. communication) compared to standard deviations of 5-10 degrees of the single station approach. Kolínský et al. [2019] have shown that the Rayleigh wave arrival angles of teleseismic events at the stations of the AlpArray seismic network can be influenced by huge structural anomalies. The single-station approach included in *AutoStatsQ* is sufficient to identify large misorientations, but is not able to obtain a precision higher than that of hand held magnetic compasses. Despite the increased standard deviation, we have shown in chapter 5 [Büyükakpınar et al., 2021] that the median of the results for azimuthally distributed events agrees well with a more precise P polarization approach. In the near future, I am planning to collaborate with L. Vecsey to integrate the extended multi station approach into *AutoStatsQ*. This will allow to obtain precise orientations of stations where physical (re-)measurements with a gyrocompass are not possible.

Since the time of development of the *AutoStatsQ* toolbox new versions of python packages that are used within the tool were distributed. Therefore the maintenance of the toolbox is an ongoing task. Although both the maintenance and as well as providing help for users is time consuming, the positive feedback of the seismological community is motivating me to continue this work. Starting in June 2021, the development of an automated update add-on included in *AutoStatsQ* for implementations at data centers will be supported by the ORFEUS software development grant.

The second major part of this thesis dealt with analyzing the source processes of earthquakes in the Alps with magnitude Mw$\geq$3.1. I found that for magnitudes from Mw 3.1 to Mw 3.3 I often struggled with instable solutions resulting from low SNRs of surface waves and significant path effects at higher frequency body waves due to insufficient velocity models. For some regions of the Alps, new velocity models are currently developed in the AlpArray project. I will test these new models in the inversions for the earthquakes for which we were not yet able to obtain stable solutions. Furthermore, I want to include topographic effects in the forward modeling of waveform data. While these effects are negligible when using low frequency surface waves, their effects on higher frequency body waves might need to be considered.

At the time of writing this thesis, other subprojects in the AlpArray initiative develop new, detailed velocity models and detect and relocate micro earthquakes within the very dense Swath-D network in the Eastern Alps [Jozi Najafabadi et al., 2020; Hofman et al., 2020]. When this work is finalized, we plan to investigate the area in more detail by performing MT inversions using the new velocity models and by applying the waveform based clustering toolbox, which was developed in the course of this thesis. In a first feasibility test, I have applied the tool to a small seismic sequence in the SE Alps in June 2019 (Fig. 9.1). The sequence consists of three earthquakes with $Mw>3.0$ and ten earthquakes with $2.1\geq Mw>1.0$ in close proximity, obtained from the catalog of the INGV. Additionally, R. Hoffman detected >30 micro earthquakes, which are not yet relocated. I applied *Clusty* to the waveforms recorded at stations in up to 100 km distance and find high waveform similarity among those events with Mw 1.0 or larger. I plan to continue this study as soon as detections and relocations of the entire operation time of the Swath-D seismic network are available. By using multiple frequency bands, I assume that events with magnitudes below Mw 1.0 can be included in the analysis. The clusters of relocated events will shed light on active faults. For each cluster, the tool provides one representative event, which is the earthquake that is most similar to all other earthquakes in the cluster. I plan to run CMT inversions for these events, as shown for the Zakynthos application example in chapter 7 [Petersen et al., 2021b]. In cases where I am not able to obtain a stable result, I will make use of the option to stack all waveforms of the earthquakes belonging to the same cluster to emphasize their characteristic features. The stacked waveforms can be used for a subsequent MT inversion, assuming a fixed location.

When identifying earthquake clusters of high waveform similarity, one cannot simply map the value of similarity into a value of maximum rotation between two focal mechanisms. We are planning to implement an additional tool to assess the maximum possible rotation by forward modeling waveforms from random mechanisms and comparing them to waveforms from a reference mechanism. This will allow the user of the clustering toolbox to better understand the physical meaning of the achieved network similarity values and it can help to understand the variability among earthquakes that belong to a common cluster.

Clusty is currently applied to new datasets, among them a dataset of induced seismicity offshore Spain [Cesca et al., 2021, in review] and an acoustic emission dataset from an in-situ hydraulic fracturing experiment in the Äspo hard rock laboratory in Sweden [Niemz et al., 2020, 2021]. Promising first results show that *Clusty* provides new insights into the growth of induced fractures [Niemz et al., 2021]. These applications demonstrate that the toolbox can be used across large magnitude scales, from $M<3.0$ to $M>5$, and for a wide spatial range, with rock volumes ranging from several square meters to regional earthquake sequences. Similar to the *AutoStatsQ* toolbox, *Clusty* is part of the Pyrocko ecosystem [Heimann et al., 2017]. As for all software developments, maintenance and user support is an ongoing task. I am convinced that the tool will be applied to many more heterogeneous datasets in the future.

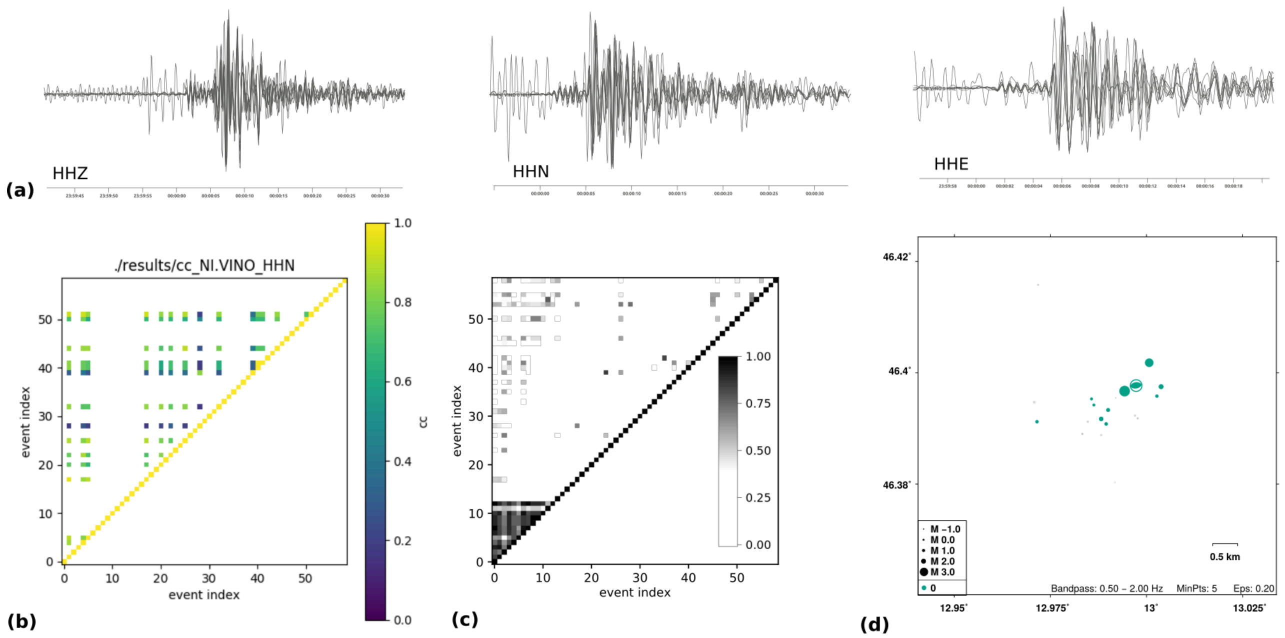

Figure 9.1: Feasibility test for the application of the clustering toolbox *Clusty* to a seismic sequence in the SE Alps, June 2019. Results were obtained using a bandpass filter from 0.5 to 2 Hz and P and S phases. (a) Stacked waveforms of result cluster at station NI.VINO. (b) Cross-correlation coefficient at N component. Only events with a SNR above 1.5 considered. (c) Max. cross-correlation of all stations as a first proxy for event similarity. (Method only used for a first test, as it may not be representative for the similarity of the events across the entire network [cf. Petersen et al., 2021b]). (d) Map view of clustered earthquakes. Note that many events overlap as they have fixed positions of the master event from the detection. Relocations may in future shed light onto the geometry of the activated faults.

CHAPTER 10

Conclusions

This thesis investigates local earthquakes in the Alps employing multiple methods: The development of an automated (meta-)data quality control toolbox laid the groundwork for the performance of CMT inversions, which generated new interpretations in the seismo-tectonic context. A waveform-based clustering tool was developed to further exploit the potential of small earthquakes for the study of seismic faults in complex tectonic settings.

With world-wide growing seismic datasets like that of the AlpArray seismic network the demand for automated quality assessment is increasing. The development of a flexible and automated toolbox for metadata and data quality control facilitates a more effective use of these large datasets, avoiding bias from e.g. misoriented sensors or erroneous amplitude gain factors. Within and beyond the AlpArray initiative, *AutoStatsQ* has been met with sustained interest and it has been applied to multiple networks.

The detailed analysis of four years of moment tensor solutions was based on extensive methodological tests. The results of this work enhanced the number of moment tensor solutions for earthquakes occurring between 2016 and 2019. Against this backdrop, a joint study, which included long-term seismicity, historical earthquakes, stress inversion and strain from GNSS data, charted spatial patterns of dominant deformation in the heterogeneous tectonic setting of the Alps. Operating with a limited time frame these patterns still prove to be representative of long-term seismological observations. This demonstrates the potential of temporary dense deployments for seismic source studies even in complex tectonic settings.

Small earthquakes are key to study active faults in areas of low to moderate seismicity or in the case of short deployment times of seismic networks. A waveform-based network similarity clustering tool was developed to meet the specific challenges arising from the low signal-to-noise ratios and complex waveform data. In order to shed light on the extent and geometry of active faults, the presented toolbox *Clusty* can be applied across multiple magnitude and spatial scales. Joining the obtained earthquake clusters with representative MT solutions can enlarge the knowledge about the complex fault systems, as we have shown in the case study of offshore Zakynthos, Greece. Additionally, it helped distinguishing the fault and auxiliary plane of moment tensors.

The outlook of this work presents ongoing and future implementations of new features and sketches out ideas for the application of the developed tools to new use cases. The usage of new velocity models in the MT inversions and the application of the waveform-based clustering tool to the Alps will hopefully provide new insights into active seismic faults at local scale. This will be of importance for understanding the link between the recent tectonic evolution and the seismic activity, and may provide information for future seismic hazard studies.

Bibliography

AlpArray Seismic Network (2015). AlpArray Seismic Network (AASN) temporary component. AlpArray Working Group. Other/Seismic Network.

Amante, C. and Eakins, B. (2009). ETOPO1 1 Arc-Minute Global Relief Model: Procedures, Data Sources and Analysis. NOAA Technical Memorandum NESDIS NGDC-24. *National Geophysical Data Center, NOAA.*

Anderlini, L., Serpelloni, E., Tolomei, C., De Martini, P. M., Pezzo, G., Gualandi, A., and Spada, G. (2020). New insights into active tectonics and seismogenic potential of the Italian Southern Alps from vertical geodetic velocities. *Solid Earth*, 11(5):1681–1698.

Aster, R. C. and Scott, J. (1993). Comprehensive characterization of waveform similarity in microearthquake data sets. *Bulletin of the Seismological Society of America*, 83(4):1307–1314.

Barth, A., Wenzel, F., and Giardini, D. (2007). Frequency sensitive moment tensor inversion for light to moderate magnitude earthquakes in eastern Africa. *Geophys. Res. Let.*, 34.

Bentz, S., Martínez-Garzón, P., Kwiatek, G., Bohnhoff, M., and Renner, J. (2018). Sensitivity of full moment tensors to data preprocessing and inversion parameters: A case study from the salton sea geothermal field. *Bulletin of the Seismological Society of America*, 108(2):588–603.

Bernardi, F., Braunmiller, J., Kradolfer, U., and Giardini, D. (2004). Automatic regional moment tensor inversion in the European-Mediterranean region. *Geophysical Journal International*, 157(2):703–716.

Bressan, G., Snidarcig, A., and Venturini, C. (1998). Present state of tectonic stress of the Friuli area (eastern Southern Alps). *Tectonophysics*, 292:211–227.

Briseghella, B., Demartino, C., Fiore, A., Nuti, C., Sulpizio, C., Vanzi, I., Lavorato, D., and Fiorentino, G. (2019). Preliminary data and field observations of the 21st August 2017 Ischia earthquake. *Bulletin of Earthquake Engineering*, 17(3):1221–1256.

Brodsky, E. E. (2019). The importance of studying small earthquakes. *Science*, 364(6442):736–737.

Büyükakpınar, P., Aktar, M., Petersen, G. M., and Köseoğlu, A. (2021). Orientations of Broadband Stations of the KOERI Seismic Network (Turkey) from Two Independent Methods: P-and Rayleigh-Wave Polarization. *Seismological Research Letters.*

Cabieces, R., Buforn, E., Cesca, S., and Pazos, A. (2020). Focal parameters of earthquakes offshore Cape St. Vincent using an amphibious network. *Pure and Applied Geophysics*, pages 1–20.

Cambaz, M. D., Özer, M., Güneş, Y., Ergün, T., Öğütcü, Z., Altuncu-Poyraz, S., Köseoğlu, A., Turhan, F., Yilmazer, M., Kekovali, K., et al. (2021). Evolution of the Kandilli Observatory and Earthquake Research Institute (KOERI) Seismic Network and the Data Center Facilities as a Primary Node of EIDA. *Seismological Research Letters.*

Cauzzi, C., Custódio, S., Evangelidis, C. P., Lanzano, G., Luzi, L., Ottemöller, L., Pedersen, H., and Sleeman, R. (2021). Preface to the Focus Section on European Seismic Networks and Associated Services and Products. *Seismological Society of America*, 92(3):1483–1490.

Cesca, S. (2020). Seiscloud, a tool for density-based seismicity clustering and visualization. *J Seismology*, 24:443–457.

Cesca, S., Heimann, S., Stammler, K., and Dahm, T. (2010). Automated procedure for point and kinematic source inversion at regional distances. *Journal of Geophysical Research: Solid Earth*, 115(B6).

Cesca, S., Rohr, A., and Dahm, T. (2013). Discrimination of induced seismicity by full moment tensor inversion and decomposition. *Journal of seismology*, 17(1):147–163.

Cheloni, D., D'Agostino, N., and Selvaggi, G. (2014). Interseismic coupling, seismic potential, and earthquake recurrence on the southern front of the Eastern Alps (NE Italy). *Journal of Geophysical Research: Solid Earth*, 119(5):4448–4468.

Cipar, J. (1980). Teleseismic observations of the 1976 Friuli, Italy earthquake sequence. *Bulletin of the Seismological Society of America*, 70(4):963–983.

Clinton, J. F., Hauksson, E., and Solanki, K. (2006). An evaluation of the SCSN moment tensor solutions: robustness of the M w magnitude scale, style of faulting, and automation of the method. *Bulletin of the Seismological Society of America*, 96(5):1689–1705.

D'Agostino, N., Avallone, A., Cheloni, D., D'anastasio, E., Mantenuto, S., and Selvaggi, G. (2008). Active tectonics of the Adriatic region from GPS and earthquake slip vectors. *Journal of Geophysical Research: Solid Earth*, 113(B12).

Dahal, N. R. and Ebel, J. E. (2020). Method for Determination of Focal Mechanisms of magnitude 2.5-4.0 Earthquakes Recorded by a Sparse Regional Seismic Network. *BSSA*.

Dahm, T. and Krüger, F. (2014). Moment tensor inversion and moment tensor interpretation. *Bohrmann, P: New Manual of Seismological Observatory Practice 2 (NMSOP-2), Deutsches GeoForschungsZentrum GFZ*, pages 1–37.

Delacou, B., Sue, C., Champagnac, J.-D., and Burkhard, M. (2004). Present-day geodynamics in the bend of the western and central Alps as constrained by earthquake analysis. *Geophysical Journal International*, 158(2):753–774.

Delouis, B. (2014). FMNEAR: Determination of focal mechanism and first estimate of rupture directivity using near-source records and a linear distribution of point sources. *Bulletin of the Seismological Society of America*, 104(3):1479–1500.

Diehl, T., Clinton, J., Cauzzi, C., Kraft, T., Kästli, P., Deichmann, N., Massin, F., Grigoli, F., Molinari, I., Böse, M., et al. (2021). Earthquakes in Switzerland and surrounding regions during 2017 and 2018. *Swiss Journal of Geosciences*, 114(1):1–29.

Diehl, T., Husen, S., Kissling, E., and Deichmann, N. (2009). High-resolution 3-DP-wave model of the Alpine crust. *Geophysical Journal International*, 179(2):1133–1147.

Domingues, A., Custodio, S., and Cesca, S. (2013). Waveform inversion of small-to-moderate earthquakes located offshore southwest Iberia. *Geophysical Journal International*, 192(1):248–259.

Dost, B., van Stiphout, A., Kühn, D., Kortekaas, M., Ruigrok, E., and Heimann, S. (2020). Probabilistic moment tensor inversion for hydrocarbon-induced seismicity in the Groningen gas field, the Netherlands, part 2: Application. *Bulletin of the Seismological Society of America*, 110(5):2112–2123.

Dufumier, H. and Cara, M. (1995). On the limits of linear moment tensor inversion of surface wave spectra. *pure and applied geophysics*, 145(2):235–257.

Dziewonski, A., Chou, T.-A., and Woodhouse, J. H. (1981). Determination of earthquake source parameters from waveform data for studies of global and regional seismicity. *Journal of Geophysical Research: Solid Earth*, 86(B4):2825–2852.

Ebel, J. E. (2008). The importance of small earthquakes. *Seismological Research Letters*, 79(4):491–493.

Ekström, G., Nettles, M., and Dziewoński, A. (2012). The global CMT project 2004–2010: Centroid-moment tensors for 13,017 earthquakes. *Physics of the Earth and Planetary Interiors*, 200:1–9.

Evangelidis, C. P., Triantafyllis, N., Samios, M., Boukouras, K., Kontakos, K., Ktenidou, O.-J., Fountoulakis, I., Kalogeras, I., Melis, N. S., Galanis, O., et al. (2021). Seismic Waveform Data from Greece and Cyprus: Integration, Archival, and Open Access. *Seismological Research Letters*.

Faenza, L., Hainzl, S., and Scherbaum, F. (2009). Statistical analysis of the Central-Europe seismicity. *Tectonophysics*, 470(3-4):195–204.

Farr, T. G., Rosen, P. A., Caro, E., Crippen, R., Duren, R., Hensley, S., Kobrick, M., Paller, M., Rodriguez, E., Roth, L., Seal, D., Shaffer, S., Shimada, J., Umland, J., Werner, M., Oskin, M., Burbank, D., and Alsdorf, D. (2007). The Shuttle Radar Topography Mission. *Reviews of Geophysics*, 45(2).

Fry, B., Deschamps, F., Kissling, E., Stehly, L., and Giardini, D. (2010). Layered azimuthal anisotropy of Rayleigh wave phase velocities in the European Alpine lithosphere inferred from ambient noise. *Earth and Planetary Science Letters*, 297(1-2):95–102.

Fuchs, F., Kolínski, P., Bokelmann, G., and the AlpArray Working Group (2016). AlpArray in Austria and Slovakia: technical realization, site description and noise characterization. *Adv Geosci*, 43:1–13.

Giardini, D., Wössner, J., and Danciu, L. (2014). Mapping Europe's seismic hazard. *Eos, Transactions American Geophysical Union*, 95(29):261–262.

Govoni, A., Bonatto, L., Capello, M., Cavaliere, A., Chiarabba, C., D'Alema, E., Danesi, S., Lovati, S., Margheriti, L., Massa, M., et al. (2017). AlpArray-Italy: Site description and noise characterization. *Adv Geosci*, 43:39.

Grützner, C., Aschenbrenner, S., Jamšek Rupnik, P., Reicherter, K., Saifelislam, N., Vičič, B., Vrabec, M., Welte, J., and Ustaszewski, K. (2021). Holocene surface rupturing earthquakes on the Dinaric Fault System, western Slovenia. *Solid Earth Discussions*, pages 1–33.

Gutenberg, B. and Richter, C. F. (1944). Frequency of Earthquakes in California. 34:185–188.

Handy, M., Babist, J., Wagner, R., Rosenberg, C., and Konrad, M. (2005). Decoupling and its relation to strain partitioning in continental lithosphere: insight from the Periadriatic fault system (European Alps). *Geological Society, London, Special Publications*, 243(1):249–276.

Handy, M. R., Schmid, S. M., Bousquet, R., Kissling, E., and Bernoulli, D. (2010). Reconciling plate-tectonic reconstructions of Alpine Tethys with the geological–geophysical record of spreading and subduction in the Alps. *Earth-Science Reviews*, 102(3-4):121–158.

Handy, M. R., Ustaszewski, K., and Kissling, E. (2015). Reconstructing the Alps–Carpathians–Dinarides as a key to understanding switches in subduction polarity, slab gaps and surface motion. *International Journal of Earth Sciences*, 104(1):1–26.

Hardebeck, J. L. and Shearer, P. M. (2002). A new method for determining first-motion focal mechanisms. *Bulletin of the Seismological Society of America*, 92(6):2264–2276.

Heidbach, O., Custodio, C., Kingdon, A., Mariucci, M. T., Montone, P., Müller, B., Pierdominici, S., Rajabi, M., Reinecker, J., Reiter, K., Tingay, M., Williams, J., and Ziegler, M. (2016). Stress map of the Mediterranean and Central Europe 2016.

Heimann, S., Isken, M., Kühn, D., Sudhaus, H., Steinberg, A., Vasyura-Bathke, H., Daout, S., Cesca, S., and Dahm, T. (2018). Grond - A probabilistic earthquake source inversion framework.

Heimann, S., Kriegerowski, M., Isken, M., Cesca, S., Daout, S., Grigoli, F., Juretzek, C., Megies, T., Nooshiri, N., Steinberg, A., Sudhaus, H., Vasyura-Bathke, H., Willey, T., and Dahm, T. (2017). Pyrocko-An open-source seismology toolbox and library.

Heimann, S., Vasyura-Bathke, H., Sudhaus, H., Paul Isken, M., Kriegerowski, M., Steinberg, A., and Dahm, T. (2019). A Python framework for efficient use of pre-computed Green's functions in seismological and other physical forward and inverse source problems. *Solid Earth*, 10:1921–1935.

Heit, B., Cristiano, L., Haberland, C., Tilmann, F., Pesaresi, D., Jia, Y., Hausmann, H., Hemmleb, S., Haxter, M., Zieke, T., et al. (2021). The SWATH-D seismological network in the Eastern Alps. *Seismological Society of America*, 92(3):1592–1609.

Hetényi, G., Molinari, I., Clinton, J., Bokelmann, G., Bondár, I., Crawford, W. C., Dessa, J.-X., Doubre, C., Friederich, W., Fuchs, F., et al. (2018). The AlpArray seismic network: a large-scale European experiment to image the Alpine orogen. *Surveys in geophysics*, 39(5):1009–1033.

Hofman, R., Kummerow, J., Cesca, S., Wassermann, J., and Plenefisch, T. (2020). Local Seismicity in the Eastern Alps From GPU-Based Template Matching. In *EGU General Assembly Conference Abstracts*, page 18781.

Jian, P.-R., Tseng, T.-L., Liang, W.-T., and Huang, P.-H. (2018). A new automatic full-waveform regional moment tensor inversion algorithm and its applications in the Taiwan area. *Bulletin of the Seismological Society of America*, 108(2):573–587.

Jost, M. u. and Herrmann, R. (1989). A student's guide to and review of moment tensors. *Seismological Research Letters*, 60(2):37–57.

Jozi Najafabadi, A., Haberland, C., Ryberg, T., Verwater, V., Le Breton, E., Handy, M. R., Weber, M., and AlpArray working group (2020). Relocation of earthquakes in the Southern and Eastern Alps (Austria, Italy) recorded by the dense, temporary SWATH–D network using a Markov chain Monte Carlo inversion. *Solid Earth Discussions*, pages 1–35.

Kanamori, H. and Rivera, L. (2008). Source inversion of W phase: speeding up seismic tsunami warning. *Geophysical Journal International*, 175(1):222–238.

Kästle, E. D., El-Sharkawy, A., Boschi, L., Meier, T., Rosenberg, C., Bellahsen, N., Cristiano, L., and Weidle, C. (2018). Surface wave tomography of the Alps using ambient-noise and earthquake phase velocity measurements. *Journal of Geophysical Research: Solid Earth*, 123(2):1770–1792.

Kawakatsu, H. (1995). Automated near-realtime CMT inversion. *Geophysical research letters*, 22(19):2569–2572.

Kolínský, P., Bokelmann, G., and Group, A. W. (2019). Arrival angles of teleseismic fundamental mode Rayleigh waves across the AlpArray. *Geophysical Journal International*, 218(1):115–144.

Kummerow, J., Kind, R., Oncken, O., Giese, P., Ryberg, T., Wylegalla, K., Scherbaum, F., Group, T. W., et al. (2004). A natural and controlled source seismic profile through the Eastern Alps: TRANSALP. *Earth and Planetary Science Letters*, 225(1-2):115–129.

Kühn, D., Heimann, S., Isken, M. P., Ruigrok, E., and Dost, B. (2020). Probabilistic Moment Tensor Inversion for Hydrocarbon-Induced Seismicity in the Groningen Gas Field, The Netherlands, Part 1: Testing. *Bulletin of the Seismological Society of America*, 110(5):2095–2111.

Le Breton, E., Brune, S., Ustaszewski, K., Zahirovic, S., Seton, M., and Müller, R. D. (2021). Kinematics and extent of the Piemont–Liguria Basin–implications for subduction processes in the Alps. *Solid Earth*, 12(4):885–913.

Le Breton, E., Handy, M. R., Molli, G., and Ustaszewski, K. (2017). Post-20 Ma motion of the Adriatic Plate: New constraints from surrounding orogens and implications for crust-mantle decoupling. *Tectonics*, 36(12):3135–3154.

Lombardi, D., Braunmiller, J., Kissling, E., and Giardini, D. (2008). Moho depth and Poisson's ratio in the Western-Central Alps from receiver functions. *Geophysical Journal International*, 173(1):249–264.

Mathey, M., Sue, C., Pagani, C., Baize, S., Walpersdorf, A., Bodin, T., Husson, L., Hannouz, E., and Potin, B. (2020). Present-day geodynamics of the Western Alps: new insights from earthquake mechanisms. *Solid Earth Discussions*, pages 1–38.

Maurer, H. and Deichmann, N. (1995). Microearthquake cluster detection based on waveform similarities, with an application to the western Swiss Alps. *Geophysical Journal International*, 123(2):588–600.

Ministrstvo za okolje in prostor Agencija RS za okolje (2020). Potresi v letu 2018 Earthquakes in 2018. *ARSO POTRESI*. ISSN 1318 - 4792.

Molinari, I., Clinton, J., Kissling, E., Hetényi, G., Giardini, D., Stipcevic, J., Dasovic, I., Herak, M., Sipka, V., Wéber, Z., et al. (2016). Swiss-AlpArray temporary broadband seismic stations deployment and noise characterization. *Adv Geosci*, 43:15.

Molinari, I., Verbeke, J., Boschi, L., Kissling, E., and Morelli, A. (2015). Italian and Alpine three-dimensional crustal structure imaged by ambient-noise surface-wave dispersion. *Geochemistry, Geophysics, Geosystems*, 16(12):4405–4421.

Moulin, A., Benedetti, L., Rizza, M., Jamšek Rupnik, P., Gosar, A., Bourles, D., Keddadouche, K., Aumaître, G., Arnold, M., Guillou, V., et al. (2016). The Dinaric fault system: Large-scale structure, rates of slip, and Plio-Pleistocene evolution of the transpressive northeastern boundary of the Adria microplate. *Tectonics*, 35(10):2258–2292.

Mouslopoulou, V., Bocchini, G. M., Cesca, S., Saltogianni, V., Bedford, J., Petersen, G., Gianniou, M., and Oncken, O. (2020). Earthquake Swarms, Slow Slip and Fault Interactions at the Western-End of the Hellenic Subduction System Precede the Mw 6.9 Zakynthos Earthquake, Greece. *Geochemistry, Geophysics, Geosystems*, 21(12):e2020GC009243.

Mouslopoulou, V. and Hristopulos, D. T. (2011). Patterns of tectonic fault interactions captured through geostatistical analysis of microearthquakes. *Journal of Geophysical Research: Solid Earth*, 116(B7).

Niemz, P., Cesca, S., Heimann, S., Grigoli, F., von Specht, S., Hammer, C., Zang, A., and Dahm, T. (2020). Full-waveform-based characterization of acoustic emission activity in a mine-scale experiment: a comparison of conventional and advanced hydraulic fracturing schemes. *Geophysical Journal International*, 222(1):189–206.

Niemz, P., Petersen, G., Cesca, S., Mouslopoulou, V., and G.M., B. (2021). Clusty, A Versatile Waveform-Based Network Similarity Clustering Toolbox . *SSA Annual Meeting Abstract*.

Niksejel, A., Shomali, Z., Cesca, S., and Moradi, A. (2020). Towards a regional, automated full moment tensor inversion for medium to large magnitude events in the Iranian plateau. *Journal of Seismology*, pages 1–17.

Ouillon, G. and Sornette, D. (2011). Segmentation of fault networks determined from spatial clustering of earthquakes. *Journal of Geophysical Research: Solid Earth*, 116(B2).

Pasyanos, M. E., Dreger, D. S., and Romanowicz, B. (1996). Toward real-time estimation of regional moment tensors. *Bulletin of the Seismological Society of America*, 86(5):1255–1269.

Patacca, E., Scandone, P., Di Luzio, E., Cavinato, G. P., and Parotto, M. (2008). Structural architecture of the central Apennines: Interpretation of the CROP 11 seismic profile from the Adriatic coast to the orographic divide. *Tectonics*, 27(3).

Pérez-Guillén, C., Tapia, M., Furdada, G., Suriñach, E., McElwaine, J., Steinkogler, W., and Hiller, M. (2014). Evaluation of a snow avalanche possibly triggered by a local earthquake at Vallée de la Sionne, Switzerland. *Cold Regions Science and Technology*, 108:149–162.

Petersen, G., Cesca, S., Heimann, S., Niemz, P., Dahm, T., Kühn, D., Kummerow, J., Plenefisch, T., and AlpArray Working Group (2021a). Regional centroid MT inversion of small to moderate earthquakes in the Alps using the dense AlpArray seismic network: challenges and seismotectonic insights. *Solid Earth Discussions*, pages 1–38.

Petersen, G., Niemz, P., Cesca, S., Mouslopoulou, V., and Bocchini, G. (2021b). Clusty, the waveform-based network similarity clustering toolbox: concept and application to image complex faulting offshore Zakynthos (Greece). *Geophysical Journal International*, 224(3):2044–2059.

Petersen, G. M., Cesca, S., Kriegerowski, M., and the AlpArray Working Group (2019). Automated Quality Control for Large Seismic Networks: Implementation and Application to the AlpArray Seismic Network. *Seismological Research Letters*, 90(3):1177–1190.

Poli, M. and Zanferrari, A. (2018). The seismogenic source of the 1976 Friuli earthquakes: a new seismotectonic model for the Friuli area. *Bollettino di Geofisica Teorica ed Applicata*, 59.

Pondrelli, S. (2002). European-Mediterranean Regional Centroid-Moment Tensors Catalog (RCMT) [Data set]. *Istituto Nazionale di Geofisica e Vulcanologia (INGV)*.

Pondrelli, S., Ekström, G., and Morelli, A. (2001). Seismotectonic re-evaluation of the 1976 Friuli, Italy, seismic sequence. *Journal of Seismology*, 5(1):73–83.

Pondrelli, S., Salimbeni, S., Ekström, G., Morelli, A., Gasperini, P., and Vannucci, G. (2006). The Italian CMT dataset from 1977 to the present. *Physics of the Earth and Planetary Interiors*, 159(3-4):286–303.

Quinteros, J., Strollo, A., Evans, P. L., Hanka, W., Heinloo, A., Hemmleb, S., Hillmann, L., Jaeckel, K.-H., Kind, R., Saul, J., et al. (2021). The GEOFON Program in 2020. *Seismological Research Letters*.

Reiter, F., Freudenthaler, C., Hausmann, H., Ortner, H., Lenhardt, W., and Brandner, R. (2018). Active seismotectonic deformation in front of the Dolomites indenter, Eastern Alps. *Tectonics*, 37(12):4625–4654.

Ross, Z. E., Trugman, D. T., Hauksson, E., and Shearer, P. M. (2019). Searching for hidden earthquakes in Southern California. *Science*, 364(6442):767–771.

Schmid, S. M., Bernoulli, D., Fügenschuh, B., Matenco, L., Schefer, S., Schuster, R., Tischler, M., and Ustaszewski, K. (2008). The Alpine-Carpathian-Dinaridic orogenic system: correlation and evolution of tectonic units. *Swiss Journal of Geosciences*, 101(1):139–183.

Schmid, S. M., Fügenschuh, B., Kissling, E., and Schuster, R. (2004). Tectonic map and overall architecture of the Alpine orogen. *Eclogae Geologicae Helvetiae*, 97(1):93–117.

Scognamiglio, L., Tinti, E., and Quintiliani, M. (2006). Time Domain Moment Tensor (TDMT). Istituto Nazionale di Geofisica e Vulcanologia (INGV). *[Data set]*.

Sen, A. T., Cesca, S., Bischoff, M., Meier, T., and Dahm, T. (2013). Automated full moment tensor inversion of coal mining-induced seismicity. *Geophysical journal international*, 195(2):1267–1281.

Serpelloni, E., Vannucci, G., Anderlini, L., and Bennett, R. A. (2016). Kinematics, seismotectonics and seismic potential of the eastern sector of the European Alps from GPS and seismic deformation data. *Tectonophysics*, 688:157–181.

Shearer, P. M., Hardebeck, J. L., Astiz, L., and Richards-Dinger, K. B. (2003). Analysis of similar event clusters in aftershocks of the 1994 Northridge, California, earthquake: NORTHRIDGE SIMILAR EVENT CLUSTERS. *Journal of Geophysical Research: Solid Earth*, 108(B1).

Shelly, D. R., Hardebeck, J. L., Ellsworth, W. L., and Hill, D. P. (2016). A new strategy for earthquake focal mechanisms using waveform-correlation-derived relative polarities and cluster analysis: Application to the 2014 Long Valley Caldera earthquake swarm: A New Strategy for Focal Mechanisms. *Journal of Geophysical Research: Solid Earth*, 121(12):8622–8641.

Slejko, D. (2018). What science remains of the 1976 Friuli earthquake? *Bollettino di Geofisica Teorica ed Applicata*, 59(4):327–350.

Spada, M., Bianchi, I., Kissling, E., Agostinetti, N. P., and Wiemer, S. (2013). Combining controlled-source seismology and receiver function information to derive 3-D Moho topography for Italy. *Geophysical Journal International*, 194(2):1050–1068.

Stähler, S. C. and Sigloch, K. (2014). Fully probabilistic seismic source inversion–Part 1: Efficient parameterisation. *Solid Earth*, 5(2).

Sternai, P., Sue, C., Husson, L., Serpelloni, E., Becker, T. W., Willett, S. D., Faccenna, C., Di Giulio, A., Spada, G., Jolivet, L., et al. (2019). Present-day uplift of the European Alps: Evaluating mechanisms and models of their relative contributions. *Earth-Science Reviews*, 190:589–604.

Stich, D., Ammon, C. J., and Morales, J. (2003). Moment tensor solutions for small and moderate earthquakes in the Ibero-Maghreb region: IBERO-MAGHREBIAN MOMENT TENSOR SOLUTIONS. *Journal of Geophysical Research: Solid Earth*, 108(B3).

Stuermer, K., Kummerow, J., and Shapiro, S. A. (2011). Waveform Similarity Analysis at Cotton Valley, Texas. *SEG San Antonio 2011 Annual Meeting*, pages 1669–1673.

Sue, C., Delacou, B., Champagnac, J.-D., Allanic, C., and Burkhard, M. (2007). Aseismic deformation in the Alps: GPS vs. seismic strain quantification. *Terra Nova*, 19(3):182–188.

Sue, C., Thouvenot, F., Fréchet, J., and Tricart, P. (1999). Widespread extension in the core of the western Alps revealed by earthquake analysis. *Journal of Geophysical Research: Solid Earth*, 104(B11):25611–25622.

TRANSALP Working Group, Gebrande, H., Lüschen, E., Bopp, M., Bleibinhaus, F., Lammerer, B., Oncken, O., Stiller, M., Kummerow, J., Kind, R., et al. (2002). First deep seismic reflection images of the Eastern Alps reveal giant crustal wedges and transcrustal ramps. *Geophysical Research Letters*, 29(10):92–1.

Trifu, C., Angus, D., and Shumila, V. (2000). A fast evaluation of the seismic moment tensor for induced seismicity. *Bulletin of the Seismological Society of America*, 90(6):1521–1527.

Vackář, J., Burjánek, J., Gallovič, F., Zahradník, J., and Clinton, J. (2017). Bayesian ISOLA: New tool for automated centroid moment tensor inversion. *Geophysical Journal International*, 210(2):693–705.

Van Hinsbergen, D. J., Torsvik, T. H., Schmid, S. M., Maţenco, L. C., Maffione, M., Vissers, R. L., Gürer, D., and Spakman, W. (2020). Orogenic architecture of the Mediterranean region and kinematic reconstruction of its tectonic evolution since the Triassic. *Gondwana Research*, 81:79–229.

Vecsey, L., Plomerová, J., Jedlicka, P., Munzarová, H., Babuska, V., and the AlpArray Working Group (2017). Data quality control and tools in passive seismic experiments exemplified on the Czech broadband seismic pool MOBNET in the AlpArray collaborative project. *Geosci Instrum Method Data Syst*, 6:505–521.

Viganò, A., Bressan, G., Ranalli, G., and Martin, S. (2008). Focal mechanism inversion in the Giudicarie–Lessini seismotectonic region (Southern Alps, Italy): insights on tectonic stress and strain. *Tectonophysics*, 460(1-4):106–115.

Wang, X. and Zhan, Z. (2020). Moving from 1-D to 3-D velocity model: automated waveform-based earthquake moment tensor inversion in the Los Angeles region. *Geophysical Journal International*, 220(1):218–234.

Wyss, M. and Brune, J. N. (1968). Seismic moment, stress, and source dimensions for earthquakes in the California-Nevada region. *Journal of Geophysical Research*, 73(14):4681–4694.

Zahradník, J. and Sokos, E. (2018). Fitting waveform envelopes to derive focal mechanisms of moderate earthquakes. *Seismological Research Letters*, 89(3):1137–1145.

Acknowledgments

First of all, I would like to thank my PhD supervisors Simone Cesca and Torsten Dahm for their support and mentoring during the work on this thesis. I am grateful for the supportive and inspiring working environments at GFZ, Uni Potsdam and within the AlpArray project. Thanks to all colleges for scientific discussions and lots of open doors and ears.

Außerdem möchte ich meinen Eltern und meiner Familie danken - für alles, und insbesondere dafür, dass ihr mich immer ermuntert habt, meinen Interessen zu folgen. Ein riesen-mega-großes Danke geht an Matthias, für viele tolle gemeinsame Jahre, und auch an alle Freund*innen und Kolleg*innen, Berliner*innen, (Ex-)Potsdamer*innen und (Ex-)Nordfries*innen, die mich in den letzten Jahren begleitet haben –> Carla, Djamil, Elif, Elli, Henning, Malte, Marcel, Marius, Martin, Nima, Oke, Ole, Peter, Philine, Pia, Sophia, Steffi, Tim, Yannic und alle HeartOfCodelerinnen <– Ihr macht das Leben schöner! Lots of love! Nach viel getaner und noch viel mehr vor uns liegenden Arbeit noch ein großes Danke an Peter für endlos viele Diskussionen und herausragende Zusammenarbeit.

Finally, I am grateful for financial support from the AlpArray initiative and the DFG project 'From Top to Bottom - Seismicity, Motion Patterns and Stress Distribution in the Alpine Crust' (Project Number 362440331), a subproject of 'SPP 2017: Mountain Building Processes in 4D' (Project Number 313806092).